

Utah State University

DigitalCommons@USU

All Graduate Theses and Dissertations, Spring
1920 to Summer 2023

Graduate Studies

5-2014

The Kimama Core: A 6.4 Ma Record of Volcanism, Sedimentation, and Magma Petrogenesis on the Axial Volcanic High, Snake River Plain, ID

Katherine Elizabeth Potter
Utah State University

Follow this and additional works at: <https://digitalcommons.usu.edu/etd>

 Part of the [Geology Commons](#)

Recommended Citation

Potter, Katherine Elizabeth, "The Kimama Core: A 6.4 Ma Record of Volcanism, Sedimentation, and Magma Petrogenesis on the Axial Volcanic High, Snake River Plain, ID" (2014). *All Graduate Theses and Dissertations, Spring 1920 to Summer 2023*. 3872.

<https://digitalcommons.usu.edu/etd/3872>

This Dissertation is brought to you for free and open access by the Graduate Studies at DigitalCommons@USU. It has been accepted for inclusion in All Graduate Theses and Dissertations, Spring 1920 to Summer 2023 by an authorized administrator of DigitalCommons@USU. For more information, please contact digitalcommons@usu.edu.



THE KIMAMA CORE: A 6.4 Ma RECORD OF VOLCANISM, SEDIMENTATION, AND MAGMA
PETROGENESIS ON THE AXIAL VOLCANIC HIGH, SNAKE RIVER PLAIN, ID

by

Katherine Elizabeth Potter

A dissertation submitted in partial fulfillment
of the requirements for the degree

of

DOCTOR OF PHILOSOPHY

in

Geology

Approved:

Dr. John Shervais
Major Professor

Dr. Anthony Lowry
Committee Member

Dr. James Evans
Committee Member

Dr. Carol Dehler
Committee Member

Dr. Paul Link
Committee Member

Dr. Mark McLellan
Vice President for Research
and Dean of the School of
Graduate Studies

UTAH STATE UNIVERSITY
Logan, Utah

2014

Copyright © Katherine Elizabeth Potter 2014

All Rights Reserved

ABSTRACT

The Kimama core: a 6.4 Ma record of volcanism, sedimentation, and magma petrogenesis
on the Axial Volcanic High, Snake River Plain, Idaho

by

Katherine Elizabeth Potter, Doctor of Philosophy

Utah State University, 2014

Major Professor: Dr. John Shervais
Department: Geology

The Snake River Plain (SRP) is one of the youngest and best-preserved examples of continental hotspot volcanism, with a continuous record of volcanism that extends over 16 Ma to the present. As part of the Yellowstone-Snake River Plain volcanic province, the Snake River records the migration of plume-tail volcanism from inception at the Bruneau-Jarbridge caldera complex at 12.6 Ma to its present locus, under the Yellowstone Plateau. Hotspot volcanic products on the Snake River Plain include rhyolite lavas and ignimbrites, minor coeval basalts, and an overlying veneer of younger basalts erupted from fissures and low shield volcanoes.

Although the eastern SRP has been the focus of scientific drilling in the past, the central SRP has received comparatively little attention. The Kimama core hole was drilled as part of Project Hotspot, the Snake River Scientific Drilling Project, which seeks to understand the long-term volcanic and sediment logical history of the SRP volcanic province. The central SRP is the

hinge point between the older western SRP province and the younger eastern province, and represents a transition between Pleistocene bimodal volcanism and the Pleistocene through Holocene olivine tholeiite basalt volcanism. It is the only part of the SRP that has not been scientifically drilled and cored to a significant depth. Investigations of subsurface stratigraphy in continental volcanic provinces such as the SRP-YP are limited by the limited depth and spatial distribution of cored wells. The Kimama core is a continuous record of basalt and minor sediment deposition.

Our investigation of the Kimama core reveals a dynamic relationship between magmatic systems, volcanic processes, and the topography of the SRP over the past ~6.4 Ma. The long-term volcanic history of the SRP, documented by magmatic flux and magma composition, demonstrates that magmatism is mantle plume-derived and does not represent melting of a shallow mid-ocean ridge basalt-source within the asthenosphere. Our investigation of the Kimama core, combined with new mantle tomography, refutes non-plume models for the origin of the Snake River Plain volcanic province.

(173 pages)

PUBLIC ABSTRACT

The Kimama core: a 6.4 Ma record of volcanism, sedimentation, and magma petrogenesis
on the Axial Volcanic High, Snake River Plain, Idaho

Katherine Elizabeth Potter

The Snake River Plain (SRP) is one of the best-preserved examples of continental hotspot volcanism, with a continuous record of volcanism that extends over 16 Ma to the present. Yellowstone-Snake River Plain records the migration of plume-tail volcanism from inception at the Bruneau-Jarbridge caldera complex at 12.6 Ma to its present locus, under the Yellowstone Plateau.

Records kept by the Snake River Plain volcanic actions include rhyolite lavas and ignimbrites, minor coeval basalts, and an overlying veneer of younger basalts. The central SRP has received comparatively little attention in the past. The Kimama core hole was drilled as part of Project Hotspot, the Snake River Scientific Drilling Project, which seeks to understand the long-term volcanic and sediment logical history of the SRP volcanic province.

The Kimama core hole is the only part of the SRP that has not been scientifically drilled and cored to a significant depth in the past. Investigations of subsurface stratigraphy in continental volcanic provinces such as the SRP-YP are limited by the by the relatively low depth and spatial distribution of cored wells. The study of the Kimama core provides us with a continuous record of basalt and minor sediment deposition.

The long-term volcanic history of the SRP, documented by moving magma and its composition, demonstrates that magmatism is mantle plume-derived. Our investigation of the Kimama core, combined with new mantle tomography, provides evidence that refutes non-plume models for the origin of the Snake River Plain volcanic province.

ACKNOWLEDGMENTS

As I reflect upon my years at Utah State, I am filled with gratitude towards the many people that made my experience so fantastic. I feel privileged to have known and worked with many amazing researchers, including my marvelous committee. Jim Evans, Paul Link, Tony Lowry, and Carol Dehler provided support and stimulating discussion to help guide my progress through the Ph.D. gauntlet. I am especially lucky to have had the pleasure of having John Shervais as my advisor and mentor. John's approachability, sense of humor, and scientific brilliance made him an invaluable resource for all of my questions regarding petrology and geochemistry on the Snake River Plain.

This work was supported by DOE award DE-EE0002848, by the International Continental Drilling Program (ICDP), and by a consortium of universities. George Gehrels and Mark Pecha at Arizona State University LaserChron Center provided lab time and helped with detrital zircon data interpretation. Scott Vetter (Centenary College) provided some of the trace element data. Robert Duncan of Oregon State University provided Ar/Ar data and interpretation, and Duane Champion of the USGS Menlo Park performed the paleomagnetic age dating and interpretation

Discussions with Eric Christiansen and the Hotspot Science Team (http://www.usu.edu/geo/shervais/Shervais-USU-Geology/Hotspot_Science_Team.html) were especially helpful, but any errors are our own.

My dissertation greatly benefitted from useful feedback from my fellow graduate students, including Mitch Prante, Dawn Hayes, Robin Nagy, Santiago Flores, Elizabeth Petrie, Kelly Bradbury, Marlon Jean, and Natalie Bursztyn, and from the assistance of the Project Hotspot student researchers. Jeff Hazboun, my brother in Ph.D suffering, was a great motivating force in completing the writing phase. Lastly, but most importantly, my parents,

family, and friends soothed my crazy episodes and increased my quotient of fun. To them I will be eternally grateful for listening to my grievances, distracting me through skiing and playing music, and encouraging me to stay the course.

Lastly, and most importantly, I'd like to dedicate this dissertation to my magnificent Great Uncle, Roderick Burnham Potter. Through these 6 years of graduate school, his encouragement and support have made the difference between my success and failure, and I'm so proud to be his "little critter".

Katherine Potter

CONTENTS

	Page
ABSTRACT	iii
PUBLIC ABSTRACT.....	v
ACKNOWLEDGMENTS.....	vi
LIST OF TABLES.....	x
LIST OF FIGURES.....	xi
CHAPTER	
1. INTRODUCTION.....	1
References.....	8
2. VOLCANIC STRATIGRAPHY AND AGE MODEL OF THE KIMAMA DEEP CORE HOLE (PROJECT HOTSPOT), CENTRAL SNAKE RIVER PLAIN, IDAHO	16
Abstract.....	16
Approach.....	19
Geologic Background.....	21
Methods.....	26
Results.....	31
Discussion.....	45
Conclusion.....	50
References.....	52
3. PETROLOGIC AND GEOCHEMICAL EVOLUTION OF BASALTS FROM THE KIMAMA 1912 M CORE HOLE, CENTRAL IDAHO	58
Abstract.....	58
Introduction.....	59
Geological Background.....	61

	ix
Methods	65
Results	66
Discussion.....	82
Conclusion	96
References.....	98
4. EVIDENCE FOR AN AXIAL VOLCANIC LOW IN THE KIMAMA CORE: HEISE FIELD VOLCANOGENIC ZIRCONS AND THE LATE MIOCENE PALEO-WOOD RIVER IN THE CENTRAL SNAKE RIVER PLAIN	104
Abstract	104
Introduction	106
Methods	111
Results	115
Discussion.....	124
Conclusion	134
References.....	135
5. CONCLUSION.....	143
APPENDIX.....	146
Curriculum Vitae.....	158

LIST OF TABLES

Table		Page
1	Summary of flows and flow units of the Kimama core	34
2	Paleomagnetic Chrons and Subchrons by depth.	41
3	^{40}Ar - ^{39}Ar age determinations for Kimama well core	44
4	Kimama core bulk rock elemental analyses.....	68-78
5	Actual and reverse fractionation compositional results for Kimama basalts.....	95
6	Regional SRP detrital zircon populations..	111
7	Detrital zircon U-Pb age data for the Kimama core hole.	116-117
8	U-Pb and Hf isotope data for sample KZ5737, 1749 m depth, and for KZ6050, 1844 m depth.....	123
9	U-Pb ages of Heise volcanic field eruptive units and volcanic detrital zircons of the Kimama core	130
App.	Stratigraphic and geochemical data used to determine flow unit, flow, flow groups And super group boundaries.	145

LIST OF FIGURES

Figure	Page
1	A shaded relief map of Idaho and the SRP. 5
2	Schematic illustration of plains-style volcanism on the eastern SRP. 23
3	Spatial relationship between inflated pahoehoe flow units, flows, and flow groups in map and cross section views. 24
4	Facies model of typical inflated basalt core as observed in the Kimama core. 27
5	Lithologic and paleomagnetic stratigraphy of the Kimama core 33
6	Composite lithologic, natural gamma, and neutron logs from 0 to 610 m in the Kimama corehole. 38
7	Plots of paleomagnetic polarity and inclination, major ratios plotted against depth for Kimama basalts 40
8	Kimama corehole age vs. depth 41
9	Step age spectra and Ar/Ar isotope correlation diagrams..... 44
10	Schematic cartoon showing calculations for SRP magmatic flux over an area of 100 km ² and a depth of 2 km..... 49
11	Map of the SRP showing the location of the Kimama core hole in relation to inferred locations of silic volcanic centers..... 62
12	Selected major and trace element variation diagrams with compositions of Kimama basalts and olivine tholeiites..... 79
13	Selected trace element depths..... 80
14	Selected major and trace element variation diagrams showing chemical trends evident in the four Kimama compositional types..... 81
15	A) Multielement spider diagram and B) rare earth element plot of Kimama basalt samples 82
16	Generalized stratigraphic column, mean paleomagnetic inclination (A), and selected chemical composition of the Kimama core as a function of depth below the surface (B). 85-86

17	COMAGMAT variation diagrams.....	89
18	Crystallization model of expected differentiation processes for Kimama basalts.....	90
19	Multielement spider diagrams normalized to primitive mantle.....	93
20	Digital elevation map (DEM) of thr SRP and Yellowstone regions showing the location of Kimama as well as topographic and geologic features.....	107
21	Lithologic and paleomagnetic stratigraphy of the Kimama core.....	108
22	Thin sections photomicrographs.....	118
23	Paleomagnetic and lithologic stratigraphy of the Kimama core showing locations of sampled intervals and detrital zircon age populations.....	119
24	Cathodoluminescence (CL) image of detrital zircons mounted in grain mounts.....	122
25	Bar graphs of U-Pb ages.....	125
26	Location map of Snake River Plain-Yellowstone eruptive centers.....	131
27	Plot of average values plotted against average values U-Pb age (Ma).....	132

CHAPTER I

INTRODUCTION

The Snake River Plain (SRP) is a 500 km long arcuate region of low relief in southern Idaho, bordered to the north and south by Basin and Range topography with its northeast apex at Yellowstone National Park. As one of the youngest and best-preserved examples of a continental hotspot volcanic province, the Yellowstone-Snake River Plain (Y-SRP) region contains a continuous record of rhyolite and post-rhyolite basaltic volcanism that extends from 12.6 Ma to the present (Pierce and Morgan, 1992; Pierce et al., 2000; Camp and Ross, 2004; Waite et al., 2006; Smith et al., 2009). The SRP records the migration of silicic volcanism from inception at the Bruneau-Jarbridge caldera complex in SW Idaho to the current locus under the Yellowstone Plateau (Pierce and Morgan, 1992; Bonnicksen et al., 2008; Shervais et al., 2006; Hanan et al., 2008). Interaction between the Y-SRP plume and overlying lithosphere has resulted in large-scale caldera-forming eruptions, and smaller-output, quiescent basaltic volcanism (Pierce et al., 2002; Mason et al., 2004; Pierce and Morgan, 2009). Rhyolite-coeval basalts exhibit compositions akin to mantle-derived melts, and post-rhyolite basalts are compositionally similar to tholeiitic ocean island basalts, such as those present in Hawaii (Kuntz et al., 1992; Hughes et al., 2002a).

Time-transgressive linear chains of volcanics, broad regions of topographic tumescence, and associated geoid anomalies are all distinct features of hotspot volcanism (Morgan, 1972; Crough, 1978, 1983; Davies, 1988; Sleep, 1990, 1992; Burov and Guillou-Frottier, 2005; Ito and van Keken, 2007; Burov et al., 2007). Along the 700-km long, eastward-younging Y-SRP chain of

silicic calderas, volcanism has modified the composition of the continental lithosphere (Morgan, 1971, 1972; Matthews and Anderson, 1973; Smith and Sbar, 1974; Armstrong et al., 1975; Smith, 1977; Bonnicksen, 1982; Morgan et al., 1984; Pierce and Morgan, 1990, 1992; Kuntz et al., 1992; Smith and Braile, 1994; Morgan et al., 1995; DeNosaquo et al., 2009). The Yellowstone geoid anomaly is a 15 m + dynamically-uncompensated topographic high that represents a zone of low-density lithospheric-asthenospheric material and mass deficit beneath the North American plate (Richards et al., 1994; Waschbusch and McNutt et al., 2009). An accounting of geophysical, structural, geochemical, and volcanological observations has led to wide acceptance that the explanation for the volcanic and physiographic features present in the SRP is the interaction between a deep mantle hotspot and the continental lithosphere (Pierce and Morgan, 1992; Anders, 1994; Smith and Braile, 1994; Saltzer and Humphreys, 1997; Camp and Ross, 2004; Shervais and Hanan, 2008; Smith et al., 2009).

Various other models of lithospheric and mantle-driven processes have been suggested for the formation of the Y-SRP volcanic province, including a propagating rift (Christiansen and McKee, 1978), edge-driven mantle convection (King and Anderson, 1998; King, 2007), a self-sustaining convective roll (Humphreys et al., 2000), and mantle upwelling through a Farallon slab gap (James et al., 2011). While these models explain some of the features unique to the Y-SRP volcanic province, most rely on a shallow asthenosphere source for post-rhyolite basaltic magmatism, similar to mid-ocean ridge basalts, which are typically depleted in incompatible trace elements.

As imaged by seismic data, the subsurface of the SRP is thought to be comprised of Paleozoic clastic and carbonate rocks and Miocene granites associated with magmatism from 6-10 km (Sparlin et al., 1982). Gravity and seismic data indicate a 2-5 km thick package of Miocene-Pliocene rhyolite lavas, tuffs, and epizonal granitic plutons above 6 km depth (Braile et

al., 1982; Sparlin et al., 1982). Regionally, drilling has indicated a ~1-2 km veneer of Pliocene-Pleistocene tholeiitic basalt, interbedded with sparse ferro-basalt lava flows and minor eolian, fluvial, and lacustrine sediments that overlie silicic volcanic products on the SRP (Doherty et al., 1979; Kuntz et al., 1992; Anderson and Liszewski, 1997). The emplacement of a dense mafic mid-crustal sill is thought to have caused subsidence of the SRP volcanic province; subsidence caused by the mafic mid-crustal sill is ongoing (Braile et al., 1982; Sparlin et al., 1982; Mabey et al., 1978; McQuarrie and Rodgers, 1998; Rodgers et al., 2002).

The SRP exhibits both vestiges of Y-SRP hotspot track-related silicic volcanism and its own unique petrogenetic and geochemical basaltic volcanic processes and products (Leeman, 1982a; Kuntz et al., 1992; Pierce and Morgan, 1992, 2009; Reid, 1995; Hanan et al., 1997; Hughes et al., 2002a,b; Geist et al., 2002; Shervais et al., 2006, Shervais and Hanan, 2008). Associated processes of assimilation, fractionation, solidification and remelting resulted in the bimodal volcanic products that characterize the SRP volcanic province (Leeman, 1982a; Hildreth et al., 1991; Hughes et al., 1999; McCurry and Rodgers, 2009; Leeman et al., 2009). Post-rhyolite mafic volcanism on the SRP began within 1 m.y. of the cessation of hotspot-track-related silicic volcanism, and has been primarily expressed by the eruption and coalescence of monogenetic, olivine tholeiite basalt shields with relatively primitive, high MgO compositions (Hughes et al., 2002b). The ubiquitous olivine tholeiite lavas of the SRP are distinguished by major MORB-like depleted mantle chemical signatures (Hart and Carlson, 1987; Carlson and Hart, 1988) as well as chemical signatures indicative of sub-continental lithospheric mantle (Leeman, 1982b; Hart and Carlson, 1987).

The topographic effects of Y-SRP hotspot magmatism during the Pliocene and Pleistocene were the development of east-northeast-migrating continental divides and related

northeastward-successive drainage captures by tributaries to the west-flowing Snake River (Pierce and Morgan, 1992; Fritz and Sears, 1993; Ore, 1999; Pierce et al., 2002; Beranek et al., 2006; Sears and Thomas, 2007). Fluvial sand deposits within the SRP preserve evidence of drainages modified by thermal uplift and subsidence associated with the migration of silicic volcanism (Beranek et al., 2006; Hodges et al., 2009). From the Miocene to the Holocene, regional drainage patterns and the history of sedimentation in the SRP can be constrained using the presence or absence of specific age-populations of detrital zircon grains. Several unique zircon point sources are located at the headwaters of stream systems in the Snake River watershed, providing an age-correlated framework upon which to identify the fluvial sources of detrital zircon grains (i.e. Geslin et al., 1999; Mahoney et al., 1999; Link et al., 2002, 2005; Beranek et al., 2006; Hodges et al., 2009). Of particular relevance to the Kimama core, fluvial sands intercalated between basalt flows demonstrate topographic and drainage system development and can provide depositional age constraints using the U-Pb ages of detrital zircons.

Although the eastern SRP has been the focus of scientific drilling in the past, the central SRP has received comparatively little attention. The central SRP is the transitional region between the older western SRP province and the younger eastern province, and represents a transition between late Miocene bimodal volcanism and the Pleistocene through Holocene olivine tholeiite basalt volcanism (Armstrong et al., 1975; Pierce and Morgan, 1992). It is the only part of the SRP that has not been scientifically drilled and cored.

The Kimama core hole (Fig. 1) was drilled as part of Project Hotspot, the Snake River Scientific Drilling Project (Shervais et al., 2013), which seeks to understand the long-term volcanic and sedimentological history of the SRP volcanic province and its potential as a

geothermal resource. Understanding the volcanic and sedimentary stratigraphy is made possible by the recovery of core, but is augmented by geophysical wire line data including natural gamma and neutron logs. These data sets, used in conjunction, provide a clear record of deposition and hiatus in the 1912 m of continuous core. Investigations of subsurface stratigraphy in continental volcanic provinces such as the Y-SRP are limited by the depth and spatial distribution of cored wells. The Kimama core hole is one of three core holes drilled through Project Hotspot, and is a continuous record of basalt and minor sediment deposition.

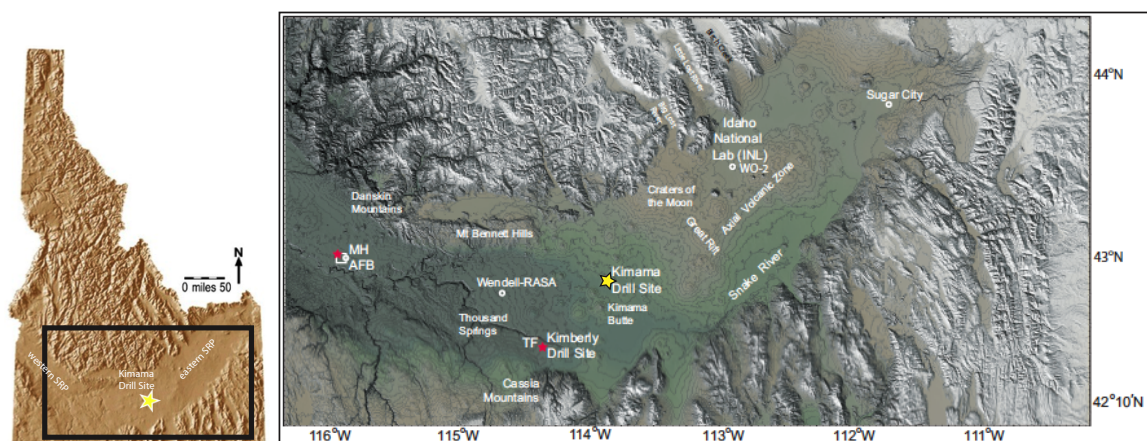


Figure 1: A shaded relief map of Idaho and the Snake River Plain (SRP) region showing locations of Project Hotspot drill sites (red stars) and older drill sites (open circles). The Kimama drill site (yellow star) is located at the hinge point between the western SRP and the eastern SRP, along the trace of the Axial Volcanic Zone. Twin Falls (TF) and Mountain Home Air Force Base (MH AFB) are shown for reference. The image is derived from NASA 10-m DEM data and contoured to 30 m intervals (modified from Shervais et al., 2013).

Based upon observations of existing core, workers have shown that cycles of upward increases in incompatible oxides such as K_2O and TiO_2 demonstrates magma fractionation. Magma replenishment is revealed by upsection increases in MgO and Cr , suggesting that the lavas reflect a system in which periodic recharge of more mafic magmas interrupts fractionation in a layered mafic sill complex (Geist et al., 2002; Hughes et al., 2002a; Shervais et al., 2006). Older basalts show chemical and isotopic variations indicative of assimilation of continental crust, whereas younger basalts pass through and assimilate genetically related crystallized melts of the layered magma system (Shervais et al., 2006; Jean et al., 2013). The proof of these interactions is the decoupling of major and trace element fractionation without substantial variation in isotopic composition (Shervais et al., 2006). SRP basalts are compositionally similar to Hawaiian basalts in their major and trace element chemistry (Hughes et al., 2002b).

Due to the subsidence and lack of uplift of the SRP, a complete analysis of the evolution of volcanism can only be obtained through drilling (Shervais et al., 2014). A core provides a powerful tool in understanding the dynamics of plume-related volcanism. Recent and ongoing studies have focused attention on hotspot activity in oceanic lithosphere (HSDP, IODP) (DePaolo and Weis, 2007), but hotspot volcanism within continental lithosphere is both more complex and less well studied.

My primary focus in the study of the Kimama core is: 1) how have the physical characteristics, frequency, and volume of post-rhyolitic SRP volcanism changed through time, and are these changes related to compositional variation? 2) Of broader importance, how do mantle hotspots interact with continental lithosphere through time, and how does this interaction affect the geochemistry of generated magmas? 3) We also hope to address: how has Y-SRP hotspot volcanism affected the topography and drainage development of the SRP, and what do populations of detrital zircon grains in cored fluvial sands tell us about the tectonic and

physiographic evolution of the SRP region? Finally, can observations of the Kimama core corroborate recent mantle tomography data in support of the mantle plume magmatic source hypothesis?

These major questions regarding the formation and evolution of the SRP volcanic province are addressed in this dissertation; and the results are presented four chapters and a concluding chapter. These chapters are as follows.

Chapter 2 describes volcanic stratigraphy and the record of basaltic volcanism and sedimentological processes through time. Here, I document the lithostratigraphy of basaltic lavas in the Kimama core, including flow and flow unit thickness, volcanic facies, the presence of sediment interbeds, and contact relationships. Using lithologic observations, wire line geophysical logs, and radiometric and paleomagnetic dating, I interpret the volcanic record and magmatic flux in the central SRP. Magma flux is a measure of the frequency and duration of volcanism through time. Distinct magmatic episodes, or flow groups, are identified through major and trace element geochemistry. I seek to identify the stratigraphic distribution of basaltic lavas in the Kimama core and to determine their temporal geochemical variability.

Chapter 3 addresses the geochemical and petrological evolution of basaltic lavas in the Kimama core. Using my established stratigraphy, the major and trace element geochemistry of cored basalts are used to locate, identify, and group geochemically-distinct flows into four compositional suites. Geochemical-stratigraphic trends within the Kimama core reveals the variable effect of fractionation, magma recharge, mixing, and assimilation of continental crust within the layered mafic sill complex. Forward and reverse fractionation modeling of compositionally primitive Kimama basalts illustrates potential genetic relationships between the

four geochemical suites identified in the Kimama core, and demonstrates whether the suites underwent similar petrogenetic processes.

Chapter 4 examines the U-Pb dating of detrital and volcanic zircon populations and volcanic zircon Lu-Hf isotope chemistry in the Kimama core. Detrital zircons recovered from sediment interbeds at 1707 and 1844 m depth and analyzed for U-Pb ages constrain periods of stream incursion and diversion. Detrital zircon geochronology is used to illustrate the timing of regional uplift and exhumation, silicic volcanism, and regional subsidence. Populations of Neogene volcanic zircons in lower interbeds were analyzed for Hf isotopes to interpret the origin of Y-SRP silicic volcanism. Epsilon Hf provides a measure of the amount of juvenile, or mantle-like magma, incorporated into a system, and therefore, the amount of crustal vs. plume material contributing to silicic volcanism on the SRP.

Chapter 4 summarizes the observations of magmatic flux, magma composition, and sediment deposition from previous chapters and integrates them into the greater history of topographic and magmatic evolution on the SRP. Finally, we state that SRP magmatism is derived from a mantle plume source rather than a non-plume, shallow mantle magma source.

References

- Anders, M.H., 1994, Constraints on North American plate velocity using the Yellowstone hotspot deformation field: *Nature*, v. 369, p. 53–55.
- Anderson, S.R., and Liszewski, M.J., 1997, Stratigraphy of the unsaturated zone and the Snake River Plain Aquifer at and near the Idaho National Engineering Laboratory, Idaho: U.S. Geological Survey Water-Resources Investigations Report 97-4183, 70 p.
- Armstrong, R.L., Leeman, W.P., and Malde, H.E., 1975, K-Ar dating, Quaternary and Neogene rocks of the Snake River Plain, Idaho: *American Journal of Science*, v. 275, p. 225-251.

- Beranek, L.P., Link, P. K., and Fanning, C.M., 2006, Miocene to Holocene landscape evolution of the western Snake River Plain region, Idaho: Using the SHRIMP detrital zircon provenance record to track eastward migration of the Yellowstone hotspot: *GSA Bulletin*, v. 118, p. 1027-1050.
- Bonnichsen, B., 1982, The Bruneau---Jarbidge eruptive center, southwestern Idaho, *in* Bonnichsen, B. and Breckenridge, R. M., eds., *Cenozoic Geology of Idaho*. Idaho Bureau of Mines and Geology Bulletin, v. 26, p. 237-254.
- Bonnichsen, B., Leeman, W. P., Honjo, N., McIntosh, W. C., and Godchaux, M. M., 2008, Miocene silicic volcanism in southwestern Idaho: geochronology, geochemistry, and evolution of the central Snake River Plain: *Bulletin of Volcanology*, v. 70(3), p. 315-342.
- Braile, L.W., Smith, R.B., Ansorge, J., Baker, M.R., Sparlin, M.A., Prodehl, C., Schilly, M.M., Healy, J.H., Mueller, S., Olsen, K.H., 1982, The Yellowstone–Snake River Plain seismic profiling experiment: crustal structure of the eastern Snake River Plain: *Journal of Geophysical Research* v. 87, p. 2597–2609.
- Burov, E., and Guillou-Frottier, L., 2005, The plume head–continental lithosphere interaction using a tectonically realistic formulation for the lithosphere: *Geophysical Journal International*, v. 161(2), p. 469-490.
- Burov, E., Guillou-Frottier, L., d'Acremont, E., Le Pourhiet, L., and Cloetingh, S. A. P. L., 2007, Plume head–lithosphere interactions near intra-continental plate boundaries: *Tectonophysics*, v. 434(1), p. 15-38.
- Camp, V.E., and Ross, M.E., 2004, Mantle Dynamics and Genesis of Mafic Magmatism in the Intermontane Pacific Northwest: *Journal of Geophysical Research*, v. 109, p. 1-14.
- Carlson, R.W., and Hart, W.K., 1988, Flood basalt volcanism in the northwestern United States, *in* Macdougall, J.D., ed., *Continental Flood Basalts*, p. 35–61.
- Christiansen, R.L., and McKee, E.H., 1978, Late Cenozoic volcanic and tectonic evolution of the Great Basin and Columbia Intermontane region, *in* Smith, R.B., and Eaton, G.P., eds., *Cenozoic tectonics and regional geophysics of the western Cordillera*, Geological Society of America Memoir 152, p. 283–312.
- Crough, S. T., 1978, Thermal origin of mid-plate hot-spot swells: *Geophysical Journal International*, v. 55(2), p. 451-469.
- Crough, S.T., 1983, Hotspot swells: *Annual Review of Earth and Planetary Sciences*, v. 11, p. 165–193.
- Davies, G. F., 1988, Ocean bathymetry and mantle convection: 1. Large-scale flow and hotspots: *Journal of Geophysical Research: Solid Earth (1978–2012)*, v. 93(B9), p. 10467-10480.

- DeNosaquo, K., Smith, R.B., and Lowry, A.R., 2009, Density and lithospheric strength models of the Yellowstone-Snake River Plain volcanic system from gravity and heat flow data: *Journal of Volcanology and Geothermal Research*, v. 188, p. 108–127.
- DePaolo, D., and Weis, D., 2007, Hotspot volcanoes and large igneous provinces, *in* Harms, U., Koeberl, C., and Zoback, M., eds., *Continental Scientific Drilling: A Decade of Progress, and Challenges for the Future*, p. 259–288.
- Doherty, D.J., McBroome, L.A., and Kuntz, M.A., 1979, Preliminary geologic interpretation and lithologic log of the exploratory test well (INEL-1), Idaho National Engineering Laboratory, Eastern Snake River Plain, Idaho: U.S. Geological Survey Open-file report, 79-1248, 10 p.
- Fritz, W.J., and Sears, J.W., 1993, Tectonics of the Yellowstone hotspot wake in southwestern Montana: *Geology*, v. 21, p. 427–430.
- Geist, D. J., Sims, E. N., Hughes, S. S., and McCurry, M., 2002, Open-system evolution of a single episode of Snake River Plain magmatism, *in* Link, P. K., and Mink, L. L., eds., *Geology, hydrogeology, and environmental remediation, Idaho National Engineering and Environmental Laboratory, eastern Snake River Plain, Idaho: Geological Society of America Special Paper 353*, p. 193-204.
- Geslin, J.K., Link, P.K., and Fanning, C.M., 1999, High Precision provenance determination using detrital-zircon ages and petrography of Quaternary sands on the eastern Snake River Plain, Idaho: *Geology*, v. 27, p. 295-298.
- Hanan, B.B., Shervais, J., and Vetter, S., 2008, Yellowstone plume-continental lithosphere interaction beneath the Snake River Plain: *Geology*, v. 36, p. 51-54.
- Hanan, B., Vetter, S., and Shervais, J., 1997, Basaltic volcanism in the eastern Snake River Plain: Lead, neodymium, strontium isotope constraints from the Idaho INEL WO-2 core site basalts: *Geological Society of America Abstracts with Programs*, v. 29, p. A298.
- Hart, W.K., and Carlson, R.W., 1987, Tectonic controls on magma genesis and evolution in the northwestern United States: *Journal of Volcanology and Geothermal Research*, v. 32, p. 119–135.
- Hildreth, W., Halliday, A. N., and Christiansen, R. L., 1991, Genesis and contamination of basaltic and rhyolitic magma beneath the Yellowstone Plateau volcanic field: *Journal of Petrology*, v. 32, p. 63-138.
- Hodges, M.K.V., Link, P.K., and Fanning, C.M., 2009, The Pliocene Lost River found to west: Detrital zircon evidence of drainage disruption along a subsiding hotspot track: *Journal of Volcanology and Geothermal Research*, v. 188, p. 237-249.

- Hughes, S.S., McCurry, M., and Geist, D.J., 2002a, Geochemical correlations and implications for the magmatic evolution of basalt flow groups at the Idaho National Engineering and Environmental Laboratory, *in* Link, P.K., and Mink, L.L., eds., *Geology, hydrogeology, and environmental remediation: Idaho National Engineering and Environmental Laboratory, Eastern Snake River Plain, Idaho: Geological Society of America Special Paper 353*, p. 151-173.
- Hughes, S.S., Wetmore, P.H., and Casper, J.L., 2002b, Evolution of Quaternary Tholeiitic Basalt Eruptive Centers on the Eastern Snake River Plain, Idaho, *in* Bonnicksen, B., White, C.M., and McCurry, M., eds., *Tectonic and Magmatic Evolution of the Snake River Plain Volcanic Province: Idaho Geological Survey Bulletin 30*, p. 363-385.
- Hughes, S., Smith, R., Hackett, W., and Anderson, S., 1999, Mafic volcanism and environmental geology of the eastern Snake River Plain, *in* S.S. Hughes and G.D. Thackray, eds., *Guidebook to the Geology of Eastern Idaho: Idaho Museum of Natural History*, p. 143-168.
- Humphreys, E.D., Dueker, K.G., Schutt, D.L., and Smith, R.B., 2000, Beneath Yellowstone: Evaluating Plume and Nonplume Models Using Teleseismic Images of the Upper Mantle: *GSA Today*, v. 10, p. 7.
- Ito, G., and van Keken, P. E., 2007, Hotspots and melting anomalies: *Treatise on Geophysics*, v. 7, p. 371-436.
- James, D. E., Fouch, M. J., Carlson, R. W., and Roth, J. B., 2011, Slab fragmentation, edge flow and the origin of the Yellowstone hotspot track: *Earth and Planetary Science Letters*, v. 311(1), p. 124-135.
- Jean, M.M., Shervais, J.W., Champion, D.E., and Vetter, S.K., 2013, Geochemical and paleomagnetic variations in basalts from the Wendell Regional Aquifer Systems Analysis (RASA) drill core: Evidence for magma recharge and assimilation–fractional crystallization from the central Snake River Plain, Idaho: *Geosphere*, v. 9, no. 5 p. 1319–1335.
- King, S.D., 2007, Hotspots and edge-driven convection: *Geology*, v. 5, p. 223–226.
- King, S.D., and Anderson, D.L., 1995, Edge-driven convection: *Earth and Planetary Science Letters*, v. 160, p. 289–296.
- Kuntz, M., Covington, H., Schorr, L., 1992, An overview of basaltic volcanism of the eastern Snake River Plain, Idaho, *in* P.K. Link, M.A. Kuntz, and L.P. Platt, eds., *Regional geology of Eastern Idaho and Western Wyoming: Geological Society of America Memoir 179*, p. 227-267.
- Leeman, W.P., 1982a, Development of the Snake River Plain-Yellowstone Plateau Province, Idaho and Wyoming: An overview and petrologic model, *in* Bonnicksen, B., and

- Breckenridge, R.M., eds., Cenozoic geology of Idaho: Idaho Bureau of Mines and Geology Bulletin 26, p. 155-177.
- Leeman, W.P., 1982b, Evolved and hybrid lavas from the Snake River Plain, Idaho, *in* Bonnicksen, B., and Breckenridge, R.M., eds., Cenozoic Geology of Idaho: Idaho Bureau of Mines and Geology Bulletin 26, p. 181-191.
- Leeman, W.P., Schutt, D.L., and Hughes, S.S., 2009, Thermal structure beneath the Snake River Plain: Implications for the Yellowstone hotspot: *Journal of Volcanology and Geothermal Research*, vol. 188, p. 57-67.
- Link, P.K., McDonald, H.G., Fanning, C.M., and Godfrey, A.E., 2002, Detrital zircon evidence for Pleistocene drainage reversal at Hagerman Fossil Beds National Monument, central Snake River Plain, Idaho, *in* Bonnicksen, B., White, C.M., and McCurry, M., eds., Tectonic and Magmatic Evolution of the Snake River Plain Volcanic Province: Idaho Geological Survey Bulletin, v. 30, p. 105–119.
- Link, P.K., Fanning, C.M., and Beranek, L.P., 2005, Reliability and longitudinal change of detrital-zircon age spectra in the Snake River system, Idaho and Wyoming: an example of reproducing the bumpy barcode: *Sedimentary Geology*, v. 182, p. 101–142.
- Mabey, D.R., Zietz, I., Eaton, G.P., and Kleinkopf, M.D., 1978, Regional magnetic patterns in part of the Cordillera in the Western United States, *in* Smith, R.B., and Eaton, G.P., eds., Cenozoic tectonics and regional geophysics of the western Cordillera: Geological Society of America Memoir 152, p. 93–106.
- Mahoney, J.B., Mustard, P.S., Haggart, J.W., Friedman, R.M., Fanning, C.M., and McNicoll, V.J., 1999, Archean zircons in Cretaceous strata of the western Canadian Cordillera: The “Baja B.C.” hypothesis fails a “crucial test”: *Geology*, v. 27, p. 195–198.
- Mason, B.G., Pyle, D.M., and Oppenheimer, C., 2004. The size and frequency of the largest explosive eruptions of Earth: *Bulletin of Volcanology*, v. 66, p. 735-748.
- Matthews, V., III, and Anderson, C.E., 1973, Yellowstone convection plume and break-up of the Western United States: *Nature*, v. 243, p. 158–159.
- McCurry, M., and Rodgers, D.W., 2009, Mass transfer along the Yellowstone hotspot track I: Petrologic constraints on the volume of mantle-derived magma: *Journal of Volcanology and Geothermal Research*, v. 188, p. 86-98.
- McQuarrie, N., and Rodgers, D., 1998, Subsidence of a volcanic basin by flexure and lower crustal flow: the eastern Snake River Plain, Idaho: *Tectonics*, v. 17, no. 2, p. 203-220.
- Morgan, L.A., and McIntosh, W.C., 2005, Timing and development of the Heise volcanic field, Snake River Plain, Idaho, western USA: *Geological Society of America Bulletin* v. 117 (3/4), p. 288–306.

- Morgan, L.A., Doherty, D.J., and Leeman, W.P., 1984, Ignimbrites of the eastern Snake River Plain: Evidence for major caldera-forming eruptions: *Journal of Geophysical Research* v. 89 (B10), p. 8665–8678.
- Morgan, J.P., Morgan, W.J., Price, E., 1995, Hotspot melting generates both hotspot volcanism and a hotspot swell?: *Journal of Geophysical Research*, v. 100, p. 8045–8062.
- Morgan, W.J., 1971, Convection plumes in the lower mantle: *Nature*, v. 230, p. 42–43.
- Morgan, W.J., 1972, Plate motions and deep mantle convection: *Geological Society of America Memoir* 132, p. 7-22.
- Ore, H.T., 1999, Topographic and geomorphic development of southeastern Idaho, segments from an essay, *in* Hughes, S.S., and Thackray, G.D., eds., *Guidebook to the geology of eastern Idaho*: Pocatello, Idaho, Idaho Museum of Natural History, p. 254–255.
- Pierce, K.L., and Morgan, L.A., 1990, The track of the Yellowstone hotspot: Volcanism, faulting, and uplift: U.S. Geological Survey Open-File Report 90-415. Geol. Surv, Denver, CO. 49 pp.
- Pierce, K.L., and Morgan, L.A., 1992, The Track of the Yellowstone Hotspot: Volcanism, Faulting, and Uplift, *in* Link, P.K., Kuntz, M.A., and Platt, L.B., eds., *Regional Geology of Eastern Idaho and Western Wyoming*: GSA Memoir 179, p. 1-53.
- Pierce, K.L., and Morgan, L.A., and Saltus, R.W., 2000, Yellowstone plume head: Postulated tectonic relations to the Vancouver slab, continental boundaries, and climate, U.S. Geological Survey Report 00-498, 39 p.
- Pierce, K.L., Morgan, L.A., and Saltus, R.W., 2002, Yellowstone Plume Head: postulated tectonic relations to the Vancouver Slab, continental boundaries, and climate, *in* Bonnicksen, B., White, C.M., McCurry, M., eds., *Tectonic and Magmatic Evolution of the Snake River Plain Volcanic Province*: Idaho Geological Survey Bulletin, v. 30. Idaho Geological Survey, Moscow, ID, United States, p. 5–33.
- Pierce, K.L. and Morgan, L.A., 2009, Is the track of the Yellowstone hotspot driven by a deep mantle plume? — Review of volcanism, faulting, and uplift in light of new data: *Journal of Volcanology and Geothermal Research*, v. 188, p. 1-25.
- Reid, M. R., 1995, Processes of mantle enrichment and magmatic differentiation in the eastern Snake River Plain: The isotope evidence: *Earth and Planetary Science Letters*, v. 131(3), p. 239-254.
- Richards, M.A., Hagar, B.H., and Sleep, N.H., 1988, Dynamically supported geoid highs over hotspots: Observations and theory: *Journal of Geophysical Research*, v. 92, p. 7690–7708.
- Rodgers, D. W., McCurry, M. O., Ford, M., Price, K., and Scarberry, K., 2002, Making space for

mantle-derived magma in the crust along the Yellowstone hotspot track, (abs.): Geological Society of America abstracts with programs, v. 34, no. 5, p. A-84.

Saltzer, R.L., and Humphreys, E.D., 1997, Upper Mantle *P* Wave Velocity Structure of the Eastern Snake River Plain and its relationship to geodynamic models of the region: *Journal of Geophysical Research*, v. 102, no. B6, p. 11829-11841.

Sears, J.W., and Thomas, R.C., 2007, Extraordinary Middle Miocene crustal disturbance in southwest Montana: bird record of the Yellowstone hot spot?: *Northwest Geology* v. 36, p. 133–142.

Shervais, J.W., Vetter, S.K., and Hanan, B.B., 2006, Layered Mafic Sill Complex Beneath the Eastern Snake River Plain: Evidence From Cyclic Geochemical Variations in Basalt: *Geology*, v. 34, p. 365- 368.

Shervais, J. W., and Hanan, B. B., 2008, Lithospheric topography, tilted plumes, and the track of the Snake River–Yellowstone hot spot: *Tectonics*, v. 27, p. 5.

Shervais, J.W., Schmitt, D.R., Nielson, D. Evans, J.P., Christiansen, E.H., and Morgan, L., et al., 2013, First Results from HOTSPOT: The Snake River Plain Scientific Drilling Project, Idaho, U.S.A.: *Scientific Drilling*, v. 15, p. 36-45.

Shervais, JW, Evans, JP, Schmitt, D., Christiansen, EH, and Alexander Prokopenko, A., 2014, HOTSPOT: The Snake River Scientific Drilling Project: EOS, *Transactions American Geophysical Union*, v. 95(10), p. 85-86.

Sleep, N. H., 1990, Hotspots and mantle plumes: Some phenomenology: *Journal of Geophysical Research: Solid Earth (1978–2012)*, v. 95(B5), p. 6715-6736.

Sleep, N. H., 1992, Hotspot volcanism and mantle plumes. *Annual Review of Earth and Planetary Sciences*, v. 20, p. 19.

Smith, R.B., 1977, Intraplate tectonics of the Western North American Plate: *Tectonophysics* v. 37, p. 323–336.

Smith, R.B., and Sbar, M., 1974, Contemporary tectonics and seismicity of the Western United States with emphasis on the Intermountain Seismic Belt: *Geological Society of America Bulletin* v. 85, p. 1205–1218.

Smith, R. B., and Braille, L.W., 1994, The Yellowstone hotspot: *Journal of Volcanology and Geothermal Research*, v. 61, p. 121-188.

Smith, R. B., Jordan, M., Steinberger, B., Puskas, C., Farrell, J., Waite, G.P., Husen, S., Chang, W. L., and O'Connell, R., 2009, Geodynamics of the Yellowstone hotspot and mantle plume: Seismic and GPS imaging, kinematics, and mantle flow: *Journal of Volcanology and Geothermal Research*, v. 188, p. 26–56

Sparlin, M.A., Braile, L.W., and Smith, R.B., 1982, Crustal structure of the eastern Snake River Plain determined from ray trace modeling of seismic refraction data: *Journal of Geophysical Research*, v. 87, no. B4, p. 2619-2633.

Waite, G.P., Smith, R.B., and Allen, R.M., 2006, VP and VS structure of the Yellowstone hot spot from teleseismic tomography: Evidence for an upper mantle plume: *Journal of Geophysical Research*, v. 111, B04303.

Waschbusch, P. J., and McNutt, M. K., 1994, Yellowstone: A continental midplate (hot spot) swell: *Geophysical Research Letters*, v. 21(16), p. 1703-1706.

CHAPTER 2

VOLCANIC STRATIGRAPHY AND AGE MODEL OF THE KIMAMA DEEP CORE HOLE (PROJECT
HOTSPOT), CENTRAL SNAKE RIVER PLAIN, IDAHO

Abstract

The Snake River Plain, central Idaho, represents the world's best example of a mantle hotspot track in continental crust, with a record of bimodal volcanism extending from over 12 Ma to the present. Project Hotspot: the Snake River Scientific Drilling Project recovered over 2 km of continuous core from the Kimama drill site, located in central Idaho on the Axial Volcanic Zone of the Snake River Plain.

We identify a total of 462 basalt flow units, representing 155 basalt flows, seventy-one basalt flow groups, twenty-seven super groups, and four compositional basalt types that are recognized using volcanic facies observations, geochemical data, stratigraphic relationships, sedimentary interbeds, borehole geophysical logs, and measurements of paleosecular variation in the magneto-stratigraphy. Intercalated sedimentary deposits represent lulls in regional volcanic activity and show a relationship to polarity reversals representing thousands of years of time. Neutron logs document individual flow units through the contrast between massive flow interiors and more porous flow tops. Gamma ray logs document the depth and thickness of sedimentary interbeds, and also highlight the occurrence of high-K₂O basalt lavas.

Six basalt lava flows were dated using ⁴⁰Ar/³⁹Ar incremental heating by broad-beam infrared laser. Flows sampled at 320 m, 454 m, 1155 m, 1184 m, 1284 m, and 1489 m provide reliable ages of 1.54 ± 0.15 Ma, 1.62 ± 0.15 Ma, 3.74 ± 0.13 Ma, 4.18 ± 0.58 Ma, 4.39 ± 0.30 Ma, and 5.05 ± 0.81 Ma respectively. Paleomagnetic inclination was measured in over 1200 samples collected at 2 m depth intervals. Twenty-one magnetic reversals were identified and correlated

to dated paleomagnetic Chrons and Subchrons using radiometric ages. Paleosecular variations in the magnetic data distinguish flow groups on time scales too short for radiometric dating. A linear fit to ages determined from $^{40}\text{Ar}/^{39}\text{Ar}$ dates and paleomagnetic time scale extrapolates to a bottom hole age of 6.4 Ma and define a mean igneous accumulation rate of 335 m/Ma.

Background

Project Hotspot: the Snake River Scientific/Geothermal Drilling Project, funded by the U.S. Department of Energy, the International Continental Drilling Program, and a consortium of universities, drilled three 1.8-1.94 km holes in the central and western Snake River Plain of Idaho (U.S.) (Shervais et al., 2013). The goals of this project were to document the history of hotspot volcanism in the wake of the Yellowstone plume, to understand how plume-related magmas interact with continental lithosphere, and to understand how this interaction affects the geochemical evolution of mantle-derived magmas and of the continental lithosphere. A further goal was to investigate innovative approaches to geothermal resource exploration in complex volcanic terranes (Shervais et al., 2011, 2012, 2013).

Although recent seismic tomography has imaged upper mantle thermal and velocity anomalies beneath the Snake River Plain-Yellowstone volcanic province (Peng and Humphreys, 1998; Schutt et al., 2008), obtaining a clear understanding of the source and evolution of magmatism and the extent of crustal interaction is only possible through the chemical analysis of erupted basalts (Hofmann, 1997; Reiners, 2002). Of further importance to continental hotspot studies is a record of how these interactions varied through time as demonstrated by stratigraphic chemical variations and age constraints. Without basalt stratigraphy and the ability to assign chemical characteristics and ages to individual basalt flows, it is impossible to accurately measure either magmatic flux or the temporal source of chemical and isotopic

heterogeneity related to the varying interaction between the continental lithosphere and a mantle hotspot source through time.

The Y-SRP hotspot represents the youngest, and most complete record of continental hotspot volcanism in the world. Investigations of stratigraphy in young continental volcanic provinces such as the SRP are restricted by the lack of uplift and tilting, and by limited stratigraphic exposure of incised river canyons. As a result, detailed stratigraphic investigations in these terranes is limited by the depth and spatial distribution of cored wells (Shervais et al., 1994; Anderson et al., 1997; Helm-Clark et al., 2005). Many of the deeper wells in the Snake River Plain have been drilled to study groundwater and contaminant flow, and most are clustered on the Idaho National Laboratory site, located along the northern margin of the Snake River Plain north of the Axial Volcanic Zone (AVZ). The AVZ is a topographic high composed of tholeiitic shield volcanoes that represents the locus of basaltic volcanism during the late Pliocene and Pleistocene, and is mirrored by a subsided keel of buried basalts that has been documented geophysically (Lindholm, 1996).

The Kimama drill site is located on the central Snake River Plain (SRP), about 21 km north of Burley, Idaho, and 65 km southwest of Craters of the Moon National Monument (see Fig. 1). Kimama drill site was chosen specifically to study the volcanic stratigraphy of the AVZ, and to investigate elevated thermal gradients beneath the Snake River Regional Aquifer (Shervais et al., 2013). Previous drilling in other areas of the SRP has indicated a veneer up to 1.2 km thick of Pliocene-Pleistocene basalt, with minor fluvial, and lacustrine sediments that overlie silicic volcanic products on the SRP (Doherty et al., 1979; Kuntz et al., 1992; Anderson and Liszewski, 1997).

The Kimama drill hole was cored continuously from below the ground surface (~12 m) to a total depth of 1912 m, with >99.5% recovery rate (as measured by length cored: (core

recovered); an additional 134 m of sidetrack core was obtained in the upper part of the drill hole. This core represents a nearly continuous record of volcanic activity and sedimentation at the Kimama site. Basalt flows make up 94% of the core, with eolian and fluvial sediments making up the remaining 6%. The drill hole spudded into hyaloclastic basalt.

When discussing volcanic stratigraphy, it is important to note that the processes of basaltic volcanism make drill cores an imperfect record of eruptive activity and hiatus. Continuous lava flow inundation on one flank of a volcano may occur while another remains unaffected; similarly, a dormant volcano may be inundated by lavas from an adjacent volcano. In addition, inter-fingering of lava flows from adjacent volcanoes may occur if both are active simultaneously (Jean et al., 2013). Despite these limitations, core provides the most complete record of deposition in the subsurface, and error may be diminished through the use of seismic data or additional, closely-spaced core holes.

Approach

We combine direct observation of drill core with wireline geophysical logs, magnetostratigraphy, radiometric ages, and geochemistry to examine the volcanic stratigraphy in the central SRP. Core provides our most direct record of the volcanic stratigraphy, flow contacts, flow characteristics, and sedimentary interbeds, as well as samples for geochemical and magnetic secular variation analyses. Wireline geophysical logs are used to supplement or replace core, especially in situations where core recovery is limited or too costly to obtain. In particular, gamma-ray and neutron logs are useful for interpreting basalt flows and interbedded sediments (Helm-Clark et al, 2005). Gamma-ray logs are sensitive to sedimentary interbeds, whereas neutron logs may document variations in porosity associated with flow unit

boundaries. Thick packages of sediments may demonstrate long periods of volcanic quiescence and bracket flow groups derived from a distinct magmatic source (typically a single volcano).

Temporal information about basalt deposition comes from paleosecular variations in the magnetic stratigraphy, magnetic reversals, and radiometrically-determined ages.

Paleosecular variations in magnetic inclination occur over decade to multi-decade time scales, while polarity reversals represent significant decade to century-scale events (Kuntz et al., 1986; Champion et al., 1988). These variations can be used to distinguish individual basalt flows (which typically comprise multiple flow units) and to identify flow groups. Radiometric dating of individual lava flows at critical depths provides direct information on ages and accumulation rates, and provides calibration of the paleomagnetic time scale, which can then be used to refine the stratigraphic age model. Geochemical data (Ti/K, La/Lu, Zr/Nb, K₂O, TiO₂ and total iron as FeO*) may be used as a tool to identify flow groups and super-groups.

We merge lithologic observations of the Kimama core with ages and with major- and trace-element concentrations, and radiogenic isotope ratios, to generate a complete history of basaltic volcanism in the central Snake River Plain. The integration of lithology, flow structures, wireline logs, magneto-stratigraphy, and geochemistry provides a powerful set of tools to interpret the timing, extent, and source of regional volcanism related to passage of the Yellowstone hotspot. The volcanic flux, and the volume of magma erupted through time, are first-order constraints on the ultimate origin of the hotspot and on its interaction with continental lithosphere. These calculations will rely critically on the stratigraphic and age models developed here.

Geologic Background

Regional Setting

The 500-km long SRP formed as the North American continent passed over the fixed SRP-YP hotspot during the late Tertiary. As the archetype of a continental hotspot track, the SRP contains a continuous record of violent, caldera-forming rhyolitic eruptions and quiescent, Hawaiian-type basaltic volcanism (Morgan, 1972; Armstrong et al., 1975; Smith and Braile, 1994; Pierce and Morgan, 1992, 2009). The sequence of rhyolite, basalt, and sediment strata that comprise the SRP, spans 12 m.y. of volcanic and inter-volcanic activity (Pierce and Morgan, 1992; Bonnicksen, 2008; Anders et al., 2009).

During the late Pliocene through Pleistocene, the SRP was the locus of densely-spaced mafic volcanic centers along the hotspot track that locally erupted thick packages of basalt flows; this volcanic activity was concentrated along the central axis of the plain to form the AVZ (Hackett and Smith, 1992; Hackett et al., 2004; Kuntz et al., 2002). Holocene lavas, e.g., the Shoshone lava flow and Craters of the Moon, erupted on the margins of the plain, or, like the Great Rift, form volcanic rift zones that cross the plain at high angles (Kuntz et al., 2002). Late Pleistocene to Holocene lavas of Craters of the Moon form multi-phase eruptions with ages of 2 ka to 480 ka (Bonnicksen and Godchaux, 2002).

Basalt Flow Stratigraphy

The unique style of volcanism along the SRP (Figure 2C) has been recognized as a product of small, mid-crustal magma chambers feeding eruptions from low shield volcanoes over relatively short durations, described as “plains-style volcanism” by Greeley (1982) (Figure 2B). The single-episode eruptives common on the SRP are similar to modern volcanic processes

on the island of Hawaii and transitional between Hawaiian-style and continental-style volcanism (Figure 2A) (Greeley, 1982; Kuntz, 1978).

Volcanic rift zones and low-relief shield volcanoes erupted olivine tholeiite basalt lavas, filling basins and controlling the direction and deposition of subsequent lava and water flow. During periods of decreased volcanism, lava flows in low areas were mantled by loess and by lacustrine and fluvial sediments. Loess deposition can occur relatively quickly, although preservation of sediments is thought to be relatively short-lived from modern observations (Kuntz et al., 1986, 1992). Vents of SRP shield volcanoes are typically low-relief, due primarily to the efficient transport of low-viscosity lava away from the vent in lava tubes and the short duration of eruptions; because relatively little lava accumulates near the vent, eruptive centers often blend in with the surrounding topography (Self et al., 1998).

As a result of these eruptive processes and flow mechanisms, the classification of multiple assemblages of lava flows is scale dependent. Basalt flows are classified as either simple or compound lava flows, depending on whether the flow consists of a single coherent flow unit, or an amalgamation of many thinner flow units (Walker, 1971, 1991, 1993). Compound flows typically comprise stacks of relatively thin shelly pahoehoe, with or without an underlying core of massive basalt (which represents another flow unit). In contrast, simple lava flows typically comprise a massive flow unit with a shelly or rubbly upper surface. In either case, the lava flow is considered to represent a single eruptive event formed over a time scale of weeks to years, but commonly less than a few decades (Figure 3A and Figure 3B).

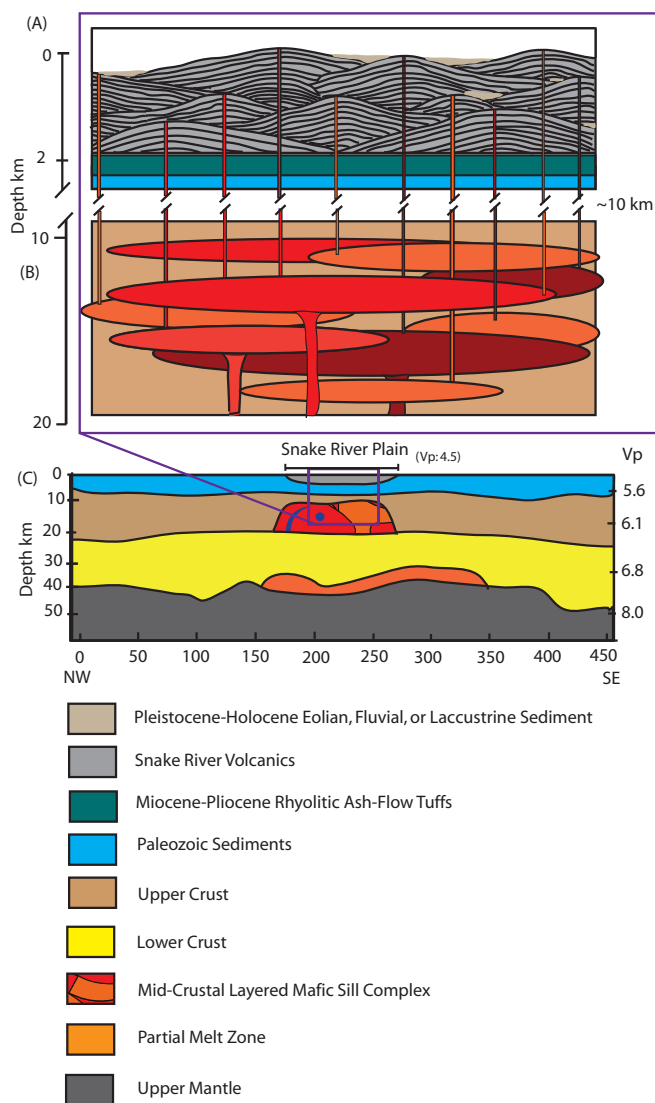


Figure 2: Schematic illustration of plains-style volcanism on the eastern Snake River Plain showing laterally extensive, stacked lava flows, coalesced shield volcanoes, and sedimentary interbeds. (A) Modified from Greeley (1977) and Hughes et al. (1999). (B) Schematic illustration of the interpreted structure of the mafic sill complex (Shervais et al., 2006). Magma batches are chemically distinct and may pond at different depths within the sill complex. Partial or residual melts in partly congealed Fe-Ti basalt cumulates may interact with stored magmas prior to eruption or replenishment. Modified from Shervais et al. (2006). (C) Cross section of the Snake River Plain region, showing the crust and mafic sill complex from the seismic velocity model of Peng and Humphreys (1998). The location and thickness of the inferred mafic sill complex are shown.

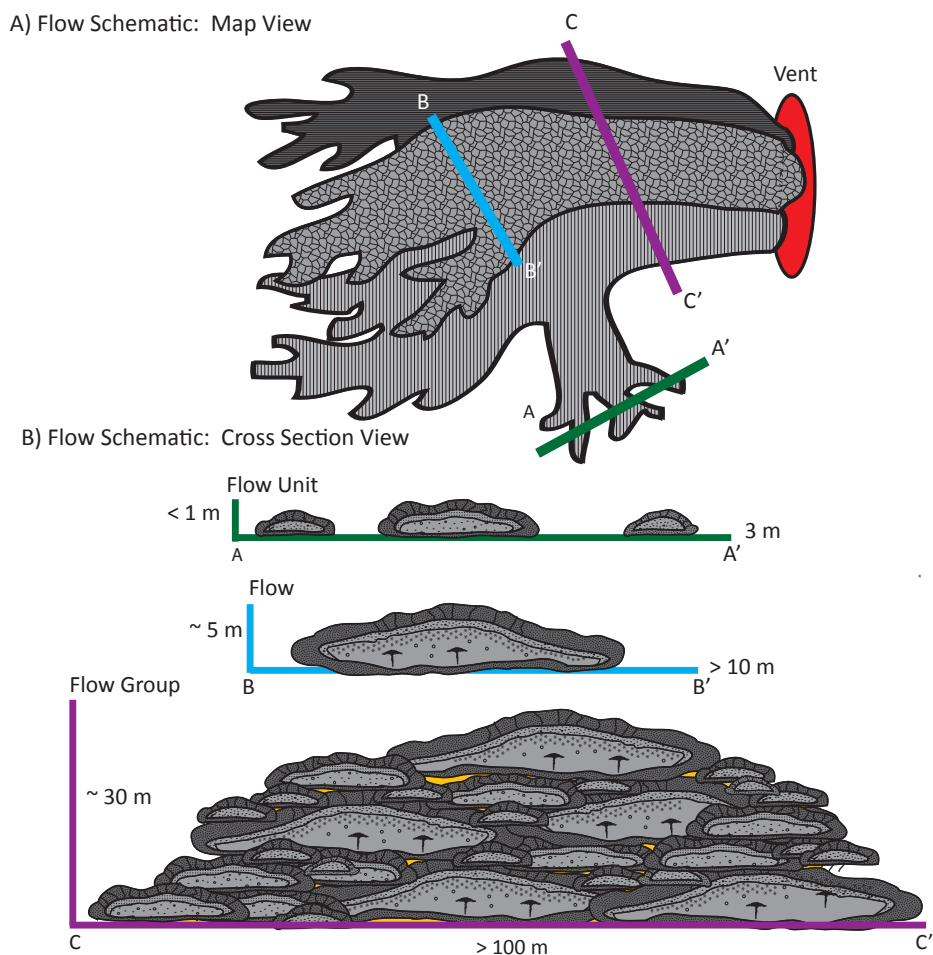


Figure 3: Spatial relationship between inflated pahoehoe flow units, flows, and flow groups in map and cross section views. Modified from Self et al. (1998). A) Map view of a flow field. Flows emanate from a central volcanic vent during a magmatic event. Older flows may be blanketed by newer flows over time. B) Cross sections of transects shown in map view: A-A' illustrates the flow front, where flow lobes (flow units), advance as incandescent lava oozes through the cooled rind at the very tip of the flow. Flow units in the Kimama core range in thickness from 0.3 to 29.6 m. Bubbles trapped in the moving lava form vesicles. Depressurization during flow lobe breakout causes a pulse of vesiculation in the liquid lava, which eventually cools into a horizontal vesicle layer (Hon et al., 1994). B-B' illustrates the lava flow, where flow units thicken by inflation as they extend outward during a volcanic eruption. Flow units in the Kimama core range in thickness from 0.3 to 48.1. Pipe vesicles form in the lower crystallization front. As the lava flow cools, vesicular residuum rises slowly through the stagnant lava and to the base of the upper crust, where it forms horizontal vesicle sheets. Cracks in the surface of the flow develop during cooling; cracks that extend into the visco-elastic layer of the flow speed cooling of the flow interior (Self et al., 1998). C-C' illustrates the lava flow group, a complex aggregate of genetically related flows and flow units erupted during the life of a volcano. In the Kimama core, flow groups range in thickness from 1.2 to 202.7 m. Sediment washed down from the surface may collect between constituent flows, but most thick sediment interbeds in the Kimama core are divide separate flow groups and/or paleomagnetic chronological boundaries.

Inflationary pahoehoe flows produce complex stratigraphy, with younger eruptions of lava conducted away from the vent through the molten interiors of older flow units, a process known as inflation (Walker, 1991; Chitwood, 1994; Self et al., 1998). Therefore, the massive core of a flow represents the last or a later pulse of an eruption, whereas the shelly and rubbly surface and basal facies represent earlier eruptions. In core, younger flow units may be bounded at top and bottom by relatively older basalt flow units from the same eruption, an observation that has important implications for stratigraphic interpretation. Self et al. (1998) recognized that the inflation mechanism of pahoehoe produces lava flows that display similar geometries at variable spatial scales. Small-scale lava flow units and larger-scale lava flows may emanate from a single monogenetic source or from coeval sources sharing a magma reservoir. Packages of lava flows erupted from a single magma reservoir form a complex aggregate of flows termed flow groups (Figure 3A) (Welhan et al., 2002; Hughes et al., 2002). Lava flow groups have areal dimensions of kilometers to tens of kilometers and are synonymous with lava fields, such as the Wapi and Hell's Half Acre lava fields (Figure 3B) (Greeley, 1982; Welhan et al., 2002). Super groups are defined by polarity and significant geochemical variation from the typical Snake River Plain olivine tholeiites. Modern basaltic shields, lava flows, and lava tubes such as those at Mauna Loa and Kilauea provide a tangible corollary to aid in the identification of subsurface features in drill core (Hon et al., 1994). Chemical distinctions between basalts of the SRP are made difficult by the general similarity between flow group compositions. Previous workers have suggested that similarity of basalts of the SRP results from a similar source and petrogenetic history within the mafic mid-crustal sill (Figure 3C) (Shervais et al., 2006).

Methods

Lithologic Logging

Detailed lithologic logging of core and high-resolution core photographs were used to interpret stratigraphy. Basalt core was visually inspected for the presence of large-scale features such as fractures, oxidation or scoriaceous regions, sediment interbeds, mega-vesicles, vesicle-rich zones (vesicle sheets, vesicle bands or vesicle cylinders), pillows, and rubble zones. Features such as ropey flow tops, flow and mold structures, and spatter are also documented. Core samples displaying alteration, oxidation, secondary mineralization, xenoliths, autoliths, anomalous vesiculation, and other distinguishing characteristics were described when observed.

Flow unit boundaries were identified throughout the entire 1912 m of Kimama core using the model of Self et al. (1998), who suggest that individual pahoehoe lava flows and their constituent flow units display three distinctive zones: surface, interior, and basal facies. The flow surface is characterized by oxidized, platy or rubbly, and highly vesicular textures, often with ropey morphology (Figure 4l). Stacks of multiple surface facies are occasionally observed, with washed-down sediment forming simple boundaries (Figure 4a and Figure 4b). Surface facies thicknesses range from 30 cm to 1 m.

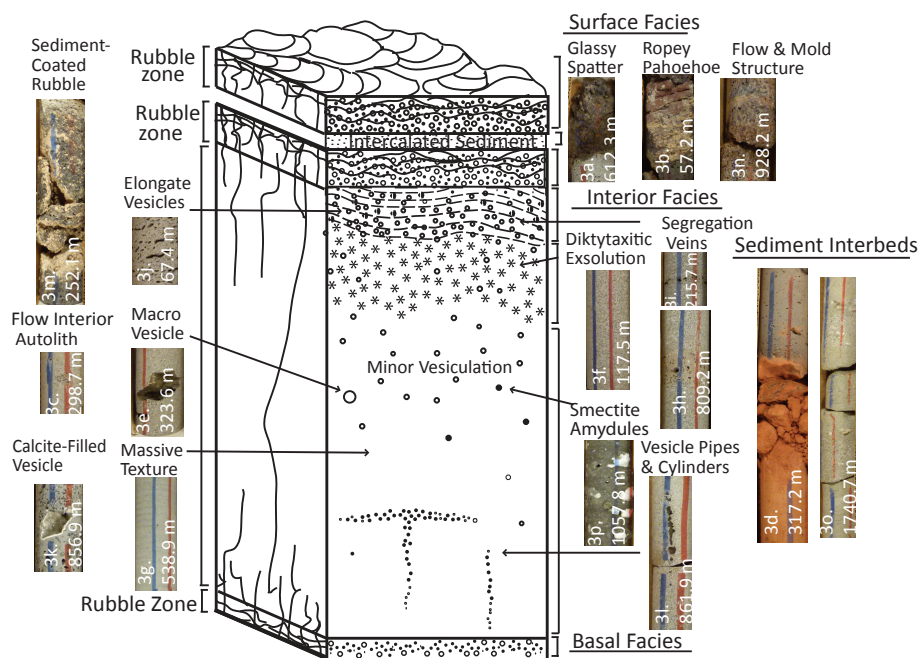


Figure 4: Facies model of typical (~6.2 m) inflated basalt flow as observed in the Kimama core. Photographs of the Kimama core illustrate lava flow facies characteristics. Surface Facies: glassy spatter (3a), ropey pahoehoe (3b), and sediment-coated rubble (3m), and flow and mold structures (3n). Interior Facies: diktytaxitic texture (3f), a result of secondary exsolution; massive flow interior, no vesicles (3g); segregation vein, about 8 cm thick (3h); segregation vein, about 4 cm thick (3i); elongate vesicles are the result of continued lava flow during the cooling stage (3j); pipe vesicles are formed near the base of the lava flow as lava interacts with a moist ground surface (3l); remobilized spatter (also referred to as autolithic basalt)(3c); macrovesicle, measuring about 5 cm across (3e); vesicle with secondary crystallization of calcite, 4.5 cm across (3k); vesicles filled with secondary mineralization of smectite-group clays (3p) (Sant and Shervais, 2011). Sediment Interbeds: baked loess, fine grained, homogenous clay baked to terra cotta by the overlying flow (3d); fluvial sediment interbed showing normal gradation of coarse to medium grained sand (3o). Detrital zircon samples were recovered from fluvial interbeds at the base of the core for U-Pb geochronology and Lu-Hf analyses. Modified from Self et al. (1998).

Wireline Geophysical Measurements

Wireline geophysical logs for both holes (Kimama 1A and 1B) occurred in stages as drilling progressed, with the final logging shortly before completion of hole 1B. The upper ~760 m were logged by the U.S.G.S. using tools and techniques described in Twining and Bartholomay (2011). Hole 1A was logged in October 2010 (0-298 m depth), Hole 1B was logged in November 2010 (0-759 m). Logs for both holes included natural gamma-ray, neutron, gamma-gamma density, temperature, and gyro deviation. Further logging was carried out by Century Wireline Services in January 2011; neutron and natural gamma log measurements were made inside the drill string in order to avoid tool loss (206-1850 m), and caliper, natural gamma, sonic porosity, resistivity, self potential, and temperature logs were measured in an open hole below the HQ drill string. Temperatures in the lower 100 m of the drill hole exceeded the limits of the instruments, resulting in electronic noise below ~1800 m depth.

Natural gamma-rays in the SRP are emitted primarily by ^{40}K , which is concentrated in the sedimentary interbeds, enabling us to identify stratigraphic breaks between basalt flow groups. Furthermore, natural gamma logs may be used to identify individual basalt flows should they contain measurable differences in the relative abundance in K_2O (Twining et al., 2008). In general, sedimentary interbeds are characterized by high natural gamma-ray (> 75 API) signals relative to the surrounding tholeiitic basalts (0-75), whereas high K_2O lavas are characterized by moderately high gamma-ray signals (higher than the tholeiitic basalts, lower than the sediments).

Neutron logs measure the absorption of neutrons by hydrogen (typically as H_2O in the SRP), such that porous, water-rich rocks have high neutron absorption (low backscattered signal), whereas dense rocks with low porosity and low water contents have low neutron absorption (high backscattered signal to the detector). The absorption of neutrons in water-

filled vesicles and fractures results contrasts sharply with dense, water-free basalt. Void spaces created by vesicles and fractures are dominantly found in rubbly lava flow tops and flow bases, whereas the massive flow interiors have low porosity. This allows us to distinguish individual lava flows and correlate them with flows and flow contacts found in core.

Paleomagnetic methods

More than 1200 paleomagnetic samples were cored out over the entire 1912 m length of the core, and subjected to AF and thermal demagnetization protocols. The Kimama drill core was carefully logged and sampled using INL Lithologic Core Storage Library protocols described in Davis et al. (1997). Prior to sampling, the core material was described and the tops and bottoms of lava flows were identified. Depths were measured from depth markers recorded by the drillers at the time of coring. Mean inclination values for each lava flow group, and 95 percent confidence limits about the mean value were calculated using the method of McFadden and Reid (1982).

To facilitate paleomagnetic interpretation, the corehole is assumed to be vertical in its original drilling orientation. A gyroscopic deviation log of the Kimama was made at 0.3 m (1 ft) intervals, and it records moderate deviations from vertical. Deviation from vertical for any particular depth interval in the Kimama corehole typically is less than one degree, and does not significantly affect paleomagnetic remanent inclination interpretations, and has no effect on the remanent polarity determinations used here. Further details of the paleomagnetic study of the Kimama corehole will be released later (Champion and others, in prep.).

Radiometric Dating

Age determinations for six samples from the recovered Kimama core were derived from groundmass separates. The groundmass samples were prepared from whole-rock core pieces

by crushing and sieving to obtain a 200-300 μm size fraction, then acid leached following the procedure described by Koppers et al. (2000). This consisted of 15 minute sequential leaching in 1 N HCl, 5 N HCl, 1 N HNO_3 , and 5 N HNO_3 . Before irradiation, 50-100 mg of material was hand picked from the final leached separate to remove fragments of phenocrysts and any remaining alteration minerals. All samples were irradiated at the Oregon State University 1 MW TRIGA Reactor. Neutron flux was monitored using a Fish Canyon Tuff biotite (FCT-3) with a monitor age of 28.02 ± 0.16 Ma (Renne et al., 1998). Argon extraction and analysis was achieved with a Merchantek 10 W CO_2 laser and an MAP-215-50 mass spectrometer following the methods outlined in Duncan and Hogan (1994) and Duncan et al. (1997). Data reduction utilized ArArCALC v.2.2 (Koppers, 2002) using decay constants proposed by Steiger and Jüger (1977).

Samples were heated from 400° to 1400°C (fusion) in 7-8 steps with gas cleanup and Ar-isotopic measurement after each temperature step. We calculated ages from the isotopic data in a number of standard ways. Total fusion ages incorporate all heating steps in a given incremental heating experiment, essentially equivalent to a conventional K-Ar age determination. Plateau ages, calculated as the weighted mean (by inverse variance) of multiple step ages, are considered reliable if they include three or more contiguous step ages constituting $> 50\%$ of the total gas released. A statistical parameter, mean square of weighted deviations (MSWD), compares error within step ages with scatter about the mean step age, and has a 2-sigma (95%) confidence limit below about 2.5 (depending on the number of heating steps). Isochron ages are calculated from the slopes of linear regressions through the step isotopic compositions ($^{40}\text{Ar}/^{36}\text{Ar}$ vs $^{39}\text{Ar}/^{36}\text{Ar}$) that comprise the plateaus, and make no assumption about the initial Ar composition ($^{40}\text{Ar}/^{36}\text{Ar}$).

Our analyzed samples show petrographic evidence for low temperature alteration, to clays and zeolites. In such cases the possibility for ^{40}Ar -loss and K-addition during fluid-rock

chemical exchange is significant. Baksi (2007) compared fresh and altered basalts dated by ^{40}Ar - ^{39}Ar incremental heating experiments and developed several quantitative measures of levels of alteration at which age data may be compromised. The first is the concentration of ^{36}Ar (atmospheric, corrected for reactor produced ^{36}Ar from Ca), which lies below about 3×10^{-14} mol/g for whole rock basalts in samples that produced acceptable (crystallization) plateau ages.

Results

Flow Units and Flows

Almost all of the lava flows identified in the Kimama core are compound flows comprising two or more flow units. The few simple flows that contain a single flow unit are generally thin sheets that are distinct from flows above and below. We identify 446 basalt flow units, which range in thickness from 0.3 m to 29.6 m and average 13.4 m thick (Figure 5). Using lithologic observations, petrography, and geochemical and paleomagnetic stratigraphy, we grouped flow units into 141 lava flows, 0.3 m to 48.1 m thick, (most 10-20 m thick; 12 m average). Flows and flow units are summarized in Table 1, and reviewed in detail in Appendix A. Massive basalt flows are commonly overlain by multiple shelly pahoehoe flow units, and typically show evidence of sediment infiltration along cooling boundaries. Intercalated sediment ranges in thickness from 0.2 m to 80 m, and the thicker layers are clearly visible in natural gamma logs as high gamma spikes (Figure 6). A total of 113 m of sediment was recovered from the Kimama core, with the majority of eolian sediment located between 115 and 560 m depth (Figure 5). Two thick packages of fluvial sediment are identified at 1707 m-1760 m depth and 1840 m-1905 m depth.

Table 1: Summary of Kimama flow groups, flows, and flow units

Super Group	Flow Group	Polarity & Inclination Range	Pmag Age (Ma)	CHRON subchron	Chem. Type	No. Flows	No. Flow Units	Start Depth (m)	End Depth (m)	Flow Group Thickness (m)	Mean Flow Thickness (m)	No. Sed. Intervals
A	1	60	~0.72	BRUNHES	SROT	4	11	13.4	25.2	11.7	8.63	0
	2	51	---		SROT	9	16	25.2	95.8	70.6	14.2	1
	3	43	---		SROT	1	2	96.0	100.6	4.60	---	0
	4	38	---		SROT	1	2	100.6	118.3	17.7	---	1
B	5	-56	0.78	MATUYAMA	SROT	1	10	123.8	142.9	19.1	---	0
	6	-63	---		Fe-Ti	1	3	142.9	164.8	21.9	---	0
C	7	-64	---	jaramillo	Fe-Ti	2	3	164.8	183.8	19.0	9.49	1
	8	22	0.99		SROT	6	9	202.3	232.8	30.5	9.07	1
D	9	-61	1.07	MATUYAMA	SROT	5	18	236.8	259.6	22.8	7.63	0
	10	-61	---		Fe-Ti	1	7	259.6	274.9	15.3	---	0
E	11	-61	---	MATUYAMA	SROT	4	9	274.9	317.2	42.3	19.9	1
	12	-63	---		High-K	1	1	317.7	319.7	2.00	---	1
F	13	-64	---	MATUYAMA	SROT	2	4	319.8	336.0	16.2	12.9	0
	14	-64	---		Low-K	1	2	336.0	342.5	6.50	---	0
	15	-62	---		Fe-Ti	2	8	342.5	358.7	16.2	8.08	1
	16	-62	---		SROT	2	8	358.8	377.2	18.4	9.19	0
G	17	-52	---	olduvai	SROT	3	18	377.2	425.1	47.9	16.0	0
	18	60	1.77		SROT	3	5	425.1	432.9	7.80	2.59	1
H	19	57	---	MATUYAMA	SROT	2	4	432.9	451.7	18.8	9.39	1
	20	22	---		Fe-Ti	3	12	453.2	489.2	36.0	12.0	0
	21	27	---		SROT	1	4	489.2	504.5	15.3	---	0
	22	56	---		SROT	2	10	504.5	527.4	22.9	11.4	1
I	23	-52	1.95	MATUYAMA	Fe-Ti	1	2	528.3	547.9	19.6	---	1
	24	-54	---		Low-K	2	7	548.4	560.7	12.3	5.58	0
	25	-54	---		Fe-Ti	1	2	560.7	566.0	5.30	---	0
	26	-54	---		SROT	1	1	566.0	570.1	4.10	---	0
	27	-54	---		Low-K	3	9	570.1	575.8	5.70	7.06	0
	28	-54	---		Fe-Ti	1	5	575.8	584.8	9.00	---	0
J	29	-54	---	MATUYAMA	SROT	3	7	584.8	591.3	6.50	11.0	0
	30	-54	---		Low-K	2	7	591.3	610.5	19.2	28.6	1
	31	-55	---		SROT	1	1	610.5	617.1	6.60	---	0
	32	32	2.43		X-Event	Fe-Ti	1	1	617.1	731.8	114.7	---
K	33	-58	---	MATUYAMA	SROT	1	6	732.4	755.4	23.0	---	1
	34	-62	---		SROT	2	5	755.6	770.1	14.5	7.27	0
	35	-45	---		SROT	3	19	776.0	831.4	55.4	19.2	1
	36	-65	---		SROT	1	2	831.7	841.3	9.60	---	0
	37	-65	---		Fe-Ti	1	2	841.3	849.1	7.80	---	0
	38	-40	---		SROT	2	8	849.1	865.1	16.0	12.6	0
L	39	-55	---	GAUSS	SROT	5	13	874.3	910.9	36.6	9.15	0
	40	65	2.58		SROT	1	6	910.9	934.4	23.5	---	0
M	41	-77	3.04	kaena	SROT	1	1	934.4	947.2	12.8	---	0
	42	-73	---		SROT	1	1	947.2	948.5	1.30	---	0
N	43	-76	---	mammoth	SROT	1	1	948.5	950.0	1.50	---	0
	44	56	3.11		SROT	2	6	950.00	961.5	11.5	5.74	1
O	45	-60	3.22	GAUSS	SROT	7	15	962.0	1022.1	60.1	9.96	2
	46	63	3.33		SROT	1	1	1022.1	1022.8	0.700	---	2
P	47	63	---	GAUSS	Low-K	1	2	1044.1	1045.0	0.900	---	0
	48	51	---		Low-K	3	4	1045.0	1076.6	31.6	10.5	1
Q	49	-71	3.58	GILBERT	High-K	1	1	1077.1	1078.5	1.40	---	1
	50	-72	---		Low-K	3	10	1079.3	1112.9	33.6	11.2	1
R	51	5	---	GILBERT	Low-K	1	1	1113.3	1115.8	2.50	---	1
	52	-69	---		Fe-Ti	1	2	1116.5	1131.0	14.5	---	1
S	53	-49	---	GILBERT	Fe-Ti	1	1	1131.0	1150.9	19.9	---	2
	54	58	4.18		SROT	1	9	1151.9	1175.1	23.2	---	0
T	55	58	---	cochiti	SROT	3	7	1175.4	1212.8	37.4	12.5	1
	56	58	---		Low-K	1	1	1212.8	1217.1	4.30	---	1
U	57	66	---	nunivak	SROT	1	1	1217.3	1234.7	17.4	---	1
	58	-60	4.29		Low-K	1	1	1236.1	1237.0	0.900	---	1
V	59	59	4.48	GILBERT	Low-K	1	8	1239.5	1272.1	32.6	---	0
	60	59	4.62		SROT	3	13	1272.1	1310.6	38.5	12.8	0
W	61	59	---	GILBERT	Low-K	3	12	1310.6	1377.2	66.6	22.2	1
	62	-43	---		Low-K	1	2	1379.0	1389.0	10.0	---	1
X	63	-58	---	GILBERT	Low-K	1	2	1389.1	1394.6	5.50	---	0
	64	-58	---		SROT	1	1	1394.6	1407.0	12.4	---	1
Y	65	68	4.98	thvera	SROT	3	20	1411.5	1460.4	48.9	16.3	1
	66	62	---		Low-K	2	9	1461.3	1510.1	48.8	24.4	1
Z	67	43	---	GILBERT	Low-K	1	2	1510.9	1526.3	15.4	---	1
	68	-45	5.23		Low-K	1	2	1527.0	1545.9	18.9	---	1
AA	69	-67	---	GILBERT	Low-K	9	34	1546.3	1729.7	183.4	21.6	2
	70	64	5.89		Low-K	2	4	1754.1	1766.4	12.3	---	1
AB	71	-45	6.14	C3An/c3an.1	Low-K	7	19	1768.5	1912.0	143.5	16.9	4

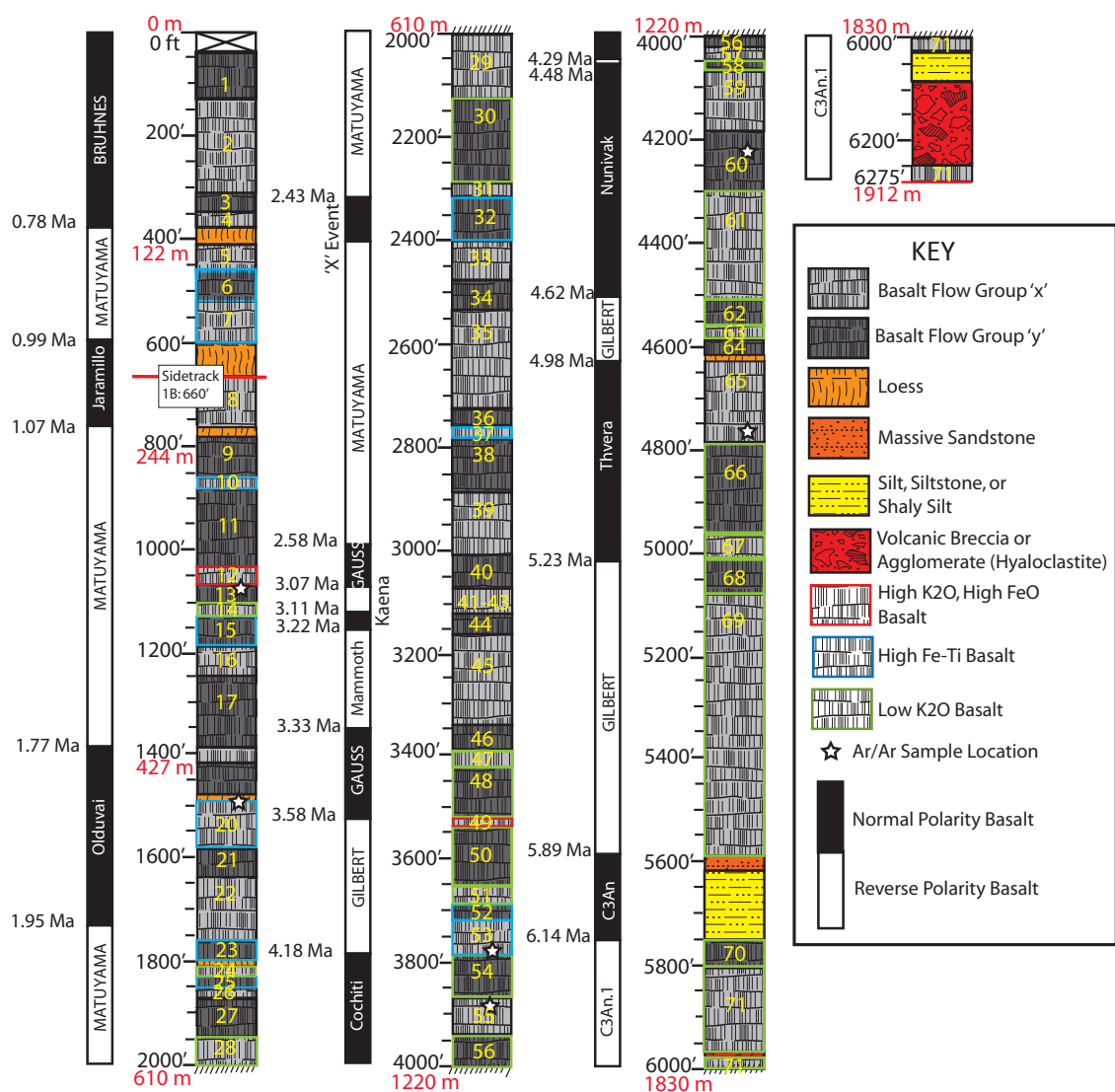


Figure 5: Lithologic and paleomagnetic stratigraphy of the Kimama core. 71 flow groups were identified based upon lithologic observations, chemical variation, and magnetic polarity. Paleomagnetic polarity and associated ages are displayed to the left of the lithologic log. Five Chrons and nine subchrons are identified in the Kimama core (Champion and Duncan, 2012).

The transition from surface facies to interior facies is observed as near-surface vesicle bands, or segregation veins, visible as sub millimeter-sized vesicles within fine-grained crystalline basalt (Figure 4). Segregation veins result from episodic gas exsolution during

repeated episodes of lava inflation. Multiple, stacked segregation veins, without chilled margins, may be present within a single lava flow and are a principle facies indicator of inflated pahoehoe flows (Smith, 1967; Walker, 1993; Chitwood, 1994; Self et al., 1998).

Flow interiors are characterized by massive fine-grained intergranular textures, to coarser-grained diktytaxitic textures with isolated vesicles. Flow interiors commonly exceed three meters in thickness (Figure 4g). Because thicker flow units take longer to solidify, their interiors typically exhibit few vesicles from the lower and middle portions (Walker, 1993). Diktytaxitic texture (Figure 4f), vesicle pipes (Figure 4k), macro vesicles (Figure 4e), and vesicle segregation veins, also present in interior flow facies, are thought to be a product of cyclic vesiculation, or repeated cycles of lava flow inflation and gas exsolution (Figure 4g) (Hughes et al., 2002).

The flow unit base contains minor vesiculation and may contain rubble (Figure 4). In Kinama drill core, the basal valve flow unit facies occurs in thicknesses generally less than 5 cm. Degassing is most efficient in the lower portion of the flow unit, resulting in relatively minor vesiculation in the basal facies relative to the interior and surface facies. A thin, > 2 cm rind of glass often designates the chilled contact of the lava flow unit with the ground surface

Individual flow units almost invariably transition from dark gray basalt in the upper and lowermost portions of the flow unit to light gray within the interior, indicating a greater content of groundmass glass in the more rapidly cooled upper and lower portions (Figure 4). Vesicles, always sub-rounded to rounded, also display an inverse trend of increased size and decreased frequency through the flow interior, after which their concentration increases and size decreases to the end of the flow unit. When flows exceed one another without sufficient time separation, new lava flows may make molds of the underlying flow surfaces as they cool, creating flow and mold structures (Twining et al., 2008) (Figure 4m).

Missing intervals (unrecovered core) within flow groups identified within the Kimama core are usually associated with rubble sections (Figure 4l) or sediment interbeds (Figure 4d), both of which are easily disturbed by drilling.

Significant time separation between eruptive events are sometimes indicated by eolian, fluvial, and lacustrine sediment horizons, which collect in topographic lows or leeward settings. Eolian sediments lack internal structure or depositional facies, whereas lacustrine and fluvial sediments in Kimama core typically contain bedforms. Fining upward sequences associated with fluvial deposition are especially apparent in cored Kimama sediments below 1730 m (Figure 4o). In some cases, sediment layers may have been baked by overlying lava flows (Figure 4d). As a result of weathering and water movement, sediment-filled vesicles are most common within flow units that are immediately beneath sediment interbeds (Figure 4l).

At two depth intervals, increased natural gamma signal response is observed without a corresponding sediment package. Geochemical analyses of samples from 319 m and 1078 m depth demonstrate high K_2O and high Fe_2O_3 (~2.0 wt.% and 19.0 to 21.0 wt.%, respectively) relative to the olivine tholeiite composition (0.25-1.00 K_2O wt.%; 13.0 to 17.0 wt.% Fe_2O_3) observed in the majority of the core. Elevated K_2O and Fe_2O_3 compositions are observed basalt compositions.

Below the ~250 m-depth of the top of the vadose zone in the Kimama drill hole, secondary mineralization by dogtooth spar commonly occurs as vesicle and fracture fillings (Figure 4k). Carbonate clay commonly coats basalt rubble zones within the vadose zone, and at depths greater than ~900 m, clay alteration is common as montmorillonite vesicle fillings (Figure 4p).

Basalt shows evidence of interaction with water (hyaloclastite) are found at depths of 1697.8 to 1704.3 m, from 1842.9 m to 1846.7, and from 1855.7 m to 1912 m. Kimama

hyaloclastites are angular basalt breccias bounded by a matrix of sand and basaltic glass fragments, which have been subsequently altered and silicified by hydrothermal fluids. Hyaloclastite overlies or is interlayered with packages of fluvial sediments.

Flow Groups

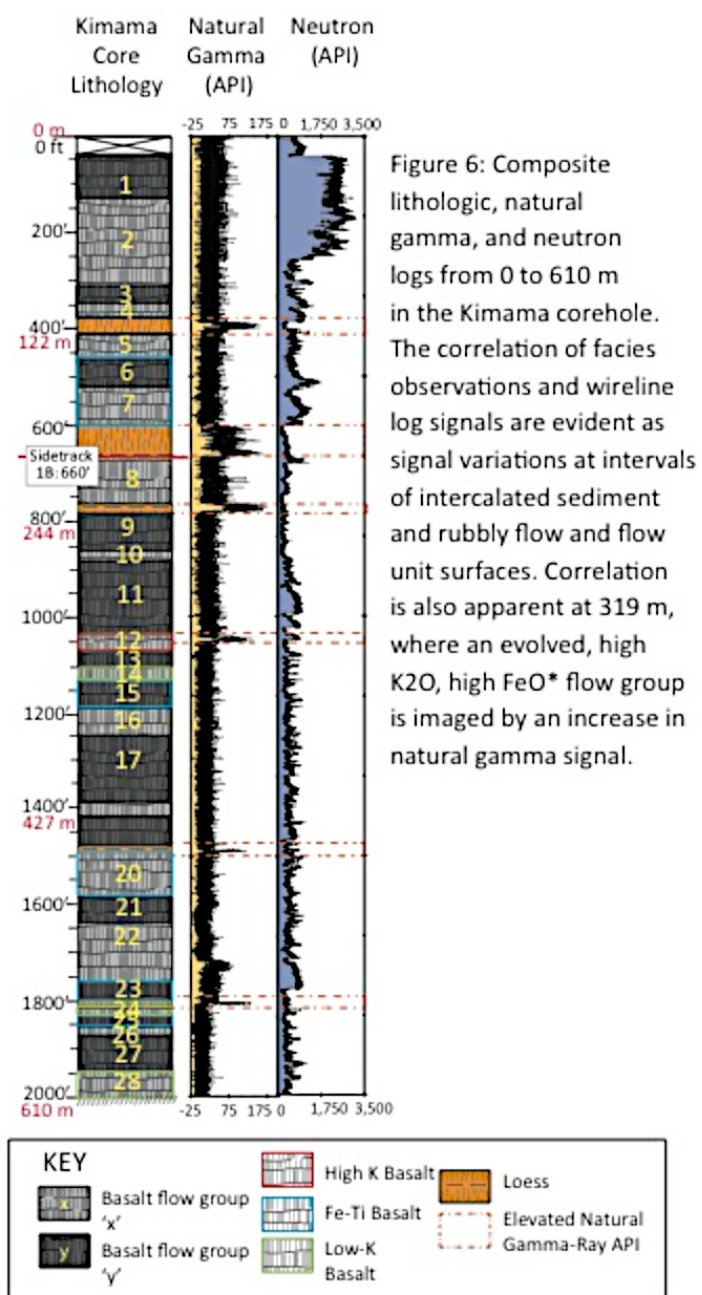
The lava flows recognized above are collated into Flow Groups based on their chemistry and petrology, magnetic polarity, and contact relations (Figure 5). In particular, sediment horizons > 1 m meter thick (and up to 80 m thick) represent interruptions in lava accumulation, or local eruptive hiatuses (Anderson et al., 1997). Previous workers suggest that typical SRP flow groups were deposited during eruptive events that lasted no more than a few hundred years, with an average lapse of 10 to 20 ka between each flow group eruption (Kuntz et al., 1980). Hiati identified in a stratigraphic interval generally represent less than a few tens of thousands of years (Anderson and Liszewski, 1997; Champion and Duncan, 2012).

We distinguished 71 flow groups, ranging in thickness from 0.7 to 183.4 m, based on these criteria (Figure 5, Table 1, see also Electronic Supplement). Four general compositional types were identified; thirty-seven flows are standard SRP olivine tholeiites, recognized in wireline logs as areas of greater neutron signal response than sediment or sediment-coated rubble stratigraphic intervals.

Two flow groups, 14 and 49 (Figure 6), consist of evolved high-K lavas that are essentially identical to those erupted within the Craters of the Moon lava field during the latest Pleistocene and Holocene (Kuntz et al., 1986; Putirka et al., 2009). These high-K flow groups, which were initially recognized based on their relatively high gamma-ray signal response, erupted from polygenetic, or multi-pulse vent systems. We identified 20 low-K lavas, which

represent the least evolved flow groups in the Kimama core (Figure 6). Twelve high-Fe and Ti (Fe-Ti) flow groups are also identified in the Kimama basalt stratigraphy.

Sharp variations in major and minor element concentrations or ratios are also used to distinguish flow groups, and these group boundaries correlate to lava flow divisions made using lithology and paleomagnetic inclination (Figure 7). Polarity reversals are also thought to represent distinct time breaks that define flow group boundaries, especially if they occur within a major sediment horizon.



Paleomagnetic Results

Magnetic susceptibility records paleomagnetic polarity and inclination, by which geologic ages of basalt flows are constrained. Polarity, K-Ar age, and stratigraphic data from the Kimama core are consistent with five paleomagnetic chrons and eight paleomagnetic Plio-Paleo

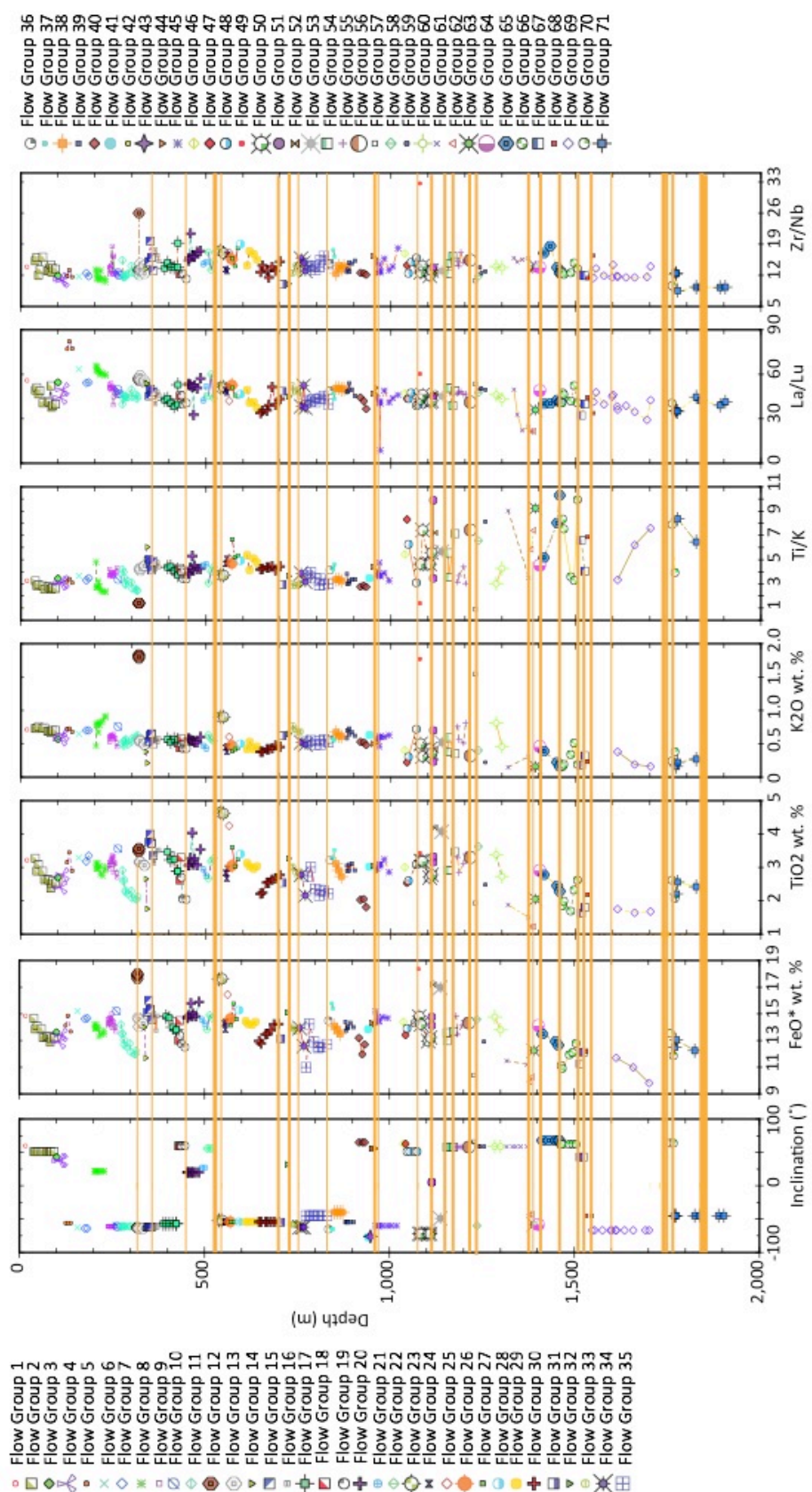
subchrons (Table 2 and Figure 8). Twenty-one magnetic reversals, where the polarity of basalt changes from normal to reversed, are recorded in the Kimama core. The distribution of basalt flows within identified subchrons and chrons demonstrates that the majority of flow groups in the Kimama core erupted over <100 years. Flow groups 32, 50, and 70 erupted over ~10,000 years, and flow group 40 erupted over ~300,000 years.

Table 2: Paleomagnetic Chrons and Subchrons by depth

Paleomagnetic Unit	Age Range (Ma)	Depth Start (m)	Depth End (m)
Brunhes Chron	0.72-0.78	120 ± 2	---
Matuyama Chron	0.78	911	120 ± 2
Jaramillo Subchron	0.99-1.07	235 ± 2	193 ± 9
Oluvai Subchron	1.77-1.95	528 ± 0.6	425
X' Event	2.43	708	---
Gauss Chron	2.58-3.58	950 ± 0.3	935
Kaena Subchron	3.04-3.11	1077	911
Mammoth Subchron	3.22-3.33	1022	962
Gilbert Chron	3.58-5.89	1728 ± 23	1077
Cochiti Subchron	4.18-4.29	1236 ± 0.61	1151 ± 1.5
Nunivak Subchron	4.48-4.62	1378 ± 0.9	1238 ± 1.2
Thvera Subchron	4.98-4.98	1526	1409 ± 2.1
C3An Chron	5.89-6.43*	T.D.	1728 ± 23
C3An.1 Subchron	6.14-6.43*	T.D.	1768

Measured depth locations of five paleomagnetic Chrons and eight Subchrons identified in the Kimama core. T.D. is 1912 m
 *6.43 Ma age estimated from modeled accumulation rate
 Ages from Champion and Duncan, 2012

Figure 7: Plots of paleomagnetic polarity and inclination, major element composition, and elemental ratios plotted against depth for Kimama basalts. These criteria were used to distinguish the 30 flow groups within the Kimama core. Major paleomagnetic and chemical variation between flow groups are often (but not always) associated with sediment interbeds.



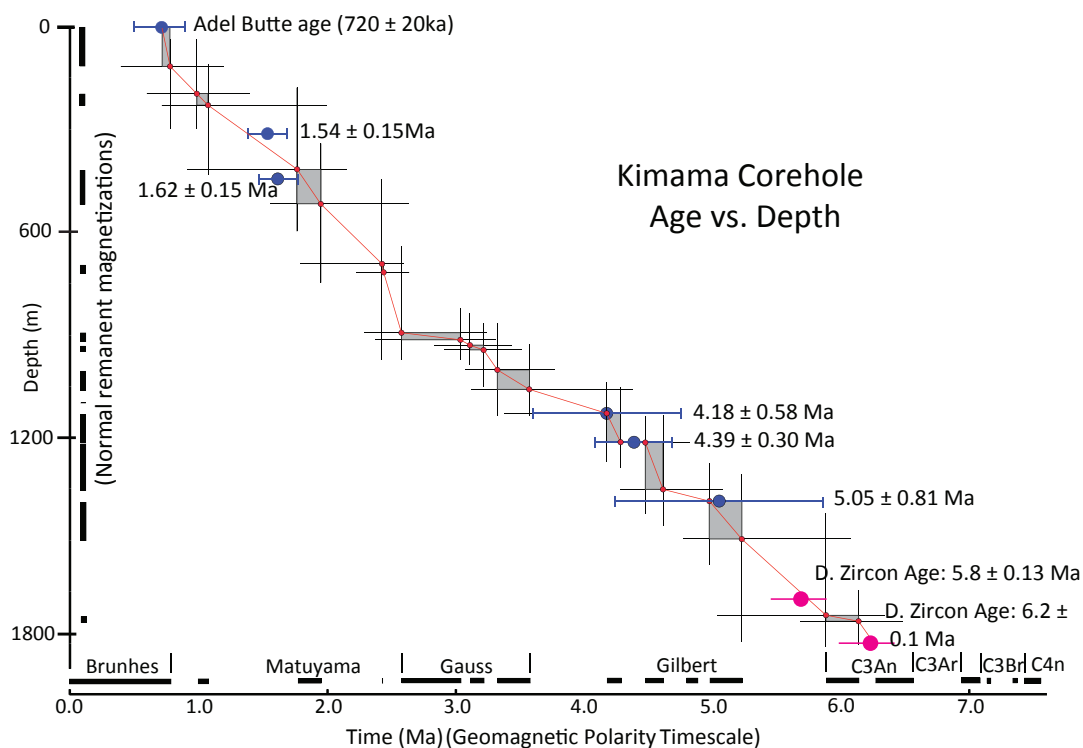


Figure 8: Kimama basalt accumulation rate estimated from linear fit model of Ar/Ar and paleomagnetic ages. The onset and termination of paleomagnetic Chrons and Subchrons are shown by the small red dots, with normal polarity intervals demonstrated by grey shading. Ar/Ar ages are indicated by filled blue circles. The youngest U-Pb ages of detrital zircon grains in the lower fluvial successions are 5.8 ± 0.1 Ma at 1749 m, and 6.2 ± 0.1 Ma at 1844 m depth; these ages (pink filled circles) are overlain on the linear fit projection to demonstrate concurrence with the 335 m/m.y. accumulation rate and indicate a depositional period of <100,000 years (modified from Champion and Duncan, 2012).

The Matuyama Chron spans 790.4 ± 2 Ma of basalt eruptions and comprises super groups B through K and flow groups five through 39. Within the Matuyama Chron, the Jaramillo subchron spans 42 ± 11 Ma. Super groups C and D and flow groups eight and nine were erupted during the Jaramillo subchron. The Olduvai subchron spans 103 ± 0.6 Ma and includes super groups G and H and flow groups 18 through 22. At 2.43 Ma, the 'X-event', a period of normal polarity within the Matuyama Chron, includes super group J and flow group 32. The 166.2 Ma Gauss Chron encompasses super groups L through Q and flow groups 40 through 49. The

Gilbert Chron spans 2.31 Ma and includes super groups R through AB and flow groups 50 through 70. Within the Gilbert Chron, the 0.11 Ma Cochiti subchron includes super group U and V and flow groups 54 through 58. The Nunivak subchron covers 0.14 Ma and includes super groups W and X and flow groups 59 and 60. The 0.25 Ma Thvera subchron includes super groups Z and AA and flow groups 65 through 68. The last identified Chron in the Kimama core is the C3An Chron, which terminates at 6.14 Ma and at a depth of 1768.5 m and continues to 1912.0 m. The paleomagnetic inclination of Kimama flow groups ranges from 22 degrees to -27 degrees, with minor variation within flows of each flow group.

Radiometric Dating Results

Total fusion, plateau, and isochron ages are summarized for all analyzed samples in Table 3, and Figure 8. In general, the incremental heating experiments produced clear age plateaus comprised of most of the gas released, although some step ages appear to be influenced by irradiation-induced ^{39}Ar , ^{37}Ar recoil, resulting in high low-temperature step ages in samples KMAB1488 (454 m depth) and KMA4788 (1459 m depth), and low high-temperature step ages in sample KMA3791 (1155 m depth). None of the samples appears to be affected by ^{40}Ar -loss. The six samples from the Kimama core hole provided reliable plateau ages, composed of 86-100% of the total gas released, ranging from 1.54 to 5.05 Ma (Table 3).

Table 3: ^{40}Ar - ^{39}Ar Age Determinations for Kimama Well Core

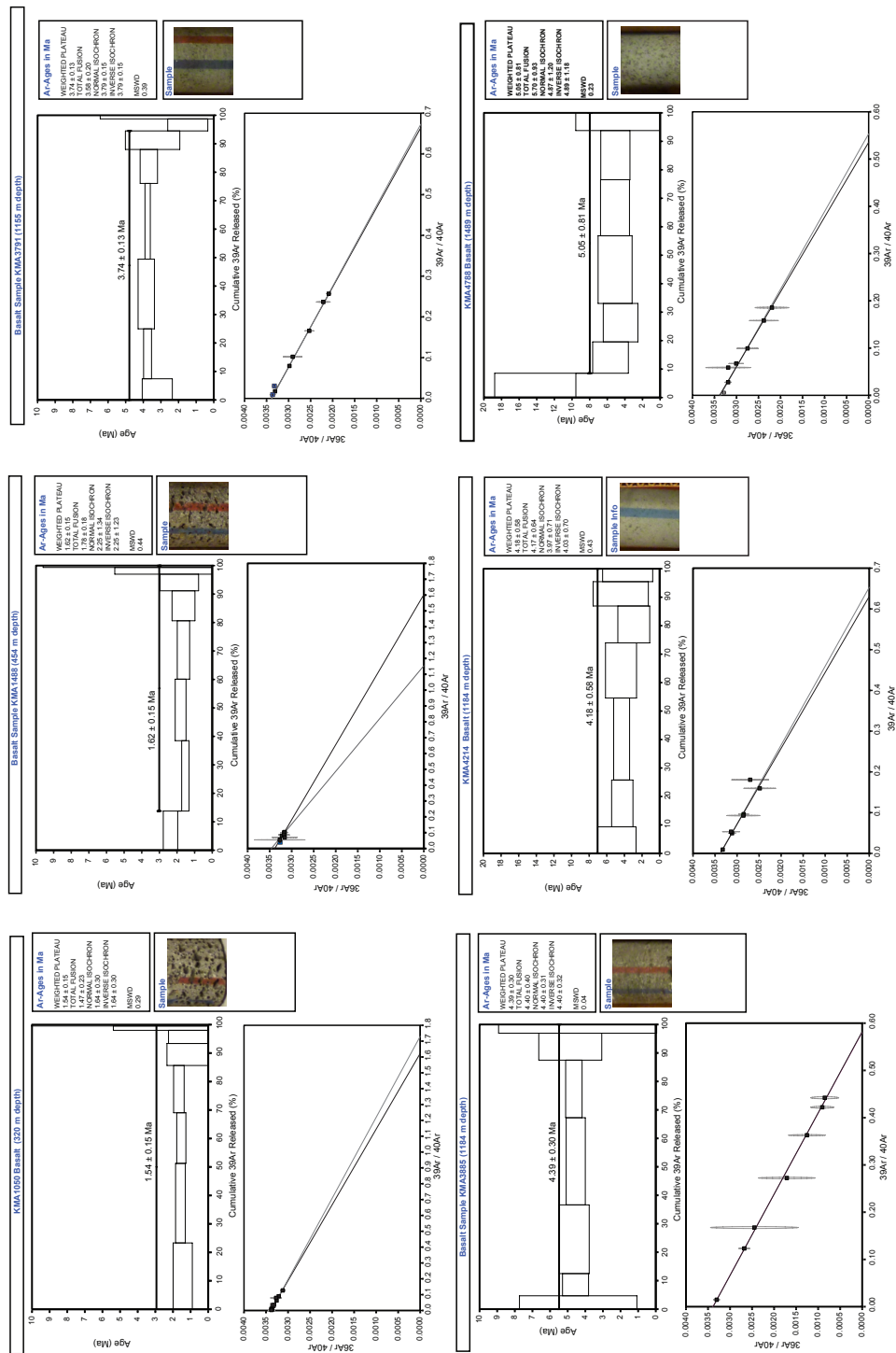
Sample	Depth (m)	Total Fusion (Ma)	2σ error (Ma)	Plateau Age (Ma)	2σ error (Ma)	N	MSWD	Isochron Age (Ma)	2σ error (Ma)	MSWD	$^{40}\text{Ar}/^{36}\text{Ar}$ Initial	2σ error	^{36}Ar E-14 mol/g
KMA1050	320	1.47	0.23	1.54	0.15	8/8	0.29	1.63	0.30	0.25	294.6	2.3	0.185
KMA1488	454	1.78	0.18	1.62	0.15	7/8	0.44	2.25	1.34	0.35	288.7	14.7	0.151
KMA3791	1155	3.58	0.20	3.74	0.13	6/8	0.39	3.79	0.15	0.18	294.5	1.7	0.127
KMA3885	1184	4.17	0.64	4.18	0.58	7/7	0.43	3.97	0.71	0.48	296.5	2.6	0.079
KMA4214	1284	4.40	0.40	4.39	0.30	7/7	0.04	4.40	0.31	0.04	295.1	5.6	0.058
KMA4788	1489	5.70	0.93	5.05	0.81	6/7	0.23	4.87	1.20	0.27	297.1	8.5	0.063

Ages calculated using biotite monitor FCT-3 (28.02 Ma) and the total decay constant $\lambda = 5.530\text{E-}10/\text{yr}$. N is the number of heating steps (defining plateau/total); MSWD is an F-statistic that compares the variance within step ages with the variance about the plateau age. J combines the neutron fluence with the monitor age.

Preferred (plateau) ages are shown in bold, concordant with isochron ages.

The ages increase with depth, in stratigraphic order. In all cases plateau ages are consistent with isochron ages and show no evidence for significant recoil, or ^{40}Ar -loss (Figure 9). Because the step compositions do not typically show large dispersion, the slopes determined by linear regressions of $^{40}\text{Ar}/^{36}\text{Ar}$ vs. $^{39}\text{Ar}/^{36}\text{Ar}$ are not well constrained and the corresponding analytical uncertainties for isochron ages are larger than for corresponding plateau ages. In all cases, however, the plateau and isochron ages are concordant and initial $^{40}\text{Ar}/^{36}\text{Ar}$ compositions are indistinguishable from the atmospheric value (295.5). Thus, we find no evidence for undegassed (“excess”) ^{40}Ar during cooling, and we report the plateau ages as our best estimate of the times of crystallization of these lava flows. The ^{36}Ar concentrations, calculated as a quantitative measure of alteration (Baksi, 2007) from the isotopic data (Table 3) are below the suggested cutoff value for whole rocks. Hence, alteration and Ar-loss have not significantly compromised the measured plateau ages as reliable estimates of the times of crystallization of these lava flows.

Figure 9: Kimama basalt accumulation rate estimated from linear fit model of Ar/Ar and paleomagnetic ages. The onset and termination of paleomagnetic Chrons and Subchrons are shown by the small red dots, with normal polarity intervals demonstrated by grey shading. Ar/Ar ages are indicated by filled blue circles. The youngest U-Pb ages of detrital zircon grains in the lower fluvial successions are 5.8 ± 0.1 Ma at 1749 m, and 6.2 ± 0.1 Ma at 1844 m depth; these ages (pink filled circles) are overlain on the linear fit projection to demonstrate concurrence with the 335 m/m.y accumulation rate and indicate a depositional period of <100,000 years (modified from Champion and Duncan, 2012).



Discussion

Measured paleomagnetic and K-Ar ages and interpreted stratigraphic relations of basalt super groups, flow groups, flows, and flow units, were used to estimate accumulation rate and volcanic flux in the Axial Volcanic High of the central Snake River Plain. Geologic ages of basalt core were constrained using paleomagnetic polarity and inclination measurements of over 1200 cores and K-Ar analyses of six basalt samples (Figure 9). Accumulation rate and volcanic flux were estimated from standard linear regressions of mean K-Ar ages, mean paleomagnetic ages, stratigraphic depths of basalt flows and flow groups, and the estimated areal dimension of Kimama basalt accumulation.

Volcanic Stratigraphy

The Kimama core contains 71 flow groups, each made up of one to seven flows of similar paleomagnetic inclination and major and trace element composition. Flow groups comprise 155 lava flows and 462 flow units, and commonly contain two to six flows and 10 to 20 flow units. Most flow groups are 10 to 60 m thick, and are compositionally similar to typical SRP olivine tholeiites (SROT). Flow groups are estimated to have erupted over durations of 100 to 10,000 years. Flow groups at the base of the Kimama core contain more flows, an observation attributed to greater accumulation from less-frequent volcanism.

High K, low K, and Fe-Ti flow groups are interpreted to represent flow groups that are petrologically distinct from the tholeiitic lavas above and below them (see Chapter 3). Although not recognized by natural gamma-ray wireline logs, Fe-Ti and low-K flow groups are also thought to represent distinct magma batches separate from typical tholeiitic basalt eruptions.

Within flow groups of the same magnetic polarity and general inclination range, abrupt chemical variance between lithologically distinct flows signal unrelated batches of magma, new

eruptive episodes, and different basalt flows. Within a basalt flow, flow units share the same general chemistry but are distinguished by lithologic facies. Variance of the inclination suggests and may require elapsed time of hundreds to tens of thousands of years, while polarity reversals may signify millennial-scale duration (Figure 8; Champion et al., 1988; Champion and Duncan, 2012).

Depth intervals of alternating magnetic polarity and subordinate intervals of similar mean remanent inclination values can be organized into 54 independent eruptive episodes ending in the Brunhes Normal Polarity Epoch and beginning within the C1An Normal Polarity Epoch. The median and range of remanent intensity and magnetic susceptibility values remain remarkably constant over the length of the drillcore. Density determinations made from the samples are also uniform in their range of values, despite significant alteration evident in the deeper parts of the core where temperatures are elevated. Density results suggest similar melting conditions in the mid crust for erupted basalts.

The use of neutron and natural gamma-ray logs for identifying porous and rubbly zones between more impermeable, massive basalt flows is validated through the results of this preliminary investigation. Using wireline data as a tool in preliminary geothermal exploration is a cost-effective method for mapping subsurface stratigraphy and probable fluid transport routes. The pronounced fluctuation of neutron and natural gamma measurements closely mirrors the location of massive flow interiors and associated flow boundaries. Increased signal response in both natural gamma and neutron logs correlate to actual sediment interbed locations identified during lithologic logging. Especially at depths of 734.8 m and 1226.4 m, spikes and dips in natural gamma and neutron log signals (respectively) accurately identify the presence of sediment interbeds.

Age and Accumulation Rate

The $^{40}\text{Ar}/^{39}\text{Ar}$ age determinations on six samples produce plateau ages that increase monotonically with depth, with an age of 5.05 ± 0.81 Ma in the deepest sample at 1459 m. The age progression determined from the paleomagnetic time scale fills in the gaps in the radiometric dates (Figure 9) and further refines the age vs. depth relationship among the lava flows (Figure 8).

In the bottom 200 m of core, basalt flows are interbedded with fluvial sand and hyaloclastite, an indication that lava flows interacted with surface water. Angular and bladed detrital zircons, interpreted to be derived from a fallout tuff source, were recovered from two fluvial interbeds and dated using laser ablation ICPMS U-Pb geochronology (see Chapter 4). The youngest magmatic zircons in each interbed are interpreted to represent (within analytical uncertainty) the depositional age of the sediment, because unwelded ash fall and ash flow tuffs will begin to erode shortly after deposition. The magmatic zircons in the lower fluvial section have ages of 6.2 ± 0.1 Ma (see Chapter 4), whereas the youngest magmatic zircons in the upper fluvial succession have ages of 5.8 ± 0.1 Ma. These ages are consistent with the age progression defined by the Ar dates and the paleomagnetic time scale, and together these data project to a bottom hole age of 6.4 Ma.

We document a linear accumulation rate through time of 335 m/Ma (Figure 8), based on an age of 720 Ka for the surface flows and 6.25 Ma for the oldest basalts (or 5.5 My elapsed time). Accumulation rates must be averaged over hundreds of thousands of years to account for hiatuses due to vent construction, periods of decreased volcanism, differential subsidence, and uplift (Anderson et al., 1997; Anderson and Liszewski, 1997). Each stratigraphic lava flow generally represents a time period of volcanic activity no longer than a few hundred years; therefore, a sedimentary interbed or variation in paleomagnetic inclination can represent 10 to

20 thousand years of volcanic inactivity. This is sufficient time to allow deposition of thick layers of sediment and for the Earth's magnetic fields to undergo several degrees of secular variation (Anderson et al., 1997; Champion et al., 1988).

The eruption rate of Kimama basalts is estimated using a linear regression model fitted to ages obtained from K-Ar and paleomagnetic age analyses. The data conform to a rate of growth of about 335 m/Ma between 6.25 Ma and 0.72 Ma. A 1912-m-thick sequence of cored basaltic lava flows yields K-Ar ages that range from about 1.54 Ma to about 5.05 Ma and paleomagnetic ages that range from 0.72 Ma to 6.14 Ma. A linear regression model fit to age data demonstrates a uniform rate of accumulation of basalt with time. In the Kimama region, one flow group erupted on average every 112 k.y.

At INL on the eastern SRP, paleomagnetic and K-Ar ages of surface and subsurface basalts were analyzed for eruptive periods ranging from 200 to 700 k.y. during the past 1.8 m.y. Rates ranging from 521.2 m/m.y. to 823.0 m/m.y., averaging 664.5 m/m.y., are estimated for areas of past subsidence (Anderson et al., 1997).

Magmatic Flux

In order to calculate the magmatic flux we make a few simplifying assumptions regarding crustal thickness and density. Since the thickness of the eruptive basalt accumulation is about 2 km in the Axial Volcanic Zone, and approaches zero on the plain margins (where rhyolites have little or no basalt cover), we calculate the cross-sectional area of the basalt as a triangular wedge 100 km across and 2 km high (Figure 10), or 100 km^2 . The velocity of North America during this time period was 29 mm/year, which for a duration of basalt volcanism of 5.5 Ma corresponds to a linear track 160 km long (parallel to plate motion). Multiplied by the cross-sectional area of 100 km^2 , we calculate a long-term post-plume eruptive flux of $16 \times 10^3 \text{ km}^3$

over 5.5 Ma, equivalent to $2.9 \times 10^3 \text{ km}^3/\text{Ma}$ or $2.9 \text{ km}^3/\text{Ka}$. This compares well with an eruptive flux for recent volcanism in the SRP of $3.3 \text{ km}^3/\text{Ka}$ calculated by Kuntz et al. (1992) or $2.5 \text{ km}^3/\text{Ka}$ calculated by McCurry and Rodgers (2009). These calculations show that eruptive flux has been remarkably consistent over the last 5.5 Ma in the central and eastern SRP, and imply a relatively stable rate of mantle upflow under the region.

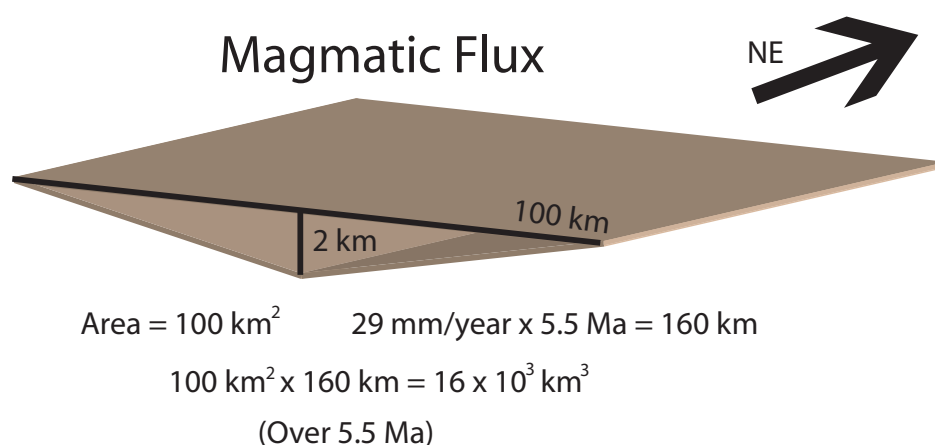


Figure 10: Schematic cartoon showing calculations for SRP magmatic flux over an area of 100 km^2 and a depth of 2 km. The post-plume eruptive basalt flux for the SRP is $\sim 16 \times 10^3 \text{ km}^3$ over 5.5 Ma. The post-plume intrusive basalt flux is calculated by using the commonly accepted 1:4 ratio of magma eruption to magma intrusion (Hughes et al., 2002). The calculation does not consider rhyolite flux. If the ratio is correct, the total amount of basalt intruded as $\sim 64 \times 10^3 \text{ km}^3$, and the total basaltic flux (intruded+extruded) as $\sim 8 \times 10^4 \text{ km}^3$, both over 5.5 Ma. This corresponds to a flux of $1.5 \times 10^4 \text{ km}^3$ per Ma, consistent with measured rates in small LIPs (Saunders, 2005).

We need to make a further assumption to calculate the total magmatic flux (= eruptive flux + intrusive flux): the ratio of magma eruption to magma intrusion. This is commonly assumed to be around 1:4, that is, 4 volumes of magma intruded for every volume erupted (Kuntz et al., 1992; Hughes et al., 2002). This ratio is consistent with the relative thickness of

erupted basalt (2 km) versus the mid-crustal sill complex (~8-10 km; Peng and Humphries, 1998). If this ratio is correct, we calculate the volume of basalt intruded as $\sim 64 \times 10^3 \text{ km}^3$, and the total basaltic flux (intruded+extruded) as $\sim 8 \times 10^4 \text{ km}^3$, both over 5.5 Ma. This corresponds to a flux of $1.5 \times 10^4 \text{ km}^3$ per Ma.

Thus, total basaltic flux in the central SRP ($\sim 10^5 \text{ km}^3$ over 6.4 Ma) is consistent with measured rates in small Large Igneous Provinces (LIPs) (Saunders, 2005). For comparison, large LIPs are thought to erupt more than $1 \times 10^5 \text{ km}^3$ of basalt in less than 10 Ma. The total flux of Hawaii (Kilauea) is $1.1 \times 10^5 \text{ km}^3/\text{Ma}$ (Denlinger, 1997), or about 10x higher than that observed in the SRP. Note however, that these calculations include *only* basaltic flux; the volume of rhyolite present (including that erupted as lavas or ash flows, and intruded into the crust as A-type granites) requires magmatic flux volumes that are 5-10x those calculated here (Leeman, 1982; McCurry et al., 2008; McCurry and Rodgers, 2009).

Conclusion

The Kimama core provides an unprecedented opportunity to interpret a continuous sequence of basalt and intercalated sediment, through which the volcanic history of the central SRP may be characterized and temporally constrained. Subsurface geophysical data provide an accurate proxy to lithologic observations made from cored basalt and sediment of the Kimama drill hole. The identification of individual basalt flow units and flows is possible through the use of natural gamma-ray and neutron well log data. Combined with magnetostratigraphic and geochemical logging tools, geophysical logs enable the interpretation of subsurface basalt flow group stratigraphy and the characterization of volcanic processes. Over the past 6.4 Ma, basalt

volcanism on the central SRP in the region of the Kimama core hole has been relatively continuous. Flow groups average most 10 m to 60 m thick and show an average accumulation rate of 335 m/Ma.

The majority of basalt flow breaks within the Kimama core are delineated by the presence sediment in fractures and vesicles. Although not a robust tool for determining avenues of porosity between basalt flows, natural gamma logs accurately delineate large sediment interbeds within the Kimama core and highlight geochemical anomalies within the basalt stratigraphy. Natural gamma anomalies highlight geochemical variations that could indicate changes in magma generation processes and associated volcanism. Furthermore, natural gamma logs provide a valuable resource in determining sample locations for geochemical studies of SRP magmatism.

Slimhole drilling used with neutron and natural gamma logs is a relatively low-cost, time-effective, and accurate means of determining viable geothermal targets. Although core provides the most reliable and tangible means of characterizing the subsurface in areas of high geothermal potential, the use of geophysical wireline logs is a reliable proxy for identifying flow boundaries, geochemical transitions, and probable routes for fluid transport in the subsurface and represents the future of efficient, geothermal exploration. The comparison of logging methods employed to characterize the Kimama core provide clear evidence that that neutron wireline logs correlate closely to actual basalt flow breaks.

References

- Anders, M.H., Saltzman, J., and Hemming, S.R., 2009, Neogene tephra correlations in eastern Idaho and Wyoming for Yellowstone hotspot-related volcanism and tectonic activity: *Geological Society of America Bulletin* v. 121, p. 837–856.
- Armstrong, R.L., Leeman, W.P., and Malde, H.E., 1975, K-Ar dating, Quaternary and Neogene rocks of the Snake River Plain, Idaho: *American Journal of Science*, v. 275, p. 225-251.
- Anderson, S.R., Liszewski, M.J., and Cecil, L.D., 1997, Geologic ages and accumulation rates of basalt-flow groups and sedimentary interbeds in selected wells at the Idaho National Engineering Laboratory, Idaho: U.S. Geological Survey Water-Resources Investigations Report 97-4010, 43 p.
- Anderson, S.R., and Liszewski, M.J., 1997, Stratigraphy of the unsaturated zone and the Snake River Plain Aquifer at and near the Idaho National Engineering Laboratory, Idaho: U.S. Geological Survey Water-Resources Investigations Report 97-4183, 70 p.
- Baksi, A.K. 2007. A quantitative tool for detecting alteration in undisturbed rocks and minerals—I: Water, chemical weathering, and atmospheric argon, *in*: Foulger, G.R. & Jurdy, D.M. (eds) *Plates, Plumes and Planetary Processes*. Geological Society of America, Special Papers, v. 430, p. 285–303.
- Bonnichsen, B., and Godchaux, M. M., 2002, Late Miocene, Pliocene, and Pleistocene geology of southwestern Idaho with emphasis on basalts in the Bruneau-Jarvis, Twin Falls, and western Snake River Plain regions: *Tectonic and Magmatic Evolution of the Snake River Plain Volcanic Province: Idaho Geological Survey Bulletin*, v. 30, p. 233-312.
- Bonnichsen, B., Leeman, W. P., Honjo, N., McIntosh, W. C., and Godchaux, M. M., 2008, Miocene silicic volcanism in southwestern Idaho: geochronology, geochemistry, and evolution of the central Snake River Plain: *Bulletin of Volcanology*, v. 70(3), p. 315-342.
- Champion, D.E., Lanphere, M.A., and Kuntz, M.A., 1988, Evidence for a new geomagnetic reversal from lava flows in Idaho—discussion of short polarity reversals in the Brunhes and Late Matuyama Polarity Chrons: *Journal of Geophysical Research*, v. 93, no. B10, p. 11,677-11,680.
- Champion, D., and Duncan, R. A., 2012. Paleomagnetic and $^{40}\text{Ar}/^{39}\text{Ar}$ studies on tholeiitic basalt samples from “HOTSPOT” corehole taken at Kimama, Idaho, central Snake River Plain. *Eos Transactions, AGU*, V13B-2842.
- Chitwood, L.A., 1994, Inflated basaltic lava—examples of processes and landforms from central and southeast Oregon: *Oregon Geology*, v. 56, no. 1, p. 11-21.
- Davis, L.C., Hannula, S.R., and Bowers, B., 1997, Procedures for use of, and drill cores and cuttings available for study at, the lithologic core storage library, Idaho National

- Engineering Laboratory, Idaho: U.S. Geological Survey Open-File Report 97-124 (DOE/ID-22135), 31p.
- Denlinger, R. P., 1997, A dynamic balance between magma supply and eruption rate at Kilauea volcano, Hawaii: *Journal of Geophysical Research: Solid Earth* (1978–2012), v. 102(B8), p.18091-18100.
- Doherty, D.J., McBroome, L.A., and Kuntz, M.A., 1979, Preliminary geologic interpretation and lithologic log of the exploratory test well (INEL-1), Idaho National Engineering Laboratory, Eastern Snake River Plain, Idaho: U.S. Geological Survey Open-file report, 79-1248, 10 p.
- Duncan, R.A., and Hogan, L.G., 1994, Radiometric dating of young MORB using the ^{40}Ar - ^{39}Ar incremental heating method: *Geophysical Research Letters*, v. 21, no. 18, p. 1927–1930.
- Duncan, R.A., Hooper, P.R., Rehacek, J., Marsh, J.S., and Duncan, A.R., 1997, The timing and duration of the Karoo igneous event, southern Gondwana: *Journal of Geophysical Research*, v. 102, p. 18,127–18,138.
- Greeley, R., 1982, The Snake River Plain, Idaho: Representative of a new category of volcanism: *Journal of Geophysical Research* v. 87(B4), p. 2705–2712.
- Greeley, R., 1977, Basaltic “plains” volcanism, *in* Greeley, R., and King, J.S., eds., *Volcanism of the Eastern Snake River Plain, Idaho: A Comparative Planetary Guidebook*: National Aeronautics and Space Administration, p. 23-44.
- Hackett, W.R., and Smith, R.P., 1992, Quaternary volcanism, tectonics, and sedimentation in the Idaho National Engineering Laboratory area. In *Utah geology and mineral field excursion meeting*, Ogden, UT (United States), May 1992, p. 1-18.
- Hackett, W.R., Smith, R.P., and Khericha, 2004, Volcanic hazards of the Idaho National Engineering and Environmental Laboratory, southeast Idaho, *in* B. Bonnicksen, C.M. White, and M. McCurry, eds., *Tectonic and Magmatic Evolution of the Snake River Plain Volcanic Province*: Idaho Geological Survey Bulletin 30, p. 461-482.
- Helm-Clark, C.M., Ansley, S., McLing, T., and Wood, T., 2005, Borehole and Well Middle-1823 and Its Relationship to the Stratigraphy of the South-Central Idaho National Laboratory: ICP/EXT-05-00790.
- Hofmann, W., 1997, Mantle Geochemistry: The Message from Oceanic Volcanism: *Nature*, v. 385, p. 219-229.
- Hon, K., Kauahihaua, J., Denlinger, R., and McKay, K., 1994, Emplacement and inflation of pahoehoe sheet flows: observations and measurements of active lava flows on Kilauea Volcano, Hawaii: *Geological Society of America Bulletin*, v. 106, p. 351-370.
- Hughes, S., Smith, R., Hackett, W., and Anderson, S., 1999, Mafic volcanism and

environmental geology of the eastern Snake River Plain, *in* S.S. Hughes and G.D. Thackray, eds., *Guidebook to the Geology of Eastern Idaho*: Idaho Museum of Natural History, p. 143-168.

- Hughes, S.S., Wetmore, P.H., Casper, J.L., 2002, Evolution of Quaternary Tholeiitic Basalt Eruptive Centers on the Eastern Snake River Plain, Idaho, *in* Bonnicksen, B., White, C.M., and McCurry, M., eds., *Tectonic and Magmatic Evolution of the Snake River Plain Volcanic Province*: Idaho Geological Survey Bulletin v. 30, p. 363-385.
- Jean, M.M., Shervais, J.W., Champion, D.E., and Vetter, S.K., 2013, Geochemical and paleomagnetic variations in basalts from the Wendell Regional Aquifer Systems analysis (RASA) drill core: Evidence for magma recharge and assimilation–fractional crystallization from the central Snake River Plain, Idaho: *Geosphere*, v. 9, no. 5, p. 1319–1335, doi: 10.1130/GES00914.1.
- Koppers, A.A.P., 2002, ArArCALC—software for $^{40}\text{Ar}/^{39}\text{Ar}$ age calculations: *Computers and Geosciences*, v. 28, p. 605–619.
- Koppers, A.A.P., Staudigel, H., and Wijbrans, J.R., 2000, Dating crystalline groundmass separates of altered Cretaceous seamount basalts by the $^{40}\text{Ar}/^{39}\text{Ar}$ incremental heating technique: *Chemical Geology*, v. 166, no. 1–2, p. 139–158.
- Kuntz, M.A., 1978, *Geology of the Arco-Big Southern Butte area, eastern Snake River Plain, and potential volcanic hazards to the radioactive waste management complex, and other waste storage and reactor facilities at the Idaho National Engineering Laboratory, Idaho with a section on Statistical treatment of the age of lava flows* by John O. Kork: U.S. Geological Survey Open-File Report 78-691, 70 p.
- Kuntz, M., Dalrymple, G., Champion, D., and Doherty, D., 1980. Petrography, age, and paleomagnetism of volcanic rocks at Radioactive Waste Management Complex, Idaho National Engineering Laboratory, Idaho, with an evaluation of volcanic hazards: U.S. Geological Survey Open-File Report 80-388, 63 p.
- Kuntz, M., Champion, D., Spiker, E., and Lefebvre, R., 1986. Contrasting magma types and steady-state, volume-predictable volcanism along the Great Rift, Idaho: *Geological Society of America Bulletin*, v. 97, p. 579-594.
- Kuntz, M., Covington, H., and Schorr, L., 1992. An overview of basaltic volcanism of the eastern Snake River Plain, Idaho, *in* P.K. Link, M.A. Kuntz, and L.P. Platt, eds., *Regional Geology of Eastern Idaho and Western Wyoming*: Geological Society of America Memoir 179, p. 227-267.
- Kuntz, M.A., Anderson, S.R., Champion, D.E., Lanphere, M.A., and Grunwald, D.J., 2002, Tension cracks, eruptive fissures, dikes, and faults related to late Pleistocene-Holocene basaltic volcanism and implications for the distribution of hydraulic conductivity in the eastern Snake River Plain, in Idaho, *in* P.K. Link, and L.L. Mink, eds., *Geology, Hydrogeology, and Environmental Remediation*: Idaho National Engineering and Environmental Laboratory,

Eastern Snake River Plain, Idaho: Geological Society of America Special Paper 353, p. 111-133.

- Leeman, W.P., 1982. Evolved and hybrid lavas from the Snake River Plain, Idaho, *in* Bill Bonnicksen and R.M. Breckenridge, eds., *Cenozoic Geology of Idaho: Idaho Bureau of Mines and Geology Bulletin 26*, p. 181-191.
- Lindholm, G. F., 1996. Summary of the Snake River regional aquifer system analysis in Idaho and eastern Oregon. U.S. Geological Survey Professional Paper 1408-A, 59 p.
- McCurry, M., Hayden, K., Morse, L., and Mertzman, S., 2008, Genesis of post-hotspot, A-type rhyolite of the eastern Snake River Plain volcanic field by extreme fractional crystallization of olivine tholeiite: *Bull. Volcanol.*, v. 70, p. 361-383.
- McCurry, M., and Rodgers, D.W., 2009, Mass transfer along the Yellowstone hotspot track I: Petrologic constraints on the volume of mantle-derived magma: *Journal of Volcanology and Geothermal Research*, v. 188, p. 86-98.
- McFadden, P.L., and Reid, A.B., 1982, Analysis of palaeomagnetic inclination data: *Geophysical Journal International*, v. 69, no. 2, p. 307-319.
- Morgan, W.J., 1972. Plate motions and deep mantle convection: *Geological Society of America Memoir 132*, p. 7-22.
- Peng, X., and Humphreys, E.D., 1998, Crustal velocity structure across the eastern Snake River Plain and Yellowstone Swell: *Journal of Geophysical Research*, v. 103, no. B4, p. 7171-7186.
- Pierce, K.L., and Morgan, L.A., 1992, The track of the Yellowstone Hotspot: volcanism, faulting, and uplift, *in* Link, P.K., Kuntz, M.A., and Platt, L.B., eds., *Regional geology of Eastern Idaho and Western Wyoming: GSA Memoir 179*, p. 1-53.
- Pierce, K.L., and L.A. Morgan. 2009, Is the track of the Yellowstone hotspot driven by a deep mantle plume? — Review of volcanism, faulting, and uplift in light of new data. *Journal of Volcanology and Geothermal Research*. 188, p. 1-25.
- Putirka, K.D., Kuntz, M.A., Unruh, D.M., and Vaid, N., 2009, Magma evolution and ascent at the Craters of the Moon and neighboring volcanic fields, Southern Idaho, USA: Implications for the Evolution of Polygenetic and Monogenetic Volcanic Fields: *Journal of Petrology*, v. 50, no. 9, p. 1639-1665.
- Reiners, P.W., 2002, Temporal-compositional trends in intraplate basalt eruptions: Implications for mantle heterogeneity and melting processes, *Geochemistry Geophysics Geosystems*, v. 3(2), paper 2001GC000250.
- Renne, P.R., Swisher, C.C., Deino, A.L., Karner, D.B., Owens, T., and DePaolo, D.J., 1998, Intercalibration of standards, absolute ages and uncertainties in $^{40}\text{Ar}/^{39}\text{Ar}$ dating:

Chemical Geology (Isotope Geoscience Section), v. 145, p. 117–152.

- Sant, C.J., and Shervais, J.W., 2011, Project Hotspot: Preliminary analysis of secondary mineralization in basaltic core, Central Snake River Plain. Geothermal Resources Council Transactions, v. 35, p. 987-989.
- Saunders, A. D., 2005, Large igneous provinces: Origin and environmental consequences: Elements, v. 1(5), p. 259-263.
- Schutt, D.L., and Dueker, K., 2008, Temperature of the plume layer beneath the Yellowstone Hotspot: Geology v. 36, p. 623–626.
- Self, S., Keszthelyi, L., and Thordarson, T., 1998, The importance of Pahoehoe: Annual Review of Earth and Planetary Sciences, v. 26, p. 81-110.
- Shervais, J., Vetter, S., and Hackett, W., 1994, Chemical stratigraphy of basalts in coreholes NPR-E and WO-2, Idaho National Engineering Laboratory, Idaho: Implications for plume dynamics in the Snake River Plain: Proceedings of the VIIth International Symposium on the Observation of Continental Crust Through Drilling, Santa Fe, New Mexico, p. 93-96.
- Shervais, J.W., Vetter, S.K., and Hanan, B.B., 2006, Layered mafic sill complex beneath the eastern Snake River Plain: evidence from cyclic geochemical variations in basalt: Geology, v. 34, p. 365- 368.
- Shervais, J.W.; Evans, J.P.; Christiansen, E.J.; Schmitt, D.R.; Kessler, J.A.; Potter, K.E.; Jean, M.M.; Sant, C.J.; and Freeman, T.G., 2011, Project Hotspot– The Snake River Scientific Drilling Project: Geothermal Resources Council Transactions, v. 35, p. 995-1003.
- Shervais, J. W., Nielson, D. L., Evans, J. P., Lachmar, T., Christiansen, E. H., Morgan, L., and Freeman, T. G., 2012, Hotspot: The Snake River Geothermal Drilling Project—Initial report: Geothermal Resources Council Transactions, v. 36, p. 767-772.
- Shervais, John W., Douglas R. Schmitt, Dennis Nielson, James P. Evans, Eric H. Christiansen, Lisa Morgan, and James A. Kessler, et al., 2013, First Results from HOTSPOT: The Snake River Plain Scientific Drilling Project, Idaho, U.S.A.: Scientific Drilling, v. 15, p. 36-45.
- Smith, R.E., 1967, Segregation vesicles in basaltic lava: American Journal of Science, v. 265, no. 8, p. 696–713.
- Smith, R. B., Braille, L.W., 1994, The Yellowstone hotspot: Journal of Volcanology and Geothermal Research, v. 61, p. 121-188.
- Steiger, R. H., and Jüger, E., 1977, Subcommittee on geochronology: Convention on the use of decay constants in geo- and cosmochronology: Earth Planet. Sci. Lett., v. 36, p. 359-362.

- Twining, B.V., Hodges, M.K., and Orr, S.M., 2008, Construction diagrams, geophysical logs, and lithologic descriptions for boreholes USGS 126a, 126b, 127, 128, 129, 130, 131, 132, 133, and 134, Idaho National Laboratory, Idaho: U.S. Geological Survey Digital Series 350.
- Twining, B.V., and Bartholomay, R. C., 2011. Geophysical logs and water-quality data collected for boreholes Kimama-1A and-1B, and a Kimama water supply well near Kimama, southern Idaho. U.S. Geological Survey Data Series 622 (DOE/ID 22215), 18 p., plus appendix.
- Walker, G.P.L., 1971, Compound and simple lava flows and flood basalts: Bulletin Volcanologique, v. 35, p. 579-590.
- Walker, G.P.L., 1991, Structure, and origin by injection of lava under surface crust, of tumuli, "lava rises", "lava-rise pits" and "lava-inflation clefts" in Hawaii: Bulletin of Volcanology, v. 53, p. 46-558.
- Walker, G.P.L., 1993, Basaltic-volcano systems: Geological Society, London, Special Publications, v. 76, p. 3-38.
- Welhan, J.A., Johannesen, C.M., Reeves, K.S., Clemo, T.M., Glover, J.A., and Bosworth, K.W., 2002, Morphology of inflated pahoehoe lavas and spatial architecture of their porous and permeable zones, eastern Snake River Plain, Idaho: Geological Society of America Special Paper, v. 353, p. 135-150.

CHAPTER 3

PETROLOGIC AND GEOCHEMICAL EVOLUTION OF BASALTS FROM THE KIMAMA 1912 M CORE
HOLE, CENTRAL IDAHO

Abstract

New geochemical data from basalts in the Kimama core hole document 6.4 m.y. of magma evolution on the central Snake River Plain. In 1912 m of continuous core, four compositional rock types are identified: olivine tholeiite, very low K, high Fe-Ti, and very high K-FeO*. Episodes of high-K, low-K, olivine tholeiite, and Fe-Ti magmatism are evident throughout the core, and are found within individual flow groups, which represent magmatic events. The chemical variation evident in 71 flow groups demonstrate source heterogeneity and differences in magma processing during ascent are important in generating basalt volcanism on the Snake River Plain.

High-K basalt is found at two depths, 319 m and 1078 m, and in flows with thicknesses less than 1.5 m. These evolved flow groups are chemically analogous to the evolved Holocene polygenetic lavas from the Craters of the Moon lava field. Snake River olivine tholeiite, low-K, and Fe-Ti basalt compositional types occur throughout the core and in thicknesses ranging from 150 m to 11 m. The presence of multiple, unrelated compositional types supports the hypothesis that different parent magmas evolve through varying degrees of crystal fractionation at shallow to intermediate depths over short durations, and are modified by episodic recharge of more primitive magmas and by assimilation of the layered mafic sill complex.

Thirty flow groups show very little chemical change with time, signifying either rapid evacuation from the magma chamber (without sufficient time for differentiation) or consistent

differentiation processes. The 16 upward fractionation cycles, 12 reversed cycles, four reverse-fractionation cycles, five fractionation-reverse cycles, and two reversal-fractionation-reversal cycles over eruption intervals generally less than 100 years show that chemical changes have continuously occurred over the 6.4 M.y. period during which Kimama basalts were erupted. We propose that typical Snake River olivine tholeiite represent typical fractionation and recharge patterns, consistent with varying degrees of assimilation with gabbroic country rock. The high-K evolved flows low-K flows, and Fe-Ti flows represent separate magma batches that infiltrated the Kimama system and are unrelated to melts that result from typical differentiation processes within the mid crustal sill.

Introduction

The Snake River Plain (SRP) of central Idaho, the manifestation Yellowstone-Snake River Plain (Y-SRP) volcanic province, contains intriguing evidence for mantle hotspot impingement on continental crust (Pierce and Morgan, 1992; Shervais and Hanan, 2008; Smith et al., 2009; Sigloch, 2011). The SRP, with a record of continuous bimodal volcanism extending over 12 M.y. to the present, documents the migration of time-transgressive rhyolitic volcanism from the Bruneau-Jarbridge caldera complex (circa 12 Ma) to its present location beneath the Yellowstone Plateau (Pierce and Morgan, 1992; Anders et al., 2009). Interaction between the mantle hotspot and overlying continental lithosphere has resulted in large rhyolite caldera-forming eruptions, followed by eruption of smaller basaltic shield volcanoes (McCurry and Rodgers, 2009; Bonnicksen et al., 2008). The post-caldera basaltic flows form a veneer over the rhyolite ash flows, masking the complete volcanic record. Understanding the origin and

evolution of the post-caldera basalts is a challenge because the lack of later uplift and erosion means that younger flows conceal older basalts that erupted in the same location.

Project HOTSPOT drilled three deep core holes in the Snake River Plain in order to provide a more complete understanding of the volcanic history of the SRP (Shervais et al., 2012; 2013). The 1912 m deep Kimama core hole, located in the Axial Volcanic Zone of the Snake River Plain, recovered over 1900 m of continuous core, including 1803 m of basalt and 110 m of intercalated sediment (including sidetrack core). We present a detailed petrologic and geochemical investigation of basalts from the Kimama core. Our main goal is to determine the nature and extent of chemical changes through time at a fixed location, where physical and chemical characteristics of the crust and mantle lithosphere are relatively set.

Other deep drill holes on the SRP include the Sugar City core hole (0.7 km; Doherty et al., 1979), the Idaho National Laboratory (INL) hole WO-2 (1.52 km; Shervais et al., 2006), and the Wendall-RASA (0.3 km; Jean et al., 2013)(Figure 11). Previous workers have shown, based on geochemical and isotope analyses that significant fractionation occurred at lower or mid-crustal depths in the layered mafic magma chambers, and that interaction with continental lithosphere is the primary influence on basalt chemistry in the SRP. Assimilation of genetically-related, previously-intruded mafic sills occurs in mid-crustal magma chambers (Shervais et al., 2006; Jean et al., 2013), and a range of primary magma compositions suggests the involvement of multiple, small magma batches (Leeman 1982b; Vetter and Shervais, 1992; Geist et al., 2002; Hughes et al., 2002a; Shervais et al., 2006; Jean et al., 2013). Shifts in the composition of primary magma sources through time have been documented by Vetter and Shervais (1992), Shervais et al. (2006), and Shervais and Vetter (2009).

I hypothesize that basalts erupted in the SRP and preserved in the Kimama core reveal temporal chemical heterogeneity related to varying processes of assimilation and fractional

crystallization through time. Using 39 documented cycles of geochemical fractionation and recharge, I seek to identify and model petrogenetic processes in basaltic lava flows cored by the Kimama drill hole, and to demonstrate temporal-compositional trends in the petrogenesis of the central SRP volcanic province.

Geological Background

Regional Setting

The central SRP is loosely defined as the portion of the SRP between the Owyhee Plateau, a highland in SW Idaho, and the Great Rift, a north-northwest-trending fissure system that extends ~50 km southward from Craters of the Moon National Monument to the Wapi National Monument (Figure 11) (Kuntz et al., 1982, 1992). Major geologic features on the central SRP include the 12.7-8.5 Ma Twin Falls eruptive center, visible today as an ovoid gravity anomaly (Shervais et al., 2011), and the 10.3-8.2 Ma Picabo eruptive center, for which the boundaries are poorly defined (Pierce and Morgan, 1992; Bonnicksen et al., 2008). Beyond the SRP, to the north and south of Kimama, is the Basin and Range Province.

The Kimama area includes late Neogene to Quaternary basalts that were erupted from low-relief shield volcanoes. Shield volcanoes and basaltic lava flows overlie rhyolite from the Twin Falls and Picabo volcanic centers (Kuntz et al., 1988; Bonnicksen et al., 2008), although rhyolite was not encountered in the Kimama drill core (Potter et al., submitted). Although inflated flow fronts and pressure ridges are still visible as rugged topography, surface flow morphology in the Kimama area includes nearly continuous loess mantles of variable thickness and well-developed soils. Surface drainages are poorly defined (Shervais et al., 2005).

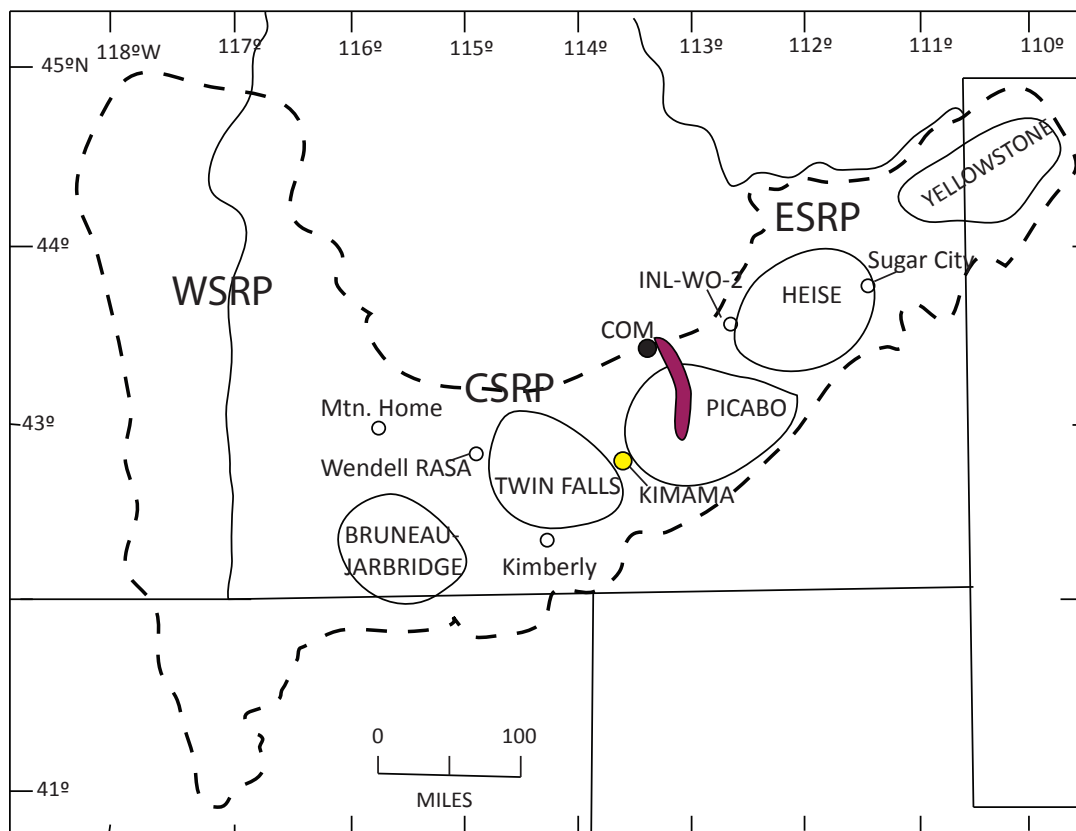


Figure 11: Map of the Snake River Plain showing location of the Kimama core hole in relation to inferred locations of silicic volcanic centers. The Great Rift, shown in purple, marks the transition between the central SRP and eastern SRP provinces. The locations of the Idaho National Lab (INL) and Craters of the Moon National Monument (COM) are also shown.

Mafic volcanism on the SRP began within 1 m.y. of the cessation of Y-SRP hotspot-track-related silicic volcanism, and is primarily expressed by the eruption and coalescence of monogenetic, diktytaxitic olivine tholeiite basalt shields with relatively primitive compositions (Hughes et al., 2002a). The unique style of volcanism along the SRP has been recognized as a product of small, mid-crustal magma chambers feeding eruptions from coalesced low-relief shield volcanoes, over relatively short durations, described as “plains-style volcanism” by Greeley (1982). “Plains-style” volcanism is similar to modern volcanic processes on the island of

Hawaii and transitional between quiescent Hawaiian-style and continental-style volcanism (Greeley, 1982; Kuntz, 1978). Vent constructs for SRP volcanoes are typically unimpressive due to the efficient transport of low-viscosity lava away from the vent in lava tubes. Because relatively little lava accumulates near the vent, eruptive centers often blend in with the surrounding topography (Self et al., 1998).

During the late Pliocene through Pleistocene, the SRP was the locus of densely-spaced mafic volcanic centers along the track of the Y-SRP hotspot that erupted thick packages of basalt flows and formed the Axial Volcanic High (AVH) (Hackett and Smith, 1992; Hackett et al., 2004). Although time-progressive basalt eruptions are evident at the inception of post-rhyolitic volcanism, Pliocene-Holocene lavas on the SRP are distributed throughout the volcanic province (Hughes et al., 1999; Bonnicksen and Godchaux, 2002). Snake River Plain basaltic volcanism is manifested as monogenetic, single-pulse lava fields, erupted as low volume ($3\text{-}5\text{ km}^3$) flows from fissures during short-duration (days) eruptions (Kuntz et al., 1992). Later volcanism at Hells Half Acre (2270 ± 50 years BP), Cerro Grande (13380 ± 350 years BP), Wapi (2270 ± 50 years BP), Shoshone (10130 ± 350 years BP), and Craters of the Moon (COM) occurred over months to decades and produced greater-volume eruptions ($3.3\text{-}30\text{ km}^3$) within a localized area (Kuntz et al., 1992). Lavas at COM are the most recent products of SRP volcanism, with multi-phase eruptions with $^{40}\text{Ar}/^{39}\text{Ar}$ ages of 480 ka to 50 ka (Bonnicksen and Godchaux, 2002).

Snake River Plain Basalt Petrology

Although SRP olivine tholeiites are relatively homogenous, previous research has demonstrated that chemical variation between basalt flows is a result of fractional crystallization, crustal contamination, and partial melting occurring within the mid-crustal sill at pressures of $\sim 8\text{-}10$ kbar and temperatures of $1205 \pm 27^\circ\text{C}$ (Wager and Brown, 1967; Irvine, 1970;

Jackson, 1970, 1971; McBirney and Noyes, 1979; Pallister and Hopson, 1981; Leeman, 1982c; Kuntz et al., 1992; Shervais et al., 2006; McCurry and Rodgers, 2009; Putirka et al., 2009; Miller and Hughes, 2009). Putirka et al. (2009) argue for a three-stage process to explain the entire range of SRP lava compositions: at depths of 10-20 km, picrites ascend to the middle crust, where they undergo partial crystallization of olivine \pm clinopyroxene. Storage of olivine tholeiite magmas in the middle crust (20-10 km) causes magma compositions to evolve to moderate MgO wt% (10%), at which point positive buoyancy is reached and migration through the middle crust occurs. Finally, at depths of 15-0 km, differentiation and resulting volatile content increases (1-2 wt% H₂O) cause the final eruption and ascent of magma through the middle and upper crust (Putirka et al., 2009). This mode of generation is in agreement with the magma-mush column model of Marsh (2004), the MASH (mixing, assimilation, storage and homogenization) model of Hildreth and Moorbath (1988) and the SRP magma petrogenetic model of Shervais et al. (2006), in which magmas are shown to evolve through complex pathways of fractional crystallization, assimilation, and mixing at multiple crustal levels before eruption.

Monogenetic eruptive centers on the SRP are most likely fed by individual magma sources, as demonstrated by chemical variation between and within flow groups (Hughes et al., 2002b). However, in order to produce separate magma batches for every monogenetic center on the SRP, a stratified source region in which melts were produced over a range of depths and degrees of melting would be required (Hughes et al., 1997). In such an environment, and with a primitive mantle magma source, chemical variations suggest that magma batches experienced differing degrees of partial melt and fractionation of a heterogeneous enriched subcontinental mantle (Leeman and Vitaliano, 1976; Menzies et al., 1984; Reid, 1995; Hanan et al., 1997; Hughes et al., 2002b).

Potter et al. (see Chapter 2) have identified 462 distinct basalt flow units which comprise 155 separate lava flows, based on physical and lithologic logs of the drill core, borehole geophysical logs, paleo-secular variations in magnetic stratigraphy, and the presence of sedimentary interbeds. Using these data and limited geochemical indicators (FeO* (total ferrous iron), K₂O, La/Lu), they recognize 71 distinct flow groups, ranging in thickness from 0.700 to 183.4 m thickness. They further document that this sequence represents ~5.5 million years of volcanism (from 6.5 Ma to 720 Ka). We will use this stratigraphic framework to interpret our results here. We seek to identify chemical variations within cored Kimama basalts to investigate magma source and differentiation processes in the central SRP.

Methods

We selected 261 whole rock samples from the Kimama core for analysis, representing all 30 basalt flow groups. Major elements and select trace elements were analyzed by fused bead X-ray fluorescence spectrometry (XRF), and trace elements were analyzed by inductively coupled plasma mass spectrometry (ICP-MS).

For major and trace element analysis, mini core plug halves were broken in two to three fragments using a rock hammer. Samples were crushed using a Gyral Grinder shatterbox with a tungsten carbide vessel, and then ground again with an agate mortar and pestle. Samples were ignited at 800°C for 24 hours, after which 1 g of sample was mixed with 5 g of a Claisse Li-borate flux and 6 drops of Lil (added as a releasing agent). Sample mixes were melted in Pt-Au metal crucibles at 1200°C in a muffle furnace, then poured into a heated Pt-Au metal disk mold and quenched into glass. Major element (SiO₂, TiO₂, Al₂O₃, MnO, FeO*, MgO, CaO, Na₂O, K₂O, P₂O₅

Cr₂O₃) were analyzed with a Philips 2400 X-Ray fluorescence (XRF) spectrometer at Utah State University.

Trace-element concentrations were measured at Centenary College (Shreveport, LA) using a PerkinElmer 600 inductively coupled plasma-mass spectrometer (ICP-MS). Approximately 60 mg of each sample was dissolved in 2 mL HF and 3 mL HNO₃ for 3 hours, with watch glasses preventing evaporation. Watch glasses were then removed and samples dried, after which another 3 mL of HNO₃ was added to the samples. The sample solution was left at 50°C overnight, and then dried at 90°C. A further addition of 3 mL of HNO₃ to the sample preceded immediate drying. Finally, the sample was brought into solution with 2-3 mL of 50% HNO₃, and brought to a total volume of 50 mL with 5% HNO₃. This procedure is modified from Jenner et al. (1990) and Neal (2001). Five milliliters of 10 ppb In, Rh, and Ru were added to the sample solution as internal standards to calibrate measured concentrations. Plasma lab software was used to map out sampling order and record measurements over the duration of the experiment.

Results

Major Elements

The whole-rock major-and trace-element compositions of Kimama samples (Table 4), and MgO-variation diagrams (Figure 12) reveal similarity to olivine tholeiite basalt compositions from the eastern SRP. Geochemistry displayed in stratigraphic context (Figure 13) demonstrates more variation. Kimama basalts have major-element compositional ranges of 43.2- 50.4 wt% SiO₂, 9.80- 17.6 wt% FeO*, 1.22-4.65 wt% TiO₂, 5.00-11.0 wt% MgO, 8.84-14.0 wt% CaO, 11.5- 15.8 wt% Al₂O₃, 1.75-2.75 wt% Na₂O, and 0.120-0.920 wt% K₂O, 0.170-1.65 wt% P₂O₅. Loss on

ignition (LOI) is less than 1%. In general, Kimama basalts demonstrate smooth to variable increasing and decreasing patterns on MgO variation plots (Figure 12). Increases in TiO₂, FeO*, and K₂O are observed with respect to decreasing MgO. Concentrations of SiO₂, Al₂O₃, CaO, and Cr decrease with decreasing MgO.

These data reveal that the Kimama basalts define four distinct, geochemically-defined groups: (1) a 'Snake River Olivine Tholeiite' (SROT) group that represents most of the basalt samples from surface outcrops on the SRP, (2) a low-K SROT group, characterized by K₂O < 0.4 wt%, but otherwise broadly similar to normal SROT is observed throughout the Kimama core, (3) iron and titanium-rich "Fe-Ti" basalts similar to many basalts found within Craters of the Moon, with 16-18 wt% FeO* and 3.0-4.5 wt% TiO₂ 3-4 wt%; and (4) a rare high-K suite, characterized by K₂O > 0.65 wt% (Figure 14). Fe-Ti basalts are preferentially located in the upper 600 m of the core, whereas the high-K flow groups are located at only two depth ranges, near 318 m and 1077 m. SROT basalts dominate the upper 1000 m of the Kimama core, whereas low-K basalts are the dominant compositional type from 1000 m to 1912 m depth.

Trace-element analyses of Kimama basalts (Table 1) indicate that compositional trends in rare earth elements (REE) are generally similar to those observed in basalts of the eastern SRP. However, Kimama basalts are generally higher in light rare earth elements (LREE) than eastern SRP basalts, a trait best observed on chondrite-normalized (McDonough and Sun, 1995) multi-element spider diagrams (Figure 15). Within the core, REE trends show no discernable trends of depletion or enrichment with depth, although upsection heavy rare earth element (HREE), LREE, and incompatible element trends correlate to recharge and fractionation cycles within individual flow groups (Figure 16).

TABLE 4: KIMAMA CORE BULK-ROCK ELEMENTAL ANALYSES

Flow Group	Flow Group 8										Flow Group 9													
	21	22	23	24	24	24	25	26	27	28	28	29	29	30	30	30	30	30	30	30				
Inch.	22*										61*													
Flow	KAI1A675 KAI1B675 KAI1A681 KAI1A686 KAI1A700 KAI1B707 KAI1A725 KAI1B747 KAI1A750 KAI1B785 KAI1A787 KAI1B789 KAI1B797 KAI1A799 KAI1B807 KAI1A809 KAI1B813 KAI1A818 KAI1B821 KAI1A822 KAI1B837 KAI1B850																							
Sample																								
Major Elements**																								
SiO2	47.9	47.9	47.6	46.8	47.6	48.3	47.3	48.3	48.4	46.8	46.3	47.1	46.2	47.3	47.3	46.5	47.4	46.2	46.2	46.2	46.2	46.2	46.3	46.8
Al2O3	13.7	13.7	13.3	14.7	13.8	14.2	14.6	13.6	13.7	13.5	14.5	13.9	14.1	13.6	13.4	14.1	13.7	13.8	14.8	14.8	14.3	14.4	14.4	14.0
FeO*	14.0	14.0	14.2	14.0	14.0	13.3	13.5	13.8	13.5	14.6	14.2	14.3	14.7	14.3	14.6	14.1	14.1	15.0	14.0	14.5	14.4	14.4	14.4	14.0
MgO	6.55	6.55	6.55	6.52	6.42	6.64	6.92	6.18	6.33	6.63	6.99	6.68	6.60	6.55	6.29	6.22	6.65	6.50	7.13	6.67	6.69	7.29	6.69	
CaO	9	9	9.19	9.33	9.22	9.02	9.11	9.13	9.07	9.53	9.50	9.35	9.49	9.33	9.37	9.46	9.32	9.50	9.45	9.56	9.55	9.63	9.63	
Na2O	2.62	2.62	2.59	2.55	2.58	2.56	2.61	2.61	2.62	2.57	2.54	2.44	2.54	2.51	2.46	2.6	2.49	2.49	2.54	2.51	2.52	2.46	2.46	
K2O	0.780	0.780	0.820	0.670	0.780	0.830	0.840	0.920	0.900	0.610	0.580	0.530	0.630	0.610	0.610	0.620	0.610	0.640	0.560	0.580	0.580	0.580	0.510	
TiO2	2.97	2.97	3.14	2.99	3.04	2.81	2.76	3.04	2.91	3.16	2.96	3.08	3.23	3.18	3.36	3.29	3.08	3.33	2.85	3.17	3.13	2.83	2.83	
P2O5	0.610	0.610	0.590	0.670	0.610	0.570	0.620	0.630	0.610	0.560	0.600	0.580	0.670	0.570	0.590	0.690	0.570	0.700	0.570	0.640	0.610	0.490	0.490	
MnO	0.200	0.200	0.200	0.200	0.190	0.190	0.200	0.200	0.190	0.200	0.210	0.200	0.210	0.200	0.200	0.210	0.200	0.220	0.200	0.210	0.210	0.210	0.190	
Mg#	32.0	32.0	31.5	31.8	31.5	33.3	33.9	31.0	31.9	31.3	33.0	31.8	31.0	31.4	30.1	29.8	32.0	30.2	33.8	31.5	31.7	34.2	34.2	
Cr	221	233	197	217	216	226	230	212	225	221	218	229	193	167	123	199	223	196	146	212	202	268	268	
K	648	648	681	556	648	689	697	764	747	506	481	440	523	506	506	515	506	531	465	481	481	423	423	
P	266	266	257	292	266	249	271	275	266	244	262	253	292	249	257	301	249	305	249	279	266	214	214	
Trace Elements***																								
Rb	18.6	17.2	21.3	14.9	16.0	24.1	14.0	20.2	28.4	10.2	8.01	12.4	12.0	7.67	12.3	13.9	12.7	4.22	4.86	12.0	11.4	9.69	9.69	
Ba	596	624	520	605	598	594	513	634	616	504	486	587	562	419	463	619	542	185	206	568	518	429	429	
Sr	800	533	469	504	480	525	428	493	510	530	466	595	547	355	220	353	203	142	589	556	523	523	523	
Pb	8.00	7.62	7.67	11.1	8.58	7.26	7.68	9.94	8.41	8.45	6.09	6.44	6.34	4.98	4.21	6.95	6.29	1.91	2.61	6.72	5.83	5.29	5.29	
Th	3.41	3.06	3.40	3.23	3.71	3.58	3.05	4.01	4.32	2.09	1.65	2.58	2.36	1.49	1.46	2.39	2.23	0.500	0.650	2.22	1.96	1.62	1.62	
U	1.02	0.920	0.910	0.980	1.04	1.09	1.04	1.22	1.21	0.740	0.670	0.680	0.730	0.430	0.470	0.760	0.720	0.160	0.220	0.700	0.640	0.510	0.510	
Zr	459	409	408	436	424	462	410	444	478	416	377	447	457	303	261	422	393	139	174	394	349	331	331	
Hf	9.48	9.56	8.84	9.59	9.79	9.14	9.06	10.7	10.3	9.70	8.65	9.68	10.1	6.98	9.80	9.22	3.34	3.91	9.38	8.36	7.82	7.82	7.82	
Ta	2.26	1.73	2.14	2.15	2.26	1.87	2.14	2.56	2.49	2.15	1.40	2.24	1.91	1.30	0.85	1.96	1.81	0.57	0.62	1.85	1.65	1.66	1.66	
Y	53.2	48.6	51.3	49.8	51.5	50.2	43.6	53.1	57.4	50.5	42.2	57.3	51.1	31.6	25.2	58.2	53.7	15.7	18.8	54.8	48.4	47.6	47.6	
Nb	40.3	33.5	36.8	37.6	38.9	35.2	36.6	42.3	42.5	33.6	27.5	32.6	32.2	21.4	14.1	34.0	31.8	8.40	10.8	32.3	28.1	27.6	27.6	
Sc	36.2	37.5	38.2	37.2	36.4	38.9	29.5	38.9	42.6	37.6	33.6	44.9	37.0	32.5	22.8	43.0	42.8	20.1	20.1	41.1	38.0	40.9	40.9	
Trace Elements***																								
Ni	98.3	110	81.5	99.3	95.0	105	109	87.8	90.1	99.0	102	101	86.2	75.9	71.2	82.2	97.1	63.9	51.1	98.4	93.9	119	119	
V	468	411	444	426	418	487	427	449	496	534	444	561	577	368	256	590	555	214	224	482	423	499	499	
La	48.1	46.3	45.2	46.7	46.5	45.5	41.2	47.4	50.4	39.7	33.9	41.8	38.8	27.5	21.7	43.5	39.3	10.6	14.8	40.3	34.5	31.8	31.8	
Ce	103.5	100.8	97.3	101.6	103.8	99.1	93.0	106	110	89.9	78.4	92.1	86.8	61.4	49.6	96.0	89.2	24.3	33.5	91.4	79.5	73.6	73.6	
Pr	13.3	12.8	12.4	12.8	13.1	12.6	11.9	13.5	13.8	12.0	10.1	12.3	11.6	8.05	6.80	12.7	11.9	3.39	4.56	12.2	10.5	9.72	9.72	
Nd	56.1	53.4	51.9	53.8	54.8	52.6	49.7	57.0	58.0	52.7	45.0	53.4	50.9	40.1	33.6	55.5	52.1	16.6	21.8	53.2	46.8	43.0	43.0	
Sm	12.1	11.5	11.2	11.7	12.0	11.5	11.0	12.4	12.7	12.1	10.3	12.2	11.5	9.03	7.63	12.7	11.8	4.05	4.99	12.0	10.7	10.0	10.0	
Eu	4.04	3.86	3.74	3.90	3.92	3.73	3.57	4.04	4.15	4.10	3.57	4.27	3.96	2.77	2.74	4.30	3.99	1.56	1.83	4.07	3.64	3.52	3.52	
Gd	13.7	13.1	12.8	13.5	13.5	13.1	12.4	14.2	14.6	13.7	11.9	14.4	13.4	10.7	8.64	14.6	13.2	4.69	5.82	13.7	12.6	11.6	11.6	
Tb	1.94	1.86	1.84	1.9	1.92	1.88	1.77	2.02	2.10	1.98	1.68	2.04	1.93	1.32	1.13	2.08	1.93	0.64	0.77	1.99	1.77	1.70	1.70	
Dy	11.1	10.7	10.6	11.00	11.2	10.8	10.1	11.7	12.2	11.6	9.54	11.8	11.3	8.78	7.61	11.9	11.3	4.34	5.33	11.4	10.4	10.0	10.0	
Ho	2.19	2.07	2.11	2.18	2.25	2.10	2.32	2.36	2.32	2.34	1.88	2.36	2.26	1.51	1.33	2.39	2.28	0.790	0.940	2.27	2.07	1.98	1.98	
Er	6.05	5.89	5.86	6.13	6.24	5.88	5.51	6.45	6.74	6.34	5.23	6.64	6.20	4.89	4.17	6.64	6.29	2.42	2.97	6.26	5.76	5.46	5.46	
Tm	0.810	0.780	0.790	0.820	0.850	0.800	0.740	0.890	0.930	0.860	0.700	0.890	0.830	0.540	0.470	0.890	0.860	0.280	0.350	0.850	0.770	0.750	0.750	
Yb	5.20	4.96	5.10	5.28	5.32	5.12	4.75	5.44	5.94	5.39	4.39	5.55	5.31	4.17	3.46	5.73	5.40	2.14	2.56	5.48	4.93	4.72	4.72	
Lu	0.760	0.710	0.730	0.750	0.780	0.740	0.680	0.800	0.840	0.640	0.640	0.820	0.780	0.510	0.430	0.840	0.780	0.270	0.330	0.790	0.700	0.700	0.700	

Note: Major oxides are in weight percent, trace elements and rare earth elements are in parts per million. Flow groups as in text.

**Measured by X-ray fluorescence

***Normalized to 100 wt% on a volatile free basis.

****Measured by inductively coupled plasma-mass spectrometer

TABLE 4: KIMAMA CORE BULK-ROCK ELEMENTAL ANALYSES

Inclin.	Flow Group 9	Flow Group 10	Flow Group 11			Flow Group 12 (VHK)			Flow Group 13			Flow Group 14				
			-61°	-61°	-61°	-61°	-61°	-61°	-61°	-61°	-61°					
Sample	KAI1855	KAI1860	KAI18910	KAI18912	KAI18927	KAI18947	KAI18977b	KAI18987	KAI18997	KAI19020	KAI19045	KAI19051	KAI19057	KAI19058	KAI19095	KAI19107
Major Elements**																
SiO2	46.3	47.6	46.0	45.4	46.1	46.6	46.3	46.4	47.1	48.0	46.2	46.1	46.6	46.5	46.6	46.6
Al2O3	15.0	12.5	14.6	14.5	14.6	14.2	14.0	15.1	14.9	14.1	11.3	11.2	14.1	14.1	13.2	14.4
FeO*	13.7	15.2	13.7	13.5	13.6	12.7	13.1	12.6	12.8	12.1	17.8	17.9	14.7	14.6	14.3	14.0
MgO	7.36	5.63	7.23	8.19	7.72	8.23	8.54	8.26	8.80	8.90	8.77	3.91	6.01	6.06	7.36	8.25
CaO	9.70	9.12	9.72	9.96	10.06	10.33	10.5	10.3	10.2	10.0	9.86	9.89	10.31	10.32	9.89	10.1
Na2O	2.51	2.58	2.50	2.33	2.41	2.31	2.43	2.39	2.42	2.42	2.36	2.72	2.44	2.45	2.31	2.28
K2O	0.450	0.760	0.500	0.470	0.540	0.570	0.490	0.530	0.580	0.580	1.81	1.84	0.530	0.560	0.490	0.380
TiO2	2.70	3.56	2.91	2.58	2.64	2.26	2.31	2.20	2.30	2.08	2.14	3.16	3.16	3.17	3.06	2.86
P2O5	0.490	0.820	0.560	0.470	0.540	0.450	0.480	0.460	0.440	0.440	2.22	2.22	0.800	0.780	0.770	0.740
MnO	0.190	0.230	0.200	0.200	0.190	0.190	0.190	0.190	0.190	0.180	0.320	0.320	0.210	0.200	0.210	0.210
Mg#	35.0	27.0	33.7	37.8	36.3	39.5	38.7	40.5	39.3	42.0	18.1	17.9	29.0	30.4	34.0	37.1
Cr	253	160	234	421	367	448	394	489	479	636	NA	192	191	185	309	367
K	374	631	415	390	448	448	473	407	440	481	1503	1527	440	465	407	315
P	214	358	244	205	236	196	201	209	223	192	969	969	349	340	336	323
Trace Elements***																
Rb	6.05	15.8	10.6	9.26	11.5	12.1	9.68	12.1	8.09	18.1	49.5	38.0	6.61	6.13	9.97	9.69
Ba	385	636	266	377	418	379	373	409	335	405	1713	1504	554	489	605	523
Sr	464	500	160	262	407	478	439	421	468	464	505	456	487	485	539	574
Pb	4.76	9.16	2.32	4.67	5.25	4.13	5.51	3.88	4.54	5.72	23.4	25.2	6.83	6.60	5.50	5.98
Th	1.13	2.64	0.93	1.28	1.69	1.50	1.32	1.58	1.48	2.43	9.96	8.82	1.42	1.35	1.57	1.15
U	0.440	0.890	0.260	0.460	0.550	0.510	0.530	0.500	0.660	0.740	3.130	3.030	0.560	0.560	0.570	0.460
Zr	295	542	160	276	312	279	279	256	239	288	1875	1760	431	461	438	373
Hf	6.46	12.2	3.78	6.57	7.72	6.51	6.49	6.10	5.45	6.56	37.1	34.3	9.53	9.65	9.75	9.96
Ta	1.32	2.54	0.68	1.47	1.8	1.44	1.37	1.27	0.88	1.38	7.98	3.42	1.88	1.54	1.86	2.28
Y	35.3	72.7	17.9	38.6	44.4	39.5	37.2	40.6	27.2	41.8	221	181	53.7	51.2	62.2	45.2
Nb	22.9	43.2	10.4	24	26.8	23.8	23.1	20.8	17.0	23.0	143	67.8	35.7	31.5	33	27.7
Sc	32.2	45.6	21.2	40.8	43.3	39.6	35.4	42.3	28.5	44.4	45.8	38.7	41.5	41.8	35.8	40.2
Trace Elements***																
Ni	117	73.0	106	153	136	150	145	150	156	167	0.500	1.00	75.6	73.8	119	121
V	509	434	219	528	527	431	421	442	329	388	134	123	478	551	505	393
La	25.1	53.1	12.7	26.4	30.5	27.1	26.0	26.6	20.9	28.7	171.4	154.6	45.2	46.1	45.0	36.1
Ce	59.8	120.4	29.2	60.9	70.0	61.1	59.8	60.2	50.4	64.1	390.7	359.9	103.3	103.2	103.6	81.9
Pr	7.96	16.1	4.01	8.01	9.31	8.19	7.98	8.04	6.40	8.43	50.1	46.5	13.5	13.4	14.1	10.8
Nd	35.6	70.2	19.3	35.6	41.1	35.5	35.1	35.6	27.9	37.2	211	199	58.9	58.6	62.0	46.6
Sm	8.10	16.0	4.59	8.44	9.51	8.47	8.23	8.16	6.36	8.62	43.1	43.1	12.9	12.8	13.8	13.7
Eu	2.92	5.26	1.68	3.02	3.33	2.98	2.87	2.87	2.22	2.92	13.3	12.4	4.48	4.55	4.77	3.81
Gd	9.43	18.4	5.41	9.73	11.2	9.89	9.44	9.64	7.51	10.1	51.3	48.5	14.7	14.8	15.8	12.2
Tb	1.36	2.69	0.72	1.43	1.62	1.42	1.38	1.40	1.09	1.48	7.35	6.88	2.09	2.09	2.21	1.72
Dy	7.81	15.8	5.01	8.48	9.73	8.64	8.07	8.40	6.23	8.91	41.6	39.6	11.8	11.9	12.3	10.0
Ho	1.57	3.12	0.91	1.69	1.94	1.72	1.61	1.70	1.24	1.78	8.23	7.89	2.32	2.35	2.46	2.00
Er	4.33	8.53	2.83	4.65	5.48	4.78	4.52	4.69	3.45	4.97	23.3	21.7	6.49	6.48	7.04	5.52
Tm	0.580	1.14	0.330	0.630	0.750	0.650	0.610	0.640	0.470	0.670	3.24	2.97	0.860	0.860	0.940	0.730
Yb	3.66	7.39	2.46	4.04	4.72	4.18	3.85	4.09	2.98	4.35	20.4	19.0	5.41	5.41	6.01	4.61
Lu	0.530	1.070	0.320	0.580	0.700	0.610	0.570	0.600	0.420	0.640	2.99	2.77	0.790	0.780	0.890	0.670

Note: Major oxides are in weight percent, trace elements and rare earth elements are in parts per million. Flow groups as in text.

*Measured by X-ray fluorescence

**Normalized to 100 wt% on a volatile free basis.

***Measured by inductively coupled plasma-mass spectrometer

TABLE 4: KIMAMA CORE BULK-ROCK ELEMENTAL ANALYSES

Flow Group	Flow Group 14		Flow Group 15 (Fe-Tl)		Flow Group 16		Flow Group 17		Flow Group 18		Flow Group 19		Flow Group 20 (Fe-Tl)						
	Inclin.	Flow	-64°	-62°	-62°	-57°	60°	60°	60°	60°	60°	60°	60°	22°					
Sample	KA1B1119	KA1B1135	KA1B1147	KA1B1175	KA1B1191	KA1B1210	KA1B1224	KA1B1300	KA1B1327	KA1B1358	KA1B1387	KA1B1391	KA1B1410	KA1B1424	KA1B1434	KA1B1467	KA1B1488	KA1B1491	KA1B1503
Major Elements**																			
SiO ₂	47.7	46.5	46.2	45.8	46.9	45.9	45.9	45.7	46.4	46.3	46.2	46.1	46.0	46.0	46.8	46.3	46.3	46.5	45.8
Al ₂ O ₃	14.0	12.3	11.8	13.0	13.2	14.4	14.1	13.9	14.1	14.5	14.2	14.4	15.8	15.3	14.1	14.9	13.3	13.3	13.6
FeO*	11.7	15.1	16.0	15.3	14.6	15.0	13.8	14.9	14.7	14.0	13.8	13.0	13.0	13.4	12.8	12.5	14.7	14.8	14.9
MgO	10.2	6.49	5.66	6.01	6.65	6.70	5.93	5.89	7.22	6.43	7.99	7.54	7.16	7.32	9.17	9.28	7.18	7.26	6.86
CaO	10.4	10.4	10.0	10.1	9.84	9.42	9.98	9.92	9.68	10.1	9.71	9.76	10.1	9.94	10.0	10.3	9.78	9.42	9.96
Na ₂ O	2.09	2.29	2.45	2.45	2.43	2.41	2.46	2.52	2.39	2.44	2.33	2.40	2.53	2.50	2.38	2.32	2.42	2.36	2.43
K ₂ O	0.210	0.540	0.630	0.650	0.500	0.580	0.530	0.570	0.530	0.570	0.500	0.560	0.440	0.490	0.430	0.430	0.580	0.570	0.550
TiO ₂	1.76	3.75	4.00	3.73	3.36	3.50	3.53	3.46	3.23	3.24	2.88	2.88	2.62	2.70	2.06	2.04	3.06	3.08	3.28
P ₂ O ₅	0.330	0.800	0.910	1.050	0.750	0.690	0.770	0.700	0.620	0.550	0.510	0.570	0.480	0.530	0.370	0.390	0.640	0.720	0.770
MnO	0.180	0.230	0.240	0.230	0.220	0.210	0.220	0.220	0.210	0.210	0.200	0.200	0.190	0.200	0.190	0.190	0.210	0.210	0.220
Mg#	46.6	30.0	26.1	28.2	31.3	30.1	28.4	30.5	32.9	31.5	36.8	35.3	35.5	35.4	41.8	42.6	32.9	33.0	31.5
Cr	352	128	202	136	215	194	98.3	122	254	247	352	167	307	287	741	703	300	317	287
K	174	448	523	540	415	481	440	481	473	440	473	415	465	407	357	357	481	473	457
P	144	349	397	458	327	301	275	305	271	240	223	249	209	231	161	170	279	314	396
Trace Elements***																			
Rb	7.78	9.09	9.24	4.87	9.03	4.92	5.81	10.7	10.5	12.5	9.73	6.66	9.75	8.59	7.20	11.1	7.85	9.01	6.82
Ba	559	218	735	260	662	289	424	638	605	561	480	270	605	435	312	295	526	533	533
Sr	544	196	543	183	629	187	370	653	586	642	539	231	636	519	379	434	471	489	425
Pb	4.88	2.36	6.27	3.49	5.22	2.61	3.81	6.85	5.14	4.66	3.96	3.13	4.02	4.10	3.20	3.76	5.64	5.65	5.97
Th	1.39	0.900	1.36	1.04	1.30	0.68	0.980	1.72	1.55	1.42	1.56	1.26	0.84	1.14	1.09	1.23	1.66	1.43	1.59
U	0.510	0.240	0.580	0.320	0.470	0.220	0.310	0.570	0.480	0.510	0.450	0.270	0.350	0.390	0.460	0.530	0.620	0.620	0.710
Zr	478	133	626	208	437	200	296	484	414	370	346	308	206	261	208	216	458	478	526
Hf	9.00	3.22	11.7	4.88	9.93	4.61	6.80	10.2	10.3	9.15	8.46	7.59	4.70	6.27	5.26	5.34	9.49	9.54	10.3
Ta	1.69	0.57	1.78	0.79	1.96	0.730	1.14	1.94	1.67	1.62	1.58	1.35	0.640	1.38	1.35	0.970	1.18	1.76	1.69
Y	55.0	16.1	61.3	22.4	58.6	22.7	30.7	61.1	55.3	51.3	50.0	41.5	20.7	40.3	38.7	28.3	35.5	45.8	46.3
Nb	31.5	8.80	31.7	13.0	33.4	11.3	18.0	31.9	27.9	26.6	25.2	22.2	10.7	21.2	23.0	16.7	19.3	30.0	24.6
Sc	43.2	17.3	43.7	21.6	45.2	25.0	31.4	44.8	44.5	42.5	40.2	20.8	43.7	37.5	35.4	45.7	34.3	36.3	32.1
Trace Elements***																			
Ni	134	46.8	57.1	50.1	91.6	60.3	75.1	105	132	98.4	177	56.8	122	119	178	161	100	108	88.5
V	543	190	720	254	461	270	360	607	481	455	535	227	560	478	413	399	507	508	580
La	43.0	11.8	46.0	17.6	41.1	15.2	23.0	38.5	35.2	30.5	24.6	18.0	26.4	18.3	22.3	22.3	37.1	38.5	37.5
Ce	95.9	26.0	108	38.8	93.9	35.3	52.9	88.1	81.7	71.3	65.1	58.0	40.2	60.0	42.7	49.9	84.2	87.5	87.9
Pr	12.8	3.52	14.6	5.26	12.8	5.00	7.08	12.2	11.4	9.83	9.14	7.89	5.35	8.10	5.57	6.57	11.2	11.6	11.4
Nd	55.9	16.8	64.7	25.1	56.6	24.1	36.5	55.0	45.2	41.1	36.6	25.8	35.7	36.1	25.3	29.4	49.3	51.2	51.0
Sm	12.2	3.90	14.9	5.89	12.9	5.74	8.59	12.8	12.3	10.6	9.92	8.74	5.84	8.33	6.01	6.90	11.3	11.6	11.6
Eu	4.30	1.45	5.22	2.10	4.69	2.18	2.88	4.74	4.51	4.10	3.78	3.35	2.10	3.19	2.25	2.50	4.11	4.2	4.19
Gd	14.3	4.71	17.0	6.87	15.0	6.85	10.2	15.2	14.3	12.5	11.9	10.2	6.80	9.84	7.22	8.42	12.8	13.5	13.5
Tb	2.04	0.620	2.40	0.92	2.15	0.91	1.27	2.07	1.81	1.72	1.51	0.86	1.42	1.43	1.07	1.26	1.85	1.9	1.87
Dy	11.7	4.28	14.0	6.17	12.4	6.11	8.57	12.4	11.0	10.3	8.76	5.80	8.36	8.43	6.44	7.43	10.4	10.8	10.9
Ho	2.28	0.770	2.80	1.12	2.53	1.11	1.44	2.47	2.38	2.21	1.76	1.03	1.63	1.67	1.28	1.53	2.04	2.12	2.16
Er	6.33	2.40	7.66	3.44	6.86	3.43	4.69	6.61	6.04	5.94	4.95	3.13	4.54	4.60	3.64	4.24	5.61	5.87	6.01
Tm	0.860	0.290	1.00	0.410	0.930	0.400	0.520	0.900	0.810	0.800	0.670	0.370	0.620	0.620	0.490	0.550	0.750	0.780	0.790
Yb	5.45	2.09	6.33	3.03	5.85	2.98	3.93	5.82	5.62	5.12	5.06	4.24	2.67	4.01	4.00	3.13	3.74	4.74	5.02
Lu	0.800	0.260	0.920	0.380	0.850	0.380	0.480	0.810	0.750	0.740	0.620	0.340	0.580	0.570	0.460	0.550	0.690	0.730	0.710

Note: Major oxides are in weight percent, trace elements and rare earth elements are in parts per million. Flow groups as in text.

**Measured by X-ray fluorescence

***Normalized to 100 wt% on a volatile free basis.

****Measured by inductively coupled plasma-mass spectrometer

TABLE 4: KIMAMA CORE BULK-ROCK ELEMENTAL ANALYSES

Flow Group Sample	Flow Group 20 (Fe-Ti)		Flow Group 21		Flow Group 22		Flow Group 23		Flow Group 24		Flow Group 25		Flow Group 26		Flow Group 27				
	52	53	54	55	56	57	58	59	60	61	62	63	64	65	66	67			
Inclin.	22°	22°	-27°	56°	56°	-52°	-54°	-54°	-54°	-54°	-54°	-54°	-54°	-54°	-54°	-54°			
Sample	KAlB1519	KAlB1530b	KAlB1538	KAlB1563	KAlB1593	KAlB1617	KAlB1643	KAlB1662	KAlB1685	KAlB1708	KAlB1767	KAlB1796	KAlB1815	KAlB1827	KAlB1834	KAlB1845	KAlB1869	KAlB1873	KAlB1923
Major Elements**																			
SiO ₂	45.2	45.4	45.4	45.0	45.4	47.0	45.8	46.2	45.5	46.6	43.2	44.4	45.6	45.4	45.4	45.0	45.5	48.0	45.5
Al ₂ O ₃	12.9	14.1	13.7	13.9	13.4	13.7	14.6	14.7	13.8	13.2	12.3	11.5	13.2	14.7	15.0	14.6	14.2	13.0	14.5
FeO*	15.8	14.8	15.0	14.8	15.9	14.6	14.3	13.8	14.9	14.7	17.6	17.6	14.3	13.8	14.4	14.6	14.6	14.1	14.6
MgO	6.39	7.31	7.18	7.10	6.48	7.10	7.56	7.36	6.99	7.00	5.73	5.53	7.30	7.71	6.96	5.50	7.12	6.07	6.77
CaO	10.1	9.82	9.83	9.75	9.70	9.36	9.85	9.73	9.93	9.59	9.09	8.84	9.87	9.90	9.99	10.3	9.90	9.69	10.0
Na ₂ O	2.42	2.38	2.42	2.36	2.56	2.42	2.41	2.46	2.37	2.36	2.70	2.69	2.47	2.41	2.44	2.38	2.44	2.47	2.45
K ₂ O	0.550	0.540	0.520	0.520	0.600	0.470	0.430	0.630	0.570	0.54	0.900	0.900	0.440	0.380	0.460	0.600	0.470	0.390	0.440
TiO ₂	4.04	3.09	3.26	3.07	3.54	2.94	2.75	2.67	3.18	3.28	4.65	4.62	2.85	2.67	2.97	4.25	3.05	3.60	3.25
P ₂ O ₅	0.760	0.720	0.740	0.690	0.840	0.450	0.410	0.520	0.960	0.670	1.650	1.430	0.610	0.710	0.690	1.010	0.750	0.620	0.640
MnO	0.230	0.220	0.220	0.210	0.230	0.210	0.200	0.200	0.220	0.210	0.280	0.270	0.210	0.200	0.210	0.250	0.210	0.190	0.210
Mg#	28.8	33.1	32.4	33.9	29.0	32.7	34.7	31.9	32.3	32.3	24.6	23.9	33.8	35.8	32.6	25.1	32.7	30.0	31.7
Cr	221	360	294	339	149	188	137	127	239	291	55.1	58.9	317	324	213	122	107	138	66.6
K	457	448	432	432	498	390	357	523	473	448	747	747	365	315	382	498	390	324	365
P	332	314	323	301	367	196	179	227	419	292	720	624	310	266	301	441	327	271	279
Trace Elements***																			
Rb	12.4	1.63	10.0	12.6	7.10	7.99	4.92	6.08	13.9	9.17	15.7	17.2	6.19	6.82	4.60	3.80	6.68	4.88	6.22
Ba	655	164	554	561	484	442	201	294	637	546	875	957	466	462	372	182	296	310	314
Sr	585	133	502	583	340	517	138	260	628	554	459	533	515	607	330	158	176	250	258
Pb	6.33	2.37	5.62	5.00	4.81	5.03	2.04	2.89	6.73	5.57	10.0	10.2	5.61	3.88	3.16	2.11	3.59	3.13	3.09
Th	2.07	0.69	1.77	1.81	1.33	1.22	0.58	0.70	2.22	1.34	3.06	3.08	1.00	0.970	0.690	0.480	1.04	0.670	0.840
U	0.740	0.200	0.650	0.580	0.450	0.460	0.180	0.250	0.740	0.490	1.140	1.140	0.430	0.340	0.250	0.170	0.330	0.240	0.280
Zr	591	137	520	464	394	328	138	233	577	443	881	920	368	291	238	152	220	228	247
Hf	11.4	3.57	10.0	9.44	8.39	7.64	3.17	5.40	10.9	9.55	18.2	17.6	8.34	6.97	5.33	3.57	5.12	5.32	5.61
Ta	2.15	0.68	1.87	1.52	1.34	1.36	0.54	0.84	2.57	1.84	2.88	3.14	1.60	1.32	0.890	0.560	0.790	0.810	0.810
Y	62.2	18.6	52.2	52.6	34.5	44.1	14.0	21.7	64.7	53.0	94.5	98.8	47.5	43.9	26.8	14.2	22.1	24.5	24.8
Nb	36.0	8.40	32.3	26.8	22.6	22.6	9.23	13.6	43.5	29.4	50.2	54.1	27.5	22.5	14.3	8.89	14.1	14.5	13.6
Sc	53.1	30.0	42.0	45.0	32.6	41.4	16.3	22.1	46.7	41.9	40.0	44.6	35.3	40.2	29.0	20.1	21.8	23.6	20.5
Trace Elements***																			
Ni	79.4	103	97.0	112	66.5	108	61.1	60.4	91.0	108	38.4	44.1	102	110	76.8	67.1	45.8	47.5	66.3
V	810	261	547	535	365	423	191	326	601	537	461	415	481	437	303	251	268	256	252
La	45.3	11.1	39.4	38.4	30.9	27.1	11.9	16.4	53.4	34.6	73.0	74.5	34.1	29.5	21.7	10.5	19.5	20.4	18.9
Ce	102	25.5	89.1	84.4	69.0	61.9	26.7	38.3	119	80.8	174	169	79.8	66.5	49.2	24.7	43.9	46.4	43.6
Pr	13.5	3.51	11.8	11.3	8.93	8.35	3.56	5.29	15.5	11.3	22.2	22.4	10.9	9.01	6.56	3.38	5.82	6.23	6.10
Nd	59.3	17.4	52.6	50.2	44.7	37.8	17.6	25.9	67.7	51.0	98.3	99.4	48.5	40.6	33.3	16.8	27.9	30.5	29.6
Sm	13.6	4.20	12.0	11.2	10.1	9.20	4.03	6.14	14.8	12.0	22.2	22.5	11.4	9.31	7.59	4.03	6.35	6.94	6.87
Eu	4.85	1.55	4.37	4.12	3.27	3.54	1.49	2.30	5.46	4.38	7.37	7.41	4.15	3.56	2.54	1.58	2.18	2.50	2.54
Gd	15.6	5.20	13.9	13.2	11.8	11.0	4.70	7.04	17.0	13.7	25.3	25.5	13.0	10.9	9.08	4.84	7.52	8.13	7.93
Tb	2.24	0.73	1.96	1.86	1.47	1.59	0.60	0.94	2.38	1.98	3.61	3.65	1.86	1.60	1.12	0.650	0.940	1.04	1.03
Dy	12.7	5.21	11.3	10.8	9.53	9.29	3.96	6.28	13.5	11.7	21.3	21.1	10.7	9.14	7.40	4.24	6.33	6.99	6.94
Ho	2.54	0.96	2.24	2.14	1.64	1.85	0.70	1.11	2.64	2.30	4.18	4.20	2.10	1.79	1.27	0.740	1.12	1.23	1.24
Er	7.15	3.04	6.12	5.90	5.21	5.13	2.18	3.37	7.28	6.35	11.6	11.7	5.73	4.94	3.07	2.29	3.53	3.77	3.87
Tm	0.950	0.370	0.810	0.800	0.560	0.690	0.250	0.400	0.970	0.850	1.570	1.550	0.770	0.680	0.450	0.260	0.420	0.440	0.450
Yb	6.05	2.79	5.19	5.04	4.37	4.36	1.86	2.90	6.19	5.37	10.0	9.83	4.80	4.28	3.54	1.97	2.96	3.17	3.34
Lu	0.880	0.340	0.750	0.760	0.540	0.640	0.230	0.360	0.890	0.790	1.430	1.450	0.690	0.620	0.420	0.250	0.370	0.400	0.420

Note: Major oxides are in weight percent, trace elements and rare earth elements are in parts per million. Flow groups as in text.

**Measured by X-ray fluorescence

***Normalized to 100 wt% on a volatile free basis.

****Measured by inductively coupled plasma-mass spectrometer

TABLE 4: KIMAMA CORE BULK-ROCK ELEMENTAL ANALYSES

Sample	Flow Group 28		Flow Group 29		Flow Group 30		Flow Group 31		Flow Group 32		Flow Group 33									
	-54°	66	-54°	67	-54°	70	-55°	71	32°	72°	-58°	73°								
	KAI1B1947	KAI1B2005	KAI1B2027	KAI1B2063	KAI1B2093	KAI1B2126	KAI1B2143	KAI1B2180	KAI1B2198	KAI1B2227	KAI1B2257	KAI1B2297	KAI1B2316	KAI1B2375	KAI1B2406	KAI1B2411	KAI1B2437	KAI1B2453	KAI1B2472	KAI1B2476
Major Elements**																				
SiO ₂	45.5	45.6	45.5	45.3	46.0	45.9	46.8	45.8	45.8	45.5	46.1	45.4	47.2	45.6	46.3	47.4	47.4	47.3	46.4	46.5
Al ₂ O ₃	13.6	14.0	14.1	14.5	14.4	15.0	14.5	14.6	14.6	14.7	13.8	14.4	14.1	14.0	14.3	13.5	13.4	13.4	14.2	14.2
FeO*	15.3	14.5	14.2	14.2	14.4	13.0	12.8	13.5	13.5	13.8	14.2	14.2	13.1	15.1	13.9	14.0	13.9	13.7	13.9	13.9
MgO	6.8	7.26	7.52	7.26	7.04	8.99	8.79	8.35	8.18	8.02	7.93	7.85	7.85	7.19	6.58	6.85	7.17	7.76	7.86	7.05
CaO	9.73	10.03	9.37	9.92	9.78	10.1	9.89	10.1	10.1	9.90	9.68	9.78	9.77	9.25	10.3	9.53	9.66	9.60	9.71	10.0
Na ₂ O	2.44	2.37	2.14	2.46	2.53	2.29	2.36	2.48	2.48	2.50	2.55	2.46	2.41	2.64	2.39	2.33	2.37	2.30	2.35	2.35
K ₂ O	0.500	0.420	0.530	0.420	0.460	0.380	0.380	0.420	0.420	0.430	0.470	0.450	0.620	0.650	0.710	0.770	0.720	0.680	0.660	0.690
TiO ₂	3.40	3.13	3.04	2.96	3.04	2.21	2.24	2.55	2.55	2.64	2.68	2.77	2.54	3.27	2.99	3.02	2.86	2.75	2.74	2.88
P ₂ O ₅	0.730	0.610	0.560	0.500	0.570	0.390	0.400	0.490	0.490	0.500	0.500	0.570	0.450	0.420	0.640	0.580	0.590	0.560	0.610	0.640
MnO	0.220	0.210	0.200	0.200	0.210	0.190	0.190	0.200	0.200	0.200	0.200	0.210	0.190	0.210	0.210	0.200	0.200	0.200	0.200	0.210
Mg#	30.8	33.4	34.6	33.8	32.8	41.0	40.8	38.3	38.2	37.3	36.1	35.8	37.4	32.3	32.1	32.8	34.1	36.2	36.1	33.7
Cr	176	118	233	215	273	626	553	473	406	154	380	272	350	177	306	318	350	435	472	384
K	415	349	440	349	382	315	315	349	349	357	390	374	515	540	589	639	598	565	548	573
P	319	266	244	218	249	170	175	214	214	218	218	249	196	183	279	253	257	244	266	279
Trace Elements***																				
Rb	6.18	9.44	5.16	4.79	9.30	8.07	4.83	8.63	15.8	8.86	9.83	5.60	13.7	13.5	14.2	14.6	15.3	16	18.8	18.2
Ba	298	285	303	314	491	320	334	372	424	280	403	299	441	471	547	520	540	533	588	560
Sr	246	258	197	319	549	481	514	501	453	564	291	201	497	564	467	441	480	502	565	495
Pb	2.96	2.88	3.38	3.11	4.50	3.12	3.00	4.29	4.54	3.70	4.43	2.78	5.27	4.82	5.23	7.15	6.04	5.25	5.52	5.62
Th	0.720	1.07	0.860	0.710	1.20	0.930	0.770	1.23	1.85	1.19	1.53	0.920	1.80	1.44	1.90	2.26	2.38	2.28	2.7	2.58
U	0.260	0.320	0.280	0.230	0.470	0.310	0.330	0.480	0.490	0.310	0.480	0.280	0.590	0.500	0.780	0.780	0.750	0.710	0.760	0.840
Zr	234	180	249	216	350	203	220	268	249	261	289	208	271	275	351	362	404	347	336	401
Hf	5.36	4.32	5.72	5.06	7.98	5.01	5.03	6.29	5.96	6.46	6.83	4.82	6.36	6.88	8.05	8.37	8.38	7.8	8.18	8.41
Ta	0.720	0.940	0.820	1.36	1.06	0.880	1.23	1.48	1.38	1.48	1.46	0.87	1.57	1.69	1.68	1.74	1.65	1.4	1.66	1.56
Y	22.6	19.0	27.4	23.9	44.5	35.3	29.9	38.1	48.3	26.4	44.9	25.1	38.5	41.3	36.5	44.0	46.8	45.8	48.1	47.8
Nb	12.3	12.7	14.3	12.9	22.6	16.0	15.5	20.5	21.6	18.8	22.3	13.8	27.2	27.3	28.1	28.8	28.5	25.6	27.1	27.2
Sc	21.3	20.3	32.4	31.8	39.6	45.0	34.7	38.6	51.7	24.1	42.7	31.2	40.8	37.1	32.6	38.3	39.8	43.3	43.1	43
Trace Elements****																				
Ni	68.7	66.0	79.8	72.8	92.5	118	113	93.2	94.8	69.7	87.9	72.3	99.4	97.8	99.2	104	111	134	136	111
V	253	240	313	351	522	411	465	420	441	262	522	332	406	506	416	446	507	435	543	515
La	17.7	16.3	18.4	16.0	25.6	17.9	16.7	21.7	27.4	22.6	26.5	17.8	28.1	27.5	27.8	31.9	34.5	32.7	33.5	35.0
Ce	41.4	35.6	42.7	37.4	60.1	41.6	40.0	53.0	60.0	52.0	60.4	40.3	63.0	62.5	68.7	73.4	77.8	73.9	73.9	79.0
Pr	5.75	4.70	5.87	5.05	8.32	5.76	5.47	6.89	8.29	7.03	8.13	5.33	8.25	8.43	8.33	9.72	10.2	9.55	9.84	10.4
Nd	28.4	22.1	30.5	26.2	37.8	26.4	25.4	30.9	37.0	34.6	36.8	27.3	35.9	38.1	36.6	43.2	45.5	42.5	43.1	45.6
Sm	6.53	4.99	7.28	6.42	9.20	6.61	6.19	7.45	8.95	7.71	8.64	6.47	8.29	9.13	8.52	10.1	10.4	9.77	9.76	10.5
Eu	2.38	1.85	2.44	2.23	3.50	2.50	2.36	2.78	3.23	2.77	3.14	2.13	3.04	3.37	3.05	3.51	3.70	3.49	3.49	3.65
Gd	7.61	5.93	8.84	7.85	11.0	7.96	7.46	9.15	10.8	8.90	10.2	7.82	9.65	10.4	9.80	11.5	12.0	11.4	11.6	12.1
Tb	0.980	0.780	1.10	0.99	1.59	1.17	1.11	1.35	1.60	1.13	1.52	1.01	1.40	1.53	1.39	1.66	1.72	1.65	1.69	1.76
Dy	6.64	5.40	7.40	6.63	9.77	7.06	6.68	8.27	9.48	7.64	9.21	6.85	8.29	8.99	7.81	9.58	10.1	9.62	10.2	10.2
Ho	1.16	0.950	1.29	1.14	1.98	1.44	1.34	1.71	1.93	1.33	1.84	1.20	1.63	1.79	1.55	1.89	2.01	1.94	2.07	2.04
Er	3.59	3.01	4.22	3.66	5.47	4.04	3.73	4.83	5.33	4.13	5.18	4.00	4.61	5.00	4.35	5.23	5.67	5.42	5.79	5.71
Tm	0.410	0.350	0.470	0.410	0.730	0.560	0.510	0.650	0.740	0.480	0.700	0.440	0.670	0.670	0.580	0.720	0.770	0.740	0.770	0.770
Yb	3.03	2.63	3.56	3.28	4.66	3.60	3.23	4.14	4.79	3.46	4.58	3.41	4.00	4.34	3.68	4.58	4.95	4.71	5.11	5.00
Lu	0.380	0.330	0.450	0.390	0.690	0.530	0.470	0.610	0.700	0.440	0.670	0.410	0.580	0.610	0.530	0.670	0.710	0.660	0.740	0.710

Note: Major oxides are in weight percent, trace elements and rare earth elements are in parts per million. Flow groups as in text.

**Measured by X-ray fluorescence

***Normalized to 100 wt% on a volatile free basis.

****Measured by inductively coupled plasma-mass spectrometer

TABLE 4: KIMAMA CORE BULK-ROCK ELEMENTAL ANALYSES

Flow Group	Flow Group 34				Flow Group 35				Flow Group 36				Flow Group 37				Flow Group 38				Flow Group 39			
	74	75	76	77	78	78	78	78	79	80	80	81	81	81	82	82	83	84	85	85	86			
Inclin.	-62°	-62°	-45°	-45°	-45°	-45°	-45°	-45°	-65°	-65°	-65°	-40°	-40°	-40°	-40°	-40°	-40°	-40°	-40°	-40°	-55°	-55°		
Sample	KA1B2485	KA1B2522	KA1B2541	KA1B2570	KA1B2612	KA1B2646	KA1B2656	KA1B2685	KA1B2727	KA1B2740	KA1B2770	KA1B2779	KA1B2794	KA1B2815	KA1B2841	KA1B2890	KA1B2911	KA1B2915	KA1B2915	KA1B2933				
Major Elements**																								
SiO ₂	46.5	46.5	50.4	46.3	46.6	46.8	46.7	47.9	47.2	46.8	44.6	45.5	46.8	46.7	45.9	46.2	47.7	47.7	47.7	46.6	46.8			
Al ₂ O ₃	14.3	15.5	13.2	13.9	15.2	15.6	15.4	14.7	15.0	13.3	13.3	13.5	13.9	14.3	14.4	14.1	13.8	13.4	13.4	14.4	13.9			
FeO*	14.0	12.6	11.0	14.2	12.9	12.5	12.5	12.5	12.7	14.5	15.8	15.4	14.1	13.8	13.5	14.4	13.8	14.0	14.1	14.1	14.3			
MgO	7.15	7.71	7.06	6.9	6.99	7.65	7.68	7.42	7.85	7.02	7.25	6.60	6.80	7.14	6.98	6.88	6.89	6.72	6.89	6.59	6.59			
CaO	9.78	10.6	11.1	10.1	11.0	10.2	10.5	10.0	9.81	9.48	9.94	9.83	9.59	9.67	10.4	9.75	9.30	9.44	9.54	9.54	9.54			
Na ₂ O	2.65	2.44	2.21	2.61	2.39	2.39	2.38	2.37	2.42	2.39	2.53	2.39	2.48	2.45	2.41	2.43	2.41	2.45	2.45	2.48	2.48			
K ₂ O	0.520	0.490	0.530	0.550	0.490	0.540	0.490	0.560	0.530	0.560	0.570	0.550	0.670	0.620	0.610	0.580	0.700	0.730	0.640	0.670	0.670			
TiO ₂	2.78	2.16	2.74	3.01	2.36	2.16	2.32	2.29	2.21	3.21	3.31	3.52	3.11	2.91	2.73	3.05	2.89	3.09	2.91	3.12	3.12			
P ₂ O ₅	0.500	0.420	0.270	0.530	0.480	0.440	0.400	0.430	0.470	0.730	0.740	0.770	0.710	0.640	0.620	0.760	0.540	0.560	0.590	0.640	0.640			
MnO	0.200	0.190	0.160	0.210	0.190	0.190	0.180	0.180	0.190	0.210	0.230	0.230	0.210	0.200	0.200	0.210	0.200	0.200	0.200	0.200	0.210			
Trace Elements***																								
Mg#	33.9	38.0	39.1	32.7	35.1	38.0	38.0	37.2	38.2	32.6	31.5	30.0	32.5	34.1	34.1	32.6	33.3	32.5	32.5	32.9	31.5			
Cr	109	192	304	310	279	295	139	218	252	124	164	164	249	287	284	256	271	202	262	183	183			
K	432	407	404	457	407	448	407	465	440	465	473	457	556	515	506	481	581	606	531	556	556			
P	218	183	118	231	209	192	175	188	205	319	323	336	310	279	271	332	236	244	257	279	279			
Rb	6.01	12.1	11.8	10.8	15.7	11.8	8.46	8.12	9.71	13.0	14.9	6.50	15.4	8.85	13.2	12.2	15.3	9.80	13.9	8.64	8.64			
Ba	231	481	507	399	499	418	278	331	354	609	350	202	567	514	585	635	584	405	548	398	398			
Sr	210	530	551	507	544	512	305	268	481	624	239	182	533	486	621	660	596	336	554	325	325			
Pb	3.18	5.91	4.93	4.29	4.68	4.79	3.36	3.58	4.12	5.28	3.92	2.34	4.80	5.12	5.00	5.65	6.32	4.46	5.56	4.65	4.65			
Th	0.72	1.59	1.92	1.69	2.00	1.91	1.02	1.33	1.57	1.71	1.43	0.860	1.79	1.38	1.65	1.67	2.19	1.47	1.97	1.48	1.48			
U	0.210	0.520	0.610	0.560	0.590	0.600	0.300	0.390	0.540	0.490	0.490	0.550	0.550	0.550	0.550	0.510	0.410	0.410	0.630	0.410	0.410			
Zr	183	361	324	280	286	273	176	215	273	429	241	146	328	334	328	415	360	271	329	265	265			
Hf	4.36	8.75	7.68	6.44	6.82	6.53	4.49	4.92	6.30	9.76	5.61	3.55	7.74	7.74	7.86	9.84	8.72	6.20	8.13	6.38	6.38			
Ta	0.72	1.69	1.38	1.14	1.37	1.17	0.76	0.800	1.08	1.75	0.840	0.560	1.59	1.20	2.02	2.02	1.61	1.09	1.46	1.19	1.19			
Y	21.8	58.3	46.5	38.8	45.1	38.9	21.2	23.2	38.8	58.3	24.3	14.7	45.4	37.2	44.1	55.4	48.9	28.3	43.6	28.6	28.6			
Nb	11.6	27.8	22.8	19.9	21.6	19.6	11.4	13.2	18.9	29.3	13.6	9.00	26.5	23.6	24.4	32.6	27.0	18.2	25.8	18.1	18.1			
Sc	23.3	50.6	46.7	42.6	46.9	37.5	23.1	29.4	39.6	44.1	22.9	22.2	39.6	30.6	37.8	42.5	39.2	32.0	35.5	30.8	30.8			
Trace Elements***																								
Ni	55.5	91.8	103	112	100	116	63.0	85.2	105	119	64.4	59.6	87.8	110	113	121	96.3	67.1	86.9	64.3	64.3			
V	267	689	549	497	524	471	303	297	400	443	264	246	493	422	418	430	494	363	548	343	343			
La	14.6	32.2	29.8	24.2	27.2	25.1	15.3	17.7	23.5	39.7	19.5	11.3	33.4	28.8	32.5	38.4	35.8	23.7	32.3	23.4	23.4			
Ce	33.2	73.3	66.9	54.6	60.8	56.7	34.7	39.2	53.0	91.4	44.9	25.5	74.2	69.0	73.9	87.3	80.9	53.8	72.7	52.1	52.1			
Pr	4.50	10.1	8.91	7.38	8.16	7.62	4.75	5.06	7.13	12.7	6.17	3.36	9.92	8.94	9.93	12.0	10.8	6.86	9.68	6.85	6.85			
Nd	21.4	45.7	39.5	32.9	35.8	33.3	23.9	25.2	31.7	57.3	30.4	16.3	43.9	39.6	43.8	53.9	47.5	34.3	42.9	34.3	34.3			
Sm	5.27	10.8	9.34	7.71	8.62	7.75	5.66	6.00	7.67	13.3	6.89	3.79	9.90	9.06	9.80	12.1	10.8	7.87	9.70	7.91	7.91			
Eu	1.87	3.80	3.39	2.82	3.11	2.78	2.11	1.93	2.71	4.97	2.52	1.42	3.64	3.35	3.63	4.55	3.76	2.50	3.44	2.49	2.49			
Gd	6.30	13.0	11.3	9.10	10.1	9.2	6.70	7.20	9.00	15.4	8.10	4.60	11.4	10.6	11.5	14.3	12.5	9.30	11.3	9.20	9.20			
Tb	0.87	1.95	1.62	1.35	1.49	1.38	0.88	0.92	1.33	2.21	1.05	0.61	1.65	1.51	1.63	2.03	1.80	1.17	1.65	1.16	1.16			
Dy	5.97	11.5	9.67	8.18	8.86	8.09	6.11	6.18	8.12	12.3	7.11	4.18	9.40	8.75	9.55	11.7	10.4	7.75	9.50	7.90	7.90			
Ho	1.08	2.34	1.95	1.64	1.80	1.61	1.08	1.09	1.62	2.38	1.25	0.70	1.84	1.73	1.91	2.36	2.09	1.32	1.87	1.36	1.36			
Er	3.42	6.62	5.37	4.62	5.06	4.51	3.33	3.58	4.61	6.62	3.89	2.43	5.19	4.77	5.27	6.44	5.83	4.19	5.22	4.36	4.36			
Tm	0.410	0.910	0.740	0.630	0.690	0.620	0.380	0.410	0.640	0.870	0.460	0.280	0.710	0.630	0.700	0.850	0.780	0.470	0.730	0.490	0.490			
Yb	3.08	5.95	4.80	3.94	4.55	4.10	2.79	3.16	4.03	5.50	3.32	2.10	4.44	3.90	4.45	5.53	5.07	3.68	4.55	3.78	3.78			
Lu	0.380	0.860	0.700	0.580	0.660	0.580	0.350	0.390	0.590	0.810	0.410	0.260	0.660	0.570	0.650	0.800	0.740	0.440	0.650	0.470	0.470			

Note: Major oxides are in weight percent, trace elements and rare earth elements are in parts per million. Flow groups as in text.
 **Measured by X-ray fluorescence
 ***Normalized to 100 wt% on a volatile free basis.
 ****Measured by inductively coupled plasma-mass spectrometer

TABLE 4: KIMAMA CORE BULK-ROCK ELEMENTAL ANALYSES

Flow Group	Flow Group 62				Flow Group 63				Flow Group 64				Flow Group 65				Flow Group 66				Flow Group 67				Flow Group 68				Flow Group 70										
	-43°		-58°		127		128		129		130		132		133		134		62°		43°		135		136		139		-45°		64°								
Sample	KAI184527	KAI184547	KAI184562	KAI184601	KAI184637	KAI184757	KAI184778	KAI184803	KAI184815	KAI184875	KAI184905	KAI184936	KAI184970	KAI184999	KAI185025	KAI185292	KAI185444	KAI185583																					
Major Elements**																																							
SiO ₂	48.9	47.0	46.0	46.6	46.4	45.4	44.8	46.7	46.8	46.2	46.9	46.4	46.1	46.2	46.5	47.1	46.7	45.5	45.1																				
Al ₂ O ₃	15.5	15.8	14.6	13.4	14.3	14.3	12.9	12.6	11.1	10.9	11.9	12.1	12.8	14.7	14.8	14.6	14.6	15.0	14.7																				
FeO*	9.9	10.3	12.3	14.1	13.5	12.9	12.6	11.1	10.9	11.9	12.1	12.8	14.7	14.8	14.6	14.6	14.6	15.0	14.7																				
MgO*	9.41	9.72	8.78	7.69	7.37	7.12	7.18	7.40	6.82	7.89	7.23	6.76	8.96	9.67	7.50	9.81	8.66	8.51	7.36																				
CaO	11.5	11.3	10.3	9.79	10.2	9.59	9.45	10.4	11.0	10.4	9.98	9.92	10.9	10.0	10.2	10.7	10.7	8.97	10.3																				
Na ₂ O	1.75	1.99	2.08	2.33	2.37	2.18	2.11	2.11	2.20	2.12	2.44	2.18	2.03	2.17	2.18	2.15	1.94	2.00	2.33																				
K ₂ O	0.150	0.120	0.160	0.460	0.390	0.220	0.160	0.160	0.190	0.340	0.510	0.190	0.180	0.320	0.230	0.380	0.190	0.160	0.240																				
TiO ₂	1.22	1.23	2.05	2.91	2.78	2.45	2.28	1.85	1.99	1.69	2.32	2.62	1.63	1.80	2.19	1.75	1.64	1.68	2.62																				
P ₂ O ₅	0.190	0.170	0.370	0.740	0.480	0.410	0.400	0.420	0.440	0.370	0.570	0.410	0.260	0.380	0.400	0.320	0.260	0.290	0.510																				
MnO	0.260	0.180	0.180	0.210	0.190	0.190	0.200	0.180	0.150	0.170	0.180	0.180	0.210	0.190	0.180	0.170	0.160	0.140	0.210																				
Trace Elements***																																							
Rb	4.93	0.87	3.81	8.91	7.66	2.96	3.62	4.68	2.35	31	11	4.83	5.14	8.77	3.59	11	3.24	4.48																					
Ba	87	118	280	622	484	426	212	192	295	288	473	319	202	336	329	262	273	108																					
Sr	151	168	350	646	485	479	472	384	433	333	467	577	311	248	420	384	351	128																					
Pb	1.82	1.95	4.26	5.49	5.49	4.38	4.24	5.14	8.27	4.24	6.23	5.55	2.97	3.94	5.16	5.05	3.82	2.58																					
Th	0.67	0.62	1.73	1.36	1.66	2.03	1.98	2.29	2.45	1.82	2.64	2.62	1.14	1.55	2.23	1.35	1.78	0.86																					
U	0.220	0.240	0.460	0.480	0.530	0.620	0.620	0.660	0.710	0.460	0.820	0.630	0.340	0.460	0.630	0.480	0.470	0.280																					
Zr	109	122	279	487	404	263	255	271	307	248	428	307	179	241	243	189	162	106																					
Hf	2.91	3.16	6.69	10.2	8.38	6.66	6.26	6.62	7.32	6.09	8.83	7.78	4.4	5.8	5.99	4.75	4.35	2.76																					
Ta	0.5	0.55	1.17	2.12	1.42	1.05	1.19	1.21	1.54	1.16	1.63	1.44	0.93	1.26	1.25	0.98	0.92	0.47																					
Y	26.2	26.1	46.3	61.6	53.4	40.8	38.1	42.1	47.5	41	52	48.6	35.9	39.4	40.6	35.1	34.9	20.9																					
Nb	8.28	9.21	19.9	35.3	23.8	19.1	20.3	21.5	25.2	19.8	28.9	22.8	15	20.3	21.4	16.2	14.1	7.59																					
Sc	46.8	48.3	48.6	45.1	45.8	39.1	33.9	44.1	47.9	45.9	40	42	49.8	43.8	42.3	40.2	48.7	27.6																					
Trace Elements***																																							
Ni	113	112	169	114	163	118	130	155	114	152	130	146	193	174	146	253	162	103																					
V	328	358	454	587	491	367	341	345	386	347	422	440	438	348	377	366	358	234																					
La	10.1	10.1	25.5	43.2	30.8	26.9	24.3	30.4	27.3	26.5	40.3	28.9	18.1	24.7	27.4	20.2	18.7	13.6																					
Ce	22.8	24.7	57.9	98.6	70.8	61.3	55.4	65.8	73.6	58.7	87.2	65.3	41.4	54.6	61.1	46.3	41.9	27.7																					
Pr	3.2	3.32	7.78	13.5	9.82	8.08	7.30	8.55	9.59	7.67	11.2	8.88	5.6	7.26	7.98	6.25	5.54	3.63																					
Nd	14.5	15.2	34.5	60.0	44.4	36.4	32.2	36.7	41.0	33.3	48.5	39.5	25.2	32.1	35.2	27.8	24.5	17.7																					
Sm	3.82	3.97	8.43	13.6	10.6	8.58	7.50	8.24	9.14	7.49	10.6	9.37	6.14	7.47	8.12	6.79	5.99	4.29																					
Eu	1.39	1.48	2.88	5.00	3.79	3.05	2.74	2.70	3.03	2.55	3.54	3.28	2.17	2.58	2.83	2.38	2.08	1.51																					
Gd	4.90	5.30	10.3	15.8	12.4	9.90	9.10	9.94	11.0	9.00	12.5	11.2	7.72	8.96	9.77	8.03	7.29	5.66																					
Tb	0.800	0.85	1.54	2.26	1.85	1.46	1.34	1.46	1.62	1.35	1.80	1.65	1.19	1.35	1.46	1.22	1.13	0.77																					
Dy	5.22	5.44	9.39	12.9	10.8	8.71	7.89	8.59	9.52	8.12	10.8	10.1	7.33	8.1	8.56	7.46	6.85	5.40																					
Ho	1.10	1.14	1.91	2.52	1.92	1.42	1.62	1.71	1.95	1.65	2.15	2.04	1.50	1.70	1.72	1.53	1.42	0.99																					
Er	3.27	3.37	5.41	6.98	6.09	4.86	4.57	4.89	5.56	4.82	6.03	5.71	4.22	4.81	4.86	4.23	4.05	3.08																					
Tm	0.470	0.490	0.760	0.930	0.830	0.660	0.620	0.670	0.760	0.670	0.810	0.760	0.590	0.660	0.660	0.590	0.570	0.360																					
Yb	3.15	3.20	4.90	5.98	5.36	4.24	3.91	4.27	4.86	4.29	5.20	4.92	3.81	4.24	3.78	3.66	2.60	1.61																					
Lu	0.470	0.470	0.710	0.880	0.770	0.630	0.590	0.640	0.720	0.630	0.770	0.710	0.560	0.620	0.620	0.560	0.440	0.320																					

Note: Major oxides are in weight percent, trace elements and rare earth elements are in parts per million. Flow groups as in text.

**Measured by X-ray fluorescence

***Normalized to 100 wt% on a volatile free basis.

****Measured by inductively coupled plasma-mass spectrometer

**TABLE 4: KIMAMA CORE BULK-ROCK
ELEMENTAL ANALYSES**

Sample	Flow Group 70			Flow Group 71		
	64*	144	145	146	146	148
Major Elements**	KAlSi799	KAlSi511	KAlSi525	KAlSi590		
SiO ₂	47.1	46.9	47.6	45.9		
Al ₂ O ₃	14.6	15.3	14.6	14.9		
FeO*	11.9	12.5	13.1	12.3		
MgO	5.81	8.09	6.92	7.85		
CaO	14.0	10.8	10.54	10.9		
Na ₂ O	2.14	2.17	2.29	2.22		
K ₂ O	0.380	0.160	0.220	0.270		
TiO ₂	2.07	2.20	2.56	2.42		
P ₂ O ₅	0.310	0.350	0.430	0.500		
MnO	0.160	0.180	0.190	0.200		
Mg#	32.9	36.3	34.7	38.1		
Cr	401	394	245	308		
K	315	133	183	224		
P	135	153	188	218		
Trace Elements***						
Rb	16.5	6.42	2.15	2.53		
Ba	239	150	325	332		
Sr	414	326	496	424		
Pb	3.78	3.60	4.43	4.14		
Th	1.99	1.99	1.43	1.70		
U	0.790	0.450	0.480	0.530		
Zr	206	207	289	252		
Hf	5.12	5.19	6.43	6.25		
Ta	1.06	1.07	1.76	1.65		
Y	36.6	36.7	57.1	47.0		
Nb	16.4	16.6	29.2	27.0		
Sc	41.5	43.8	66.2	47.4		
Trace Elements***						
Ni	166	159	135	121		
V	320	338	697	460		
La	19.7	19.9	30.7	31.3		
Ce	45.0	46.2	71.3	71.1		
Pr	6.30	6.34	9.82	9.49		
Nd	28.1	28.9	44.1	41.9		
Sm	6.90	7.04	10.8	9.57		
Eu	2.50	2.52	3.78	3.25		
Gd	8.35	8.50	12.9	11.3		
Tb	1.24	1.29	1.95	1.66		
Dy	7.60	7.65	11.7	9.89		
Ho	1.54	1.53	2.34	1.98		
Er	4.31	4.35	6.78	5.50		
Tm	0.600	0.590	0.940	0.760		
Yb	3.86	3.85	6.07	4.83		
Lu	0.570	0.560	0.880	0.700		

Note: Major oxides are in weight percent, trace elements and rare earth elements are in parts per million. Flow groups as in text.
 **Measured by X-ray fluorescence
 ***Normalized to 100 wt% on a volatile free basis.
 ****Measured by inductively coupled plasma mass spectrometer

Trace Elements

Kimama basalts are LREE enriched compared to basalts of the eastern SRP. The HREE compositions of Kimama basalts plot in a narrower range of values compared to other SRP basalts, but compositions are generally similar (Hughes et al., 2002a). Although the basalts in the Kimama core are less enriched in LREE than COM (exceptions being the two highly evolved flow groups), their REE patterns are similar. Kimama basalts have a steeper LREE and HREE pattern than other SRP basalts (Figure 15). Similar incompatible element trends exist between SRP and Kimama basalts, i.e. Ba, Ta, Nd, Hf, Tm, and Lu, but subtle depletions in Sr, and Y are evident in Kimama samples.

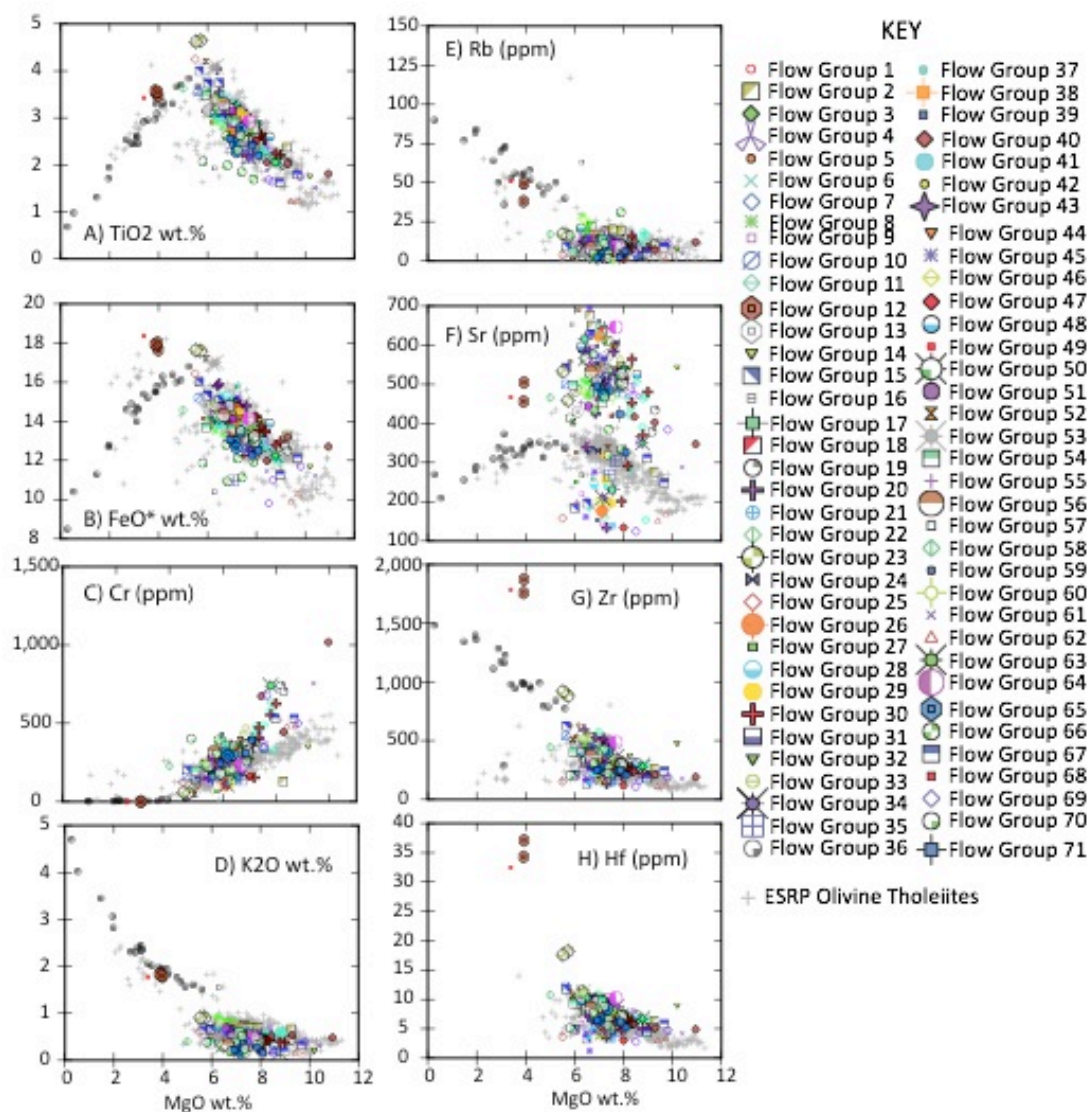
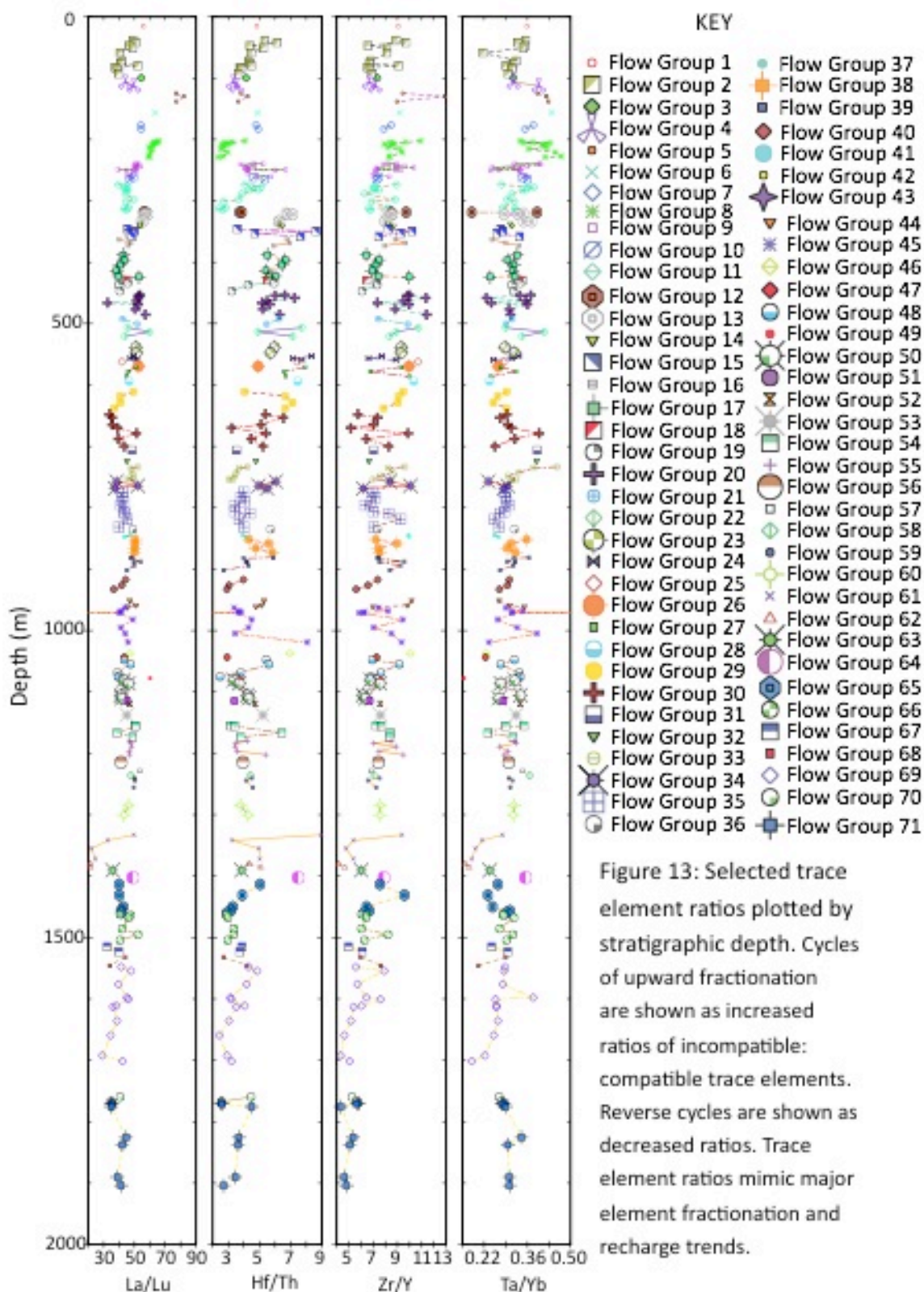


Figure 12: Selected major and trace element variation diagrams with compositions of Kimama basalts compared to compositions of eastern Snake River Plain (ESRP) olivine tholeiites (Hughes et al., 2002). Kimama flow groups are distinguished by colored symbols, ESRP samples are distinguished by gray crosses.



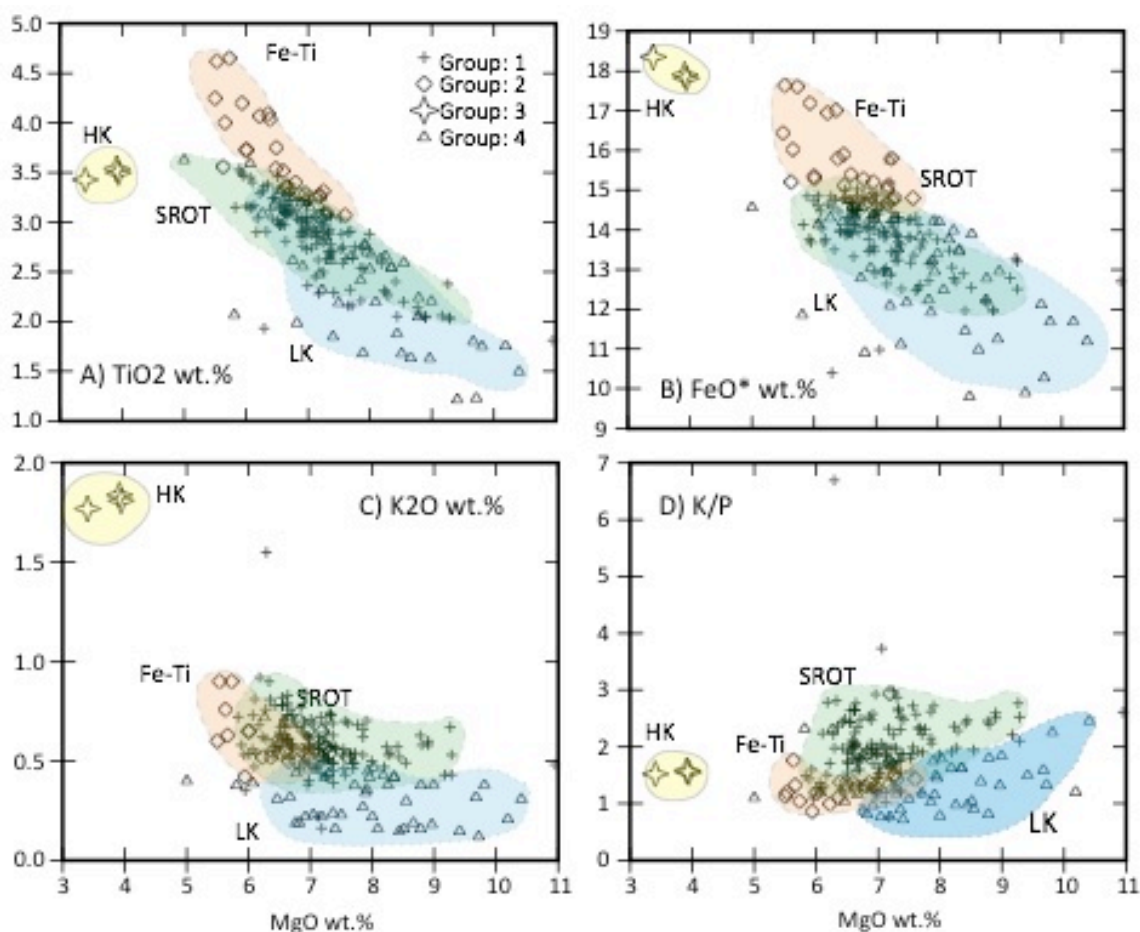


Figure 14: Selected major and trace element variation diagrams showing chemical trends evident in the four Kimama compositional suites. The Fe-Ti flows are represented by the diamond shape and are shaded in orange. The SROT flows are represented by the cross shape and are shaded in green. HK flows are represented by the star shape and are shaded in yellow. LK flows are represented by the triangle shape and are shaded blue.

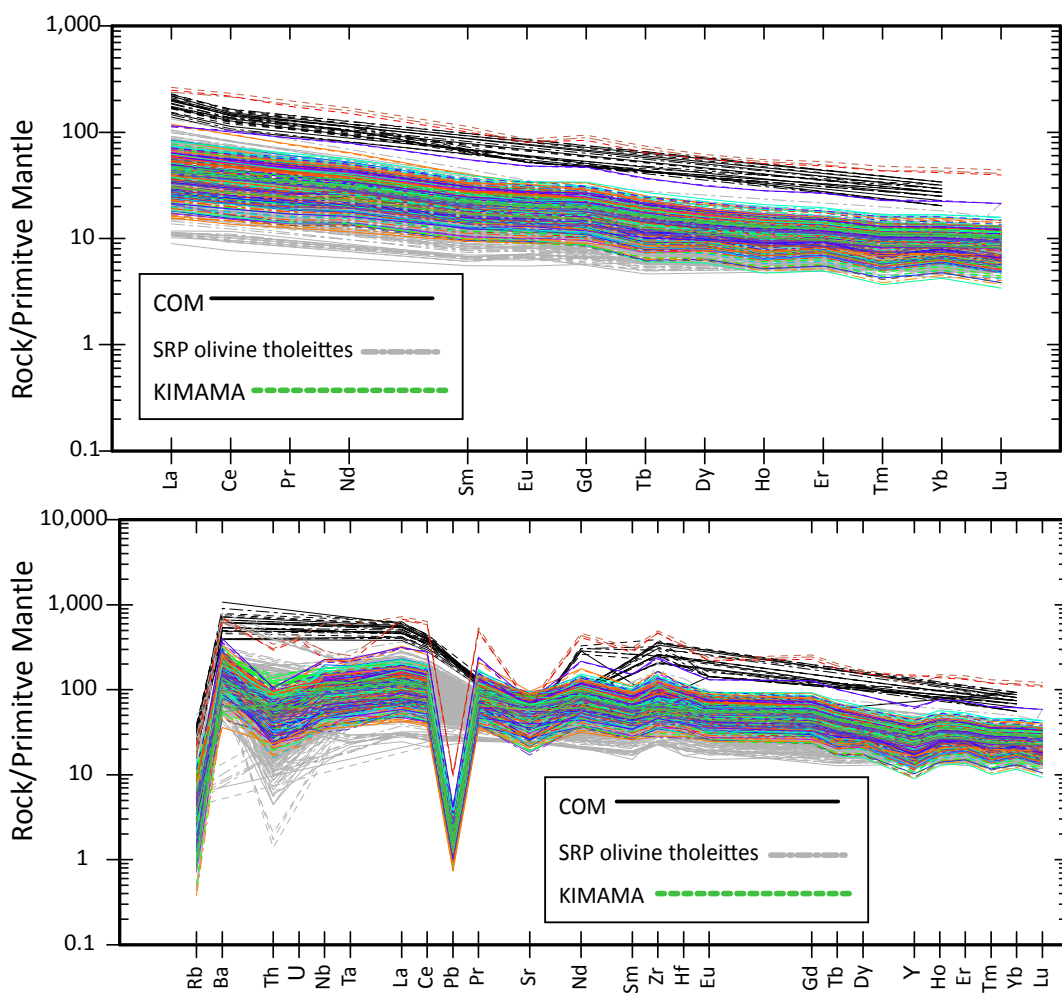


Figure 15: A) Multi-element spider diagram and B) rare earth-element (REE) plot of Kimama basalt samples (colored lines), normalized to primitive mantle (McDonough and Sun, 1995). Snake River Plain (SRP) olivine tholeiites and Craters of the Moon (COM) evolved lavas are plotted for comparison. Trace elements are arranged in order of decreasing compatibility from right to left.

Discussion

Chemical Suites and Stratigraphic trends

Lava flows in Kimama core are classified as basalts, and plots of major and trace elements plotted against depth identify four basalt compositional types (Figure 16). Thirty-five

flow groups are standard SROT basalts. Two flow groups consist of high-K, high-Fe (high K) lavas that are essentially identical to those erupted within COM during the latest Pleistocene and Holocene. We identified 22 low-K lava flow groups, which represent the least evolved flow groups in the Kimama core. Eleven high-Fe, high-Ti (Fe-Ti) flow groups are also identified in the Kimama basalt stratigraphy. Fe-Ti, low-K, and high-K flow groups are thought to represent distinct magma batches separate from SROT magmas. Whether Fe-Ti, low-K, high-K, and SROT are compositionally related will be discussed herein.

Despite the overall chemical similarity in SRP Neogene basalts, individual flow groups in the Kimama core exhibit several temporal-compositional trends. The 71 flow groups identified in the Kimama core are classified into four compositional types based upon whole rock TiO_2 wt%, K_2O wt%, FeO^* wt%, and ratios of K/P (Figure 14). Oxides such as CaO, Al_2O_3 , and Na_2O vary without discernable trend, perhaps owing to the crystallization and flotation of plagioclase within the magma. A total of 39 flows and 18 flow groups are classified as SROT, based upon compositional ranges of 5.00 to 11.0 wt% MgO, 11.0 to 15.8 wt% FeO^* , 0.210 to 0.920 wt% K_2O , and 1.76 to 3.63 wt% TiO_2 . SROT flows are found through the entire Kimama core, with the highest concentration in the 16 m to 1236 m depth range. Six Fe-Ti flow groups and 18 flows are recognized in the Kimama core based upon elevated concentrations of FeO^* , 13.8 to 17.6 wt. %, and TiO_2 , 2.67 to 4.65 wt. %. Fe-Ti flows are preferentially located in the upper 754 m of the core in flow groups 3, 10, 13, 15, 16, and 25. Six low-K flow groups and 31 flows are distinguished by low K_2O , ≤ 0.3 wt. %, low FeO^* : 9.80 to 14.8 wt. %, and higher MgO: 5.81 to 10.4 wt. %. Low-K flow groups are concentrated from 4500 m to 1912 m depth and comprise flow groups 27, 28, 29, and 30. The two flow groups and flows of the high-K suite are the most chemically distinct flows in the Kimama core, with FeO^* of ≥ 17.8 wt. %, K_2O of 1.77 to 1.84 wt. %, TiO_2 of 3.43 to 3.54 wt. %, and MgO of 3.40 to 3.94 wt. % (Figure 14). High-K flow groups 8

and 23 are located at 318 m and 1077 m depths, respectively. The REE patterns of SROT, Fe-Ti, and low-K suites are broadly similar, but high-K flow groups are 10x more enriched in both LREE and HREE compositions, and fall within the COM compositional array (Figure 14).

Fractionation/Enrichment and Recharge Cycles

The progressive enrichment of incompatible elements between flow units upsection stratigraphically is commonly interpreted to represent ongoing eruptions from a fractionating magma chamber (e.g., Shervais et al., 2006). Likewise, progressive depletion in incompatible elements, and concomitant enrichment of compatible elements upsection, is interpreted to represent magma chamber recharge with primitive or parental melt compositions (Shervais et al., 2006). These trends are best illustrated by plots of element concentrations MgO, FeO*, TiO₂, and K₂O vs. depth (Figure 16). Upward fractionation cycles are indicated by a decrease in MgO and increases in FeO*, TiO₂, K₂O. Recharge cycles are indicated by increasing MgO, and decreases in FeO*, TiO₂, K₂O (Figure 16).

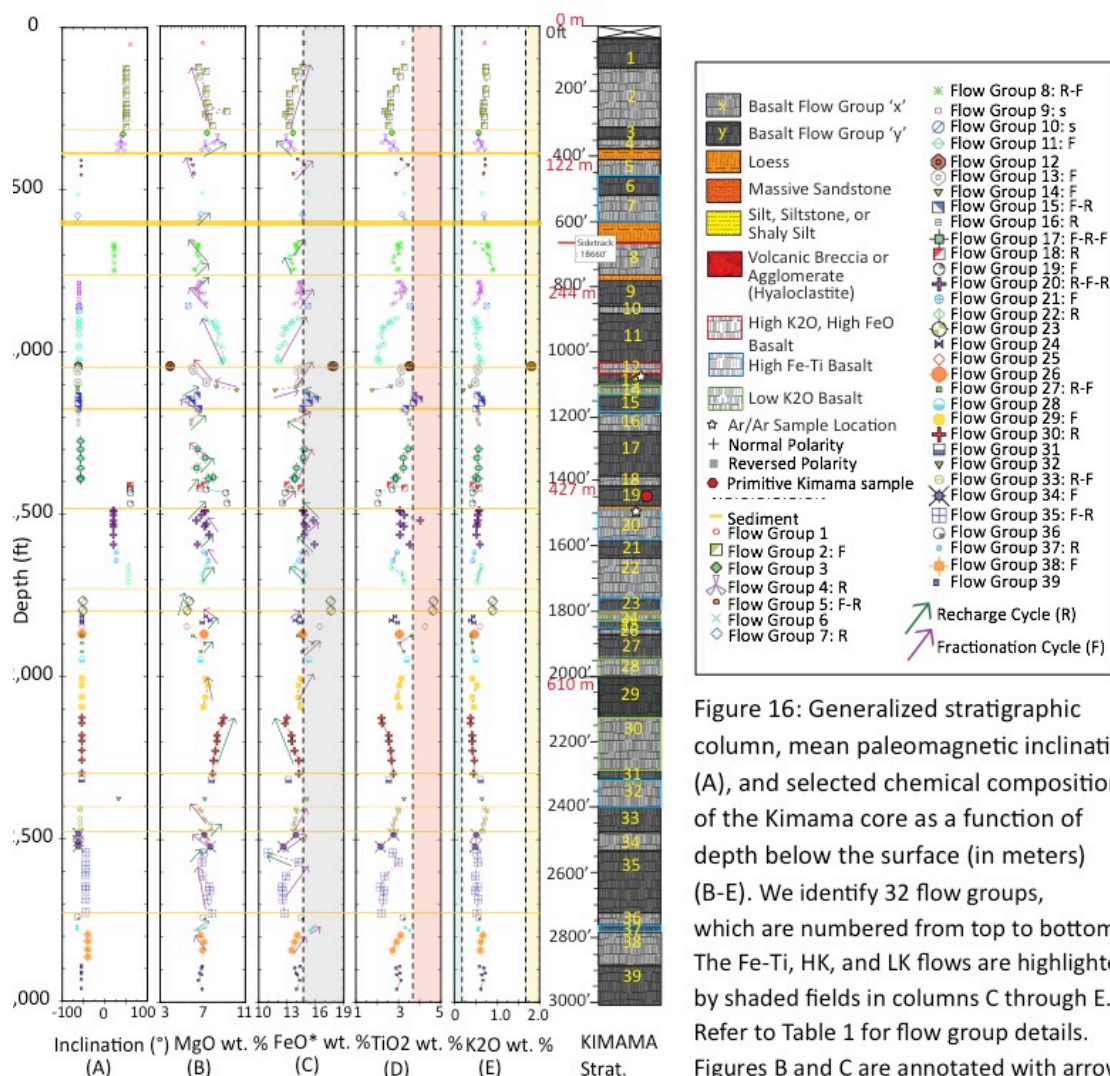
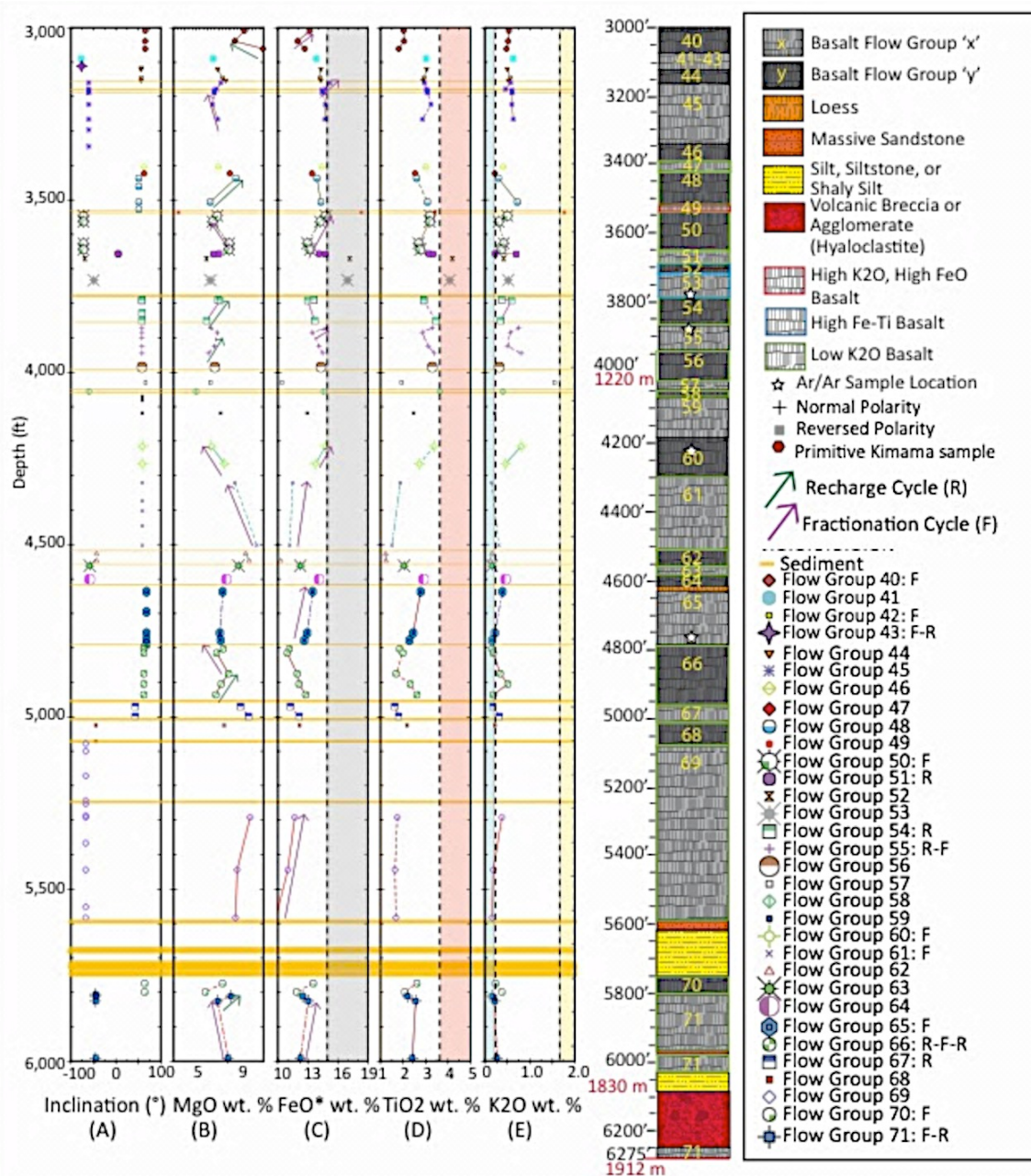


Figure 16: Generalized stratigraphic column, mean paleomagnetic inclination (A), and selected chemical compositions of the Kimama core as a function of depth below the surface (in meters) (B-E). We identify 32 flow groups, which are numbered from top to bottom. The Fe-Ti, HK, and LK flows are highlighted by shaded fields in columns C through E. Refer to Table 1 for flow group details. Figures B and C are annotated with arrows, displaying our interpretation of fractionation (F) and recharge (R) cycles. Flow groups 1 and 22 show upsection recharge followed by a fractionation event. Flow group 20 shows upsection fractionation followed by recharge. Flow groups 6, 7, 9, 10, 11, 12, 15, 17, 27, and 29 show upsection fractionation. Flow groups 17, 24, 26, and 28 show upsection recharge. Flow groups 2, 3, 4, 5, 8, 13, 14, 18, 19, 21, 23, 25, 30, 31, and 32 show relatively constant upsection composition. See text for full discussion of recharge and fractionation cycles.



Stratigraphically defined flow groups based on lithology, paleosecular magnetic variations, and sediment intercalations, as defined by Potter et al. (see Chapter 2), do not correspond directly to magma fractionation or recharge cycles (Figure 12). Thirty flow groups, beginning with the uppermost flow groups 1, 3, 6, 9, 10, 12, 23, 24, 25, 26, 28, 31, 32, 36, 39, 41,

46, 47, 49, through the lower flow groups 52, 53, 56, 57, 59, 62, 63, 64, 68, and 69, show relatively constant compositional trends with depth, suggesting the emptying of a magma chamber over relatively short time spans, with little or no coeval fractional crystallization. This is consistent with relatively high eruption rates that empty the magma chamber quickly.

Upward fractionation cycles are recognized in twenty flow groups in the Kimama core: flow groups 2, 8, 11, 13, 14, 19, 21, 27, 29, 33, 34, 38, 40, 42, 50, 55, 60, 61, 65, and 70. A few groups show brief intervals of upward fractionation superimposed on recharge trends (flow groups 20, and 66). These short upward fractionation “steps” probably represent periods of quiescence during which neither eruptions nor recharge occur.

Other flow groups document progressive recharge of their magma chambers coeval with ongoing eruptions, such that lavas become progressively more primitive upsection, trending to low-K, high MgO compositions. This can be observed in 16 flow groups: 4, 7, 8, 16, 17, 18, 22, 27, 30, 35, 37, 43, 48, 51, 54, 67, and 71. Flow groups 13, 17, 20 and 24 also display brief intervals of upward fractionation superimposed on the dominant recharge trends.

HK flow groups (flow groups 12 and 49) are compositionally constant, but too thin to represent prolonged time intervals. Although both sit atop underlying upward fractionation cycles, the need for a separate parent magma makes connecting these to underlying flow groups problematic.

The occurrence of upward fractionation cycles and recharge cycles is consistent with the proposal of Shervais et al. (2006), which suggests that basalt magmas are processed through a mid-crustal sill complex, in which individual sills commonly form layered mafic intrusions as the cumulate extract of crystal-melt fractionation. These layered mafic intrusions act as reactive filters which process the magma before it erupts. Individual sills may represent a single pulse of primitive magma, which then feeds a single monogenetic volcano on the surface.

Crystallization Models

The low-pressure fractional crystallization of olivine and plagioclase has historically been accepted as the dominant process controlling the composition and evolution of SRP olivine tholeiite basalts (Leeman and Vitaliano, 1976; Leeman, 1982a, 1982b, 1982c; Geist et al., 2002). We used COMAGMAT to model fractional crystallization (FC) processes in the Kimama core. Sample KA1A263 of flow group 1 was modeled as a representative, unaltered SROT basalt (Figure 17).

Fractional crystallization appears to play a moderate role in the generation of observed compositions. Compositional trends in Figure 16 appear to align with expected paths for assimilation-fractional crystallization (AFC) of previously intruded basalt (AFC-gabbro). Our COMAGMAT model used olivine and plagioclase fractionating phases in a 40:60 ratio; changing this ratio or introducing clinopyroxene into the system did not change the results.

We used the four primitive flows, KA1B1467, KA1B3061, KA1B4502, and KA1B4527 and the FC-AFC-FCA-mixing Excel spreadsheet of Erstoy and Helvaci (2010) to generate step-wise and end-member chemical compositions for comparison to the less evolved low-K flow groups, and to the more evolved Fe-Ti and high-K flow groups observed in the Kimama core (Figure 18).

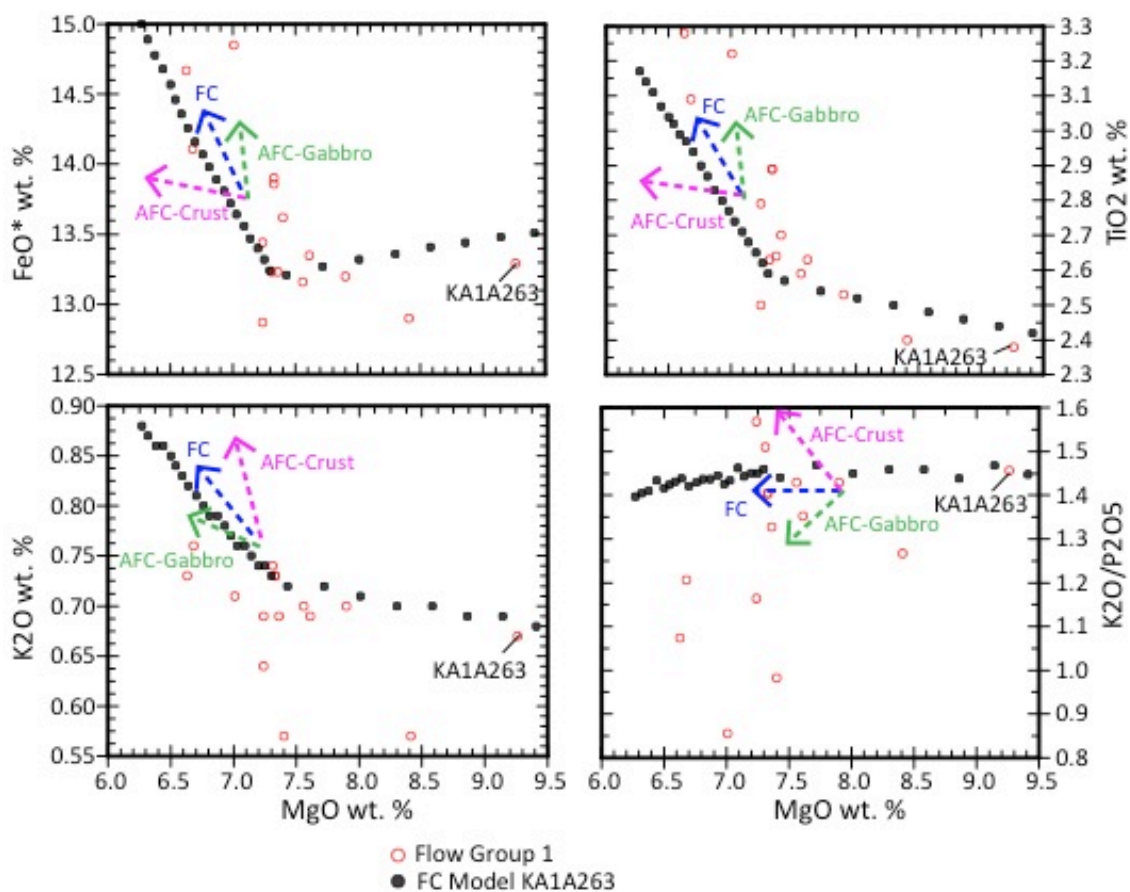


Figure 17: COMAGMAT variation diagrams showing the expected fractionation path of a primitive basalt (black filled circles) as compared to actual chemical values for the flow group (red circles) KA1A263, sampled from 80.2 mbs, has MgO 9.26 wt% and is the most primitive lava in flow group 1 (13.1-118.3 mbs). Arrows show predicted fractional crystallization (FC), fractional crystallization with assimilation of felsic crust (AFC-crust), and fractional crystallization with assimilation of previously intruded gabbro (AFC-gabbro).

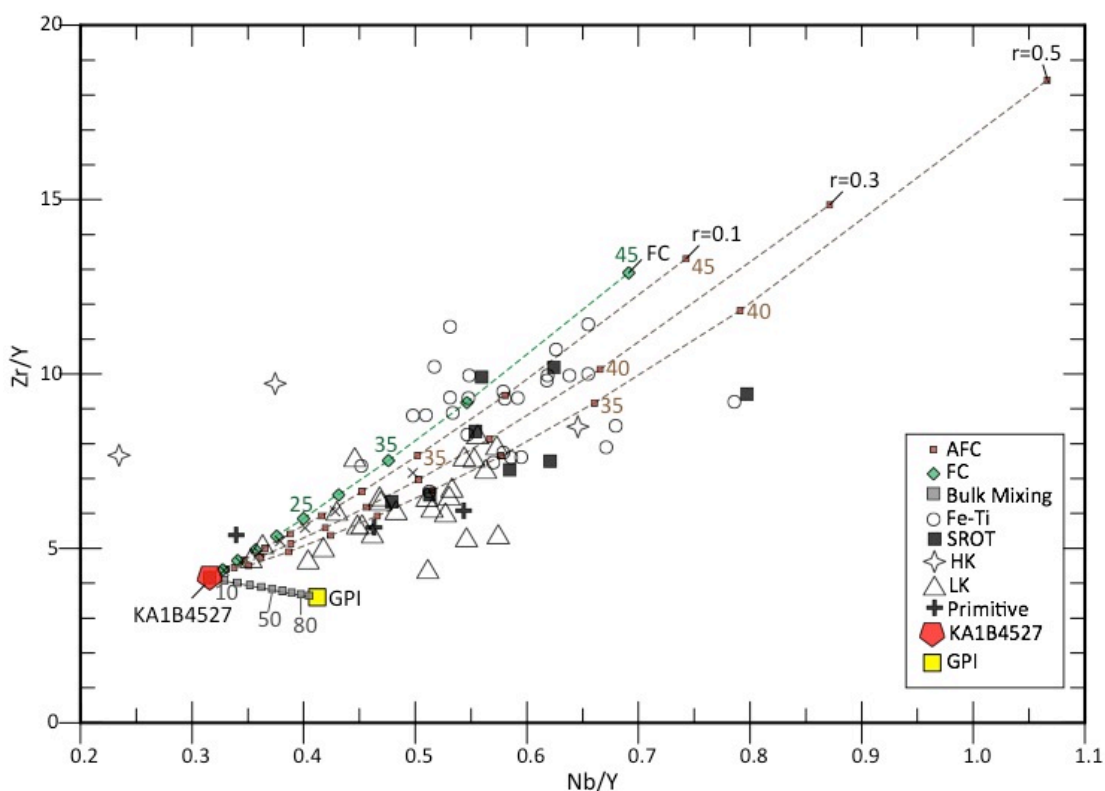


Figure 18: Crystallization model of expected differentiation processes for Kimama basalts. Compositions of Fe-Ti, SROT, HK, and LK basalts are plotted with four primitive basalt samples as proxies for parent magma compositions. Fractional crystallization values (FC; green diamond) are shown in percent crystallization, in increments of 5%. Bulk mixing values (grey squares) are shown as percent assimilated in increments of 10%. Assimilation-fractional crystallization (AFC) values are shown in percent crystallization in increments of 5%, with r values presented at the end of each AFC trend. GPI is Graveyard Point Intrusion. Calculations made from the model of Estoy and Helvacı (2010).

Melt Source

Chemical variations in basalts may be attributed to different petrogenetic conditions in the middle crust. Differing degrees of partial melting can cause compositional disparities in magmas of similar source regions, and partial melting of magma source regions that vary significantly in trace elements may also cause variations in basalt chemistry (Leeman, 1982b; Hughes et al., 2002a; Putirka et al., 2009). Subsequent fractional crystallization of primitive magma may also cause compositional changes. Since small amounts of fractional crystallization

have little effect on incompatible element compositions, our models of Kimama basalts focus on the effect of variations in the amount of partial melting and of source composition.

We use multi-element (spider) diagrams normalized to primitive mantle concentrations to evaluate fractional crystallization and partial melting processes. Spider diagrams efficiently organize large amounts of data for easier comparison.

We have constructed a series of spider diagram melting models in order to interpret Kimama melt variations (Figure 19). Chemical compositions in Kimama basalts represent the source regions of normal mid-ocean ridge basalts (N-MORB; depleted relative to primitive mantle), primitive mantle (PM), and enriched mid ocean ridge basalts (E-MORB; enriched relative to primitive mantle). Source modes used are spinel and garnet lherzolite, representing relative shallow (spinel: <20 Kb or 66 km depth) and deep (> 20 kb or 66 km depth) melting regimes. We compared these models to five representative high-MgO basalts from the Kimama core. Partition coefficients are from McKenzie and O'Nions (1991, 1995) and Arth (1976); primitive mantle and N-MORB source compositions are from McKenzie and O'Nions (1995). The E-MORB source composition is from Mertz et al. (2001) using N-MORB source + 8% metasomatic melt (0.3% fractional melt of MORB source; Mertz et al., 2001). The non-modal batch melting equation was used to calculate melt variations, and the primitive mantle-normalized results are shown in Figure 19.

Partial melting of an N-MORB composition source in the spinel lherzolite facies results in depleted LREE concentrations (relative to HREE) in model melts. At extremely low melt fractions (less than 2%), HREE concentrations in the model melts are too high and LREE/HREE ratios too low to match observed primitive basalt compositions (Figure 19). High field strength elements (HFSE) and K₂O also show suppressed values in the model melts. Within the garnet lherzolite facies, partial melting of an N-MORB composition source results in model melts that are

depleted in LREE relative to HREE. An exception to this observation occurs at extremely low melt fractions (< 2%), in which case HREE, K₂O, and HFSE concentrations in the model melts are too low to fit the data.

When primitive mantle source compositions are melted in the spinel lherzolite facies, the model melts generated are too low in LREE and LREE/HREE ratios. Partial melting of a primitive mantle composition in the garnet lherzolite facies (4% modal garnet) produces model melts that are too low in LREE at large melt fractions and too low in HREE at low melt fractions. At all but the lowest melt fractions, the model melts are too low in HFSE.

We observed the best fit to the Kimama primitive basalts when we compared model melts generated from the partial melting of the calculated E-MORB source composition in the spinel lherzolite facies (Figure 19b). Coherence is observed for all elements in the 7% to 15% melting range with the exception of Sr, which is consistently high in all of the model melts. Using the same source composition in a garnet-poor lherzolite mode (4% modal garnet) resulted in good fits for the LREE within the ~10% to 20% melting range, but poor fits for the HREE (Figure 19b).

The relatively high concentrations of Sr, both in source composition and facies models, suggest small amounts of plagioclase fractionation (which would have a minor effect on the other elements modeled), or a mantle source region with lower Sr than our modeled source. Considering that the composition of the E-MORB source was calculated to model oceanic island basalts and not continental tholeiites (Mertz et al., 2001), the fit of the model melts derived from the E-MORB source to our observed data is unexpectedly good for basalt magmas generated in continental lithosphere.

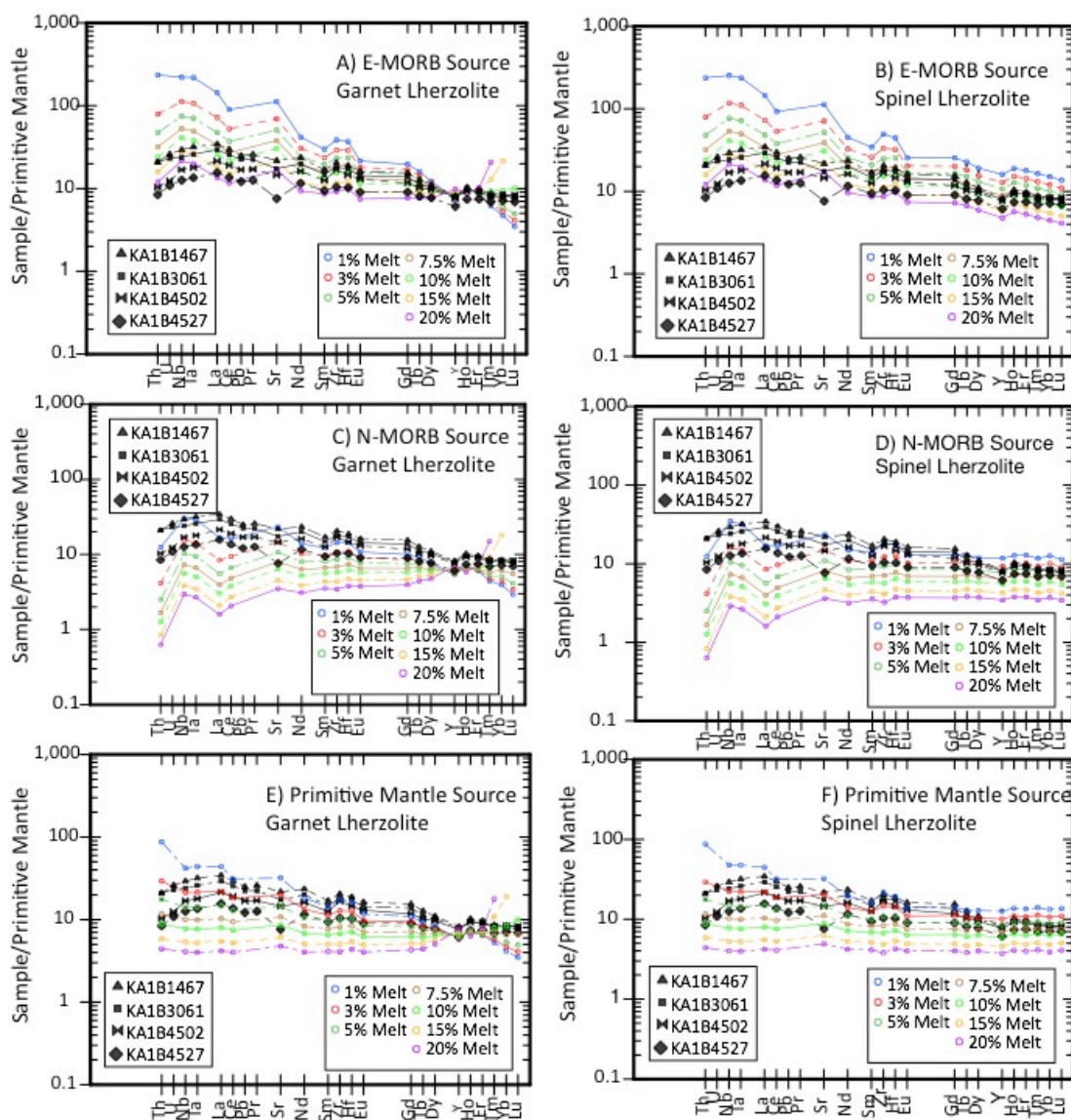


Figure 19: Multi-element spider diagrams normalized to primitive mantle (McDonough and Sun, 1995). Six source compositions are plotted after varying percentages of melting. A) and B): Enriched mid ocean ridge basalt (E-MORB), C) and D): normal mid ocean ridge basalt (N-MORB), and E) and F): primitive mantle (PM) source compositions of spinel lherzolite and garnet lherzolite are used. We compare compositions of four primitive basalt samples, proxies for parent magma to determine the composition and melting conditions of the Kimama source magma. Trace elements are arranged in order of decreasing compatibility from right to left.

Pressures inferred from major phase equilibria are consistent with observed upper mantle pressures; the observed peridotite facies assemblages imply pressures within the spinel lherzolite to garnet-poor facies (1.0-2.4 GPa for the spinel facies and probably < 3.0 GPa for the garnet-poor facies).

Potential Temperatures

Potential temperature of the source mantle represents the hypothetical temperature that the mantle would have if it were to reach Earth's surface uncompressed and unmelted (McKenzie and Bickle, 1988). Increasingly, mantle potential temperature (T_p), is used in the absence of reliable or coherent seismic data as a tool to discern the mantle thermal anomalies that herald the presence of mantle plumes (Putirka, 2005). At Iceland, T_p is estimated to be 1480-1520°C (MacLennan et al., 2001), while at Hawaii, T_p is estimated to be 1558°C (Watson and McKenzie (1991).

We used PETROLOG to model reverse fractionation in four high-MgO basalts, used as proxies for parent magma compositions, in order to calculate their primitive parent magma compositions and olivine equilibration temperatures, which should equal the temperature of the mantle source region. Each sample represents the most primitive basalt erupted in a chemical cycle, based upon high Mg#, high MgO content, low Ni content. All but sample KA1B3061 and 4527 are the oldest flows in their respective flow groups. Input parameters were 15Kbar pressure and Fo89, conditions thought to exist within the mid-crustal sill. Sample compositions and modeled parent magma compositions are shown in Table 5. Although no compositional trends are evident in most major element oxides, MgO composition appears to decrease with depth in reverse fractionation models.

Table 5: Actual and reverse fractionation compositional results for primitive Kimama basalt samples at Fo 89 using PETROLOG. T_p refers to the potential temperature of the mantle.

SAMPLE	T_p (°C)	Olv Kd	Lg(fO2)	Density	Viscosity	Starting melt %	Olv %	SiO2	TiO2	Al2O3	Fe2O3	FeO	FeO*	MnO	MgO	CaO	Na2O	K2O	P2O5	Cr2O3
KA1B1467						Sample Composition:	46.3	2.04	14.9	13.9		12.5	0.190	9.28	10.3	2.32	0.430	0.390	0.100	
1467	1407	0.314	-6.3	2.771	4.13	81.8	18.2	45.1	1.67	12.2	1.59	11.2	12.7	0.155	16.0	8.39	1.90	0.352	0.319	0.083
KA1B3061						Sample Composition:	44.9	1.81	13.8	14.1		12.7	0.190	11.0	11.0	2.40	0.480	0.350	0.150	
3061	1401	0.304	-6.37	2.785	2.35	87.7	12.3	44.2	1.58	12.0	1.67	11.1	12.6	0.166	15.4	9.64	2.10	0.419	0.306	0.13
KA1B4502						Sample Composition:	46.8	1.50	15.1	12.4		11.2	0.190	10.4	10.9	2.06	0.310	0.240	0.110	
4502	1372	0.316	-6.61	2.752	4.61	89.0	11.0	46.0	1.33	13.4	1.37	10.1	11.3	0.169	14.4	9.70	1.83	0.275	0.213	0.099
KA1B4527						Sample Composition:	48.9	1.22	15.5	11.0		9.9	0.26	9.41	11.5	1.75	0.15	0.19	0.700	
4527	1345	0.326	-6.82	2.714	5.00	89.1	10.9	48.4	1.10	13.9	1.19	9.18	10.3	0.234	13.6	10.3	1.57	0.135	0.171	0.063

Melt density is calculated following the model of Lange & Carmichael 1987

Parameters to stop calculations at: final olv composition: Fo = 89 mol%

Melt viscosity is calculated following the model of Bottinga & Weill 1972

The amount of a mineral phase added to 100% of melt on each step is: 0.01 %

From these calculations, Kimama mantle potential temperatures are estimated to be between 1345° and 1407°C, lower than known plume temperatures, but higher than MORB-source mantle ($T_p = 1250^\circ\text{-}1300^\circ\text{C}$). However, this could be explained by the calculation of T_p at 50 km depth, the suggested depth of the mantle beneath the SRP (i.e. mantle potential temperature from a mantle depth). Perhaps more relevant is the position of the Y-SRP hotspot underneath the Heise volcanic field during the eruption of Kimama basalts. At a distance of ~150 km from Kimama, there may have been significant heat loss from the plume by the time mantle-derived Heise melts intruded into the mid-crustal sill beneath the Kimama core hole site.

Using geochemical data with previously-determined core stratigraphy and paleomagnetic data, we show that Kimama basaltic lavas have varied in composition from low-K to SROT to high-K to Fe-Ti lavas throughout 6.4 Ma of continuous deposition. We interpret the multiple chemical cycles evident in stratigraphic comparisons of Kimama geochemistry to represent the fractionation of individual magmas and the progressive recharge of crustal magma reservoirs, with each cycle representing an eruption from a vent or vent system. Fractionation and assimilation of continental crust does not explain the trends of enrichment in P_2O_5 and Cr and depletion in K_2O and Zr, and in agreement with Shervais et al. (2006) and Jean et al. (2013), our FC-AFC models suggest that fractionation and assimilation of previously intruded gabbro

best explain the overall geochemistry of Kimama basalts. The Graveyard Point Intrusion (gabbro), is used as an analog for the composition of the gabbro within the mid crustal sill complex, and demonstrates the mafic compositions necessary to generate observed trends in primitive flows through assimilation (White, 2007). Melting models of primitive Kimama compositions suggest a petrogenetic history of 7-15% melting of an E-MORB spinel lherzolite source, also in accord with previous models of SRP basaltic magmas.

Contrary to previous models of SRP volcanism, evolved, COM-type lava flows are not confined to the margins of the SRP, nor are they temporally limited to the last 15 k.y. (Kuntz et al., 1986, 2007; Leeman, 1982c; Putirka et al., 2009). The two HK lava flow groups identified in the Kimama core represent unrelated batches of magma that tapped a source similar to that of COM. The incompatible element-enriched Fe-Ti basalt flows may demonstrate longer-duration storage in magma reservoirs, where fractionation was not cut short by the rapid ascent of magma to the surface.

Conclusion

The Kimama core samples lava flows presumably erupted from multiple shields in the region, but the similarity of mantle melting conditions and transport paths has resulted in lavas with generally similar compositions. The compositional variance of the four compositional types observed in the Kimama core must reflect differing processes of petrogenesis from magmas of the same source.

Upward fractionation, or upsection increases in incompatible elements and K_2O and FeO^* wt%, suggest fractional crystallization cycles as observed in layered mafic intrusions. Chemical reversals, or upsection increases in compatible elements and MgO wt%, suggest

episodes of recharge of the system by more primitive melt. The chemical stratigraphy of the Kimama core provides evidence of the changing influences of continental lithosphere and mantle hotspot material over relatively short to long periods of time.

Cycles of fractionation and recharge are demonstrated in gradual variations in major and trace element trends. Evidence for upward fractionation is thought to lie in the upsection decrease in MgO and Cr and the increase in Fe₂O₃, K₂O, TiO₂, P₂O₅, Zr, and La (Shervais et al., 2006). Phase assemblage changes may indicate the influx of a new magma, while phase composition changes may result from the ascent of magma through lower temperature conditions. The repetition of cycles upsection that involve the same or similar phase assemblages suggests the system was drawn back to its original chemistry through an influx of primitive magma (Shervais et al., 2006).

Other possible consequences of magma transport through the mid-crustal mafic sill are evident as gradual to abrupt geochemical transitions. Shervais et al. (2006) suggests magma recharge, occurring over a period of time and without sufficient volume to significantly overwhelm residual magma from previous fractionation cycles, to explain progressive upsection variations in lava geochemistry. Conversely, abrupt transitions between cycles suggest a complete turnover of magma or the tapping of a new magma storage chamber (Shervais et al., 2006). Once a conduit has been established, ascending magma bodies are shielded from interaction and assimilation with felsic crust; it is possible for magma batches to travel through thick sections of continental crust without substantial interaction. The lack of geochemical disparity between SROT can be attributed to processes of fractionation and assimilation in the middle crust, processes that homogenize major and trace element geochemistry.

References

- Anders, M.H., Saltzman, J., and Hemming, S.R., 2009, Neogene tephra correlations in eastern Idaho and Wyoming for Yellowstone hotspot-related volcanism and tectonic activity: *Geological Society of America Bulletin* v. 121, p. 837–856.
- Arth J. G., 1976, Behavior of trace elements during magmatic processes--a summary of theoretical models and their applications: *Journal of Research U.S. Geological Survey*, v. 4, p. 41-47.
- Bonnichsen, B., Leeman, W. P., Honjo, N., McIntosh, W. C., and Godchaux, M. M., 2008, Miocene silicic volcanism in southwestern Idaho: geochronology, geochemistry, and evolution of the central Snake River Plain: *Bulletin of Volcanology*, v. 70(3), p. 315-342.
- Bonnichsen, B., and Godchaux, M. M., 2002, Late Miocene, Pliocene, and Pleistocene geology of southwestern Idaho with emphasis on basalts in the Bruneau-Jarbridge, Twin Falls, and western Snake River Plain regions: *Tectonic and Magmatic Evolution of the Snake River Plain Volcanic Province: Idaho Geological Survey Bulletin*, v. 30, p. 233-312.
- Ersoy, Y., and Helvaci, C., 2010, FC–AFC–FCA and mixing modeler: A Microsoft Excel spreadsheet program for modeling geochemical differentiation of magma by crystal fractionation, crustal assimilation and mixing: *Computers & Geosciences*, v. 36, p. 383–390.
- Geist, D. J., Sims, E. N., Hughes, S. S., and McCurry, M., 2002, Open-system evolution of a single episode of Snake River Plain magmatism, *in* Link, P. K., and Mink, L. L., eds., *Geology, hydrogeology, and environmental remediation, Idaho National Engineering and Environmental Laboratory, eastern Snake River Plain, Idaho: Geological Society of America Special Paper 353*, p. 193-204.
- Greeley, R., 1982, The Snake River Plain, Idaho: Representative of a new category of volcanism: *J. Geophys. Res.*, v. 87(B4), p. 2705–2712.
- Hackett, W., and Smith, R., 1992, Quaternary volcanism, tectonics, and sedimentation in the Idaho National Engineering Laboratory area, *in* J.R. Wilson, ed., *Field Guide to Geologic Excursions in Utah and Adjacent areas of Nevada, Idaho and Wyoming: Utah Geological Survey Miscellaneous Publications* v. 92-3, p 1-18.
- Hackett, W.R., Smith, R.P., and Khericha, 2004, Volcanic hazards of the Idaho National Engineering and Environmental Laboratory, southeast Idaho, *in* B. Bonnichsen, C.M. White, and M. McCurry, eds., *Tectonic and Magmatic Evolution of the Snake River Plain Volcanic Province: Idaho Geological Survey Bulletin* 30, p. 461-482.
- Hanan, B., Vetter, S., and Shervais, J., 1997. Basaltic volcanism in the eastern Snake River Plain: Lead, neodymium, strontium isotope constraints from the Idaho INEL WO-2 core site basalts: *Geological Society of America Abstracts with Programs*, v. 29, p. A298.

- Hughes, S., Wetmore, P., Casper, J., 1997, Geochemical interpretation of basalt stratigraphy and Quaternary mafic volcanism, eastern Snake River Plain, Idaho: Geological Society of America Abstracts with Programs, v. 29, p. A-298.
- Hughes, S., Smith, R., Hackett, W., and Anderson, S., 1999, Mafic volcanism and environmental geology of the eastern Snake River Plain, *in* S.S. Hughes and G.D. Thackray, eds., Guidebook to the Geology of Eastern Idaho: Idaho Museum of Natural History, p. 143-168.
- Hughes, S.S., McCurry, M., and Geist, D.J., 2002a, Geochemical correlations and implications for the magmatic evolution of basalt flow groups at the Idaho National Engineering and Environmental Laboratory, *in* Link, P.K., and Mink, L.L., eds., Geology, Hydrogeology, and Environmental Remediation: Idaho National Engineering and Environmental Laboratory, Eastern Snake River Plain, Idaho: Geological Society of America Special Paper 353, p. 151-173.
- Hughes, S.S., Wetmore, P.H., and Casper, J.L., 2002b, Evolution of Quaternary Tholeiitic Basalt Eruptive Centers on the Eastern Snake River Plain, Idaho, *in* Bonnicksen, B., White, C.M., and McCurry, M., eds., Tectonic and Magmatic Evolution of the Snake River Plain Volcanic Province: Idaho Geological Survey Bulletin 30, p. 363-385.
- Irvine, T.N., 1970, Crystallization sequences in the Muskox intrusion and other layered intrusions, *in* Symposium on the Bushveld Igneous complex and other layered intrusions: Geological Society of South Africa Special Publication 1, p. 441-476.
- Jackson, E.D., 1970, The cyclic unit in layered intrusions—A comparison of repetitive stratigraphy in the ultramafic parts of the Stillwater, Muskox, Great Dyke, and Bushveld complexes, *in* Symposium on the Bushveld Igneous complex and other layered intrusions: Geological Society of South Africa Special Publication 1, p. 391-424.
- Jackson, E.D., 1971, The origin of ultramafic rocks by cumulus processes: *Fortschritte Der Mineralogie*, v. 48, p. 128-174.
- Jean, M.M., Shervais, J.W., Champion, D.E., and Vetter, S.K., 2013, Geochemical and paleomagnetic variations in basalts from the Wendell Regional Aquifer Systems Analysis (RASA) drill core: Evidence for magma recharge and assimilation-fractional crystallization from the central Snake River Plain, Idaho: *Geosphere*, v. 9, no. 5, p. 1319-1335.
- Jenner, G.A., Longerich, H.P., Jackson, S.E., and Fryer, B.J., 1990, ICP-MS—A powerful tool for high-precision trace-element analysis in Earth Science: Evidence from analysis of selected U.S.G.S. reference samples: *Chemical Geology*, v. 83, p. 133-148.
- Kuntz, M.A., 1978, Geology of the Arco-Big Southern Butte area, eastern Snake River Plain, and potential volcanic hazards to the radioactive waste management complex, and other waste storage and reactor facilities at the Idaho National Engineering Laboratory, Idaho with a section on Statistical treatment of the age of lava flows *by* John

O. Kork: U.S. Geological Survey Open-File Report 78-691, 70 p.

- Kuntz, M., Champion, D., Spiker, E., Lefebvre, R., Covington, H., and McBroome, L., 1982. The Great Rift and the evolution of the Craters of the Moon lava field, Idaho, *in* Bill Bonnicksen and R.M. Breckenridge, eds., *Cenozoic Geology of Idaho: Idaho Bureau of Mines and Geology Bulletin 26*, p. 423-438.
- Kuntz, M., Champion, D., Spiker, E., and Lefebvre, R., 1986. Contrasting magma types and steady-state, volume-predictable volcanism along the Great Rift, Idaho: *Geological Society of America Bulletin*, v. 97, p. 579-594.
- Kuntz, M., Champion, D., Lefebvre, and Covington, H., 1988. Geologic map of the Craters of the Moon, Kings Bowl, Wapi lava fields and the Great Rift volcanic rift zones, south-central Idaho: U.S. Geological Survey Miscellaneous Investigations Series Map I-1632, scale 1:100,000.
- Kuntz, M., Covington, H., and Schorr, L., 1992, An overview of basaltic volcanism of the eastern Snake River Plain, Idaho, *in* P.K. Link, M.A. Kuntz, and L.P. Platt, eds., *Regional Geology of Eastern Idaho and Western Wyoming: Geological Society of America Memoir 179*, p. 227-267.
- Kuntz, M.A., Skipp, B., Champion, D.E., Gans, P.B., Van Sistine, D.P., and Snyders, S.R., 2007, Geologic map of the Craters of the Moon 30' x 60' quadrangle, Idaho: U.S. Geological Survey Scientific Investigations Map 2969, 64-p. pamphlet, 1 plate, scale 1:100,000.
- Leeman, W.P., 1982a, Development of the Snake River Plain-Yellowstone Plateau Province, Idaho and Wyoming: An overview and petrologic model, *in* Bonnicksen, B., and Breckenridge, R.M., eds., *Cenozoic geology of Idaho: Idaho Bureau of Mines and Geology Bulletin 26*, p. 155-177.
- Leeman, W.P., 1982b, Olivine tholeiitic basalts of the Snake River Plain, Idaho, *in* Bonnicksen, B., and Breckenridge, R.M., eds., *Cenozoic geology of Idaho: Idaho Bureau of Mines and Geology Bulletin 26*, p. 181-191.
- Leeman, W.P., 1982c, Evolved and hybrid lavas from the Snake River Plain, Idaho, *in* Bill Bonnicksen and R.M. Breckenridge, eds., *Cenozoic Geology of Idaho: Idaho Bureau of Mines and Geology Bulletin 26*, p. 181-191.
- Leeman, W.P., and Vitaliano, C., 1976, Petrology of the McKinney basalt, Snake River Plain, Idaho: *Geological Society of America Bulletin*, v. 87, p. 1777-1792.
- McBirney, A.R., and Noyes, R.M., 1979, Crystallization and layering of the Skaergaard Intrusion: *Journal of Petrology*, v. 20, p. 487-554.
- McCurry, M., and Rodgers, D.W., 2009, Mass transfer along the Yellowstone hotspot track I: Petrologic constraints on the volume of mantle-derived magma: *Journal of Volcanology and Geothermal Research*, v. 188, p. 86-98.

- McDonough, W. F., and Sun, S. S., 1995, The composition of the Earth, *Chemical Geology*, v. 120(3), p. 223-253.
- McKenzie, D., and Bickle, M. J., 1988, The volume and composition of melt generated by extension of the lithosphere: *Journal of Petrology*, v. 29(3), p. 625-679.
- McKenzie, D.A.N., and O'Nions, R. K., 1991, Partial melt distributions from inversion of rare earth element concentrations: *Journal of Petrology*, v. 32(5), p. 1021-1091.
- McKenzie, D.A.N., and O'Nions, R.K., 1995, The source regions of ocean island basalts: *Journal of Petrology*, v. 36(1), p. 133-159.
- Menzies, M., Leeman, W., and Hawkesworth, C., 1984, Geochemical and isotopic evidence for the origin of continental flood basalts with particular reference to the Snake River Plain Idaho, U.S.A.: *Philosophical Transactions of the Royal Society of London*, v. 310, p. 643-660.
- Mertz, D. F., Weinrich, A. J., Sharp, W. D., and Renne, P. R., 2001, Alkaline intrusions in a near-trench setting, Franciscan complex, California: constraints from geochemistry, petrology, and $40\text{Ar}/39\text{Ar}$ chronology: *American Journal of Science*, v. 301(10), p. 877-911.
- Miller, M., and Hughes, S., 2009, Mixing primitive and evolved olivine tholeiite magmas in the Eastern Snake River Plain, Idaho: *Journal of Volcanology and Geothermal Research*, v. 188, p. 153-161.
- Moye, F. J., Hackett, W. R., Blakley, J. D., and Snider, L. G., 1988, Regional geologic setting and volcanic stratigraphy of the Challis volcanic field, central Idaho: *Guidebook to the geology of central and southern Idaho: Idaho Geological Survey Bulletin*, v. 27, p. 87-97.
- Neal, C.R., 2001, The interior of the Moon: The presence of garnet in the primitive, deep lunar mantle: *Journal of Geophysical Research*, v. 106, p. 27865–27885.
- Pallister, J.S., and Hopson, C.A., 1981, Samail ophiolite plutonic suite; field relations, phase variation, cryptic variation and layering, and a model of a spreading ridge magma chamber, *in* Coleman, R.G., and Hopson, C.A., eds., *Oman ophiolite: Journal of Geophysical Research*, p. 2593–2644.
- Pierce, K.L., and Morgan, L.A., 1992, The Track of the Yellowstone Hotspot: Volcanism, faulting, and uplift, *in* Link, P.K., Kuntz, M.A., and Platt, L.B., eds., *Regional geology of eastern Idaho and western Wyoming: GSA Memoir 179*, p. 1-53.
- Putirka, K. D., 2005, Mantle potential temperatures at Hawaii, Iceland, and the mid-ocean ridge system, as inferred from olivine phenocrysts: Evidence for thermally driven mantle plumes: *Geochemistry, Geophysics, Geosystems*, v. 6(5).
- Putirka, K.D., Kuntz, M.A., Unruh, D.M., and Vaid, N., 2009, Magma Evolution and Ascent at the

Craters of the Moon and Neighboring Volcanic Fields, Southern Idaho, USA: Implications for the Evolution of polygenetic and monogenetic volcanic fields: *Journal of Petrology*, v. 50, no. 9, p. 1639–1665.

Reid, M. R., 1995, Processes of mantle enrichment and magmatic differentiation in the eastern Snake River Plain: Th isotope evidence: *Earth and Planetary Science Letters*, v. 131(3), p. 239-254.

Self, S., Keszthelyi, L., and Thordarson, T., 1998, The Importance of Pahoehoe: *Annual Review of Earth and Planetary Sciences*, v. 26, p. 81-110.

Sigloch, K., 2011, Mantle provinces under North America from multi-frequency P-wave tomography: *Geochemistry Geophysics Geosystems*, v. 12, p. 1–27.

Shervais, J. W., Kauffman, J. D., Gillerman, V. S., Othberg, K. L., Vetter, S. K., Hobson, V. R., and Hanan, B. B., 2005, Basaltic volcanism of the central and western Snake River Plain: A guide to field relations between Twin Falls and Mountain Home, Idaho: *Field Guides*, v. 6, p. 27-52.

Shervais, J.W., Vetter, S.K., and Hanan, B.B., 2006, Layered mafic sill complex beneath the eastern Snake River Plain: Evidence From cyclic geochemical variations in basalt: *Geology*, v. 34, p. 365- 368.

Shervais, J. W., and Hanan, B. B., 2008, Lithospheric topography, tilted plumes, and the track of the Snake River–Yellowstone hot spot: *Tectonics*, v. 27, p. 5

Shervais, J.W., Evans, J.P., Christiansen, E.H., Schmitt, D.R., Kessler, J.A., Potter, K.E., Jean, M.M., Sant, C.J., and Freeman, T.G., 2011, Project Hotspot: The Snake River Scientific Drilling Project. *Geothermal Resources Council Transactions*, v. 35, p. 995-1003.

Shervais, J. W., Nielson, D. L., Evans, J. P., Lachmar, T., Christiansen, E. H., Morgan, L., and Freeman, T. G., 2012, Hotspot: The Snake River Geothermal Drilling Project—Initial report: *Geothermal Resources Council Transactions*, v. 36, p. 767-772.

Shervais, John W., Douglas R. Schmitt, Dennis Nielson, James P. Evans, Eric H. Christiansen, Lisa Morgan, and James A. Kessler, et al., 2013, First Results from HOTSPOT: The Snake River Plain Scientific Drilling Project, Idaho, U.S.A.: *Scientific Drilling*, v. 15, p. 36-45.

Smith, R. B., Jordan, M., Steinberger, B., Puskas, C., Farrell, J., Waite, G.P., Husen, S., Chang, W. L., and O'Connell, R., 2009, Geodynamics of the Yellowstone Hotspot and mantle plume: Seismic and GPS imaging, kinematics, and mantle flow: *Journal of Volcanology and Geothermal Research*, v. 188, p. 26–56.

Wager, L.R., and Brown, G.M., 1967, Layered igneous rocks: San Francisco, California, W.H. Freeman and Company, 588 p.

Watson, S., and McKenzie, D., 1991, Melt generation by plumes: A study of Hawaiian volcanism: *J. Petrol.*, v. 32, p. 501–537.

White, C.M., 2007, The Graveyard Point Intrusion: An example of extreme differentiation of Snake River Plain Basalt in a shallow crustal pluton: *Journal of Petrology*, v. 48, p. 303–325.

CHAPTER 4

EVIDENCE FOR AN AXIAL VOLCANIC LOW IN THE KIMAMA CORE: HEISE FIELD
VOLCANOGENIC ZIRCONS AND THE LATE MIOCENE PALEO-WOOD RIVER IN THE
CENTRAL SNAKE RIVER PLAIN

Abstract

The 1912 m Kimama deep drill hole and core is located on the axial volcanic high of the central Snake River Plain, NE of Twin Falls, Idaho and provides a depositional record of basaltic lava flows, loess, and fluvial sand on the central Snake River Plain from the late Miocene through Pleistocene epochs. Based on Ar/Ar and paleomagnetic dating records, we infer that these sands were deposited within a relatively linear basalt accumulation rate of ~ 335 m/m.y. ($\sim 1,100$ ft/my), with a projected bottom hole age of 6.4 Ma.

Detrital zircons were recovered from two upward fining sandstone interbeds at 1842-1844 m (6044-6050 ft) and 1707-1748 m (5602-5737 ft) depth and analyzed for U-Pb and ϵ Hf at the University of Arizona LaserChron laboratory. At the base of the core, both interbeds contain mainly Miocene detrital zircons of the Yellowstone-Snake River Plain magmatic system (5 to 10 Ma). Higher sands contain successively older, pre-Neogene zircon grains including Challis magmatic event (45 to 50 Ma), Idaho batholith (90 to 100 Ma), Paleozoic magmatic grains recycled from Devonian Milligen Formation and Pennsylvanian-Permian Sun Valley Group, and, variable Grenvillean and Meso- and Paleoproterozoic grains or and Archean grains.

Detrital zircon ages (barcodes) within the five samples indicate two incursions of the Wood River system at depths of 1842-1844 m (6044-6050 ft) and 1707-1748 m (5602-5737 ft).

Each fluvial succession systematically changes upward from dominantly Neogene zircons to mainly Paleogene zircons, but inconstant Archean vs. Proterozoic populations in the upper succession suggest that the paleo-Wood River tributary tapped the structurally uplifted lower and middle plates of the Pioneer core complex. This observation, coupled with the 5.7 Ma estimated depositional age of the sand, constrains the unroofing of the Pioneer core complex and the exhumation of the Wildhorse complex to between 5.6 and 5.8 Ma. The top of the upper succession records the only population of Paleozoic grains present within the Kimama core, indicating a source west of the Pioneer thrust fault. We suggest that after 5.7 Ma, the paleo-Wood River system shifted westward, and that after 5.6 Ma, basaltic volcanism along the Axial Volcanic Zone diverted the paleo-Wood River system southwestward through the Hagerman area between 3.8 and 3 Ma.

In addition to older recycled grains, a large fraction of the recovered grains represent Neogene primary zircons formed during eruptions of rhyolite ash from the Y-SRP magmatic system. The fresh, rod- and blade-shapes of grains, with minimal rounding, suggest a primary fallout origin of these volcanic zircon grains. These volcanogenic detrital zircons were likely ejected during caldera-forming eruptions in the central SRP, transported by aeolian or fluvial processes, and deposited within the fluvial deposits shortly after their eruption. This implies that the depositional age of the sediment intervals corresponds to the age of youngest zircons in each unit (5.8 Ma and 6.2 Ma).

Hf isotopic compositions vary from ϵ_{Hf} of -7.3 to -3.9, and the Hf variation is highly correlated with age: volcanogenic zircons ages of 7.1, 6.7, 6.2, and 5.8 Ma have on average corresponding ϵ_{Hf} of -7.3, -6.4, -4.9, -3.9. This progressive decrease in ϵ_{Hf} in the younger zircons indicates an increase in mantle-derived Hf through time, with a corresponding decrease in crustal Hf. Furthermore, U-Pb ages of younger volcanogenic zircons in each interbed are in

accord with the depositional age inferred from the calculated accumulation rate, consistent with deposition less than 100,000 years after their eruption.

Introduction

The motion of the North American Plate over the fixed Snake River Plain (SRP) mantle hotspot is thought to have resulted in a northeastward-propagating track of silicic volcanic fields and the formation of the Yellowstone-Snake River Plain province (Pierce and Morgan, 1992). Explosive rhyolitic volcanism began at ~16 Ma on the Oregon-Nevada border and progressed across the Owyhee Plateau and the eastern SRP to a present location beneath the Yellowstone Plateau (Pierce and Morgan, 1992; Smith and Braile, 1994; Camp, 1995; Camp and Ross, 2004; Schmandt et al., 2012). The chemical and isotopic characteristics of eastern SRP basalts are consistent with a mantle plume source with varying degrees of interaction with continental lithosphere, and with residence within a mid-crustal sill complex prior to eruption (Shervais et al., 2006; Hanan et al., 2008; Jean et al., 2014).

The Kimama core hole was drilled on the axis of the YP-SRP hotspot track, primarily for the purpose of recovering the thickest and most continuous record of basalt volcanism (Figure 20). The 1912 m of core consists of basaltic lava flows intercalated with minor loess deposits. Potter et al. (2013) have identified 30 separate magmatic episodes, or basalt flow groups, based upon geochemical and paleomagnetic characteristics. Two packages of upward-fining fluvial sandstone were identified at 1707 m and 1842 m measured depth (Figure 21). Five detrital zircon samples from these two fluvial interbeds were analyzed for U-Pb ages and ϵ_{Hf} .

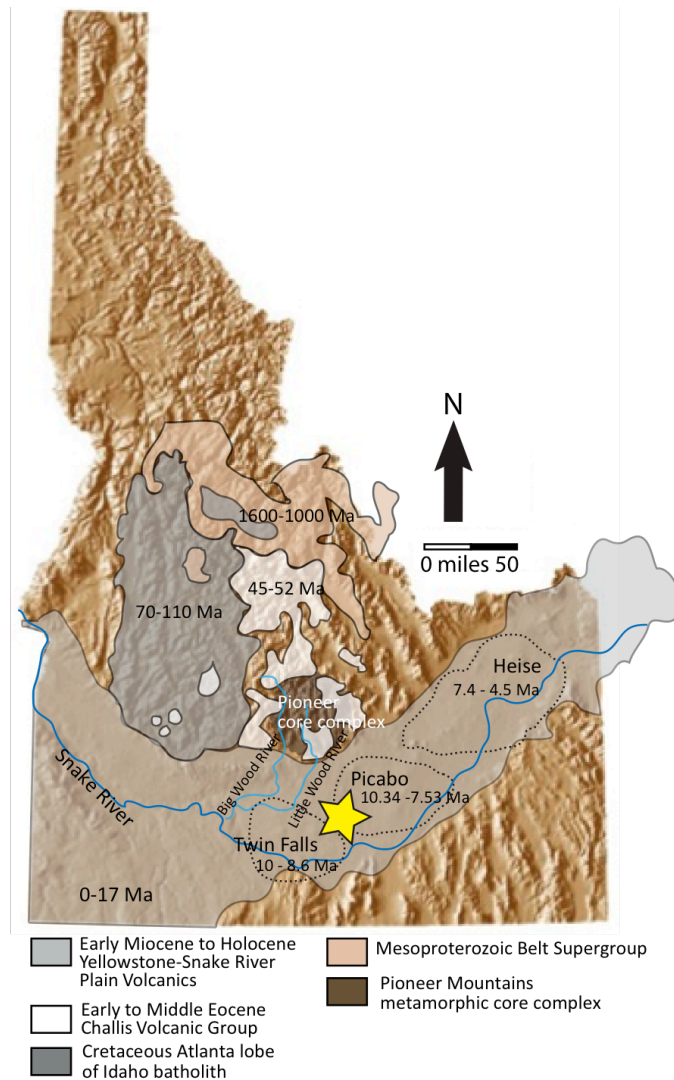


Figure 20: Digital elevation map (DEM) of the Snake River Plain and Yellowstone regions showing the location of Kimama, as well as topographic and geologic features. The long dashed lines delimit the location of the Yellowstone crescent of high terrain, while the short dashed lines indicate the position of drainage divides on the margin of the Snake River Plain (SRP). The white outlined polygons are silicic volcanic centers and ages (Pierce and Morgan, 1992; Bonnicksen et al., 2008). Solid white lines show the locations of selected normal faults. The locations of the Kimama and INEL-1 core holes are shown by white circles. Figure 2 is a more detailed map of the region within the black frame, with P indicating the Pioneer Mountains and B indicating the Boulder Mountains. Rivers north of the SRP drain to southeast, following the NW-SE vergence of range-front faults. Modified from Vogl et al. (2014).

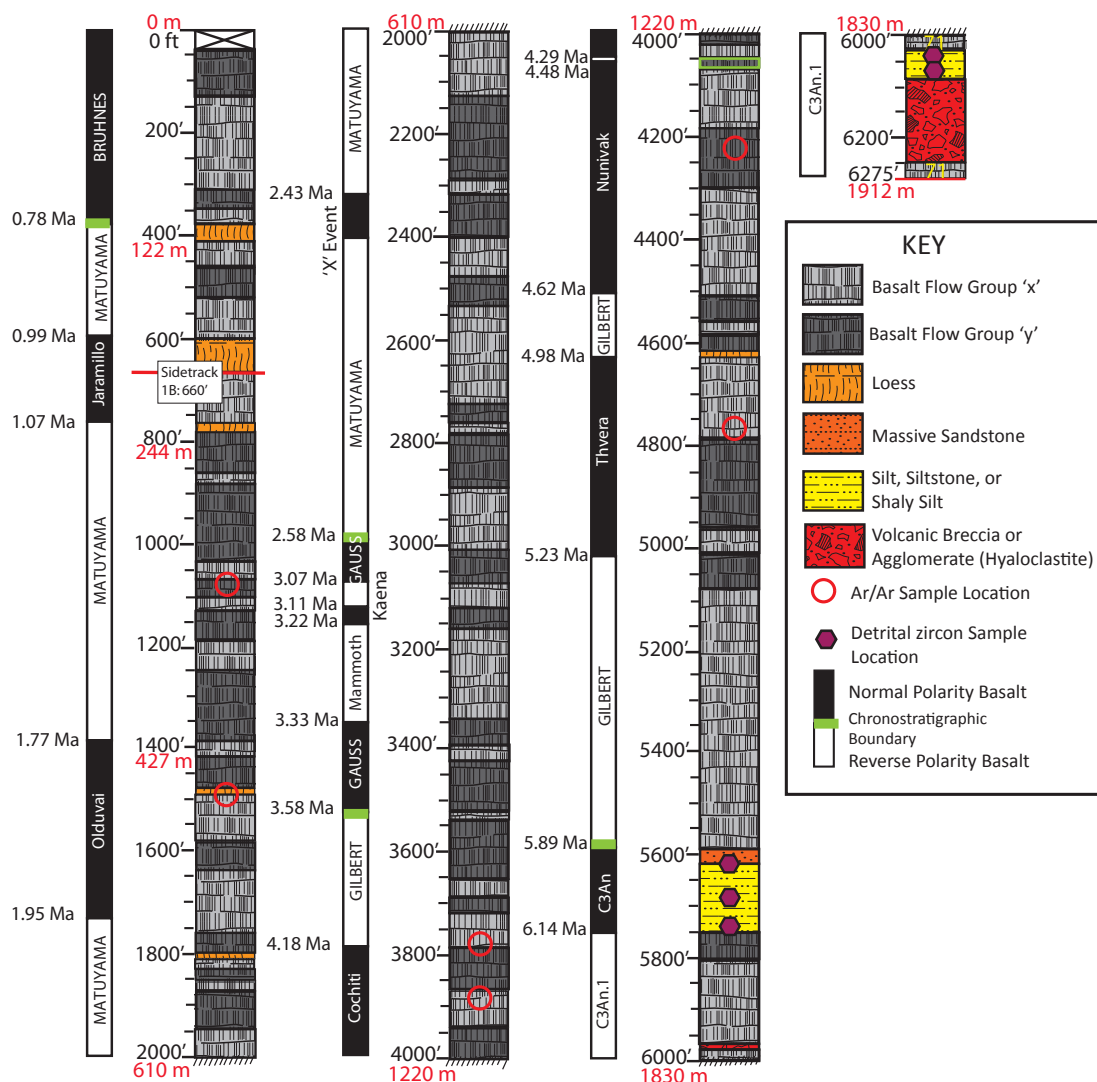


Figure 21: Lithologic and paleomagnetic stratigraphy of the Kimama core (see Chapter 1). Seventy-one flow groups were identified based upon lithologic observations, chemical variation, and magnetic polarity. Paleomagnetic polarity and associated ages are displayed to the left of the lithologic log. Five Chrons and nine subchrons are identified in the Kimama core (Champion and Duncan, 2012).

Regional Geology

The SRP and the Basin and Range region to the north have experienced an extended history of magmatism and regional tectonics beginning from the late Cretaceous through the

early Cenozoic (Armstrong, 1982; Burchfiel et al., 1992; DeCelles, 1994, 2004). Proterozoic and Mesozoic strata in the Snake River Plain region were influenced by east-vergent Antler, Sevier, and Laramide contraction (Burchfiel and Davis, 1975; DeCelles, 2004) followed by Cenozoic extensional collapse and magmatism (Armstrong, 1982; Dickinson, 2002). The central Idaho and Idaho-Wyoming thrust belts bound the SRP to the north and south and are overprinted by Basin and Range normal faults. Also to the north of the SRP is the 110-70 Ma Atlanta lobe of the Idaho batholith, which intrudes the Idaho-Wyoming thrust belt at its eastern extent (Armstrong et al., 1977; Criss and Fleck, 1987; Foster et al., 2007; Johnson et al., 1988). Volcanism in the Challis volcanic field of north central Idaho began at 51 Ma and covered much of the state of Idaho with voluminous eruptive products over the next ~5-10 Ma (Moye et al., 1988; Janecke and Snee, 1993; Gaschnig et al., 2010).

The SRP is bounded to the north and south by the northern Basin and Range province. Dominantly east-west extension in the northern Basin and Range since ~15-10 Ma (Colgan and Henry, 2007; Egger et al., 2003, 2010; Fosdick and Colgan, 2008; Wells et al., 2000) has led to the development of detachment fault systems, the exhumation of metamorphic core complexes, and the formation of extensional basins (Coney, 1980; Janecke, 1992; Foster and Fanning, 1997; Foster et al., 2007, 2010). Basin and Range extension is thought to have occurred south of the SRP both before and during plume-related magmatism (Colgan and Henry, 2007; Egger et al., 2010; Konstantinou et al., 2012).

A ~750 m to 2 km layer of Quaternary basalt obscures overlapping caldera complexes and associated deposits along the length and width of the eastern SRP (Doherty et al., 1979; Kuntz et al., 1992; Whitehead, 1992; Pierce and Morgan, 1992). Isostatic gravity and aeromagnetic and Bouger anomalies show approximate locations of caldera complexes in the general absence of exposed outflow deposits (Pierce and Morgan, 1992). This geological history

resulted in the exposure and exhumation of a wide range of sedimentary sources, which can be deciphered with detrital zircon analyses (Link et al., 2005; Beranek et al., 2006).

Detrital Zircon Provenance

Detrital zircon studies demonstrate Neogene drainage reversal in the Snake River watershed, with streams that flowed away from the tumescent Yellowstone highland during active volcanism, and reversed flow direction into the subsiding SRP following the migration of silicic volcanism to the northeast (Beranek et al., 2006). Using the current topographically high position of Yellowstone National Park as an analog, Pierce and Morgan (1992) inferred that previous positions of hotspot volcanism along the eastern SRP acted as continental divides with about 1 km relief (Pierce et al., 2002; Pierce and Morgan, 2009), directing drainage away from the highland in all directions (cf. Crough, 1983; Hill et al., 1992). As volcanism moved eastward, cooling and subsidence of the plateau allowed streams that had previously drained from the highland to be captured and redirected into the Snake River watershed (Link et al., 1999, 2002). Radial paleocurrent patterns in the sedimentary record are possible evidence of this migrating topographic bulge (Morgan and McIntosh, 2005; Beranek et al., 2006).

Previous workers have used the detrital zircon age populations from modern stream deposits and sedimentary rocks within the SRP region to piece together the geochronology of the Northern Rockies (Geslin et al., 1999, 2002; Link et al., 2002, 2005; Beranek et al., 2006). Detrital zircon geochronology in the SRP region (Table 6) provides evidence for migrating uplift and erosion from the Miocene to Holocene, processes associated with the passage of the North American plate over the SRP-YP hotspot since 17 Ma (Beranek et al., 2006).

Table 6: Regional Snake River Plain Detrital Zircon Populations. Modified after Beranek et al. (2006).

Detrital zircon population	Minimum age (Ma)	Maximum age (Ma)	Source regions
Yellowstone Hotspot system	0	17	Snake River Plain and Yellowstone system, north-central Nevada to northwest Wyoming (Pierce and Morgan, 1992)
Early to middle Eocene Challis Volcanic Group	42	52	South-central Idaho, north of Snake River Plain
Cretaceous Atlanta lobe of the Idaho batholith and equivalents	70	110	South-central Idaho, north of Snake River Plain; Owyhee Mtns., south of Snake River Plain
Jurassic intrusive rocks of northern Nevada	150	170	Point source in Contact pluton, Salmon Falls Ck.
Early to middle Paleozoic	330	450	Central ID thrust belt (Antler allocthon), Idaho-Wyoming thrust belt
Neoproterozoic Bannock Volcanic Member	680	720	Pocatello, Idaho area (Fanning and Link, 2004)
Pioneer Mtns. metamorphic core complex	580	800	Pioneer Mtns. metamorphic core complex (Beranek et al., 2004) recycled through Cretaceous granites, unmapped Neoproterozoic rocks
Recycled Grenville grains	950	1300	Central Idaho and Idaho-Wyoming thrust belts; Neoproterozoic to Paleozoic miogeoclinal (Gehrels, 2000; Link et al., 2005)
Syn-Belt Supergroup volcanics and A-Type Wyoming magmatism	1400	1470	Missoula and Lemhi groups (Evans et al., 2000; Link and Fanning, 2003); Wyoming anorogenic granites (Frost et al., 1993)
Non-North American grains recycled through Belt Supergroup	1500	1610	South Australia, Gawler Craton (Ross et al., 1992; Link and Fanning, 2003)
Recycled Yavapai-Mazatzal Province and southwest Montana Proterozoic grains	1600	1800	Recycled from Cretaceous sandstones, Mesoproterozoic Missoula and Lemhi Groups, Cordilleran miogeoclinal, Pennsylvanian-Permian Sun Valley Group and Albion Mtns. Core complex (Link et al., 2005)
Recycled Peace River Arch grains	1800	2000	Recycled through Ordovician sandstones and Mississippian Copper Basin Group (Smith and Gehrels, 1994; Link et al., 1999)
Archean basement	2400	2800	Exposed Archean Wyoming Province; also recycled through Cordilleran miogeoclinal (Gehrels, 2000; Link et al., 2005)

Methods

The sedimentary petrology classification of Ingersoll (1990) and Ingersoll et al. (1993) forms the basis for provenance determination of detrital zircons in sedimentary systems. Detrital zircon age-groupings are generally classified as either *defining*, *major* or *minor* (Link et al., 2005) based upon the statistical model of Vermeesch (2004). Defining populations of detrital zircons comprise over 50% of zircons in a sample, while populations that range from 10% to 50% are classified as major, and those below 10% are classified as minor (Link et al., 2005). Previous studies, i.e. Link et al. (2005), Beranek et al. (2006), have established the consistency of detrital zircon age spectra of first and second-order drainage systems with exposed bedrock at the headwaters and along the drainage. First-order sedimentary systems include talus piles to small drainages, while second-order systems include streams and rivers

that drain mountain ranges, fold and thrust belts, or magmatic arcs.

Fluvial sediment packages were identified within Kimama core in two depth intervals: an upper sequence from 1707 m to 1755 m measured depth and a lower sequence from 1841 m to 1900 m measured depth. Approximately 1 kilogram of the cleanest medium or finer-grained rock was collected from these two upward-fining sedimentary cycles. Samples were taken at 1842 m and 1844 m in the lower sequence and at 1708 m, 1733 m, and 1749 m in the upper sequence. Specimens from each depth were made into thin sections for textural and compositional evaluation. Separation methods, with the Wilfley table, heavy liquids, and Frantz magnetic separation, were conducted at Boise State University. Zircons were retained in the final heavy mineral fraction and split so that ~500-1000 grains were incorporated into a 1" epoxy mount along with fragments of zircon standards. Grain mounts were polished to a depth of ~20 microns and polished, imaged, and cleaned prior to analysis.

Approximately 100 detrital zircon grains were analyzed from each of five sediment samples using laser ablation-multicollector-inductively coupled mass spectrometry (LA-MC-ICPMS) at the Arizona LaserChron Center. The ablation of zircon grain mounts was conducted using a New Wave UP193HE Excimer laser operating at a wavelength of 193 nm, using a spot diameter of 30 microns, and with ablation pits typically ~15 microns in depth. Helium gas carried ablated material into the Nu HR ICPMS plasma source, the flight tube of which has a width sufficient to simultaneously measure U, Th and Pb. Faraday detectors with 3×10^{11} ohm resistors were used to measure isotopes of ^{238}U , ^{232}Th , ^{208}Pb - ^{206}Pb , and discrete dynode ion counters for ^{204}Pb and ^{202}Hg while in static mode. Ion yields during measurements were ~0.8 mv per ppm. Isotopic analyses consisted of one 15-second integration on peaks with the laser off in order to produce backgrounds, followed by 15 one-second integrations with the laser firing. A 30 second delay insured the purge of previous sample material, readying the laser for the next

analysis. The interference of ^{204}Hg with ^{204}Pb was corrected by measurement of ^{202}Hg during laser ablation and subsequent subtraction of ^{202}Hg in accordance to the natural $^{202}\text{Hg}/^{204}\text{Hg}$ ratio of 4.35. Most analyses demonstrated the insignificance of ^{202}Hg corrections due to their generally low backgrounds (<150 cps at mass 204).

The correction of common Pb was carried out using Hg-corrected ^{204}Pb values and the assumption that initial compositions from Stacey and Kramers (1975) were applicable. Variation in Pb isotopic compositions in modern crustal rocks were accounted for in assigning uncertainties to assumed compositions of initial $^{206}\text{Pb}/^{204}\text{Pb}$ (± 1.5) and $^{207}\text{Pb}/^{204}\text{Pb}$ (± 0.3). Initial $^{206}\text{Pb}/^{204}\text{Pb}$ uncertainties were used in determining total age uncertainties.

Isotope fractionation of Pb/U and Pb during analysis was corrected by the in-run analysis of Sri Lanka zircon standard fragments. With a known age of 563.5 ± 3.2 Ma (2σ error), Sri Lanka zircons were analyzed every fifth measurement. The inter-element fractionation of Pb/U was recognized in <5% of analyses, and apparent fractionation of Pb isotopes was recognized in <0.2% of analyses. Calibration correction uncertainty was generally 1-2% (2σ error) for $^{206}\text{Pb}/^{207}\text{Pb}$ and $^{206}\text{Pb}/^{238}\text{U}$ ages. Lastly, concentration of U and Th were calibrated using the ~518 ppm U and 68 ppm Th concentrations of the Sri Lanka zircon standard.

Resulting data are plotted in U-Pb concordia diagrams and age-probability diagrams following the routines in Isoplot software (Ludwig, 2008). Age-probability diagrams use a combination of age and measurement error uncertainty as the Gaussian distribution for each zircon grain. Distributions from all grains are summed into a single composite sample distribution. Probability plots of composite ages are made such that each curve is normalized according to the number of constituent analyses; each curve contains the same area so that probability curves may be more accurately compared.

Hf Methods

Hf isotopes were measured on the youngest, Late Miocene zircon crystals at the Arizona LaserChron Center at the University of Arizona by Nu Plasma HR-LA-ICPMS. The mass spectrometer has 12 fixed Faraday detectors that are equipped with $3 \times 10^{11} \Omega$ resistors to measure masses ^{171}Yb through ^{180}Hf for improved detection. The Lu-Hf decay system is used to understand the growth and evolution of the crust through time. Magmatic rocks, whether juvenile (mantle-derived), recycled (remelted crust), or mixed or derived from multiple sources, can be genetically identified using the behavior of the whole-rock Lu-Hf isotopic system.

Crustal-evolution models have made extensive use of the Sm-Nd isotopic system, especially in combination with age data from the U-Pb dating of zircons. Zircon is stable up to high metamorphic grade following crystallization. Non-metamict zircons resist isotopic diffusion and exchange (e.g. Cherniak et al., 1997) and contain very low concentrations of Lu/Hf. We use $^{176}\text{Hf}/^{177}\text{Hf}$ in SRP zircons to model the composition, age, and origin of the parental magma at the time of crystallization. Values of $^{176}\text{Hf}/^{177}\text{Hf}$ in zircon demonstrate the origin of magma; high values indicate juvenile melts, while low values indicate recycled crust (Amelin et al., 2000; Griffin et al., 2000; Condie et al., 2005; Harrison et al., 2005; O'Reilly et al., 2008). Epsilon units express the ratio $^{176}\text{Hf}/^{177}\text{Hf}$ in terms that relate the analyzed rock sample to bulk silicate earth (CHUR), where

$$\epsilon_{\text{Hf}}^0 = \left\{ \left[\frac{(^{176}\text{Hf}/^{177}\text{Hf})_{\text{sample}}^0}{(^{176}\text{Hf}/^{177}\text{Hf})_{\text{CHUR}}^0} - 1 \right] \times 10^4 \right\}.$$

We use ϵ_{Hf} to determine the influence of mantle material in the generation of SRP magmas.

Values for ϵ_{Hf}^0 in the present-day range from +15 to -70.

Results

U-Pb Dates of Detrital Zircons

Here we present LA-MC-ICPMS U-Pb ages and sedimentary petrology for each sample. Complete provenance details on specific detrital zircon populations are given in Table 6. Detailed age data results and thin section photographs are shown in Table 7 and Figure 22, respectively.

KZ6050

Sample KZ6050, recovered from 1844 m depth, is a medium-grained, clay-cemented grey sand with > 3 mm angular lithic fragments. In thin section, the sample shows fine-grained clay cement (20%) possibly derived from devitrified glass; subhedral angular quartz (40%); subhedral subrounded, resorbed plagioclase (30%); and subhedral to euhedral zircon, clinopyroxene, angular glass fragments, microcrystalline quartz, and lithic fragments of gneiss, chert, and volcanics (10%) (Figure 22a). Sample KZ6050 is classified as an immature feldspathic volcanic lithic arenite. Dominant detrital zircon populations from sample KZ6050 (n=65) are combined in Figure 23a. The populations include: (1) Miocene (10-6 Ma; 23 grains; 35%); (2) Eocene (51-38 Ma; 18 grains; 28%); (3) Cretaceous (95-90 Ma; 5 grains; 8%); (4) Mesoproterozoic (1563-1034 Ma; 6 grains; 9%); (5) early to middle Paleoproterozoic (1936-1638 Ma; 9 grains; 14%); (6) and Archean (3229-2730 Ma; 4 grains; 6%).

Table 7
Detrital zircon U-Pb age data for the Kimama core hole

Sample KZ6050 1846 m depth			Sample KZ6044 1842 m depth			Sample KZ5737 1749 m depth			Sample KZ5684 1732 m depth			Sample KZ5602 1704 m depth		
Grain Spot	Best age (Ma)	±	Grain Spot	Best age (Ma)	±	Grain Spot	Best age (Ma)	±	Grain Spot	Best age (Ma)	±	Grain Spot	Best age (Ma)	±
17	6.1	2.6	12	6.1	2.9	62	3.5	3.4	98	5.3	0.2	85	89.5	1.7
49	6.2	2.7	55	6.1	1.6	58	4.6	4.2	36	5.6	2.3	95	93.4	1.5
13	6.3	3.0	43	6.3	2.6	13	4.6	2.3	45	6.2	2.3	89	95.7	1.6
9	6.3	2.6	64	6.4	1.7	49	4.8	2.7	93	22.1	0.9	70	95.8	1.4
63	6.4	1.5	30	6.7	1.0	23	5.0	4.7	86	26.8	3.9	53	97.8	2.3
1	6.4	2.0	31	8.7	2.4	71	5.0	2.3	58	33.1	4.7	39	99.9	9.3
54	6.6	3.0	15	11.6	4.0	78	5.0	3.9	56	34.8	2.9	13	100.8	4.2
8	6.9	1.2	1	42.0	4.7	46	5.0	3.4	66	46.6	2.0	72	100.9	2.8
55	6.9	3.1	84	44.0	2.6	97	5.1	4.8	47	46.8	1.6	80	165.7	2.4
44	7.0	3.0	39	44.1	4.3	75	5.2	4.1	91	48.4	2.1	3	388.7	7.5
51	7.1	0.4	52	45.3	1.5	52	5.2	5.2	48	48.6	3.3	38	409.1	3.3
28	7.3	3.4	86	45.3	2.3	95	5.5	1.5	18	48.6	3.7	97	416.6	7.2
42	7.3	1.3	65	45.3	3.2	77	5.6	4.3	61	49.0	2.9	44	417.3	6.5
29	7.4	0.3	20	45.5	1.8	3	5.6	2.7	77	49.0	1.6	49	418.9	6.1
56	7.5	0.6	27	46.0	2.1	40	5.8	1.8	83	49.3	3.9	2	419.1	2.8
22	8.0	2.8	14	46.1	1.2	20	5.9	2.9	26	49.4	2.3	30	430.5	7.3
31	8.1	2.4	37	46.1	1.4	55	6.0	5.9	52	51.2	5.6	65	437.3	16.7
50	8.2	3.7	38	46.2	3.2	54	6.0	4.3	54	67.5	8.3	75	439.2	5.9
61	8.3	2.9	5	46.3	3.2	33	6.1	4.7	25	92.6	4.7	98	500.8	6.1
16	8.9	3.0	24	46.3	2.0	4	6.1	2.6	76	94.6	1.7	100	609.1	10.1
34	9.0	4.0	70	46.4	1.9	8	6.1	4.4	91	95.8	2.1	6	992.3	56.4
5	9.1	4.4	6	46.5	1.8	74	6.2	2.5	88	95.9	2.1	23	1006.9	48.2
65	10.2	3.2	21	46.6	3.0	11	6.2	3.3	59	96.4	2.0	43	1010.1	18.9
67	38.3	1.0	13	46.7	3.5	80	6.3	2.4	51	98.4	1.6	73	1019.5	84.6
14	41.4	2.1	80	46.8	2.5	50	6.3	0.9	44	99.4	1.7	25	1027.5	119.9
15	46.9	5.6	73	46.8	2.3	94	6.4	0.4	27	99.5	2.1	19	1050.1	98.0
23	47.7	1.6	71	46.9	2.1	19	6.4	5.3	96	99.9	3.6	83	1055.4	49.2
7	47.8	1.6	78	47.0	2.7	66	6.4	0.8	84	101.4	5.5	24	1064.9	49.5
26	48.0	1.3	89	47.0	1.4	88	6.5	2.0	24	102.7	2.8	40	1066.7	32.6
64	48.1	1.3	44	47.0	1.7	43	6.5	1.9	90	103.4	2.1	31	1068.8	43.1
19	48.4	1.6	7	47.0	4.4	92	6.6	1.4	46	109.2	2.7	92	1070.4	11.5
6	48.4	2.7	81	47.1	2.7	6	6.6	1.0	99	134.6	10.2	33	1070.5	66.6
25	48.8	1.8	63	47.1	2.4	1	6.7	1.8	62	155.8	2.8	62	1075.0	23.9
60	49.2	1.6	25	47.2	1.2	86	6.7	3.6	100	168.1	3.8	63	1095.7	40.7
33	49.3	1.4	67	47.5	2.9	89	6.7	3.7	95	249.1	4.4	34	1102.3	195.5
41	49.4	2.7	49	47.7	1.9	36	6.7	4.3	53	352.3	6.3	50	1109.0	64.6
40	49.5	1.2	41	47.8	3.8	79	6.9	1.7	1	429.6	6.0	51	1152.8	182.8
66	49.6	1.4	46	47.8	2.7	21	6.9	1.4	75	445.6	15.2	22	1186.9	81.0
58	49.8	1.9	3	48.0	1.7	60	7.0	2.2	33	465.4	9.3	10	1187.9	5.8
18	49.8	1.3	32	48.1	1.8	31	7.2	1.2	69	499.3	7.0	86	1201.9	14.0
38	50.9	3.8	61	48.2	1.0	25	7.3	5.1	9	570.0	10.4	8	1209.6	8.3
21	89.5	1.1	17	48.2	1.6	61	7.4	6.4	39	682.9	8.2	15	1222.5	19.0
47	91.9	1.6	47	48.2	3.1	9	7.5	4.5	19	1024.7	22.9	61	1240.3	26.6
46	94.5	5.9	18	48.2	2.8	42	7.5	2.6	17	1028.5	11.1	84	1341.5	11.2
52	94.8	1.0	68	48.4	3.7	99	7.7	5.4	4	1037.6	45.5	48	1408.0	12.2
27	95.0	6.3	91	48.5	1.8	98	7.8	0.5	38	1087.6	78.3	59	1428.5	33.0
45	1034.2	18.0	92	48.6	3.0	38	7.8	3.1	71	1089.6	80.7	76	1470.0	105.0
12	1131.0	13.0	48	48.6	1.7	57	7.8	6.4	74	1090.0	62.9	14	1480.2	22.6
24	1181.9	16.6	66	48.8	1.2	41	8.0	0.8	85	1097.9	34.7	69	1492.6	8.0
10	1428.4	35.6	58	48.9	1.3	44	8.1	4.7	22	1110.3	102.4	99	1502.3	14.4

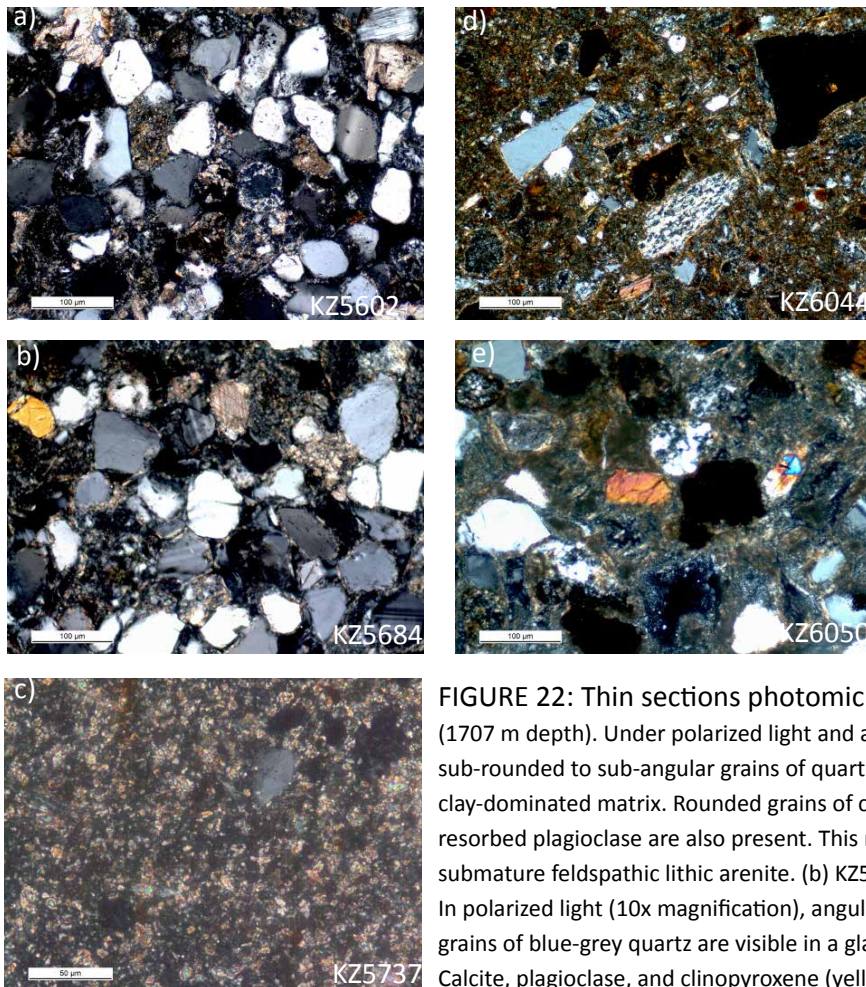


FIGURE 22: Thin sections photomicrographs. (a) KZ5602 (1707 m depth). Under polarized light and at 10x magnification, sub-rounded to sub-angular grains of quartz are visible in a clay-dominated matrix. Rounded grains of calcite and partially resorbed plagioclase are also present. This rock is classified as a submature feldspathic lithic arenite. (b) KZ5684 (1733 m depth). In polarized light (10x magnification), angular to sub-angular grains of blue-grey quartz are visible in a glassy-clay matrix. Calcite, plagioclase, and clinopyroxene (yellow) are present in lesser amounts. This rock is classified as a submature feldspathic volcanic lithic arenite. (c) Thin section of sample KZ5737 (1749 m depth). Very fine-grained clay is visible under 44x magnification and polarized light. Although rare, most mineral grains are subhedral to anhedral, and there is some evidence of clay pseudomorphs after plagioclase due to secondary alteration. Additionally, isotropic glass in the sample appears to be altering to clay. The image is representative of the sample, with clay-dominated matrix and a scarcity of mineral grains and lithic fragments; imaged is grey, sub-angular subhedral quartz with ragged margins and black glass fragments. The rock sample is classified as a mudstone. (d) KZ6044 (1842 m depth). Under polarized light and 10x magnification, angular fragments of isotropic glass, sub-angular to angular grey-white quartz, and sub-angular lithic fragments of metamorphosed rocks are visible. Minor amounts of subhedral resorbed plagioclase, and mm to sub-mm lithics and glass fragments are also present. The sample is dominated by fine-grained, oxidized clay matrix. The rock sample is classified as a volcanic lithic wacke. (e) KZ6050 (1844 m depth). In polarized light and under 10x magnification, the sample is dominated by angular to sub-angular grey to white quartz and black angular glass fragments. Minor grains of angular brown clinopyroxene, sub-rounded and partially resorbed plagioclase, rounded calcite, and a fine-grained clay matrix are also observed in the sample. This sample is classified as an immature feldspathic volcanic lithic arenite.

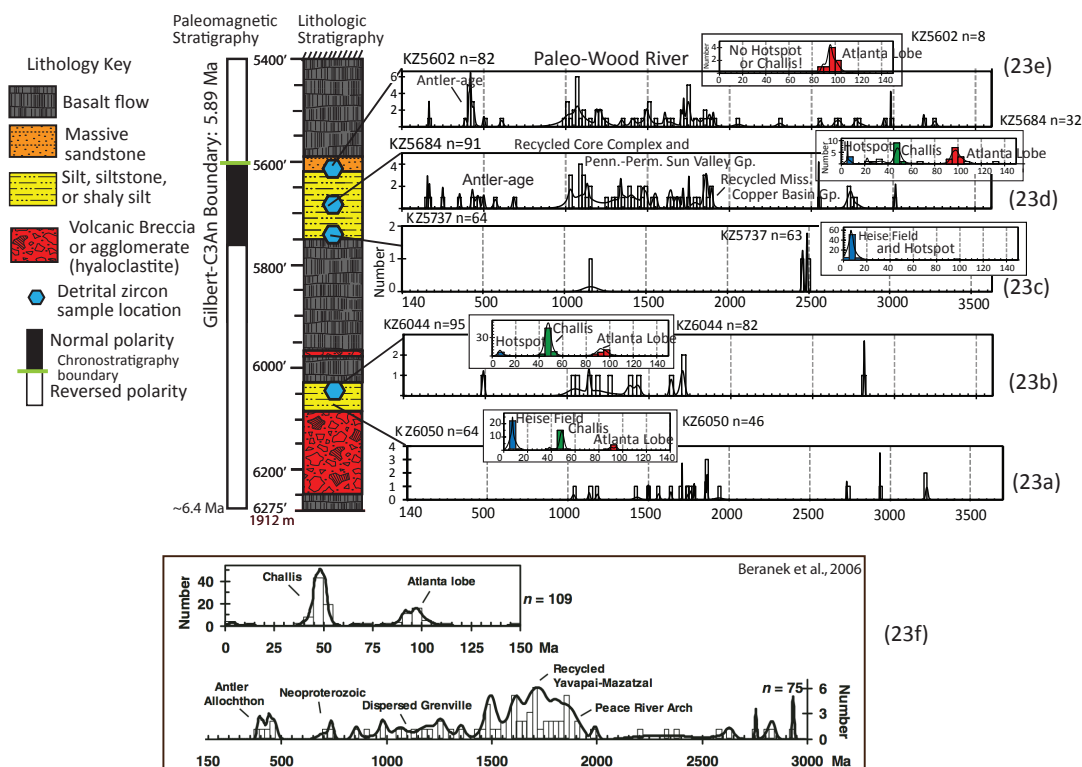


Figure 23: Paleomagnetic and lithologic stratigraphy of the Kimama core showing locations of sampled intervals and detrital zircon age populations. Histograms, overlain by probability-density curves (figures 23a-23e), show detrital zircon age spectra and probable source provenance (after Link et al., 2005 and Beranek et al., 2006). Plots are shown for 0 to 150 Ma and 0 to 3500 Ma grains. Two upward-fining interbeds are recognized from 1749 to 1707 m depth and from 1844 to 1842 m depth. Each interbed changes upward from mainly Heise field Miocene zircons to Paleozoic and Proterozoic zircons derived the paleo- Wood River drainage. Figure 23f: Histogram with superimposed relative probability curve of modern Wood River stream sediment detrital zircon age data (From Beranek et al., 2006).

KZ6044

Sample KZ6044, recovered from 1842 m depth, is fine to medium grained tan oxidized sand with clay cement and angular < 5mm lithic fragments. In thin section, the sample is cemented with fine-grained clay with iron-oxide staining (70%); and contains rounded to angular quartz (10%); subhedral, resorbed plagioclase (15%); and mm to sub-mm lithics and glass fragments (5%) (Figure 22b). Sample KZ6044 is classified as a volcanic lithic wacke. Grain-age populations from sample KZ6044 (n=95) include: (1) Miocene (11.6-6.1 Ma; 7 grains; 7%); (2)

Eocene (53-42 Ma; 55 grains; 58%); (3) Cretaceous (100-85 Ma; 20 grains; 21%); (4) late Silurian to early Ordovician (488-433 Ma; 2 grains; 2%); and (5) early Mesoproterozoic to early Paleoproterozoic (1707-1044 Ma; 10 grains; 11%) (Figure 23b).

KZ5737

Sample KZ5737 was recovered from 1749 m depth, and is a very fine-grained, brick-red laminated oxidized siltstone with clay cement. In thin section, the sample is very fine-grained clay (95%), with minor subhedral angular quartz (5%) (Figure 22c). This particular sample is classified as a mudstone. Detrital zircon age populations (n=66) from sample KZ5737 are combined in Figure 23c. The populations include: (1) Miocene (11-4 Ma; 59 grains; 89%); Cretaceous (125-98 Ma; 3 grains; 5%); and Mesoproterozoic to Paleoproterozoic (2490-1160; 3 grains; 5%).

KZ5687

Sample KZ5687, recovered from a depth of 1733 m, is coarse to medium-grained sand, showing normal gradation of grains and lithic fragments and cemented by clay. In thin section, the sample is made up of fine-grain and clay cement (20%); subhedral to angular quartz (40%); subrounded to angular subhedral plagioclase (35%); subhedral to euhedral zircon, plagioclase, and lithics (5%)(Figure 22d). KZ5687 is classified as a submature feldspathic volcanic lithic arenite. The following detrital zircon populations were observed in sample KZ5687 (n = 89; Figure 23d: (1) Miocene (22-5 Ma; 4 grains, 4%); (2) Eocene (51-33 Ma; 11 grains; 12%); Cretaceous (135-93 Ma; 14 grains; 16%); Devonian-Cambrian (570-352 Ma; 6 grains; 7%); Neoproterozoic to early Mesoproterozoic (1150-683 Ma; 14 grains; 16%); middle

Mesoproterozoic to late Mesoproterozoic (1550.9-1253.8 Ma; 16 grains; 18%); Paleoproterozoic (1892-1620 Ma; 14 grains; 16%); and Archean (2771-2545; 4 grains; 4%).

KZ5602

Sample KZ5602, recovered from a depth of 1707 m, is a medium-grained lithic sandstone with clay cement. Thin section observations show it to be a submature feldspathic lithic arenite, with fine-grained clay cement (20%); subhedral angular quartz (40%); resorbed, sub-rounded plagioclase (30%); and subhedral to euhedral zircon, clinopyroxene and lithics (10%)(Figure 22e). Dominant detrital zircon populations (n=82) from KZ5602 are combined in Figure 23e. The populations do not include any Paleogene or Neogene grains and are (1) Cretaceous (104-88 Ma; 8 grains; 10%); (2) Devonian-Ordovician (445-380 Ma; 9 grains; 10%); (3) Neoproterozoic to early Mesoproterozoic (1202-600 Ma; 22 grains; 25%); middle to late Mesoproterozoic (1605-1210 Ma; 13 grains; 15%); Paleoproterozoic (2554-1627 Ma; 20 grains; 23%); and Archean (3252-2647 Ma; 8 grains; 9%).

Neogene Grains

In the two lowermost fluvial successions, a large percentage of the grains are bladed, euhedral, and angular zircons with Neogene U-Pb ages (Figure 24). In order to trace the origin of these magmatic grains, additional U-Pb ages were collected and Lu-Hf isotope ratios were measured in samples KZ5737 (1749 m depth) and KZ6050 (1844 m depth) using Nu Plasma HR MC-ICPMS at the Arizona LaserChron Center. The instrument is optimized for analysis of U-Th-Pb and Hf isotopes, and contains 12 faraday collectors arranged to measure ^{238}U , ^{232}Th , and

180-171 (for Hf, Lu, and Yb). Epsilon Hf and high precision U-Pb results are shown in Table 8 (U-Pb and Hf isotopic data).

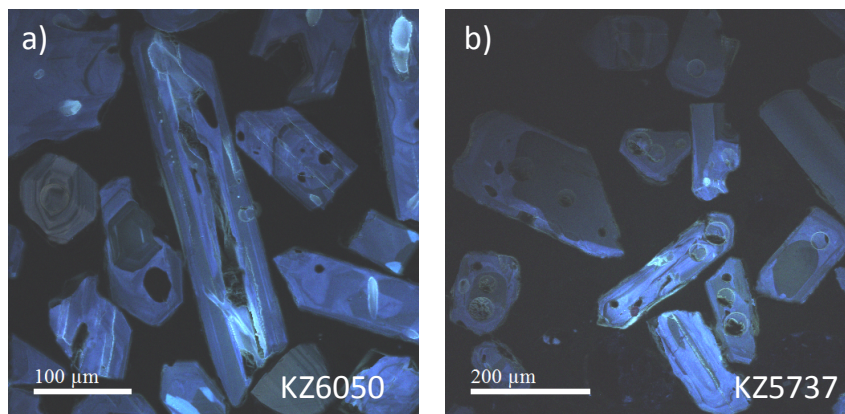


Figure 24: Cathodoluminescence (CL) image of detrital zircons mounted in grain mounts. (a) KZ5737 (1749 m depth). Grains are euhedral, angular, and bladed, suggesting a more recent volcanic origin. Internal concentric zonation is also present. Spot locations for laser ablation (LA) Nu plasma high-resolution multi-collector inductively-coupled plasma mass spectrometry (HR-MC-ICPMS) are visible as circular craters in the core and margin regions of the grains. (b) KZ6050 (1850 m depth). Grains are euhedral, angular, and bladed, suggesting a more recent volcanic origin. Internal concentric zonation is also present. Spot locations for LA-HR-MC-ICPMS are visible as circular craters in the core and margin regions of the grains.

KZ6050

Sample KZ6050 (Figure 24a) higher resolution U-Pb measurements of grains in sample KZ6050 yielded ages that range from 6.2 ± 0.1 Ma to 7.4 ± 0.3 Ma (Table 8). The ϵ_{Hf} in sample KZ6050 ranges from -5.1 in a 6.9 ± 0.2 Ma grain, to -9.7 in a 6.7 ± 0.2 Ma grain. The oldest and youngest grains have ϵ_{Hf} of -6.4 and -7.6, respectively. Most grains have ϵ_{Hf} of -7.6. Ages for the Neogene grains recovered from 1749 m and 1844 m depth fall into four main statistical populations: 5.84 ± 0.13 Ma, 6.2 ± 0.08 Ma, 6.86 ± 0.09 Ma, and 7.25 ± 0.14 Ma (Figure 25).

Table 8: U-Pb and Hf isotopic data for sample KZ5737, 1749 m depth, and for KZ6050, 1844 m depth.

Sample	Grain Spot	Best age (Ma)	\pm (Ma)	E-Hf (T)
KZ5737	71	5.7	0.1	-3.3
KZ5737	95	5.8	0.4	---
KZ5737	46	5.8	0.1	-5.8
KZ5737	8	5.9	0.5	---
KZ5737	103	5.9	0.5	---
KZ5737	97	5.9	0.1	-2.7
KZ5737	11	5.9	0.3	---
KZ5737	102	6.0	0.2	-7.1
KZ5737	52	6.1	0.2	-2.0
KZ5737	77	6.1	0.1	-2.8
KZ5737	33	6.3	0.1	-2.5
KZ5737	3	6.3	0.1	-4.0
KZ5737	54	6.3	0.2	-4.0
KZ5737	62	6.5	0.1	-5.6
KZ5737	74	6.8	0.1	-6.3
KZ5737	60	6.8	0.2	-5.9
KZ5737	4	6.8	0.1	-5.8
KZ5737	79	6.9	0.3	---
KZ5737	80	7.3	0.8	---
KZ5737	78	7.6	0.2	-4.3
KZ6050	101	6.2	0.1	-7.6
KZ6050	93	6.2	0.0	-9.3
KZ6050	10	6.7	0.2	-9.7
KZ6050	103	6.9	0.2	-5.1
KZ6050	13	7.0	0.1	-7.0
KZ6050	80	7.0	0.1	-9.0
KZ6050	104	7.1	0.2	-6.7
KZ6050	41	7.1	0.1	-9.1
KZ6050	65	7.2	0.1	-6.1
KZ6050	102	7.2	0.4	-6.6
KZ6050	105	7.3	0.1	-8.3
KZ6050	58	7.4	0.3	-6.4

KZ5737

Sample KZ5737 (Figure 24b) the second measurement of ages from sample KZ5737

yielded ages that range from 5.7 ± 0.1 Ma to 7.6 ± 0.2 Ma (Table 8). Epsilon Hf ranges from -3.3

in the youngest (5.7 Ma) sample to -7.0 in a sample with a measured age of 6.0 ± 0.1 Ma. The oldest measured grain (7.6 ± 0.2 Ma) has a corresponding ϵ_{Hf} of -4.3.

Discussion

Robust detrital zircon provenance studies require a point source—an origin that is characterized by a specific age and geologic framework. Provenance signature changes with distance from the headwaters of second-order systems as major tributaries join the main stem (Link et al., 2005). Large river and marine systems are classified as third-order systems and have uniform provenance; they are the only reliable predictors of plate tectonic setting (Ingersoll et al., 1993; Critelli et al., 1997).

The modeled response of continental lithosphere to plume impact is large-scale uplift, a process complicated by the multilayered (elastic-brittle-ductile) nature of the lithosphere (Burov and Guillou-Frottier, 2005; Burov et al., 2007). Central uplift over the plume head may be accompanied by the formation of an annulus of lower elevation (e.g. Burov and Guillou-Frottier, 2005; Burov et al., 2007), that may accommodate future basalt eruptions (Shervais et al., 2006).

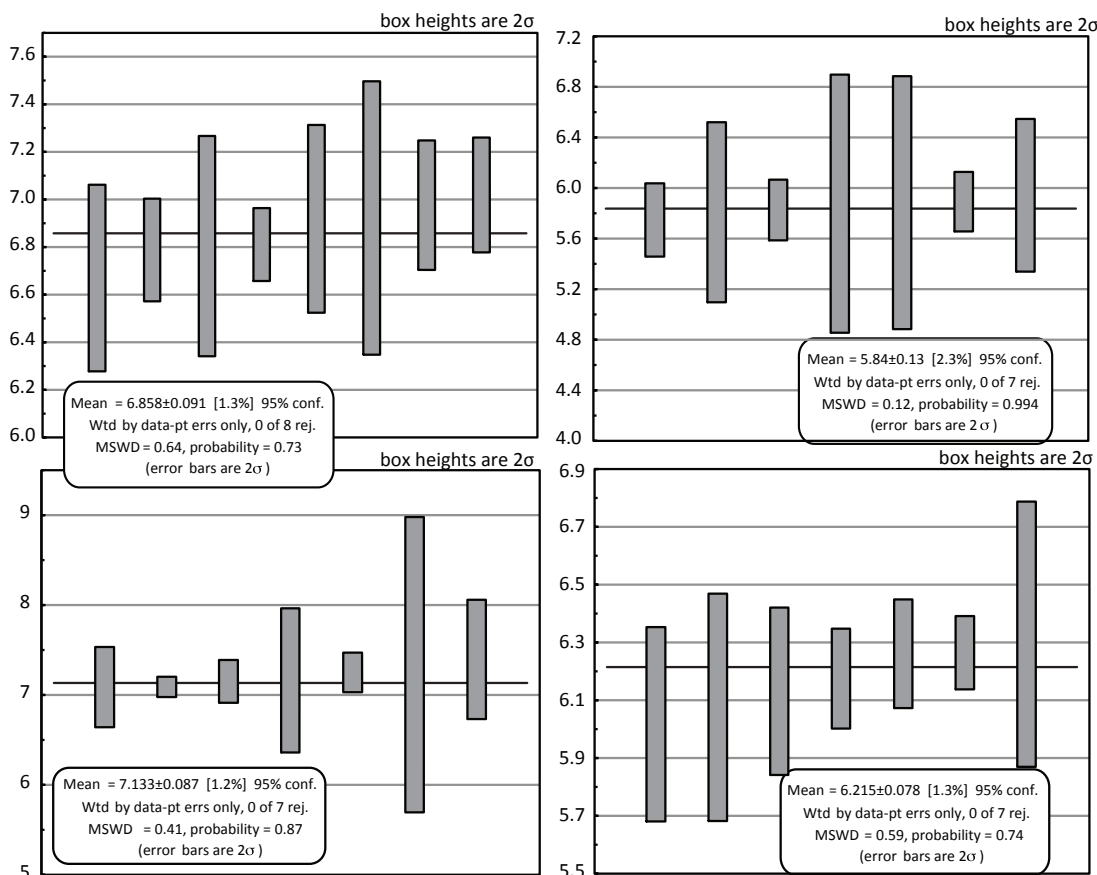


FIGURE 25: Bar graphs of U-Pb ages for samples KZ5737 and KZ6050 (1749 and 1850 m depth, respectively). Each plot shows averages obtained from a combination of KZ5737 and KZ6050 volcanic zircon ages. Ages were obtained using Nu plasma HR-MC-ICPMS during a secondary analysis of Kimama Neogene grains at the Arizona LaserChron laboratory. The four plots generate age means of 5.84 ± 0.13 Ma, 6.215 ± 0.78 Ma, 6.858 ± 0.091 Ma, and 7.133 ± 0.087 Ma.

Basin and Range extensional basins to the north and south of the SRP accommodate multiple river drainages, many with unique geology (Ore, 1999). Geological characteristics of several drainage systems in the SRP region generate distinct detrital zircon age population spectra, or barcodes, that are traceable in fluvial sands (Link et al., 2005). In particular, populations of detrital zircon grains record ages that are characteristic of their drainage basin source. Within fluvial systems, the presence of minor defining populations of similarly-aged

detrital zircons (5 to 10% of total population) is a consistent indicator of provenance. In situations where populations of detrital zircons are less than 60 zircon grains per sample, provenance may be indicated by the absence of a specific detrital zircon population (Dickinson and Gehrels, 2008; Hodges et al., 2009).

Provenance of Zircon Grains

The lower parts of each sandstone bed sequence contain mainly Miocene detrital zircons of the Yellowstone-Snake River Plain (YSRP) magmatic system (10 to 5 Ma), and Archean to Paleoproterozoic 2.6 and 2.1 Ga zircon grains. We interpret the Archean and Paleoproterozoic grains to be inherited based upon observations of complex zonation and the lack of a likely geological point source in the region. Sands at 1732 m contain zircon groupings representing the Challis magmatic event (50 to 45 Ma), Idaho batholith (100 to 90 Ma), recycled Paleozoic magmatic grains, plus recycled Grenvillian and Meso- and Paleoproterozoic grains. Sands at 1707 m depth lack Yellowstone and Challis-age grains but contain very similar populations of Cretaceous through Meso- and Paleoproterozoic grains to sample KZ5684.

We interpret the absence of detrital zircon barcodes from regions south of the SRP and the predominance of Atlanta and Challis-aged grains to signify a drainage source north of the SRP. Based upon characteristic detrital zircon barcodes (Figure 23), we interpret the interbeds to represent two incursions of the Wood River system (Link et al., 2005; Beranek et al., 2006). Each fluvial succession systematically changes upward from dominantly hotspot zircons to mainly detrital grains. Our findings agree with Hodges et al. (2009), who showed that ca. 695 Ma detrital zircon grains derived from the Pioneer core complex were deposited in the central Snake River plain by the earliest Pliocene, indicating eastern SRP subsidence by that time.

Variable Archean and Proterozoic populations in the upper interbed suggest a paleo-Wood River tributary that tapped the structurally uplifted Pioneer core complex. U-Th/He apatite ages from the Pioneer Core Complex show evidence for rapid exhumation since 33 Ma, with a rate of ~ 0.3 km/my. Thermochronology also documents an extensional exhumation event at ~ 10 Ma (Vogl et al., 2014). The 5.8 Ma estimated age of the upper interbed suggests unroofing of the Pioneer core and breaching of the Wildhorse detachment occurred by that time. The absence of Challis grains in the uppermost sample requires either localized, large-scale erosion or a drainage source west of the Pioneer core complex, where Challis volcanic units have been largely eroded (Vogl et al., 2014).

Rivers and Core Complex

The Wood River System is classified as a second-order system (Link et al., 2005) and includes the Big Wood River, the Little Wood River, Trail Creek, and the headwaters of the Salmon River (Beranek et al., 2006). The Big Wood River drains from the headwaters of the Salmon River along the western slope of the Pioneer Mountains core complex, where it incises the Wood River and Milligen Formations along the Wood River thrust (Hall et al., 1978; Dover, 1983; Link et al., 2005). The barcode-defining detrital zircon grains in the Wood River System are Challis (~ 52 - 42 Ma peak), followed by grains from the Cretaceous Atlanta Lobe of the Idaho batholith (~ 100 - 70 Ma peak), and Miocene grains (~ 8 - 12) (Link et al., 2005; Beranek et al., 2006). Small populations of Paleozoic and Proterozoic populations also are present within Big Wood River detrital zircon grain samples, including Ordovician to Devonian (ca. 450-350 Ma), early Neoproterozoic to middle Mesoproterozoic (1300-900 Ma), late Mesoproterozoic (1610-1580 Ma), late to middle Paleoproterozoic (1800-1600 Ma), early Paleoproterozoic (2000-1800 Ma), and early Paleoproterozoic to Archean (2200-2900 Ma). Miocene grains are absent from

the Big Wood River as sampled upstream from the ~5 Ma Magic Volcanic complex (Figure 23f) (Honjo et al., 1986; Worl et al., 1991; Kuntz et al., 1994; Link et al., 2005).

The Little Wood River, with headwaters in the Pioneer Mountains, accumulates zircons from the Antler allochthon, the Wood River basin, and the Pioneer core complex (Worl et al., 1991; Kuntz et al., 1994; Link et al., 1994). Collectively, the Wood River System drains the Cretaceous Atlanta lobe of the Idaho Batholith, the early to middle Eocene Challis Volcanic Group (Johnson et al., 1988; Worl and Johnson, 1995), Paleozoic rocks of the Cordilleran eastern and western assemblages of the central Idaho thrust belt (Dover, 1980; Turner and Otto, 1988; Rodgers et al., 1995), and westerly-sourced siliciclastic rocks of the Antler foreland flysch in the Mississippian Copper Basin Group (mainly Ordovician quartzite source) and the Pennsylvanian-Permian Wood River Group (Laurentian source) (Mahoney et al., 1991; Link and Rodgers, 1995; Link et al., 1996; Geslin, 1998). The system also drains the Pioneer Mountains metamorphic core complex, an early to middle Cenozoic extensional province that exposes Paleoproterozoic to Neoproterozoic crystalline basement (Wust and Link, 1988; Burton and Link, 1995; Beranek et al., 2006).

The Little Wood River contains Miocene detrital zircon grains from ~8-12 Ma Idavada and ~6-10 Ma Yellowstone Hotspot volcanism. Detrital zircons are recycled through Paleozoic rocks of the Cordilleran passive margin, as indicated by the large presence of Proterozoic (1300-950 Ma; 1800-1600 Ma; 2000-1800 Ma) populations (Beranek et al., 2006).

The Pioneer Mountains core complex is located ~15 km to the north of the Kimama corehole in the Lost River Range of central Idaho, at the northwest boundary of the Miocene Basin and Range province, the eastern boundary of the Atlanta lobe of the Idaho batholith, and at the headwaters of the Wood River system. The Pioneer Mountains show evidence of Mesozoic synkinematic plutonism and Paleogene extensional movement along the Wildhorse

detachment system, which includes the Wildhorse thrust and a portion of the Pioneer thrust system (Dover, 1983; Wust and Link, 1988). Cooling ages from $^{40}\text{Ar}/^{39}\text{Ar}$, U-Pb, and U-Th/He data show evidence for very slow cooling since 33 Ma, with an average rate of $<5^\circ\text{C}/\text{Ma}$. U-Th/He apatite ages document an extensional exhumation event at ~ 10 Ma and suggest an exhumation rate of ~ 0.3 km/Ma (Vogl et al., 2014). It appears that volcanism, extension, and exhumation were widespread during the period over which the Pioneer core complex was exhumed (11-8 Ma) (Clemens, 2003; Bonnicksen et al., 2008; Vogl et al., 2014). Prior to core complex exhumation, the Challis magmatic event (51-43 Ma) and the intrusion(s) of the Atlanta lobe (83-67 Ma), both in response to widespread extension, modified the western border of the Pioneer core complex (Gaschnig et al., 2010).

The Wildhorse detachment system separates the metamorphosed Precambrian lower plate (core) from the unmetamorphosed Paleozoic rocks of the upper plate (Pavlis and O'Neill, 1985, 1987; Wust and Link, 1988). The core contains Ordovician to Archean orthogneisses and paragneisses that were intruded by granitic melts at 50-70 Ma (Vogl et al., 2012). Within the upper plate of the Pioneer core complex, the Pioneer thrust plate contains of mostly unmetamorphosed Paleozoic units that have been proposed to be equivalent to "western or oceanic assemblage" Antler belt sequences exposed in Nevada (Wust and Link, 1988).

Volcanogenic Zircon Grains

A large number of the detrital zircon grains represent Neogene primary magmatic zircons formed during eruptions of rhyolite ash from the YSRP magmatic system (Figure 26). Four U-Pb age populations of volcanic zircons are observed: 7.1 Ma, 6.7 Ma, 6.2 Ma, and 5.8 Ma (Figure 25). The fresh, rod- and blade grains, with minimal rounding, suggest a primary fallout

origin. Rounded Heise volcanogenic grains would imply fluvial transport over an approximate distance of 150 km to the Kimama site (Figure 26). The ages of volcanic zircon grains in the Kimama core are coincident with eruptive events from the Heise volcanic center (Table 8) (Anders et al., 2009).

Table 9: U-Pb ages of Heise volcanic field eruptive units and volcanic detrital zircons of the Kimama core. Eruptive unit ages from Anders et al. (2009).

Source	Age (Ma)
Kimama Core	5.84 ± 0.13
Tuff of Wolverine Creek	5.84 ± 0.03
Kimama Core	6.22 ± 0.078
Walcott Tuff	6.23 ± 0.01
Kimama Core	6.86 ± 0.091
Tuff of Edie School	6.61 ± 0.01
Kimama Core	7.25 ± 0.014
VPT-1 tephra of Grand Valley	7.27 ± 0.03

We interpret that volcanogenic detrital zircons to have been ejected during caldera eruptions in the Heise volcanic field, transported westward by aeolian or fluvial processes, and deposited at the base of fluvial sands in the Kimama drill hole. Thin sections (Figure 22) obtained from fluvial sands demonstrate immature textures and extensive devitrification of glass, indicative of minimal transport distance and rapid burial. The youngest zircon grains match the projected age of the core derived from accumulation rate alone, so that depositional lag time must have been substantially less than 100 k.y. after eruption. Therefore, the age of the interbeds approximates the age of youngest zircons in each unit, 5.8 ± 0.1 Ma at 1749 m depth and 6.2 ± 0.1 Ma at 1844 m depth (Potter et al., 2013).

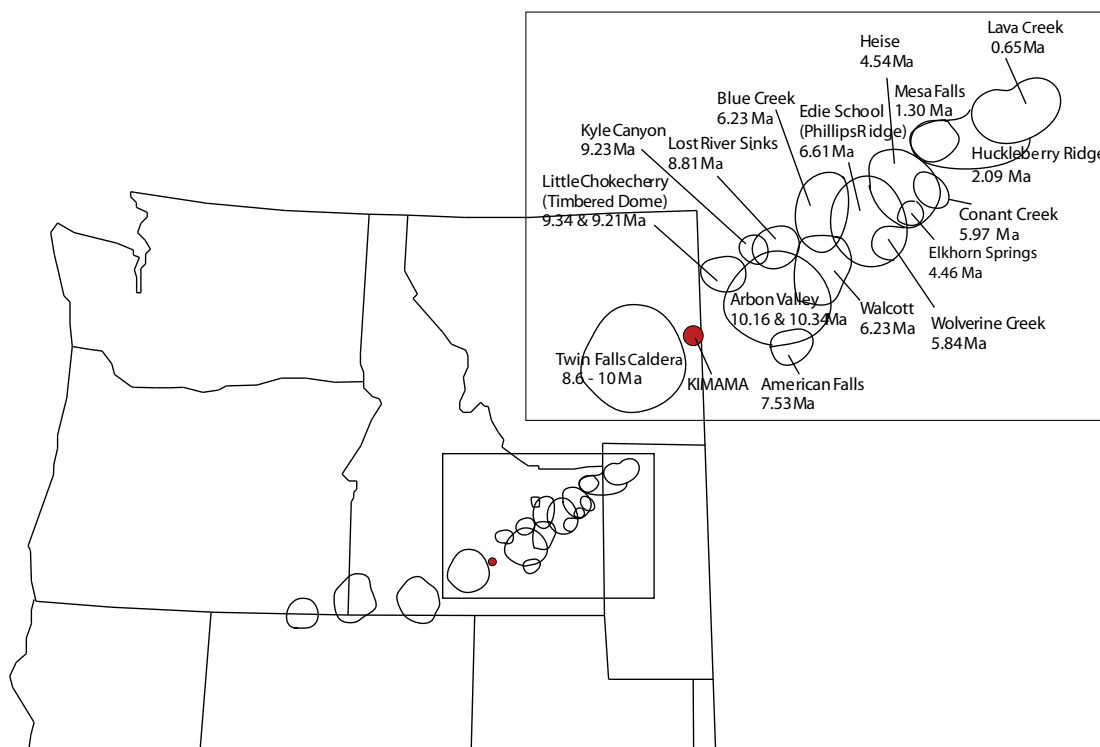


Figure 26: Location map of Snake River Plain-Yellowstone eruptive centers. Caldera and volcanic center locations are modified from Christiansen (1982) and Perkins et al. (1995). The location of the Kimama site is marked by the red circle. Lanphere et al. (2002) obtained the three youngest $^{40}\text{Ar}/^{39}\text{Ar}$ ages from corrections based on Renne et al. (1998). Unit ages older than 2.09 Ma and younger than 10.35 Ma are measured $^{40}\text{Ar}/^{39}\text{Ar}$ ages from the Lamont-Doherty Earth Observatory argon laboratory (modified from Anders et al., 2009).

The Hf isotopic compositions of hotspot zircons vary from ϵHf of -7.3 to -3.9, and the variation is highly correlated with age: volcanogenic zircons with ages of 7.1, 6.7, 6.2, and 5.8 Ma have corresponding Hf of -7.3, -6.4, -4.9, -3.9 (Table 8, Figure 27). This progressive increase in ϵHf in the younger zircons indicates an increase in mantle-derived Hf through time, evidence for greater mantle input in younger volcanics. Although the continental lithosphere thickens to the east, the continued action of the SRP-Yellowstone plume is thought to have structurally eroded and chemically modified the overlying lithosphere (e.g. Shervais and Hanan, 2008). We

propose that increasingly mantle-like ϵHf signatures in young zircons reveal the continued action of a thermally and chemically buoyant mantle plume that has etched a channel into cratonic lithosphere (i.e. Shervais and Hanan, 2008).

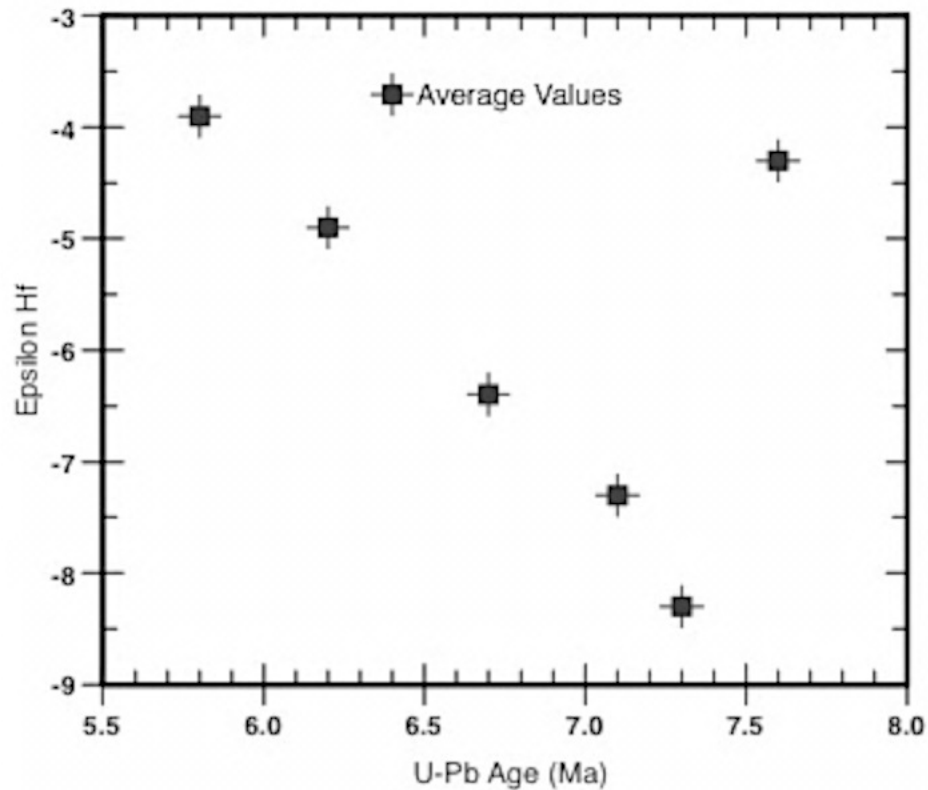


Figure 27: Plot of average values ϵHf plotted against average values U-Pb age (Ma). A negative correlation between ϵHf and U-Pb age is especially apparent in the lower plot. A progressive increase in ϵHf in the younger zircons indicates an increase in mantle-derived Hf through time, signifying that Kimama basalts have become more mantle-like in more recent SRP mafic volcanism.

The top of the upper succession contains the only significant population of Paleozoic grains within the Kimama core and lacks Eocene Challis grains. We suggest that after 5.8 Ma, the source of the paleo-Wood River system shifted westward to west of the Pioneer thrust fault.

After 5.6 Ma, basaltic volcanism along the Axial Volcanic Zone (AVZ) diverted the paleo-Wood River system southward to the reach the Hagerman area between 3.8 and 3 Ma.

Yellowstone-SRP volcanism from 10 Ma to 5 Ma in the central SRP is broadly coeval with exhumation and breaching of the Pioneer core complex and development of the Wood River System. U-Pb age data of detrital zircons in the Kimama core record volcanic events as young as 5.8 Ma superimposed upon an active extensional system. Although the 10.44-6.62 Ma Picabo volcanic center (Drew et al., 2013) was active immediately prior to the deposition of Kimama basalts, volcanic zircons from the Heise volcanic center, further east of Picabo, are the only identified Neogene population. We propose that the conspicuous absence of volcanic zircon grains derived from the Picabo volcanic complex is explained by rapid erosion and deposition of volcanic zircons derived from eruptions of the Heise volcanic center, evidence for which are angular and bladed grains, and their rapid, <100 k.y. burial by basalt flows. If mechanisms of ash eruption and transport were similar throughout the 10 Ma history of silicic volcanism, it is presumed that ash derived from Picabo volcanic eruptions had been largely eroded and deposited prior to eruptions of Heise ignimbrites.

Conclusion

Our new data on fluvial-derived volcanic and detrital zircons from the Kimama drill hole from Project Hotspot suggest: 1) Neogene volcanic activity in the Heise volcanic center began as early as 7.3 Ma, 2) Yellowstone-Snake River Plain volcanism coincided with the unroofing of the Pioneer core complex as early as 10 Ma, and 3) the Wood River System originally flowed south and east into the central SRP before being smothered and diverted southwestward by recurrent

volcanism from the AVZ. The lower fluvial sands in the Kimama core record fallout deposits of Heise ash. An upward increase in Proterozoic grains signals two incursions of the paleo Wood River System. The ash was rapidly buried by fluvial deposits of distal sands derived from the unroofing of the Pioneer and Smoky mountains to the north.

References

- Amelin, Y., Lee, D.C., and Halliday, A.N., 2000, Early-middle Archaean crustal evolution deduced from Lu-Hf and U-Pb isotopic studies of single zircon grains, *Geochimica et Cosmochimica Acta*, v. 64, p. 4205-4225.
- Anders, M.H., Saltzman, J., and Hemming, S.R., 2009, Neogene tephra correlations in eastern Idaho and Wyoming Yellowstone for hotspot-related volcanism and tectonic activity: *Geological Society of America Bulletin* v. 121, p. 837–856.
- Armstrong, R.L., 1982, Cordilleran metamorphic core complexes—From Arizona to southern Canada: *Annual Review of Earth and Planetary Sciences*, v. 10, p. 129-154.
- Armstrong, R.L., Taubeneck, W.H., and Hales, P.O., 1977, Rb-Sr and K-Ar geochronometry of Mesozoic granitic rocks and their Sr isotopic composition, Oregon, Washington, and Idaho: *Geological Society of America Bulletin*, v. 88, p. 397–411.
- Beranek, L.P., Link, P. K., and Fanning, C.M., 2006, Miocene to Holocene landscape evolution of the western Snake River Plain region, Idaho: Using the SHRIMP detrital zircon provenance record to track eastward migration of the Yellowstone hotspot: *GSA Bulletin*, v. 118, p. 1027-1050.
- Bonnichsen, B., Leeman, W. P., Honjo, N., McIntosh, W. C., and Godchaux, M. M., 2008, Miocene silicic volcanism in southwestern Idaho: geochronology, geochemistry, and evolution of the central Snake River Plain: *Bulletin of Volcanology*, v. 70(3), p. 315-342.
- Burchfiel, B.C., and Davis, G.A., 1975, Nature and controls of Cordilleran orogenesis, western United States: Extensions on an earlier synthesis: *American Journal of Science*, v. 272, p. 97–118.
- Burchfiel, B.C., Cowan, D. S., and Davis, G. A., 1992, Tectonic overview of the Cordilleran orogen in the western United States, *in* Burchfiel, B.C., Lipman, P. W., and Zoback, M. L., eds., *The Geology of North America*, v. G3, *The Cordilleran Orogen: Conterminous United States*: Geological Society of America, p. 407-479.

- Burov, E., and Guillou-Frottier, L., 2005, The plume head–continental lithosphere interaction using a tectonically realistic formulation for the lithosphere: *Geophysical Journal International*, v. 161(2), p. 469-490.
- Burov, E., Guillou-Frottier, L., d'Acremont, E., Le Pourhiet, L., and Cloetingh, S. A. P. L., 2007, Plume head–lithosphere interactions near intra-continental plate boundaries: *Tectonophysics*, v. 434(1), p. 15-38.
- Burton, B.R., and Link, P.K., 1995, Structural setting of ore deposits in the Lake Creek mineralized area, Blaine County, south-central Idaho, *in* Worl, R.G., Link, P.K., Winkler, G.R., and Johnson, K.M., eds., *Geology and mineral resources of the Hailey 1° x 2° Quadrangle and the western part of the Idaho Falls 1° x 2° Quadrangle, Idaho: U.S. Geological Survey Bulletin 2064-A-R*, p. F1–F15.
- Camp, V.E., 1995, Mid-Miocene propagation of the Yellowstone mantle plume head beneath the Columbia River basalt source region: *Geology*, v. 23, p. 435–438.
- Camp, V.E., and Ross, M.E., 2004, Mantle dynamics and genesis of mafic magmatism in the Intermontane Pacific Northwest: *Journal of Geophysical Research*, v. 109, p. 1-14.
- Champion, D., and Duncan, R. A., 2012, Paleomagnetic and $^{40}\text{Ar}/^{39}\text{Ar}$ studies on tholeiite basalt samples from “HOTSPOT” corehole taken at Kimama, Idaho, central Snake River Plain: *Eos Transactions, AGU*, v. 13B-2842.
- Cherniak, D.J., Hanchar, J.M., and Watson, E.B., 1997, Diffusion of tetravalent cations in zircon: *Contributions to Mineralogy and Petrology*, v. 127, p. 383-390.
- Christiansen, R.L., 1982, Late Cenozoic volcanism of the Island Park area, eastern Idaho, *in* Bonnicksen, B., and Breckenridge, R.M., eds., *Cenozoic geology of Idaho: Idaho Bureau of Mines and Geology Bulletin 26*, p. 345–368.
- Clemens, J. D., 2003, S-type granitic magmas—petrogenetic issues, models and evidence: *Earth-Science Reviews*, v. 61(1), p. 1-18.
- Colgan, J.P., and Henry, C.D., 2007, Rapid middle Miocene collapse of the Mesozoic orogenic plateau in north-central Nevada: *International Geology Review* v. 51, p. 9-11.
- Condie, K.C., Beyer, E., Belousova, E., Griffin, W.L., and O'Reilly, S.Y.O., 2005, U–Pb isotopic ages and Hf isotopic composition of single zircons: The search for juvenile Precambrian continental crust: *Precambrian Research*, v. 139, p. 42–100.
- Coney, P. J., Jones, D. L., and Monger, J. W. H., 1980, Cordilleran suspect terranes: *Nature*, v. 288, p. 329–333.
- Criss, R.E., and Fleck, R.J., 1987, Petrogenesis, geochronology, and hydrothermal systems of the northern Idaho batholith and adjacent areas based on $^{18}\text{O}/^{16}\text{O}$, D/H, $^{87}\text{Sr}/^{86}\text{Sr}$, K–Ar, and $^{40}\text{Ar}/^{39}\text{Ar}$ studies, *in* Vallier, T.L., and Brooks, H.C., eds., *Geology of the Blue*

Mountains region of Oregon, Idaho, and Washington: U.S. Geological Survey Professional Paper 1436, p. 95–170.

- Critelli, S., Le Pera, E., and Ingersoll, R. V., 1997, The effects of source lithology, transport, deposition and sampling scale on the composition of southern California sand: *Sedimentology*, v. 44: p. 653–670.
- Crough, S.T., 1983. Hotspot swells: *Annual Review of Earth and Planetary Sciences*, v. 11, p. 165–193.
- DeCelles, P.G., 1994, Late Cretaceous-Paleocene synorogenic sedimentation and kinematic history of the Sevier belt, northeast Utah and southwest Wyoming: *Geological Society of America Bulletin*, v. 106, p. 32-56.
- DeCelles, P.G., 2004, Late Jurassic to Eocene evolution of the Cordilleran thrust belt and foreland basin system, western U.S.A.: *American Journal of Science*, v. 304, p. 105–168.
- Dickinson, W. R., and Gehrels, G. E., 2008, Sediment delivery to the Cordilleran foreland basin: Insights from U-Pb ages of detrital zircons in Upper Jurassic and Cretaceous strata of the Colorado Plateau: *American Journal of Science*, v. 308(10), p. 1041-1082.
- Dickinson, W.R., 2002, The Basin and Range province as a composite extensional domain: *International Geology Review*, v. 44, p. 1–38.
- Doherty, D.J., McBroome, L.A., and Kuntz, M.A., 1979, Preliminary Geologic Interpretation and Lithologic Log of the Exploratory Test Well (INEL-1), Idaho National Engineering Laboratory, Eastern Snake River Plain, Idaho: U.S. Geological Survey Open- File Report 79-1248, 10 p.
- Dover, J.H., 1980, The status of the Antler orogeny in central Idaho—Clarifications and constraints from the Pioneer Mountains, *in* Fouch, T.D., and Magathan, E.R., eds., *Paleozoic paleogeography of western United States: Rocky Mountain Section*, Society of Economic Paleontologists and Mineralogists, p. 275–299.
- Dover, J.H., 1983, Geologic map and sections of the central Pioneer Mountains, Blaine and Custer Counties, central Idaho: U.S. Geological Survey Miscellaneous Investigations Series, Map I-1319, scale 1:48,000.
- Egger, A.E., Dumitru, T.A., Miller, E.L., and Savage, C.F.E., 2003, Timing and nature of Tertiary plutonism and extension in the Grouse Creek Mountains, Utah: *International Geology Review*, v. 45, p. 497–532.
- Egger, A.E., Glen, J.M., and Ponce, D.A., 2010, The northwestern margin of the Basin and Range province. Part 2: Structural setting of a developing basin from seismic and potential field data: *Tectonophysics*, v. 488, p. 150–161.

- Fosdick, J.C., and Colgan, J.P., 2008, Miocene extension in the East Range, Nevada: A two-stage history of normal faulting in the northern Basin and Range: *Geological Society of America Bulletin*, v. 120, p. 1198–1213.
- Foster, D. A., and Fanning, C. M., 1997, Geochronology of the northern Idaho batholith and the Bitterroot metamorphic core complex: Magmatism preceding and contemporaneous with extension. *Geological Society of America Bulletin*, v. 109, p. 379-394.
- Foster, D. A., Doughty, P. T., Kalakay, T. J., Fanning, C. M., Coyner, S., Grice, W. C., and Vogl, J., 2007, Kinematics and timing of exhumation of metamorphic core complexes along the Lewis and Clark fault zone, northern Rocky Mountains, USA: *Geological Society of America Special Papers*, v. 434, p. 207-232.
- Foster, D.A., Grice, W.C., and Kalakay, T.J., 2010, Extension of the Anaconda metamorphic core complex: $^{40}\text{Ar}/^{39}\text{Ar}$ thermochronology and implications for Eocene tectonics of the northern Rocky Mountains and the Boulder batholith: *Lithosphere*, v. 2, p. 232-246.
- Gaschnig, R.M., Vervoort, J.D., Lewis, R.S., and McClelland, W.C., 2010, Migrating magmatism in the northern US Cordillera: in situ U-Pb geochronology of the Idaho batholith: *Contributions to Mineral Petrology*, v. 159, p. 863-883.
- Geslin, J.K., 1998, Distal Ancestral Rocky Mountains tectonism: Evolution of the Pennsylvanian-Permian Oquirrh–Wood River basin, southern Idaho: *Geological Society of America Bulletin*, v. 110, p. 644–663.
- Geslin, J.K., Link, P.K., and Fanning, C.M., 1999, High Precision provenance determination using detrital-zircon ages and petrography of Quaternary sands on the eastern Snake River Plain, Idaho: *Geology*, v. 27, p. 295-298.
- Geslin, J. K., Link, P. K., Riester, J. W, Kuntz, M. A., and Fanning, M. C., 2002, Pliocene and Quaternary stratigraphic architecture and drainage systems of the Big Lost Trough, northeastern Snake River Plain, Idaho, *in* Link, P. K., and Mink, L. L., eds., *Geology, hydrogeology, and environmental remediation*, Idaho National Engineering and Environmental Laboratory, eastern Snake River Plain, Idaho: *Geologic Society of America Special Paper 353*, p. 11-26.
- Griffin, W.L., Pearson, N.J., Belousova, E., Jackson, S.E., O'Reilly, S.Y., van Achterberg, E., Shee, S.R., 2000, The Hf isotope composition of cratonic mantle: LAM-MC-ICPMS analysis of zircon megacrysts in kimberlites: *Geochimica et Cosmochimica Acta*, v. 64, p. 133–147.
- Hall, W. E., Batchelder, J. N., and Tschanz, M., 1978, Preliminary geologic map of the Sun Valley 7.5 minute quadrangle, Idaho: U. S. Geological Survey Open-File Report 78-1056, scale 1:24,000.
- Hanan, B., Shervais, J., Vetter, S., 2008, Yellowstone plume-continental lithosphere interaction beneath the Snake River Plain: *Geology*, v. 36, p. 51-54.

- Harrison, T.M., Blichert-Toft, J., Müller, W., Albarède, F., Holden, P., and Mojzsis, S.J., 2005, Heterogeneous Hadean hafnium: Evidence of continental crust at 4.4 to 4.5 Ga: *Science*, v. 310, p. 1947–1950.
- Hill, R.I., Campbell, I.H., Davies, G.F., and Griffiths, R.W., 1992, Mantle plumes and continental tectonics: *Science*, v. 256, p. 186–193.
- Hodges, M.K.V., Link, P.K., Fanning, C.M., 2009, The Pliocene Lost River found to west: Detrital zircon evidence of drainage disruption along a subsiding hotspot track: *Journal of Volcanology and Geothermal Research*, v. 188, p. 237-249.
- Honjo, N., McElwee, K.R., Duncan, R.A., Leeman, W.P., 1986, K–Ar ages of volcanic rocks from the Magic Reservoir eruptive center, Snake River plain, Idaho: *Isochron/West* v. 46, p. 15–17.
- Ingersoll, R.V., 1990, Actualistic sandstone petrofacies: Discrimination of modern and ancient source rocks: *Geology*, v. 18, p. 733–736.
- Ingersoll, R.V., Kretchmer, A.G., and Valles, P.K., 1993, The effect of sampling scale on actualistic sandstone petrofacies: *Sedimentology*, v. 40, p. 937–953.
- Janecke, S.U., 1992, Kinematics and timing of three superposed extensional systems, east central Idaho; evidence for an Eocene tectonic transition: *Tectonics*, v. 11, p. 1121–1138
- Janecke, S.U., Snee, L.W., 1993, Timing and episodicity of middle Eocene volcanism and onset of conglomerate deposition, Idaho: *J Geol* v. 101, p. 603–621
- Jean, M.M., Hanan, B.B., Shervais, J., W, 2014, Yellowstone hotspot-continental lithosphere interaction, *Earth and Planetary Science Letters*, v. 389, p. 119-131.
- Johnson, K.M., Lewis, R.S., Bennett, E.H., and Kiilsgaard, T.H., 1988, Cretaceous and Tertiary intrusive rocks of south-central Idaho, *in* Link, P.K., and Hackett, W.R., eds., *Guidebook to the geology of central and southern Idaho: Idaho Geological Survey Bulletin 27*, p. 55–86.
- Konstantinou, A., Strickland, A., Miller, E. L., & Wooden, J. P., 2012, Multistage Cenozoic extension of the Albion–Raft River–Grouse Creek metamorphic core complex: Geochronologic and stratigraphic constraints. *Geosphere*, v. 8, p. 1429-1466.
- Kuntz, M., Covington, H., Schorr, L., 1992. An overview of basaltic volcanism of the eastern Snake River Plain, Idaho, *in* P.K. Link, M.A. Kuntz, and L.P. Platt, eds., *Regional Geology of Eastern Idaho and Western Wyoming: Geological Society of America Memoir 179*, p. 227-267.
- Kuntz, M., Skipp, B., Lanphere, M., Scott, W., Pierce, K., Dalrymple, G., Champion, D., Embree, G., Page, W., Morgan, L., Smith, R., Hackett, W., and Rodgers, D., 1994, *Geologic map of*

the Idaho National Engineering Laboratory and adjoining areas, eastern Idaho: U.S. Geological Survey Miscellaneous Investigations Series Map 1-2330, scale 1:100,000.

- Link, P.K., Miller, J.M.G., and Christie-Blick, N., 1994, Glacial-marine facies in a continental rift environment: Neoproterozoic rocks of the western United States Cordillera, *in* Deynoux, M., Miller, J.M.G., Domack, E.W., Eyles, N., Fairchild, I.J., and Young, G.M., eds., International Geological Correlation Project 260: Earth's glacial record: Cambridge, UK, Cambridge University Press, p. 29–59.
- Link, P.K., and Rodgers, 1995, Geologic Map of the Northeastern Part of the Hailey 1° x 2° Quadrangle, South-Central Idaho: U.S. Geological Survey Bulletin 2064-B, plate 1, scale 1:100,000.
- Link, P.K., Warren, I., Preacher, J.M., and Skipp, B., 1996, Stratigraphic analysis and interpretation of the Copper Basin Group, McGowan Creek Formation and White Knob Limestone, south central Idaho, *in* Longman, M.W., and Sonnenfeld, M.D., eds., Paleozoic systems of the Rocky Mountain region: Denver, Rocky Mountain Section, Society of Economic Paleontologists and Mineralogists, p. 117–144.
- Link, P.K., Kaufman, D.S., and Thackray, G.D., 1999, Field guide to Pleistocene Lakes Thatcher and Bonneville and the Bonneville Flood, southeastern Idaho, *in* Hughes, S.S., and Thackray, G.D., eds., Guidebook to the geology of eastern Idaho: Pocatello, Idaho, Idaho Museum of Natural History, p. 251–266.
- Link, P.K., McDonald, H.G., Fanning, C.M., and Godfrey, A.E., 2002, Detrital zircon evidence for Pleistocene drainage reversal at Hagerman Fossil Beds National Monument, central Snake River Plain, Idaho, *in* Bonnicksen, B., White, C.M., McCurry, M., eds., Tectonic and Magmatic Evolution of the Snake River Plain Volcanic Province: Idaho Geological Survey Bulletin, v. 30, p. 105–119.
- Link, P.K., Fanning, C.M., and Beranek, L.P., 2005, Reliability and longitudinal change of detrital-zircon age spectra in the Snake River system, Idaho and Wyoming: an example of reproducing the bumpy barcode: *Sed. Geol.* v. 182, p. 101–142.
- Link, P.K., Fanning, C.M., Lund, K.I., and Aleinikoff, J.N., 2007, Detrital zircons, correlation and provenance of Mesoproterozoic Belt Supergroup and correlative strata of east-central Idaho and southwest Montana. In: Link, P.K., Lewis, R.S. (Eds.), Proterozoic geology of western North America and Siberia: *SEPM Spec. Pub.*, v. 86, p. 101–128.
- Ludwig, K.R., 2008, Isoplot 3.60: Berkeley Geochronology Center, Special Publication No. 4, 77 p.
- Mahoney, J.B., Link, P.K., Burton, B.R., Geslin, J.K., and O'Brien, J.P., 1991, Pennsylvanian and Permian Sun Valley Group, Wood River Basin, south-central Idaho, *in* Cooper, J.D., and Stevens, C.H., eds., Paleozoic paleogeography of the western United States, Volume II: Pacific Section, Society of Economic Paleontologists and Mineralogists Publication 67, p. 551–579.

- Morgan, L. A., and McIntosh, W. C., 2005, Timing and development of the Heise volcanic field, Snake River Plain, Idaho, western USA: *Geological Society of America Bulletin*, v. 117, p. 288 – 306.
- Moye, F. J., Hackett, W. R., Blakley, J. D., and Snider, L. G., 1988, Regional geologic setting and volcanic stratigraphy of the Challis volcanic field, central Idaho: *Guidebook to the geology of central and southern Idaho: Idaho Geological Survey Bulletin*, v. 27, p. 87-97.
- O'Reilly, S.Y., Griffin, W.L., Pearson, N.J., Jackson, S.E., Belousova, E.A., Alard, O., and Saeed, A., 2008, Taking the pulse of the earth: linking crust and mantle events: *Australian Journal of Earth Sciences*, v. 55, p. 983–995.
- Ore, H.T., 1999, Topographic and geomorphic development of southeastern Idaho, segments from an essay, *in* Hughes, S.S., and Thackray, G.D., eds., *Guidebook to the geology of eastern Idaho: Pocatello, Idaho, Idaho Museum of Natural History*, p. 254–255.
- Pavlis, T. L., and O'Neill, R. L., 1985, Superposition of Cenozoic extension on Mesozoic compressional structures of the Pioneer Mountains, central Idaho: *Geological Society of America Abstracts with Programs*, v. 17, p. 397-398.
- Pavlis, T. L., and O'Neill, R. L., 1987, Comment on "Extensional deformation with northwest vergence, Pioneer core complex, central Idaho": *Geology*, v. 15, p. 283-284.
- Perkins, M. E., Nash, W. P., Brown, F. H., and Fleck, R.J., 1995, Fallout tuffs of Trapper Creek, Idaho—a record of Miocene explosive volcanism in the Snake River Plain volcanic province: *Geological Society of America Bulletin*, v. 107, p. 1484–1506.
- Pierce, K.L., and Morgan, L.A., 1992, The Track of the Yellowstone Hotspot: Volcanism, faulting, and uplift, *in* Link, P.K., Kuntz, M.A., and Platt, L.B., eds., *Regional geology of eastern Idaho and western Wyoming: GSA Memoir 179*, p. 1-53.
- Pierce, K.L., Morgan, L.A., and Saltus, R.W., 2002. Yellowstone Plume Head: postulated tectonic relations to the Vancouver Slab, continental boundaries, and climate, *in*: Bonnicksen, B., White, C.M., and McCurry, M., eds., *Tectonic and Magmatic Evolution of the Snake River Plain Volcanic Province: Idaho Geol. Survey Bull.*, vol. 30. Idaho Geological Survey, Moscow, ID, United States, p. 5–33.
- Pierce, K.L. and Morgan, L.A., 2009, Is the track of the Yellowstone hotspot driven by a deep mantle plume? — Review of volcanism, faulting, and uplift in light of new data: *Journal of Volcanology and Geothermal Research*. v. 188, p. 1-25.
- Potter, K.E., Link, P.K., Shervais, J.W., and Janecke, S.U., 2013, Volcanogenic detrital zircons from the Kimama Drill core (Project Hotspot): Evidence for source evolution in the Yellowstone-Snake River Plain magmatic system, central Snake River plain, ID. *Geological Society of America Abstracts with Programs*, v. 45, no. 7, p. 345

- Renne P.R., Swisher C.S., Deino A.L., Karner, D.B., Owens, T.L., and DePaolo, D.J., 1998, Intercalibration of standards, absolute ages and uncertainties in $^{40}\text{Ar}/^{39}\text{Ar}$ dating: *Chemical Geology*, v. 145, p. 117–152.
- Rodgers, D.W., Link, P.K., and Huerta, A.D., 1995, Structural Framework of Mineral Deposits Hosted by Paleozoic Rocks in the Northeastern Part of the Hailey $1^\circ \times 2^\circ$ Quadrangle, South-Central Idaho, *in* Worl, R.G., Link, P.K., Winkler, G.R., and Johnson, K.M., *Geology and Mineral Resources of the Hailey $1^\circ \times 2^\circ$ Quadrangle and the Western Part of the Idaho Falls $1^\circ \times 2^\circ$ Quadrangle, Idaho: U.S. Geological Survey Bulletin 2064-B*, p. 1–18.
- Schmandt, B., Dueker, K., Humphreys, E., and Hansen, S., 2012, Hot mantle upwelling across the 660 beneath Yellowstone, *Earth and Planetary Science Letters*, v. 331, p. 224–236.
- Shervais, J.W., Vetter, S.K., and Hanan, B.B., 2006, Layered mafic sill complex beneath the eastern Snake River Plain: evidence from cyclic geochemical variations in basalt: *Geology*, v. 34, p. 365–368.
- Shervais, J. W., and Hanan, B. B., 2008, Lithospheric topography, tilted plumes, and the track of the Snake River–Yellowstone hot spot: *Tectonics*, v. 27, p. 5.
- Smith, R. B., and Braille, L.W., 1994, The Yellowstone hotspot: *Journal of Volcanology and Geothermal Research*, v. 61, p. 121–188.
- Stacey, J. T., and Kramers, J.D., 1975, Approximation of terrestrial lead isotope evolution by a two-stage model: *Earth and Planetary Science Letters*, v. 26(2), p. 207–221.
- Turner, R.J.W., and Otto, B.R., 1988, Stratigraphy and structure of the Milligen Formation, Sun Valley area, Idaho, *in* Link, P.K., and Hackett, W.R., eds., *Guidebook to the geology of central and southern Idaho: Idaho Geological Survey Bulletin v. 27*, p. 153–167.
- Vermeesch, P., 2004, How many grains are needed for a provenance study?: *Earth and Planetary Science Letters*, v. 224, p. 441–451.
- Vogl, J. J., Foster, D. A., Fanning, C. M., Kent, K. A., Rodgers, D. W., and Diedesch, T., 2012, Timing of extension in the Pioneer metamorphic core complex with implications for the spatial-temporal pattern of Cenozoic extension and exhumation in the northern US Cordillera: *Tectonics*, v. 31, 22 p.
- Vogl, J.J., Min, K., Carmenate, A., Foster, D.A., and Marsellos, A., 2014, Miocene regional hotspot-related uplift, exhumation, and extension north of the Snake River Plain: Evidence from apatite (U-Th)/He thermochronology: *Lithosphere*, v. 6, p. 108–123.
- Wells, M.L., Snee, L.W., and Blythe, A.E., 2000, Dating of major normal fault systems using thermochronology: An example from the Raft River detachment, Basin and Range, western United States: *Journal of Geophysical Research*, v. 105, p. 16,303–16,327.

- Whitehead, R. L., 1992, Geohydrologic framework of the Snake River Plain regional aquifer system, Idaho and eastern Oregon: US Geological Survey professional paper (USA).
- Worl, R.G., Kiilsgaard, T.H., Bennett, E.H., Link, P.K., Lewis, R.S., Mitchell, V.E., Johnson, K.M., and Snyder, L.D., 1991, Geologic map of the Hailey 1°2° quadrangle, Idaho. U.S. Geol. Surv. Open- File Rep. 91-340, scale 1:250,000.
- Worl, R.G., and Johnson, K.M., 1995, Geology and mineral deposits of the Hailey 1° x 2° Quadrangle and western part of the Idaho Falls 1° x 2° Quadrangle, south-central Idaho—An overview, *in* Worl, R.G., Link, P.K., Winkler, G.R., and Johnson, K.M., eds., Geology and mineral resources of the Hailey 1° x 2° Quadrangle and the western part of the Idaho Falls 1° x 2° Quadrangle, Idaho: U.S. Geological Survey Bulletin 2064-A-R, p. A1–A21
- Wust, S.L., and Link, P.K., 1988, Field guide to the Pioneer Mountains core complex, south-central Idaho, *in* Link, P.K., and Hackett, W.R., eds., Guidebook to the geology of central and southern Idaho: Idaho Geological Survey Bulletin 27, p. 43–54.

CHAPTER 5

Conclusion

As one of the youngest and best-preserved continental hotspot provinces, the SRP of Idaho provides an unprecedented record of volcanism, sedimentation, and magma genesis, and of the dynamic effect of these mechanisms on surface topography. The Kimama core samples 1912 m of continuous basalt stratigraphy along the Axial Volcanic High of the SRP. We have combined a variety of tools and methods to piece together the stratigraphy of volcanism and sedimentation, the frequency and timing of basalt accumulation, and the magnitude and origin of magma compositional variability. Our major goals in this research were to generate complete lithologic, geochemical, and stratigraphic records of the Kimama core.

In chapter two, we identified 71 basalt flow groups, 141 flows, and 446 flow units based upon lithologic observations and Ar/Ar and paleomagnetic age data. Our Ar/Ar and paleomagnetic ages show that basalt volcanism on the central Snake River has been relatively continuous over the past 6.4 Ma, and our basalt facies observations suggest very similar eruptive and emplacement processes through time. Flow groups average 10 m to 60 m thick and show an average accumulation rate of 335 m/M.y. The relatively gentle relief of the SRP and the lack of an elevated edifice at the Kimama site belies the vertical accumulation of 1912 m of basalts, especially as little erosion was observed in cored basalts. The basalts must have filled almost 2 km of accommodation space in the vicinity of the Kimama core hole. The temporally-steady input of erupted lavas into the Kimama basin (displayed in chapter 1, figure 9), and very few facies observations very thick, ponded lava flows in the Kimama core, imply a steady-state equilibrium of basalt deposition and subsidence over 6.4 M.y.

In the third chapter, our goal was to recognize variations in magma chemistry and to identify the processes responsible for compositional differences in basalts of the Kimama core. To determine the extent by which magma chemistry is controlled by differentiation, we modeled potential paths of partial melting, assimilation of crust or the mid-crustal sill, and fractionation. Although chemical trends within the Kimama olivine tholeiites are broadly similar, upsection chemical variability in the Kimama core suggests a dynamic mid-crustal sill magma storage system. Periods of magma storage and fractionation are punctuated by episodes of magma recharge from more primitive batches, and ascending magma bodies are filtered through and react with previously emplaced gabbro. Variation diagrams show that gabbro assimilation is the most important cause of chemical changes in Kimama basalts, more so than fractionation and the assimilation of more felsic continental crust. Melting models of E-MORB spinel lherzolite source produce similar rare earth element compositional trends as those observed in Kimama at 7-15% melting.

Our geochemical results have two important implications: 1) Petrogenetic processes of Kimama basalts have remained largely similar over the 6.4 Ma record. Progressions from more primitive, low K_2O basalt compositions to more evolved, high K_2O , FeO^* , and TiO_2 basalt compositions, have occurred at multiple time/depth intervals. These results imply that the mid-crustal sill and magma ascent paths were established well before 6.4 Ma. 2). Highly evolved, Craters of the Moon-type lavas are not confined to the margins of the Snake River Plain, and are not temporally limited to the last 15 k.y. Although only two such flow groups were observed, the Kimama core demonstrates that Craters of the Moon-type lavas erupted at two separate intervals, almost 2 Ma apart.

Two important implications arise from our work in chapter four, regarding the deposition of volcanogenic and detrital zircons in fluvial sediments within the Kimama core. 1)

Each sampled fluvial interbed contains a different distribution of age populations of detrital zircon grains. We interpret a broad similarity of the age spectrum to the Wood River system, but the varying detrital zircon barcodes demonstrates the effect of silicic and basaltic volcanism during the relatively short depositional duration of fluvial sediments in the Kimama core. Furthermore, the interruption of fluvial sedimentation from depths of 1874-1753 m and above 1707 m depth, and hyaloclastitic basalt at multiple depths below 1753 m, suggest interaction between lava and water in the early part of the Kimama volcanic record. 2) Although the Kimama core did not intercept the rhyolite at depth, we identified volcanogenic zircons with ages ranging from 7.1 to 5.8 Ma in fluvial sediment interbeds at depths between 1844 to 1749 m. Neogene volcanogenic zircons represent eruptive products from Yellowstone-Snake River Plain hotspot track caldera complexes. In Project Hotspot's Kimberley core, drilled within the Twin Falls caldera complex, rhyolite on the surface is dated at 6.25 Ma), implying a temporal and depositional correlation to the 5.8 to 6.2 Ma sediments in the Kimama core, which are buried by almost 1750 m of basalt. These observations suggest the existence of a depositional basin within the central SRP, the study of which is a topic for future research.

The Kimama core records 6.4 M.y. of volcanic and sedimentological history, including magmatic flux and magma compositional changes through time. We observe that Kimama SROT basalts are higher in Fe, Ti, K, etc., than MORB magmas and are compositionally equivalent to OIB magmas. Our data demonstrate that SRP magmatism is mantle-plume derived and does not originate from the melting of a shallow MORB-source asthenosphere. Our observations, combined with new mantle tomography, refute non-plume models for the origin and development of the SRP volcanic province.

APPENDIX

Stratigraphic and Geochemical data used to determine flow unit, flow group, and super group boundaries

Sample	K/P	F40*	K2O	TiO2	T/K	Zr/Nb	La/Alu	Depth (m)	Bound type	Inclin.	Super Group	Flow Group #	Flow Type	Flow Unit	Flow Unit	Depth Flow Top (m)	Depth Flow Bottom (m)	Mean Flow Thickness (m)	Depth Flow Top (ft)	Depth Flow Bottom (ft)	Unit Thick (ft)	BOX	DESCRIPTION
KAI1A22	2.04	14.07	0.73	3.29	3.24	15.23	49.3	127.0	incl.	51	A	1	SHOT	1	1	13.41	25.15	11.73	44	82.5	38.5	A5	Oxidized
KAI1A23	1.62	14.85	0.71	3.23	3.27	13.90	55.9	52.0	Chem.			2		2	1	13.41	25.15	11.73	44	82.5	38.5	A5	Oxidized
KAI1A24	1.62	14.85	0.71	3.23	3.27	13.90	55.9	52.0	Chem.			3		3	3	25.1	36.5	11.4	82.5	119.8			
KAI1A25	1.62	14.85	0.71	3.23	3.27	13.90	55.9	52.0	Chem.			4		4	5	36.52	39.29	2.77	119.8	128.9	9.1	A10	
KAI1A26	2.04	14.07	0.73	3.29	3.24	15.23	49.3	127.0	incl.	51	A	2	SHOT	5	2	25.15	36.52	11.37	8.63			A9	Oxidized rubby interval ~8"
KAI1A27	2.04	14.07	0.73	3.29	3.24	15.23	49.3	127.0	incl.	51	A	3		6	4	39.29	42.34	3.05	128.9	138.9	10.0	A11	
KAI1A28	1.23	12.33	0.59	3.40	4.1	12.6	138.7		Chem.			7		7	54.53	57.18	2.65	178.9	187.6	8.7	A16	Oxidized flow top	
KAI1A29	1.23	12.33	0.59	3.40	4.1	12.6	138.7		Chem.			8		8	62.06	64.28	2.22	203.6	210.9	7.3	A18	Oxidized flow top with sediment vesicle/fracture fill	
KAI1A30	1.23	12.33	0.59	3.40	4.1	12.6	138.7		Chem.			9		9	62.06	64.28	2.22	203.6	210.9	7.3	A18	Oxidized flow top with sediment vesicle/fracture fill	
KAI1A31	1.23	12.33	0.59	3.40	4.1	12.6	138.7		Chem.			10		10	64.28	72.97	8.69	210.9	239.4	28.5	A21	Shelly pahoehoe to 214.2'	
KAI1A32	1.23	12.33	0.59	3.40	4.1	12.6	138.7		Chem.			11		11	72.97	76.81	3.84	239.4	252.0	12.6	A22	Oxidized, sparry, obvious vesicular manifestation	
KAI1A33	1.23	12.33	0.59	3.40	4.1	12.6	138.7		Chem.			12		12	76.81	78.52	1.71	142.3	142.3	0.0	A23	Possible flow break color change and vesicle increase	
KAI1A34	1.23	12.33	0.59	3.40	4.1	12.6	138.7		Chem.			13		13	78.52	82.88	4.36	252.6	271.9	14.3	A23	Somewhat oxidized, beginning of shelly pahoehoe	
KAI1A35	1.23	12.33	0.59	3.40	4.1	12.6	138.7		Chem.			14		14	82.88	85.95	3.08	271.9	282.0	10.1	A26	Weathered surfaces on vesicular rubble	
KAI1A36	1.23	12.33	0.59	3.40	4.1	12.6	138.7		Chem.			15		15	85.95	90.34	4.39	282.0	296.4	14.4	A27	Oxidized and glassy, high vesicle abundance	
KAI1A37	1.23	12.33	0.59	3.40	4.1	12.6	138.7		Chem.			16		16	90.34	94.58	4.24	296.4	310.3	13.9	A29	Increase in vesicle abundance, glassy, possible flow mold	
KAI1A38	1.23	12.33	0.59	3.40	4.1	12.6	138.7		Chem.			17		17	94.58	95.77	1.19	310.3	314.2	3.9	A29	Glassy, oxidized, increased vesicle abundance	
KAI1A39	1.23	12.33	0.59	3.40	4.1	12.6	138.7		Chem.			18		18	95.77	95.98	0.21	314.2	314.9	0.7	A29	Baked sediment interval of ~5" thickness	
KAI1A40	1.23	12.33	0.59	3.40	4.1	12.6	138.7		Chem.			19		19	97.87	100.55	2.68	321.1	329.9	8.8	A31	Oxidized and increased vesicle abundance	
KAI1A41	1.23	12.33	0.59	3.40	4.1	12.6	138.7		Chem.			20		20	100.55	109.39	8.84	329.9	358.9	29.0	A34	Vesicular (rare), no oxidation present (pink massive)	
KAI1A42	1.23	12.33	0.59	3.40	4.1	12.6	138.7		Chem.			21		21	109.39	118.26	8.87	358.9	388.0	29.1	A37	End of previous flow, start of thick sediment interval	
KAI1A43	1.23	12.33	0.59	3.40	4.1	12.6	138.7		Chem.			22		22	118.26	123.75	5.49	388.0	406.0	18.0	A38	Thick sediment interval	
KAI1A44	1.23	12.33	0.59	3.40	4.1	12.6	138.7		Chem.			23		23	123.75	124.91	1.16	406.0	409.8	3.8	A38	Flow break out, oxidized and vesicular	
KAI1A45	1.23	12.33	0.59	3.40	4.1	12.6	138.7		Chem.			24		24	124.91	126.22	1.31	409.8	414.1	4.3	A39	Oxidized, glassy and vesicular; start of shelly pahoehoe	
KAI1A46	1.23	12.33	0.59	3.40	4.1	12.6	138.7		Chem.			25		25	126.22	126.98	0.76	414.1	416.6	2.5	A39	Oxidized, vesicular, glassy	
KAI1A47	1.23	12.33	0.59	3.40	4.1	12.6	138.7		Chem.			26		26	126.98	127.99	1.01	416.6	419.9	3.3	A40	Oxidized, vesicular, glassy	
KAI1A48	1.23	12.33	0.59	3.40	4.1	12.6	138.7		Chem.			27		27	127.99	131.34	3.35	419.9	430.9	11.0	A41	Vesicular gradation, somewhat weathered	
KAI1A49	1.23	12.33	0.59	3.40	4.1	12.6	138.7		Chem.			28		28	131.34	134.39	3.05	430.9	440.9	10.0	A42	Oxidized, vesicular; shelly pahoehoe (could be flow break?)	
KAI1A50	1.23	12.33	0.59	3.40	4.1	12.6	138.7		Chem.			29		29	134.39	136.34	1.95	440.9	447.3	6.4	A42	Oxidized, vesicular; shelly pahoehoe (could be flow break?)	
KAI1A51	1.23	12.33	0.59	3.40	4.1	12.6	138.7		Chem.			30		30	136.34	137.22	0.88	447.3	450.2	2.9	A43	Scoriaceous and spattery, oxidized	
KAI1A52	1.23	12.33	0.59	3.40	4.1	12.6	138.7		Chem.			31		31	137.22	137.22	0.0	450.2	450.2	0.0			
KAI1A53	1.23	12.33	0.59	3.40	4.1	12.6	138.7		Chem.			32		32	137.22	137.22	0.0	450.2	450.2	0.0			
KAI1A54	1.23	12.33	0.59	3.40	4.1	12.6	138.7		Chem.			33		33	137.22	137.22	0.0	450.2	450.2	0.0			
KAI1A55	1.23	12.33	0.59	3.40	4.1	12.6	138.7		Chem.			34		34	137.22	137.22	0.0	450.2	450.2	0.0			

Brunhes Normal Chron

Reverse Chron

Oliva! Normal Subchron

114	155	390.72	395.39	4.66	1281.9	1297.2	6.3	868	Rubby & vesicular, oxidized & vesicular coating, shiny granular
115	156	395.39	397.46	2.07	1297.2	1304.0	6.50	869	Oxidized & glassy, sediment coating in fissures (flow nodules)
116	157	397.46	398.10	0.64	1304.0	1306.1	12.1	871	Sediment coated rubble with vesicular interstitial flow breccia
117	158	398.10	400.60	2.50	1306.1	1314.3	7.1	871	Oxidized & glassy, sediment-coated vesicles
118	159	400.60	402.52	1.92	1314.3	1320.6	3.4	872	Oxidized & glassy, sediment coating, rubby
46	160	402.52	405.35	2.83	1320.6	1329.9	8.8	873	Rubby, oxidized & sediment coated vesicles & fractures
120	161	405.35	409.04	3.69	1329.9	1342.0	27.3	876	Oxidized, glassy, and sediment coated. Also rubby
121	162	409.04	411.21	2.16	1342.0	1349.1	6.2	876	Glassy & oxidized rubble
122	163	411.21	412.24	1.04	1349.1	1352.5	4.8	877	Vesicle distribution, sediment coating, glassy
123	164	412.24	414.92	2.68	1352.5	1361.3	4.0	877	Fractured glassy with thick sediment coating, shiny granular
47				15.98					
105	165	414.92	423.25	8.32	1361.3	1388.6	4.00	877	Rubby, oxidized & vesicular with sediment coating
106	166	423.25	425.14	1.89	1388.6	1394.8	5.0	878	Rubby, oxidized & vesicular with sediment coating

107	167	425.14	426.60	1.46	1394.8	1399.6	2.6	878	Rubby, sediment coated with vesicles coated, only for flow breccia	
108	168	426.60	427.82	1.22	2.68	1399.6	1403.6	4.9	880	Rubby, oxidized & glassy, glass granules to be showing, unoxidized
49	109	169	427.82	430.59	2.77	1403.6	0.0	12.7	881	Rubby, sediment coated, & glassy
50	110	170	430.59	432.11	1.52	1412.7	1417.7	14.1	882	Glassy vesicles coated (covered from fr. cover vesicles, with and without)
111	171	432.11	434.01	0.79	2.32	1417.7	1420.3	29.9	885	Basalt overlying baked sediment
112	172	432.11	434.40	1.49	1420.3	1425.2	4.9	886	Sediment overlying contact with basalt, "T" transition	
52	113	173	434.40	438.27	3.87	1425.2	1437.9	6.1	887	Oxidized glassy, and sediment coated (basalt & vesicles, with and without)
114	174	438.27	442.57	4.30	9.39	1437.9	1452.0	11.9	887	Glassy, vesicular
115	175	442.57	451.68	9.11	17.28	1452.0	1481.9	19.7	890	Glassy vesicles vesicular contact with sediment coating, sediment coated

116	176	451.68	453.18	1.49	1481.9	1486.8	7.5	891	Oxidized, sediment & glassy, with sediment coating (flow breccia)		
53	20	Fe-Ti	453.18	455.04	1.86	5.49	1486.8	1492.9	3.1	891*	Oxidized, rubby & glassy, sediment coating, no basal "T" transition
117	177	455.04	458.66	3.63	1492.9	1504.8	10.9	893	Oxidized & glassy, sediment coating, shiny granular		
54	118	178	458.66	464.67	6.00	12.01	1504.8	1524.5	11.60	893	Rubby, glassy, appears to be weathered, shiny granular
55	119	179	464.67	466.95	2.29	24.54	1524.5	1532.0	5.0	894	Glassy, oxidized & rubby, minor sediment coating, shiny granular
120	180	466.95	467.90	0.94	1532.0	1535.1	3.4	895	Glassy, oxidized & vesicular, possible flow nodules, shiny granular		
121	181	467.90	471.43	3.54	1535.1	1546.7	3.8	895	Glassy, vesicular (concentrated), vesicular vesicles transition		
122	182	471.43	474.76	3.32	1546.7	1557.6	31.1	898	Glassy, oxidized, rubby with minor sediment coating		
123	183	474.76	476.01	1.25	1557.6	0.0	20.9	8100	Rubby, glassy, oxidized & sediment coated		
124	184	476.01	477.53	1.52	1561.7	1566.7	19.6	8102	Rubby, sediment coating, increased vesiculation		
125	185	477.53	478.57	1.04	1566.7	1570.1	6.2	8103	Oxidized & glassy with sediment coating, vesicle transition		
126	186	478.57	479.72	1.16	1570.1	1573.9	3.6	8103	Oxidized, vesicular, & rubby, minor sediment coating		
127	187	479.72	489.20	9.48	1573.9	1605.0	10.5	8104	Oxidized, glassy, & sediment coating, vesicle transition		

128	188	489.20	495.57	6.37	1605.0	1625.9	5.6	8105	Vesicle transition, oxidized & glassy, sediment coating, shiny granular		
129	189	495.57	501.55	5.97	1625.9	1645.5	3.6	8105	Rubby, vesicular, sediment coating, vesicle transition, possible flow breccia		
130	190	501.55	503.44	1.89	1645.5	1651.7	2.5	8106	Rubby, glassy, & oxidized sediment coating, shiny granular		
131	191	503.44	504.54	1.10	1651.7	1655.3	9.1	8107	Oxidized, rubby & vesicular, sediment coating		
132	192	504.54	507.74	3.20	1655.3	1665.8	5.4	8107	Oxidized, glassy, & rubby, overlies rubby zones		
133	193	507.74	509.44	1.71	1665.8	1671.4	13.2	8108	Glassy & oxidized with sediment coating, rubby		
134	194	509.44	510.54	1.10	1671.4	1675.0	3.4	8109	Oxidized, glassy & vesicular, possible flow nodules, shiny granular		
135	195	510.54	511.30	0.76	6.77	1675.0	1675.5	4.1	8109	Rubby, oxidized, & sediment coated	
58	136	196	511.30	514.08	2.77	11.43	1677.5	1686.6	17.6	8111	Basalt overlying baked sediment & basalt rubble
137	197	514.08	515.72	1.65	1686.6	1692.0	3.1	8112	Sediment & basalt rubble overlying basalt flow		
138	198	515.72	519.74	4.02	1692.0	1705.2	59.3	8118	Rubby, vesicular, sediment coated vesicles "T" of shiny granular		
139	199	519.74	520.78	1.04	1705.2	1708.6	4.7	8118	Basalt contact overlying baked sediment (interstitial "T")		
140	200	520.78	522.03	1.25	1708.6	1712.7	1.8	8119	Sediment transition with a bit, oxidized, vesicular, shiny granular		
141	201	522.03	527.40	5.36	1712.7	1730.3	17.6	8119	Shiny granular, glassy, oxidized with sediment coating		

142	202	527.40	532.03	4.63	1730.3	1743.9	14.6	8120	Sediment coated, oxidized & glassy, sediment coating, shiny granular
143	203	532.03	537.40	5.36	1743.9	1761.5	17.6	8120	Sediment coated, oxidized & glassy, sediment coating, shiny granular

Oliva! Normal Subchron

144	204	537.40	542.03	4.63	1761.5	1779.1	14.6	8121	Sediment coated, oxidized & glassy, sediment coating, shiny granular
145	205	542.03	547.40	5.36	1779.1	1796.7	17.6	8121	Sediment coated, oxidized & glassy, sediment coating, shiny granular

Oliva! Normal Subchron

146	206	547.40	552.03	4.63	1796.7	1814.3	14.6	8122	Sediment coated, oxidized & glassy, sediment coating, shiny granular
147	207	552.03	557.40	5.36	1814.3	1831.9	17.6	8122	Sediment coated, oxidized & glassy, sediment coating, shiny granular

Oliva! Normal Subchron

148	208	557.40	562.03	4.63	1831.9	1849.5	14.6	8123	Sediment coated, oxidized & glassy, sediment coating, shiny granular
149	209	562.03	567.40	5.36	1849.5	1867.1	17.6	8123	Sediment coated, oxidized & glassy, sediment coating, shiny granular

Oliva! Normal Subchron

150	210	567.40	572.03	4.63	1867.1	1884.7	14.6	8124	Sediment coated, oxidized & glassy, sediment coating, shiny granular
151	211	572.03	577.40	5.36	1884.7	1902.3	17.6	8124	Sediment coated, oxidized & glassy, sediment coating, shiny granular

Gauss Normal C Gilbert Reverse Chron Cochit Normal Subchron

Sample ID	12.10	0.47	2.18	3.3	88.3	3421.5	274	1044.12	1045.04	0.91	3425.6	3428.6	15.6	B298
KA1B3437	0.91	1.39	0.3	2.61	12.42	43.5	3437.0	Incl.	51					
KA1B3461	1.18	0.28	2.12	5.4	13.6	3456.7								
KA1B3506	2.32	14.31	0.72	3.10	3.10	3506.0								
KA1B3527						3527.0								
KA1B3536	1.52	18.36	1.77	3.44	1.40	3267	60.3	3536.0	Incl./Chem.	-71				
KA1B3546	1.26	14.8	0.5	3.21	4.62	3546.0								
KA1B3563	1.05	14.22	0.31	3.20	7.43	3563.0								
KA1B3626	1.45	12.96	0.42	2.71	4.64	3626.0								
KA1B3644	1.18	13.23	0.36	2.79	5.58	3644.0								
KA1B3656	1.09	13.68	0.35	3.48	7.16	3656.0								
KA1B3671	0.86	17.19	0.42	4.11	7.22	3671.0								
KA1B3790	1.18	13.59	0.38	2.93	5.55	3790.0								
KA1B3792	1.78	0.57	3.18	4.0	3.8	3792.0								
KA1B3828	1.625	38.8	3828.0											
KA1B3850	1.59	14.12	0.51	3.13	4.42	3850.0								
KA1B3871	2.22	14.85	0.76	3.32	3.14	3871.0								
KA1B3884	1.87	13.46	0.56	2.86	3.67	3884.0								
KA1B3901	1.59	14.12	0.51	3.13	4.42	3901.0								
KA1B3925	1.59	14.12	0.51	3.13	4.42	3925.0								
KA1B3945	2.23	14.48	0.81	3.41	3.03	3945.0								
KA1B3985	1.17	14.31	0.32	3.31	7.45	3985.0								
KA1B4030	6.7	20.4	1.55	1.94	0.90	4030.0								
KA1B4056	1.10	14.58	0.4	3.64	6.55	4056.0								

1T Reverse Chron

Cochit Normal Subchron

Gilbert Reverse Chron

Gauss Normal C

nal Subchron

Gilbert Reverse
Chron

Nunivak Normal Subchron

Sample ID	1337.03	1239.47	2.44	4058.5	4066.5	8.90	B364
KAI184070	373	1239.47	2.80	4065.5	4075.7	13.2	B365
KAI184082	315	1242.27	3.35	4075.7	4086.7	22.1	B367
	316	1245.63	3.92	4086.7	4093.0	5.70	B368
	317	1247.55	4.44	4093.0	4101.0	9.50	B369
	318	1249.98	5.00	4101.0	4111.0	7.30	B370
KAI184118	319	1253.03	5.58	4111.0	4129.3	9.70	B371
	320	1258.61	6.25	4129.3	4149.8	9.60	B372
	321	1264.86	7.23	4149.8	4173.6	12.4	B373
	322	1272.11	8.21	4173.6	4200.0	12.4	B374
	323	1278.85	9.20	4200.0	4230.0	12.4	B375
	324	1285.59	10.20	4230.0	4263.0	12.4	B376
	325	1292.33	11.20	4263.0	4300.0	12.4	B377
	326	1299.07	12.20	4300.0	4341.0	12.4	B378
	327	1305.81	13.20	4341.0	4386.0	12.4	B379
	328	1312.55	14.20	4386.0	4435.0	12.4	B380
	329	1319.29	15.20	4435.0	4488.0	12.4	B381
	330	1326.03	16.20	4488.0	4545.0	12.4	B382
	331	1332.77	17.20	4545.0	4606.0	12.4	B383
	332	1339.51	18.20	4606.0	4671.0	12.4	B384
	333	1346.25	19.20	4671.0	4740.0	12.4	B385
	334	1353.00	20.20	4740.0	4813.0	12.4	B386
	335	1359.74	21.20	4813.0	4890.0	12.4	B387
	336	1366.48	22.20	4890.0	4971.0	12.4	B388
	337	1373.22	23.20	4971.0	5056.0	12.4	B389
	338	1379.96	24.20	5056.0	5145.0	12.4	B390
	339	1386.70	25.20	5145.0	5238.0	12.4	B391
	340	1393.44	26.20	5238.0	5335.0	12.4	B392
	341	1400.18	27.20	5335.0	5436.0	12.4	B393
	342	1406.92	28.20	5436.0	5541.0	12.4	B394
	343	1413.66	29.20	5541.0	5650.0	12.4	B395
	344	1420.40	30.20	5650.0	5763.0	12.4	B396
	345	1427.14	31.20	5763.0	5880.0	12.4	B397
	346	1433.88	32.20	5880.0	6001.0	12.4	B398
	347	1440.62	33.20	6001.0	6126.0	12.4	B399
	348	1447.36	34.20	6126.0	6255.0	12.4	B400
	349	1454.10	35.20	6255.0	6388.0	12.4	B401
	350	1460.84	36.20	6388.0	6525.0	12.4	B402
	351	1467.58	37.20	6525.0	6666.0	12.4	B403
	352	1474.32	38.20	6666.0	6811.0	12.4	B404
	353	1481.06	39.20	6811.0	6960.0	12.4	B405
	354	1487.80	40.20	6960.0	7113.0	12.4	B406
	355	1494.54	41.20	7113.0	7270.0	12.4	B407
	356	1501.28	42.20	7270.0	7431.0	12.4	B408
	357	1508.02	43.20	7431.0	7596.0	12.4	B409
	358	1514.76	44.20	7596.0	7765.0	12.4	B410
	359	1521.50	45.20	7765.0	7938.0	12.4	B411
	360	1528.24	46.20	7938.0	8115.0	12.4	B412
	361	1534.98	47.20	8115.0	8296.0	12.4	B413
	362	1541.72	48.20	8296.0	8481.0	12.4	B414
	363	1548.46	49.20	8481.0	8670.0	12.4	B415
	364	1555.20	50.20	8670.0	8863.0	12.4	B416
	365	1561.94	51.20	8863.0	9060.0	12.4	B417
	366	1568.68	52.20	9060.0	9261.0	12.4	B418
	367	1575.42	53.20	9261.0	9466.0	12.4	B419
	368	1582.16	54.20	9466.0	9675.0	12.4	B420
	369	1588.90	55.20	9675.0	9888.0	12.4	B421
	370	1595.64	56.20	9888.0	10105.0	12.4	B422
	371	1602.38	57.20	10105.0	10326.0	12.4	B423
	372	1609.12	58.20	10326.0	10551.0	12.4	B424
	373	1615.86	59.20	10551.0	10780.0	12.4	B425
	374	1622.60	60.20	10780.0	11013.0	12.4	B426
	375	1629.34	61.20	11013.0	11250.0	12.4	B427
	376	1636.08	62.20	11250.0	11491.0	12.4	B428
	377	1642.82	63.20	11491.0	11736.0	12.4	B429
	378	1649.56	64.20	11736.0	11985.0	12.4	B430
	379	1656.30	65.20	11985.0	12238.0	12.4	B431
	380	1663.04	66.20	12238.0	12495.0	12.4	B432
	381	1669.78	67.20	12495.0	12756.0	12.4	B433
	382	1676.52	68.20	12756.0	13021.0	12.4	B434
	383	1683.26	69.20	13021.0	13290.0	12.4	B435
	384	1689.99	70.20	13290.0	13563.0	12.4	B436
	385	1696.73	71.20	13563.0	13840.0	12.4	B437
	386	1703.47	72.20	13840.0	14121.0	12.4	B438
	387	1710.21	73.20	14121.0	14406.0	12.4	B439
	388	1716.95	74.20	14406.0	14695.0	12.4	B440
	389	1723.69	75.20	14695.0	14988.0	12.4	B441
	390	1730.43	76.20	14988.0	15285.0	12.4	B442
	391	1737.17	77.20	15285.0	15586.0	12.4	B443
	392	1743.91	78.20	15586.0	15891.0	12.4	B444
	393	1750.65	79.20	15891.0	16199.0	12.4	B445
	394	1757.39	80.20	16199.0	16510.0	12.4	B446
	395	1764.13	81.20	16510.0	16824.0	12.4	B447
	396	1770.87	82.20	16824.0	17141.0	12.4	B448
	397	1777.61	83.20	17141.0	17461.0	12.4	B449
	398	1784.35	84.20	17461.0	17784.0	12.4	B450
	399	1791.09	85.20	17784.0	18110.0	12.4	B451
	400	1797.83	86.20	18110.0	18439.0	12.4	B452
	401	1804.57	87.20	18439.0	18771.0	12.4	B453
	402	1811.31	88.20	18771.0	19106.0	12.4	B454
	403	1818.05	89.20	19106.0	19444.0	12.4	B455
	404	1824.79	90.20	19444.0	19785.0	12.4	B456
	405	1831.53	91.20	19785.0	20129.0	12.4	B457
	406	1838.27	92.20	20129.0	20476.0	12.4	B458
	407	1845.01	93.20	20476.0	20826.0	12.4	B459
	408	1851.75	94.20	20826.0	21179.0	12.4	B460
	409	1858.49	95.20	21179.0	21534.0	12.4	B461
	410	1865.23	96.20	21534.0	21891.0	12.4	B462
	411	1871.97	97.20	21891.0	22250.0	12.4	B463
	412	1878.71	98.20	22250.0	22611.0	12.4	B464
	413	1885.45	99.20	22611.0	22974.0	12.4	B465
	414	1892.19	100.20	22974.0	23339.0	12.4	B466
	415	1898.93	101.20	23339.0	23706.0	12.4	B467
	416	1905.67	102.20	23706.0	24075.0	12.4	B468
	417	1912.41	103.20	24075.0	24446.0	12.4	B469
	418	1919.15	104.20	24446.0	24819.0	12.4	B470
	419	1925.89	105.20	24819.0	25194.0	12.4	B471
	420	1932.63	106.20	25194.0	25571.0	12.4	B472
	421	1939.37	107.20	25571.0	25950.0	12.4	B473
	422	1946.11	108.20	25950.0	26331.0	12.4	B474
	423	1952.85	109.20	26331.0	26714.0	12.4	B475
	424	1959.59	110.20	26714.0	27100.0	12.4	B476
	425	1966.33	111.20	27100.0	27488.0	12.4	B477
	426	1973.07	112.20	27488.0	27879.0	12.4	B478
	427	1979.81	113.20	27879.0	28272.0	12.4	B479
	428	1986.55	114.20	28272.0	28667.0	12.4	B480
	429	1993.29	115.20	28667.0	29064.0	12.4	B481
	430	2000.03	116.20	29064.0	29463.0	12.4	B482
	431	2006.77	117.20	29463.0	29864.0	12.4	B483
	432	2013.51	118.20	29864.0	30267.0	12.4	B484
	433	2020.25	119.20	30267.0	30672.0	12.4	B485
	434	2026.99	120.20	30672.0	31079.0	12.4	B486
	435	2033.73	121.20	31079.0	31488.0	12.4	B487
	436	2040.47	122.20	31488.0	31899.0	12.4	B488
	437	2047.21	123.20	31899.0	32312.0	12.4	B489
	438	2053.95	124.20	32312.0	32727.0	12.4	B490
	439	2060.69	125.20	32727.0	33144.0	12.4	B491
	440	2067.43	126.20	33144.0	33563.0	12.4	B492
	441	2074.17	127.20	33563.0	33984.0	12.4	B493
	442	2080.91	128.20	33984.0	34407.0	12.4	B494
	443	2087.65	129.20	34407.0	34832.0	12.4	B495
	444	2094.39	130.20	34832.0	35259.0	12.4	B496
	445	2101.13	131.20	35259.0	35688.0	12.4	B497
	446	2107.87	132.20	35688.0	36119.0	12.4	B498
	447	2114.61	133.20	36119.0	36552.0	12.4	B499
	448	2121.35	134.20	36552.0	36987.0	12.4	B

Curriculum Vitae

Katherine Elizabeth Potter,

(July 2014)

Education:

B.S.: Geology, 2005, Fort Lewis College, Durango, CO; May, 2005, GPA: 3.30

M.S.: Geology, 2010, Idaho State University, Pocatello, ID; May 2010, GPA: 3.82

PhD: Geology, 2014, Utah State University, Logan, UT; May, 2012, GPA: 3.71

Honors and Awards:

Rocky Mountain Association of Geologists Neal J. Harr Outstanding Student Award, Fort Lewis College, 2005.

Student Membership Nomination, Sigma Xi, Fort Lewis College, 2005

'Outstanding Presentation' Geothermal Resources Council National Meeting, San Diego, CA, 2012.

Outstanding PhD researcher, 2012, Utah State University

Dr. Bob Oakes Citizenship Award, 2014, Utah State University

Membership in Professional Societies:

American Association of Petroleum Geologists (Vice President, 2013-2014)

American Geophysical Union

Geological Society of American

Sigma Xi (student member)

Professional Experience:

Geologist Intern, Anadarko Petroleum Corporation

May 2013-August 2013

- Interpreted seismic data and correlated gamma and resistivity logs to identify exploration targets in the Gulf of Mexico
- Learned and used a variety of new software and tools to reconstruct the basin history, determine charge timing, and estimate resource volume
- Carried out full petroleum system evaluation in a structurally complex area with limited available data

Project Hotspot Chief Scientist

October 2010-January 2011

- Manage core logging team & supervise core logging operations
- Coordinate with DOSECC drill crews to optimize drilling progress
- Evaluate and document mineralogical and structural anomalies in core
- Identify rock and soil types and probable depositional history
- Report progress of drilling & summarize petrologic observations for Project Hotspot/DOE/DOSECC investigators

USGS Lab Tech

June 2008-August 2008 USGS, Idaho National Laboratory

- Examined 1198 feet of basalt core (and some sediment interbeds) from core hole USGS 135 in the southwest corner of INL
- Interpreted basalt flow boundaries based upon lithologic and textural features
- Created a lithologic, conductivity, and porosity log of USGS 135 for future publication and use in SRP aquifer studies

Geologist

January 2007-June 2008 EMC/Golden Predator/Uranium One, Durango, CO

- Evaluated assay values, geologic maps, and geophysical/lithologic logs
- Recommended viable U.S. & Canadian mining properties based upon the above evaluations
- Acted as a consultant at a newly acquired tungsten mine outside of Winnemucca, NV, where I assisted in organizing, digitizing and evaluating older assay data, stope and geologic maps, and lithologic logs

Academic Experience:

Senior (Undergraduate) Thesis, Fort Lewis College, May 2006

'A petrochemical test of competing ideas on the emplacement of South Mountain Rhyolite, Valles Caldera, NM.'

- Advised by Dr. David Gonzales (Fort Lewis College) and Drs. Fraser and Cathy Goff (University of New Mexico and formerly Los Alamos National Laboratory)
- Used ICP-MS major and trace element data and petrography to determine the origin and relationship of rhyolite flows on South Mountain, a post eruptive dome emplaced within the Valles Caldera.
- Presented poster and published abstract: Potter, K., Gonzales, D., Goff, F., Goff, C., 2006, 'A petrochemical test of competing ideas on the emplacement of South Mountain Rhyolite, Valles Caldera, NM: Geological Society of America 58th Annual Meeting, Gunnison, Colorado, GSA Abstracts with programs, vol. 38, No. 6, p. 37 (Abstract attached)
- Invited speaker, Four Corners Geological Society, May 2006

Publication:

Gonzales, D.A., Potter, K.E., Turner, B.E., 2010, Geologic Map of the Bayfield Quadrangle, La Plata County, Colorado: Colorado Geological Survey Open File Report 08-15, scale 1:24,000

Masters Thesis, Idaho State University, August 2010

'Subsurface stratigraphy of the Arco-Big Southern Butte volcanic rift zone and implications for late Pleistocene volcanism, Eastern Snake River Plain, Idaho'

- Advised by Dr. Scott Hughes
- Used Inductively Coupled Plasma Mass Spectrometry (ICP-MS) and X-ray Fluorescence (XRF) for major and trace element analysis of 56 samples collected from USGS 135 core, drilled in the Idaho National Laboratory on the eastern Snake River Plain
- Identified and correlated basalt flow groups based upon geochemistry, lithologic logs, petrographic analyses, published geophysical logs, and paleomagnetic logs
- Presented poster at December 2009 annual American Geophysical Union (AGU) national meeting. (Abstract attached)

Publication:

Hodges, M.K.V., Potter, K.E., LeMaitre, T.R., (in press), Construction diagrams, geophysical logs, and lithologic descriptions for boreholes NRF 15, NRF 16, USGS 103, 105, 108, and 135, Idaho National Laboratory, Idaho: U.S. Geological Survey Data Series Report

PhD Dissertation, Utah State University, Spring 2014

'The Kimama Core: A 6.4 Ma Record of Volcanism, Sedimentation, and Magma Petrogenesis on the Axial Volcanic High, Snake River Plain, ID'

- Advised by Dr. John Shervais
- Using ICP-MS and XRF for major and trace element analysis, and Thermal Ionization Mass Spectrometry (TIMS) and NU-1700 High Resolution Multi-Collector Inductively Coupled Mass Spectrometry (MC-ICPMS) for isotope analysis, of 250 basalt samples collected from the 1912 m Kimama core. This core was drilled approximately 20 miles north of Burley, Idaho in the central Snake River Plain through the DOE/ICDP-funded Project Hotspot
- Identified and correlated individual basalt eruptive suites within the Kimama core based upon lithological, geochemical, and geophysical log data
- Presented talk at the May 2011 annual meeting of the Rocky Mountain/Cordilleran sections of the Geological Society of America (GSA) (Abstract attached)
- Presented talk at the October 2011 annual meeting of the Geothermal Resources Council (GRC).
- Speaker at the December 2013 annual AGU national meeting.
- Speaker at the 2013 annual GSA national meeting.

Publication:

Potter, K.E., Shervais, J.W., Sant, C.J., (2011) Project Hotspot: Insight into the subsurface stratigraphy and geothermal potential of the Snake River Plain: Geothermal Resources Council Transactions, vol. 35.

Software Experience:

Familiarity with and/or proficiency in use of Petrosys, Petra, Landmark, Seisworks, Adobe Illustrator, Matlab, and Excel.